Precision element modelling for long term tracking in the LHC luminosity upgrade

A thesis submitted to the University of Manchester for the degree of
Doctor of Philosophy
in the Faculty of Engineering and Physical Sciences

2014

David Brett

School of Physics and Astronomy

Contents

Total word count: 36,920

List of Tables

List of Figures

Abstract

As part of the Large Hadron Collider high luminosity upgrade it is proposed to include crab cavities and large aperture Nb_3Sn final focussing magnets in the lattice in order to enhance the luminosity. In this thesis the dynamics of a proposed cavity design were considered in terms of their impact upon the dynamic aperture of the machine. Taylor maps for the cavity were created and used to perform this analysis with a full assessment of their validity. A set of symplectic thin cavity models were also developed and cross checked with the Taylor maps. Finally, dynamic aperture studies were performed using these models in order to determine which components of the crab cavity dynamics are important when considering the long term stability of the beam in the LHC upgrade. It is shown that crab cavities exhibit little impact on the LHC beam stability. For the final focussing magnets a preliminary study was conducted into the importance of including their fringe fields in a model of the LHC upgrade. A technical study was carried out into developing a symplectic model which was compatible with the current magnet models use for dynamic aperture studies. A preliminary dynamic aperture study was performed with the inclusion of fringe fields for the final focussing magnets from which the fringe fields are shown to have a negative impact on the long term beam stability.

Declaration

No portion of the work referred to in this thesis has been submitted in support of an application for another degree or qualification of this or any other university or other institution of learning.

David Brett
School of Physics and Astronomy
University of Manchester
Oxford Road
Manchester
M13 9PL
2014

Copyright

Library, The University Librarys regulations (see `http://www.manchester.ac.uk/library/aboutus/regulations`) and in The Universitys policy on presentation of Theses.

The Author

The author was awarded a first class MPhys (Hons) degree in Physics with Theoretical Physics at the University of Manchester in 2010, and began the work presented in this thesis shortly afterwards. This research was undertaken at the University of Manchester between October 2010 and March 2014 in collaboration with the CERN accelerator and beam physics group.

Acknowledgements

I'd firstly like to thank my supervisor Rob Appleby whose careful supervision and guidance has enabled this project to happen. In the first year of my PhD, studies were dedicated to backgrounds in the LHCb detector, however, after discussions at a conference in Glasgow with Graeme Burt, whose cavity is the main focus of this thesis, the project completely changed.

I have received a large amount of support from CERN and the Cockcroft Institute. Special thanks goes to Javier Barranco, Rogelio Tomás and Riccardo De Maria for their support in developing crab cavity models in SixTrack and interpretation of results, Alexej Grudiev for providing the field data, and Ben Hall and Graeme Burt for designing the cavity. Further thanks goes to Massimo Giovannozzi and Frank Schmidt for their fruitful discussions on the dangers of non-symplectic objects and complexities of SixTrack.

I'd like to the thank the Manchester High Energy Particle group for their hospitality and copious supply of chocolate and cake. Thanks to Sabah Salih for seemingly being able to fix the computers at any time of day, 365 days a year.

I'm grateful to all those who have painstakingly read through this thesis in an attempt to reduce mistakes, with special thanks to my mother-in-law Bridget and colleagues Ewen and Aaron. I'd also like to thank all those with whom I have shared an office over the past few years for encouragements, fruitful discussions and off the wall conversations. Furthermore, I'd like to thank my friends and family whose thoughts and prayers have been a great support.

Finally I'd like to thank my wife Lou who has been a constant support practically, emotionally and spiritually through the process of finishing my PhD.

The heavens declare the glory of God; the skies proclaim the work of his hands. (Psalm 19:1)

Chapter 1

Aim

In 2010 the Large Hadron Collider (LHC) became the world's largest and most powerful particle accelerator. The LHC is a 27 km ring of superconducting magnets, which is buried over 100 m below the France-Switzerland border near Geneva. It delivers proton-proton collisions to four different high energy particle physics detectors. A key performance factor in its operation is the rate at which collisions can be delivered to these detectors, which is proportional to the luminosity. A number of new technologies are being developed to increase luminosity for a proposed upgrade to in 2022. This thesis considers two questions about these new technologies:

1. **Which components of the crab cavity dynamics are important when considering the long term stability of the LHC upgrade?**

   Crab cavities are a new technology being introduced as part of this upgrade. Crab cavities are RF cavities which rotate bunches in order that they can overlap completely at the collision point thereby providing an increase in luminosity. Furthermore, not only do they allow complete correction of the overlap but also control over the luminosity. The crab cavity designs have

significant geometric constraints in order to fit into the LHC machine, leading to exotic cavity designs which exhibit complex electromagnetic fields. These fields lead to complex non-linear dynamics which must be understood with respect to their affect upon the LHC.

2. **Are fringe fields important when considering the long term stability of the LHC upgrade?**

   New final focussing magnets are another addition necessary for the LHC upgrade. A rectangular function (or hard edge model) is normally used to describe a magnet in LHC models. The magnetic field in this model fails Maxwell's equations as they go to zero at the edges of the magnet. The additional components of the field neglected in this hard edge model are described as fringe fields and the new large aperture Nb_3Sn final focussing magnets of the upgrade have fringe fields which are possibly significant to the long term stability of the machine.

In chapter 2 the context and the theory required to understand the dynamics of the LHC are introduced. The need for the new final focussing magnets and crab cavities is also explained. It shows that a hadron machine's stability can be particularly vulnerable to non-linear motion due to the lack of any damping mechanisms such as synchrotron radiation. In order to predict the beam stability of a machine such as the LHC, a large number of turns are required to be tracked in order to understand the impact of the non-linear motion. This long term tracking requires both numerical stability and a precise model of the accelerator. As accelerators have developed many different mathematical methods have been considered for tracking particles through them.

In chapter 3 a generalised model to represent a crab cavity is considered in the form of a Taylor map. The methods to construct the Taylor map and the dynamics contained within provide a method to consider the complete picture

of the crab cavity dynamics. Furthermore the non-symplectic nature of Taylor maps is also discussed.

In response to the non-symplectic nature of Taylor maps a series of thin lens models are considered in chapter 4. These models provide a symplectic approach to modelling the crab cavities considering only specific components of the crab cavity dynamics. These can be compared directly with the Taylor maps to consider the model limitations in terms of the missing dynamics.

In chapter 5, the impact of the crab cavities on the long term stability of the LHC upgrade is investigated. This long term stability is defined in terms of a dynamic aperture which is a time based measurent of the hypersphere in phase space within which particles remain in the machine i.e. not lost. By using a number of crab cavity models, devised in this thesis, a series of studies are performed to determine the components of the crab cavity dynamics that are important to the long term stability of the LHC upgrade.

Finally, in chapter 6 a preliminary study is performed to consider the methods in which to simulate the fringe fields in the LHC upgrade. The limitations of a proposed model are then considered and a first study performed to determine whether fringe fields need to be considered in future long term stability studies for the LHC upgrade.

Overall, in this thesis, the dynamics of the crab cavities and fringe fields in the context of the LHC upgrade are studied in terms of their impact upon long term stability.

Chapter 2

Introduction to the HL-LHC and single particle dynamics

In order to understand the need for crab cavities, in the context of the LHC upgrade, the dynamics of proton colliders, including the transverse beam dynamics and concept of luminosity, must first be introduced. These are introduced in sections 2.1 and 2.2. The details of the upgrade and the specifics of the crab cavities are required in order to develop models of crab cavities. These are presented in sections 2.3 and 2.4. Finally in section 2.5, the mathematical framework required to develop these models is explained. Overall this chapter provides an overview of the beam dynamics of particle colliders, the high luminosity LHC upgrade and the framework for constructing new models for accelerator elements.

2.1 Introduction to colliders

2.1.1 A brief history of accelerators

Accelerators from their earliest development have allowed greater understanding of the fundamental constituents of our observable universe. The very first discoveries were made by J.J. Thomson [1] in 1896 who used a cathode ray tube to measure the charge to mass ratio of an electron, as shown in figure 2.1. This type of accelerator used direct current (DC) to develop a potential between a cathode (C in figure 2.1) and an anode (A in figure 2.1) inside a vacuum vessel and a pair of charged plates (D and E in figure 2.1) were used to bend the beam.

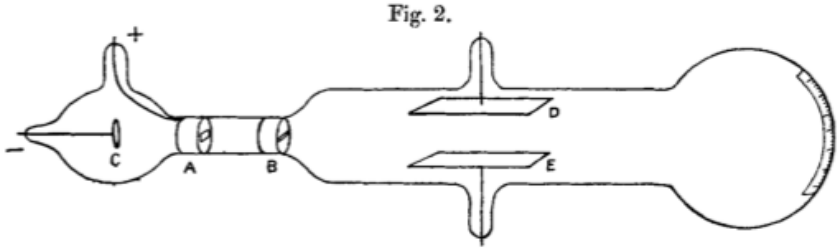

Figure 2.1: J.J. Thomson's cathode ray tube [1]

In 1932, the next major particle physics discovery made with an accelerator was developed by Cockcroft and Walton [2] in which a lithium nucleus was bombarded with 800 KeV protons to form two helium nuclei. This kind of nuclear experiment, involving a fixed target and acceleration via a direct current, continued to be developed with further discoveries about the nucleus. However, this DC approach has a limit of around 20 MV at which point it becomes very hard to accelerate the particles to higher energies due to electrical breakdown on surfaces. The largest such machine was the Nuclear Structure Facility at Daresbury shown in figure 2.2.

To overcome the limitations of DC acceleration two methods were proposed, one a linear accelerator, and the other a circular accelerator. The initial concept

Figure 2.2: The Nuclear Structure Facility, Daresbury [3], the world's highest voltage machine (1983-1992)

for a linear accelerator came from Ising in 1924 [4]. The idea was developed and eventually patented by Widerøe in 1928 [5], who used a series of increasing length drift tubes with an alternating current (AC) voltage applied to the tubes. The particles see the accelerating voltage in the gaps between tubes, with increasing drift tube length required to allow the particle to synchronise with the kick applied by the field between the tubes. Based on this principle of accelerating across gaps with an AC voltage, Lawrence in 1934 patented the cyclotron [6]. Lawrence had noted from Widerøe's work that each accelerating gap required increasing spacing in order to account for the particle's increasing velocity. He realised that by passing through the same gap multiple times and using a magnet to bend the path of the particles only one gap would be required. This is shown in figure 2.3 and was the first machine to exhibit multiple pass and resonant acceleration features.

The fundamental idea underpinning the cyclotron is that the path length exhibited by the charged particle when crossing the gap increases with the path's radius r, while the transit time remains constant. In a cyclotron the radius, r, of

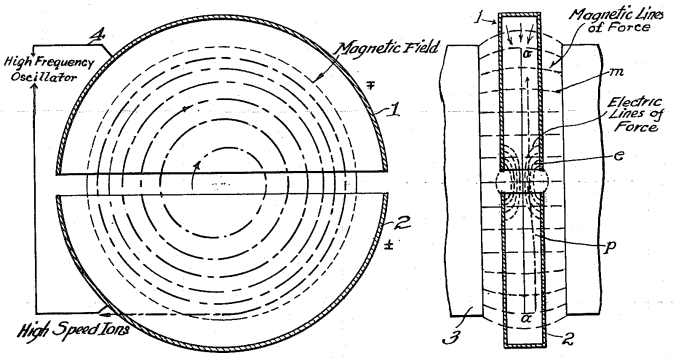

Figure 2.3: Cyclotron schematic from Lawrence's 1934 patent [6]

the accelerated particle has the dependency,

$$r = \frac{\gamma m v}{eB} \tag{2.1}$$

where γ is the relativistic factor, m is mass, v is speed, e is charge and B is the magnetic field strength perpendicular to the plane of motion.

In order for synchronism, in which the high frequency oscillator's frequency matched the rotation frequency of the accelerated particle, $\gamma \approx 1$ must hold. With larger cyclotrons even higher energies of particles were attained heading towards a limit at which synchronism is lost as $\gamma \not\approx 1$. In order to overcome this relativistic effect the first proposed solution was the synchrocyclotron which was patented by McMillan [7], in which the radio frequency source is varied to compensate for the variation in rotation frequency of the accelerating particle. In 1957 the first accelerator to be built at CERN was a 600 MeV synchrocyclotron accelerating protons for fixed target experiments, shown in figure 2.4.

The synchrotron was the advance in which the relativistic effects were overcome by varying the magnetic fields rather than the RF frequency. In 1952 a very important breakthrough came in the form of the principle of strong focussing [9] which allows the components of the accelerator to be separated rather than have

Figure 2.4: 600 MeV Synchrocyclotron, CERN [8]

one singular massive magnet. Such synchrotrons with separated magnetic components are called strong-focussing synchrotrons. In 1959 the Proton Synchrotron (PS) was the first sychrotron to be built at CERN, and accelerated protons to an energy of 28 GeV.

Early particle physics experiments, such as those of Cockcroft and Walton [2], were performed using fixed targets. However, fixed target experiments are limited in terms of their centre of mass energy, where significant gain can be made in colliding two beams. Considering the simple case of two particles colliding with masses m_1 and m_2, both with the same beam energy E_{beam}. The centre of mass energy for two colliding beams is given by,

$$E_{\text{CM}} = 2E_{\text{beam}}. \tag{2.2}$$

The centre of mass energy for a fixed target of particle type 2 and a beam of particle type 1 is given by,

$$E_{\text{CM}} = \sqrt{m_1^2 + m_2^2 + 2m_2E_{\text{target}}}, \tag{2.3}$$

where E_{target} is the energy of the beam. In order to reach the same center of mass energy the fixed target beam energy, in terms of the collision beam energy,

is given by,

$$E_{\text{target}} = \frac{4E_{\text{beam}}^2 - m_1^2 - m_2^2}{2m_2}. \tag{2.4}$$

There are two groupings of species used in colliders: leptons and hadrons. Lepton machines, in terms of particle physics, provide clean collisions in which the centre of mass energy of the collision is directly known. Lepton colliders, such as LEP and PEP-II, specialise in precision measurements. Synchrotron radiation occurs when a charged particle is accelerated radially and is a mechanism for particle energy loss [10]. The total radiated power from synchrotron radiation for a particle in a bending magnet is proportional to

$$P \propto \frac{E^4}{\rho^2}, \tag{2.5}$$

where E is the particle's energy and ρ is the bending radius of the particle's trajectory [10]. This synchrotron radiation loss requires additional power from the RF system to maintain the beam energy, leads to radiation damage in the accelerator [10] and generates a background in particle detectors. A hadron machine can attain a higher beam energy in a smaller radius machine for the equivalent power of a lepton machine, since hadrons are considerably heavier than leptons. The main disadvantage of hadron colliders is that hadrons are not fundamental particles and are instead made up of quarks and gluons. This property leads to the centre of mass energy of the actual collision having some level of uncertainty due to interactions occurring between individual quarks of unknown energy rather than fundamental particles of known energy. In a detector some particle species produced in a collision will not generate a signal and instead the missing energy will be used to determine the missing species. However, due to the uncertainty in the original collision centre of mass energy in a hadron collider it is not possible

to accurately determine this missing energy from a single collision.

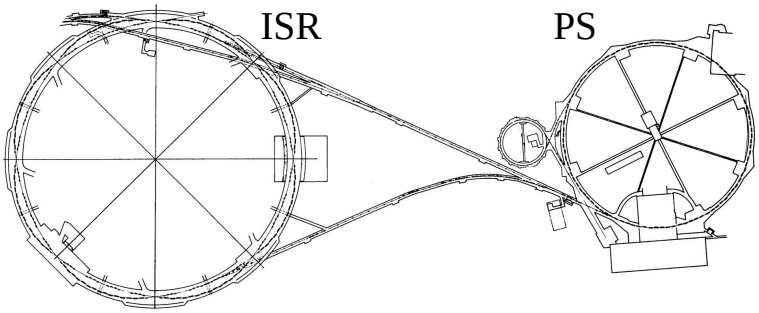

Figure 2.5: Intersecting Storage Rings (ISR) and the proton synchrotron (PS), CERN [11]

The first hadron collider was developed at CERN and was called the Intersecting Storage Rings (ISR), shown in figure 2.5. It consisted of 2 interlaced rings of diameter 150 m, colliding protons with a centre of mass energy of 62 GeV and operated between 1971 and 1984. A low β insertion is a region of an accelerator in which the beams are strongly squeezed in order to achieve very small transverse cross sections. The ISR was the first machine to exhibit include low β insertions at its interaction points (IPs) [12]. Relatively little physics was investigated at the ISR due to a significant lack of detector capabilities. However, it did enable greater understanding of the physics required to build and operate large scale hadron colliders.

The Large Electron-Positron Collider (LEP) [14] operated at CERN between 1989 and 2000, with a circumference of 27 km and top centre of mass energy of 209 GeV. This machine enabled precise measurements of the properties of the W and Z bosons. At a similar time the Tevatron (shown in figure 2.6) operated at Fermilab between 1987 and 2011, during which the top quark was discovered, colliding protons with antiprotons with, after many upgrades, a top centre of mass energy of 1.96 TeV. In terms of physics, these two colliders hinted at the existence of the theorised Standard Model Higgs Boson [15], however, during their

Figure 2.6: Tevatron, Fermilab [13] (1987-2011)

operation they were unable to conclude its existence. The principle of colliding particles with their antiparticles allows the same dipole magnets to be shared for the two counter-rotating beams, however, the difficulty in producing large numbers of antiparticles creates a limit in the beam intensities. For this reason the LHC [16] was designed to collide two counter-rotating proton beams.

2.1.2 LHC

The LHC is a two ring, superconducting accelerator and collider. The first collisions occurred in March 2010 with a centre of mass energy of 7 TeV. It was installed in a 27 km tunnel previously used for LEP [14], with the physics objective of searching for the Higgs boson and other new particles as well as studying rare events [16]. The observation of an event is dependent on the collision rate generated by the LHC machine such that the number of events per second N_{event} is given by,

$$N_{\text{event}} = \mathcal{L} \times \sigma_{\text{event}} \tag{2.6}$$

where $\mathcal{L}$ is the luminosity and σ_{event} is the cross section of the event. The luminosity of the machine will deteriorate over time due to various loss mechanisms,

primarily proton burn from collisions at the interaction point, but also collisions with restrictive apertures resulting from chaotic motion, reducing the effective performance of the machine. The stated performance factor of a collider is given by its peak luminosity, at the end of the first run the LHC had a peak luminosity of $\approx 7 \times 10^{33}\text{cm}^{-2}\text{s}^{-1}$, with a centre of mass energy of 8 TeV [17].

The LHC has 4 interaction points (IP) at which the beams cross and experimental detectors exist. ATLAS [18] and CMS [19] are located at IP1 and IP5 and are general purpose experiments which have the highest delivered luminosity, created through having the greatest squeezed beams. LHCb [20] investigates b quark and CP violation and exploits the copious amounts of b quarks produced at the LHC. It is located at IP8 and operates at a luminosity ≈ 20 times lower than the general purpose experiments. ALICE [21] is a dedicated heavy-ion detector, particularly optimised for use during Pb-Pb collisions in the LHC which is located at IP2 and operates at a luminosity of $\approx 10^5$ times lower than that of ATLAS and CMS; this is a result of the slow triggering rate of ALICE's sub detectors, which require a low number of collisions at each bunch crossing in order to limit the signal from the detector.

The machine is made up of eight octants, as shown in figure 2.7, made up of a straight insertion region (IR), and arc regions, which contain the main bending dipoles. The bending dipoles define the energy limit of the machine, with the nominal field of 8.33 T corresponding to a beam energy of 7 TeV [16]. The LHC as it stood before its first long shut down was unable to attain this beam energy due to issues surrounding the power connections between superconducting magnets. A series of further planned shutdowns are included in the lifetime of the LHC in order to increase the operating performance of the machine, and allow for the experiments to upgrade in order to make full use of the increased machine performance.

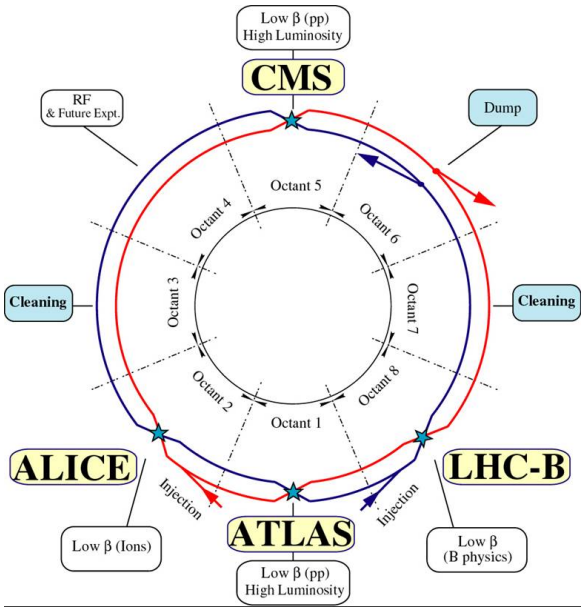

Figure 2.7: Schematic of the basic LHC layout [22].

Two long shutdowns, starting around 2013 and 2018 and lasting approximately 18 months, were planned before the upgrade of the machine to the HL-LHC, shown in figure 2.8 along with the planned luminosity. The main aim of the first long shutdown is to repair the superconducting interconnection between magnets. In 2008, during the first powering tests of the machine, a fault occurred

Figure 2.8: Proposed long shutdown time plan against luminosity [23].

in one such interconnection leading to significant damage to a section of the machine. In order to prevent other such incidents the current passing through these interconnects has been limited during the first operational period of the machine, preventing the dipole magnets from reaching their nominal field and the machine from reaching its maximum design energy. In order to overcome this limitation the interconnects are being upgraded with the addition of a shunt. This is a low resistance path alternative to the superconducting connection used in the event that the interconnect loses its superconducting state [24].

The second long shutdown is aimed to begin in 2017, and will be focussed primarily on upgrading the injection chain to the LHC to reduce the machine emittance below that of the nominal LHC [25, 17]. This upgrade includes the addition of Linac4 to the injection chain to increase the available beam current (see figure 2.9), reducing the electron cloud in the SPS, and the application of transverse dampers in the PS and SPS. The transverse dampers dampen injection errors by using a feedback loop including pickups and electrostatic kickers. Furthermore the second long shutdown seeks to upgrade the LHC collimation with dispersion suppression section collimation (if needed) [26].

2.2 Collider beam dynamics

The dynamics of hadron colliders, in general, are dominated by the transverse motion of the particles as they orbit inside the machine. This transverse motion is often non-linear and can lead to it being chaotic, thereby leading to losses in the restrictive apertures of the machine. It is important to build an understanding of the features of this motion in order to better design, develop and operate a hadron collider.

The basic accelerator coordinate system, shown in figure 2.10, considers the motion of a particle relative a reference particle travelling around a reference orbit

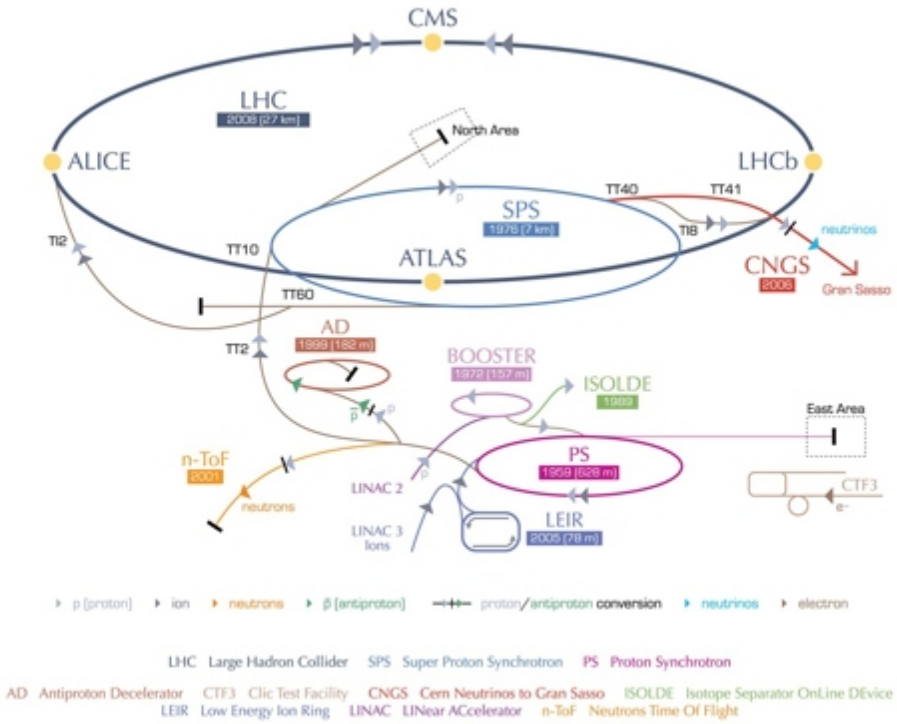

Figure 2.9: CERN accelerator complex including the addition of Linac4 [27].

s of length L. The reference orbit is often chosen to coincide with the closed orbit which is defined by the orbit at a given energy which has the same initial and final positions over one period of the machine. The period of the machine relates to its design and for larger machines such as the LHC often equates to one turn. The transverse unit vector in the plane of the reference orbit, perpendicular to the unit vector $\hat{s}$, is $\hat{x}$. The vector perpendicular to this is $\hat{y}$.

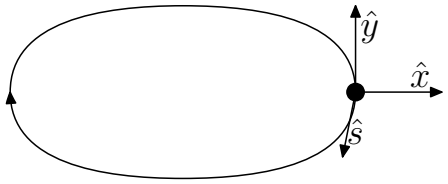

Figure 2.10: Accelerator coordinate system.

2.2.1 Transverse beam dynamics

Hill's equations and β-functions

In the transverse plane there are two degrees of freedom, with the spatial coordinates x and y and respective associated angles x' and y'. Hill's equations [28] describe the equations of motions for a linearised system with periodic focussing properties, such as those in the transverse plane of a circular accelerator,

$$\begin{aligned} x'' + K_x(s)x = 0, \\ y'' + K_y(s)y = 0, \end{aligned} \tag{2.7}$$

where K is a position dependent force, which for a periodic machine is therefore a periodic force. These equations neglect higher order terms in x and momentum dependence. From this information a periodic harmonic motion can be described [9], where the amplitude β and phase ψ will depend on the position s in the ring such that,

$$x(s) = \sqrt{\varepsilon}\sqrt{\beta(s)}\cos(\psi(s) + \phi) \tag{2.8}$$

where ε and ϕ are constants. Due to the periodicity for a machine of circumference L, the β-function has a periodic boundary condition such that $\beta(s) = \beta(s + L)$. Furthermore, the phase advance $\psi(s)$ is defined by,

$$\psi(s) = \int_0^s \frac{ds}{\beta(s)}. \tag{2.9}$$

The tune is defined by the number of oscillations per turn and hence is dependent on the phase advance over the whole turn such that

$$Q_x = \frac{1}{2\pi}\int_s^{s+L} \frac{ds}{\beta(s)} = \frac{1}{2\pi}\oint \frac{ds}{\beta(s)}. \tag{2.10}$$

In a similar definition to the transverse position, $x(s)$, around the ring, the transverse angle, $x'(s)$, can also be defined in terms of the amplitude and phase,

$$x'(s) = -\frac{\sqrt{\varepsilon}}{\sqrt{\beta(s)}}\left(\alpha(s)\cos(\psi(s)+\phi) + \sin(\psi(s)+\phi)\right) \tag{2.11}$$

where $\alpha(s) \equiv -\beta'(s)/2$. The transverse angle $x'(s)$ is defined by the rate of change of x with s. Introducing one more variable $\gamma(s) \equiv (1+\alpha(s)^2)/\beta(s)$ and inserting into Hill's equations, the Courant-Snyder invariant [9] is derived,

$$\gamma x^2 + 2\alpha x x' + \beta x'^2 = \varepsilon. \tag{2.12}$$

This invariant ε in phase space takes the form of an ellipse as shown in figure 2.11, where the area of the ellipse is the invariant and the shape of the ellipse is defined by β, α and γ.

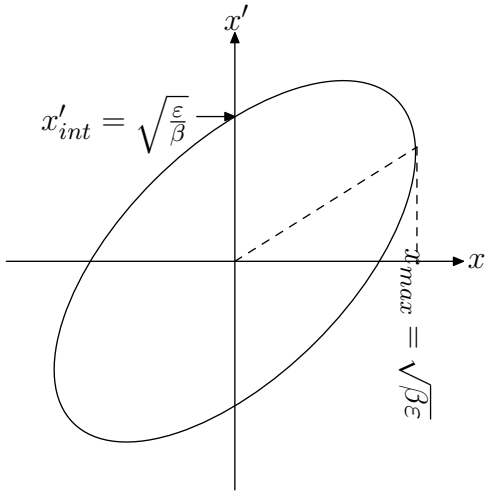

Figure 2.11: Relationship between β and ε and beam phase space ellipse [29, p. 73]

The β-function is directly related to the phase space area occupied by the beam and is characterised by the emittance ε. The emittance remains invariant under the condition that there are no collective effects [30], such as interaction

with other particles in a bunch, at a fixed energy. As a bunch accelerates inside an accelerator the process of adiabatic damping occurs at which the emittance reduces as the momentum increases. Normalised emittance is an energy independent measurement and is defined by,

$$\varepsilon^* = \beta_0 \gamma_0 \varepsilon \tag{2.13}$$

where β_0 is the speed as a fraction of c and γ_0 is the relativistic factor. For a Gaussian bunch, which is Gaussian distributed in all three spatial directions, with a standard deviation σ, 15% of the area occupied by the phase space ellipse encloses the beam [29, p. 66], where σ is related to the β-function by,

$$\sigma_{x,y} = \sqrt{\varepsilon_{x,y} \beta_{x,y}}. \tag{2.14}$$

The emittance of a Gaussian bunch defines the phase space area containing a fraction F of the beam [29],

$$\varepsilon = -\frac{2\pi\sigma^2}{\beta} \ln(1 - F). \tag{2.15}$$

The control of the amplitude and phase around a strong focussing synchrotron is performed using a series of magnets.

Magnets

The lattice of an accelerator describes the composition of the series of magnets surrounding the vacuum pipe. These magnets are categorised in terms of their rotational symmetry, with 3 examples shown in figure 2.12.

In the ultra-relativistic limit these magnets are often expressed solely in terms of their transverse magnetic fields. In the simplest case this is expressed as a

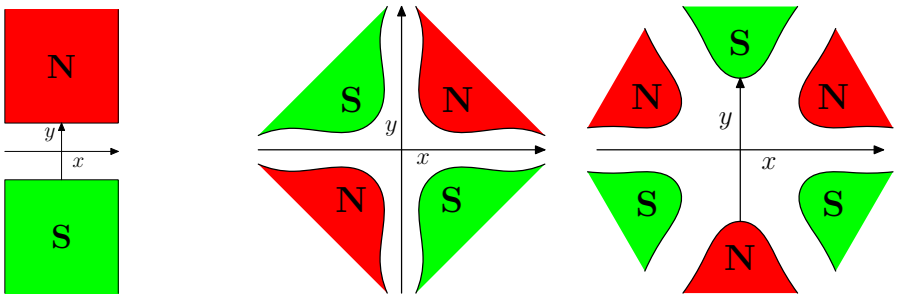

Figure 2.12: Magnet profiles with rotational symmetries. (a) Dipole b_1, (b) quadrupole b_2, and (c) sextupole b_3.

multipole expansion [31][1],

$$B_y + \mathrm{i}B_x = \sum_{n=1}^{\infty} (b_n + \mathrm{i}a_n)\,(x + \mathrm{i}y)^{n-1}\,, \tag{2.16}$$

where b_n and a_n are the normal and skew coefficients and n refers to a magnet with $2n$ poles. This follows from the Laplace equation in two dimensions where it is assumed there are no B_z fields. Real magnets, owing to their construction, exhibit a range of errors in the form of these magnetostatic multipoles. In this ultra-relativistic limit, considering a charged particle undergoing a periodic orbit, the relationship between the radius of curvature ρ and perpendicular magnetic field B_y is given by,

$$qvB_y = \frac{\gamma m v^2}{\rho}, \tag{2.17}$$

where q is the charge of the particle, v is the speed on the path of the orbit, m is the mass of the particle, ρ is the radius of curvature, and B_y is the magnetic field perpendicular to the plane of motion. This was already seen to describe the motion of the particle in a cyclotron in equation 2.1. Rearranging equation 2.17

[1] European multipole convention.

in terms of momentum, which is defined by $p = \gamma mv$, results in,

$$\frac{1}{\rho(x,y,s)} = \frac{e}{p}B_y(x,y,s). \tag{2.18}$$

In the case where B_y is constant there is no option to focus or control the size of the beam, but by Taylor expansion of B_y and $1/\rho$ for small variations in x the separated magnets described by the multipole expansion arise,

$$\frac{1}{\rho} + kx + \frac{1}{2!}mx^2 + \ldots = \frac{e}{p}B_y + \frac{e}{p}\frac{dB_y}{dx}x + \frac{1}{2!}\frac{e}{p}\frac{d^2B_y}{dx^2}x^2 + \ldots \tag{2.19}$$

where the dipole magnet determines the curvature ρ, the quadrupole magnet with strength k applies a linear force in the plane of the orbit and the sextupole with strength m applies a non-linear force in the plane of the orbit.

Chromaticity and dispersion

A stable particle in a circular accelerator will have an equilibrium orbit about which the particle will undergo betatron oscillations. This orbit will have a momentum dependency described by the dispersion function D such that,

$$x(s) = \mathrm{D}(p,s)\frac{\Delta p}{p_0}. \tag{2.20}$$

The dispersion function is periodic therefore $\mathrm{D}(p,s) = \mathrm{D}(p,s+L)$ and in a circular accelerator this leads to differing path lengths in equilibrium orbit. This variation in path length is described by the compaction factor α_p,

$$\alpha_p = \left\langle \frac{D}{\rho} \right\rangle, \tag{2.21}$$

where ρ is the radius of curvature. This describes the linear path variation such that,

$$\frac{\Delta L}{L} = \alpha_p \frac{\Delta p}{p_0}, \tag{2.22}$$

where L is the path length at the reference momentum p_0.

Chromaticity is the change in linear optics parameters with the beam energy. In addition it defines the change in tune with respect to the change in momentum [29, p. 66]. Linear chromaticity, Q', arises from the linear optics (i.e. quadrupoles) and is corrected for by sextupoles,

$$Q'(p) = \mp \frac{1}{4\pi} \oint \beta(s) \left[k(s) + m(s) D(p,s)\right] \, \mathrm{d}s, \tag{2.23}$$

where $k(s)$ and $m(s)$ are the quadrupole and sextupole strengths. The component of the linear chromaticity resulting from the quadrupoles is called the natural chromaticity. The chromaticity correction from the sextupoles is proportional both to the β-function and sextupole strength at a given point of correction. Nonlinear chromaticity, Q'', is defined by the quadratic and higher dependencies of the tune on the momentum. This tune variation with momentum can be expressed in the form of a Taylor expansion,

$$Q(p_0 + \Delta p) = Q(p_0) + Q'(p_0)\Delta p + \frac{1}{2!} Q''(p_0) \Delta p^2 + \frac{1}{3!} Q'''(p_0) \Delta p^3 + \ldots \tag{2.24}$$

As greater amounts of beam focussing are used in accelerators more terms of this expansion are required to describe the chromatic dynamics of particle motion [32].

2.2.2 Luminosity

For a collider, the centre of mass energy and collision rate are its key performance goals [33]. The collision rate $\frac{dR}{dt}$ is related to the properties of the accelerator in

the form of the luminosity $\mathcal{L}$ by,

$$\frac{dR}{dt} = \mathcal{L} \times \sigma_p \tag{2.25}$$

where σ_p is the collision cross section.

Head on collision

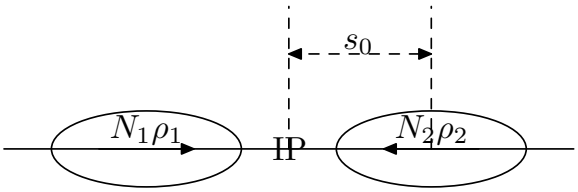

Figure 2.13: Head on bunch crossing [33].

From the simplest case of two bunches colliding head on, as shown in figure 2.13, with charge densities ρ_1 and ρ_2 respectively, N_1 and N_2 particles per bunch, the luminosity is given by [33],

$$\mathcal{L} \propto K N_1 N_2 \int\int\int\int \rho_1(x, y, s, -s_0)\rho_2(x, y, s, s_0)\,\mathrm{d}x\,\mathrm{d}y\,\mathrm{d}s\,\mathrm{d}s_0 \tag{2.26}$$

where K is a kinematic factor relating to the velocities $\vec{v}_{1,2}$ of the two bunches,

$$K = \sqrt{(\vec{v}_1 - \vec{v}_2)^2 - \frac{(\vec{v}_1 \times \vec{v}_2)^2}{c^2}}, \tag{2.27}$$

and $s_0 = ct$. By making a number of assumptions a simple luminosity relation can be derived. Firstly, assuming that the charge densities for each bunch are independent and separable in x, y and s, they can be factorised,

$$\rho(x, y, s, s_0) = \rho_x(x) \cdot \rho_y(y) \cdot \rho_s(s \pm s_0). \tag{2.28}$$

In the case of head on collisions the velocities will be equal and opposite such that $\vec{v}_1 = -\vec{v}_2$, this simplifies the luminosity to [33],

$$\begin{aligned}\mathcal{L} =& 2N_1N_2fn_b \\ &\times \int\int\int\int \rho_{1x}(x)\rho_{1y}(y)\rho_{1s}(s-s_0)\rho_{2x}(x)\rho_{2y}(y)\rho_{2s}(s+s_0)\,\mathrm{d}x\,\mathrm{d}y\,\mathrm{d}s\,\mathrm{d}s_0\end{aligned} \tag{2.29}$$

where f is the revolution frequency about the whole machine, and n_b the number of bunches per beam. Assuming that the bunches are Gaussian distributions, with standard deviation $\sigma^*_{x,y,s}$ at the IP, that there is zero dispersion at the IP, and that the two beams are equal ($\sigma_{1x} = \sigma_{2x}$, $\sigma_{1y} = \sigma_{2y}$ and $\sigma_{1s} = \sigma_{2s}$), the luminosity is given by [33],

$$\mathcal{L} = \frac{N_1N_2fn_b}{4\pi\sigma^*_x\sigma^*_y}. \tag{2.30}$$

This simple luminosity relationship is dependent on the number of bunches and the number of particles in each bunch. From equation 2.14 the luminosity is dependent on the emittance ε and β-function at the IP, β^*, such that,

$$\mathcal{L} \propto \frac{1}{\sqrt{\varepsilon_x\varepsilon_y\beta^*_x\beta^*_y}}. \tag{2.31}$$

Collision with long bunches

A further effect that occurs, in particular with long bunches, is the hour glass effect [33], which arises from the s dependence of the β-function. The β-function is a minimum at the IP, increasing either side approximately quadratically,

$$\beta_{x,y}(s) \approx \beta^*_{x,y}\left(1 + \left(\frac{s}{\beta^*_{x,y}}\right)^2\right), \tag{2.32}$$

leading to a variation in the σ with s,

$$\sigma_{x,y}(s) \approx \sigma^*_{x,y}\sqrt{1+\left(\frac{s}{\beta^*_{x,y}}\right)^2}. \tag{2.33}$$

This hour glass effect is important in the case where β^* is smaller than the bunch length σ_s and leads to a luminosity reduction factor of [33],

$$\mathcal{L}(\sigma_s) = \frac{N_1 N_2 f n_b}{4\pi\sigma^*_x\sigma^*_y}\cdot\left(\sqrt{\pi}\frac{\beta^*}{\sigma_s}e^{\left(\frac{\beta^*}{\sigma_s}\right)^2}\left(1-\mathrm{erf}\left(\frac{\beta^*}{\sigma_s}\right)\right)\right). \tag{2.34}$$

Collision with a crossing angle

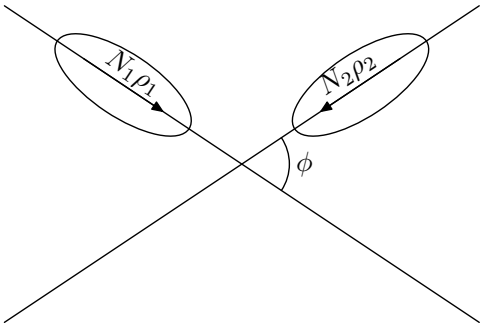

Figure 2.14: Bunch crossing with a crossing angle; required for colliders with many bunches or coasting beams to avoid unwanted collisions.

In a collider with many bunches or coasting beams it is necessary to have a crossing angle ϕ at the IP in order to avoid unwanted collisions. In figure 2.14 the crossing angle is shown to be defined as the acute angle between the two beams. There is a loss in luminosity, compared to that of a head on collision, due to the loss in overlap of the bunches as they cross at a crossing angle ϕ, with a $\mathcal{L}$ reduction of

$$\mathcal{L} = \frac{N_1 N_2 f n_b}{4\pi\sqrt{\varepsilon_x\varepsilon_y\beta^*_x\beta^*_y}}\frac{1}{\sqrt{1+\left(\frac{\sigma_s}{\sigma_x}\tan\frac{\phi}{2}\right)^2}}. \tag{2.35}$$

This effect can be seen graphically in figure 2.15. The Piwinski angle,

$\phi_p = \frac{\sigma_s}{\sigma_x} \tan \frac{\phi}{2}$, is the scaled angle to describe the combined effect of the dimensions of the bunch and the crossing angle upon the reduction in luminosity.

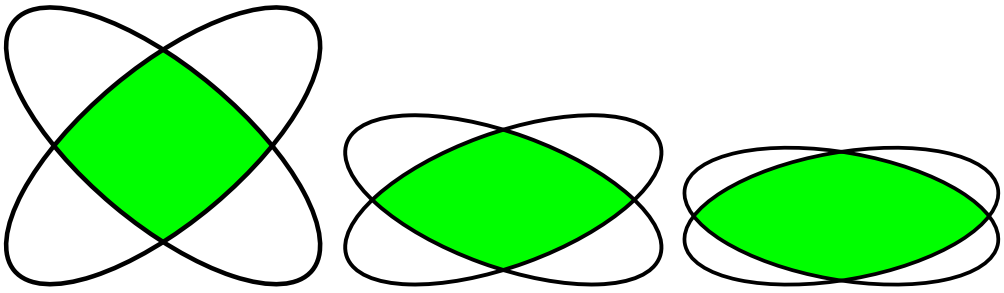

(a) (b) (c)

Figure 2.15: Effect of changing crossing angle ϕ, on the geometric overlap. ϕ set to (a) 40°, (b) 20°, and (c) 10°.

Beam-beam interaction

The beam-beam interaction is the electromagnetic interaction between the two beams, leading to a net defocussing of the beams in the case where the charge of the two beam species is of the same sign. This leads to tune shifts and instabilities in the accelerator. There are two types of electromagnetic beam-beam interaction, dependent upon the model required to describe their behaviour. The "weak-strong" interaction is where a single particle in the opposing beam can be treated with a force applied by a strong unperturbed beam. When the perturbation of both beams is important the interaction is described as "strong-strong" and single particle dynamics is no longer considered [34]. As the crossing angle is reduced the impact of beam-beam interaction is amplified. In equation 2.35 reducing the β^* of a beam would appear to allow for an increased luminosity. However, beam-beam interaction is also dependent upon β^* such that the beam-beam parameter is defined,

$$\xi_x = \frac{e_0^2}{4\pi\epsilon_0 mc^2} \frac{N_1 \beta_x^*}{2\pi\gamma\sqrt{\sigma_x^2 + \phi^2\sigma_s^2}(\sqrt{\sigma_x^2 + \phi^2\sigma_s^2} + \sigma_y)}, \tag{2.36}$$

where e_0, ϵ_0, m are the charge of an electron, permittivity of free space and mass of a proton respectively [29, p. 91]. The beam lifetime is determined in part by the Piwinski angle and the beam-beam parameter ξ_x [35], hence reduction of the β^* and changing ϕ do not directly lead to an integrated luminosity increase. Therefore, controlling the luminosity of a collider is not trivial. Methods such as the use of correction wires and electron lenses [34, 36] are proposed to overcome the dominant linear part of the force resulting from the beam-beam interaction.

Integrated luminosity

The instantaneous luminosity is time dependent, arising from the dependency of $N_{1,2}$ on time. The decay in $N_{1,2}$ is caused by proton burn at the IP, collective effects [30] and unbounded chaotic motion which lead to losses within the expected lifetime of the beam [37] in the accelerator. Collective effects are the interaction of accelerated particles with other accelerated particles, such as beam-beam interaction, and interaction of accelerated particles with the machine, such as wakefields. These collective effects lead to emittance growth, which leads to losses on restrictive apertures in the accelerator.

Pileup describes the number of collisions in one bunch crossing at an IP. With increased pileup a detector must be able to disentangle the products resulting from multiple collisions, however, the detectors ability to disentangle collisions is limited. With no other alterations to the luminosity over the beam lifetime the luminosity will undergo a continuous decay, leading to greater pileup at the beginning of a run beyond the capabilities of the detector, and under utilising the detector towards the end of the run. In order to overcome this, a technique known as luminosity levelling has been developed whereby altering the machine during operation the luminosity can be decreased at the beginning leading to a more even pileup over the course of a run. The luminosity without such alteration

is called the virtual luminosity and is higher than the levelled luminosity.

Luminosity can be controlled in a number of ways; crab cavities can be used to recover the loss due to crossing angle, varying the β^* can vary the amount the beam is squeezed and offsetting the bunches at crossing can reduce the geometric overlap. The pileup density, which is defined as the pileup per unit length along the length of the bunches, is another issue for the detectors. Reducing the pileup density (i.e. flattening the distribution of the pileup density) makes identifying each collision vertex simpler for the detector thereby allowing a greater total pileup.

2.2.3 Non-linear phenomena

Action-Angle coordinate systems

In accelerator physics a number of coordinate systems are used to simplify analysis of the lattice. In table 2.1 the generally recognised 4D coordinate systems are shown, describing the transverse motion in the machine.

Coordinate system	Variables
Accelerator variables	x,x',y,y'
Linear action-angles	J_x, ϕ_x, J_y, ϕ_y
Non-linear action-angles	I_x, ψ_x, I_y, ψ_y

Table 2.1: 4D accelerator coordinate systems

The accelerator variables allow the consideration of the actual motion of particles in the machine relative to the physical closed orbit. This is particularly useful when considering the motion relative to the physical aperture; e.g collimation studies. Transforming to an action-angle coordinate system removes the s dependence of the coordinate system giving an effective global coordinate system which is independent of the optics at a given location. This is useful in the

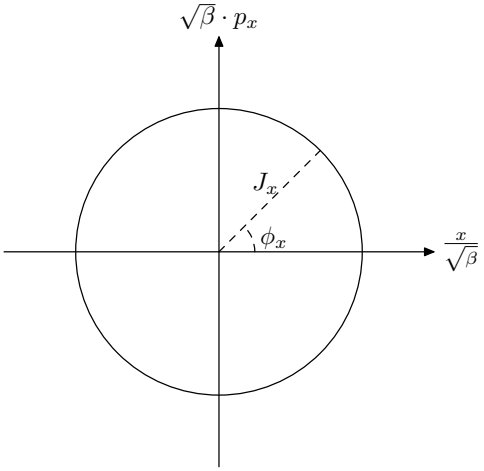

Figure 2.16: Action-angles on normalised phase space

study of dynamic aperture where the stable aperture around the whole lattice is required. The linear action-angle variables allow for the effects of higher order non-linear terms to be considered by reducing the linear motion to a constant amplitude and phase [38]. This technique can be extended further to express coordinates in the form of non-linear action angles where all stable trajectories can be described with a constant action. For linear motion in the machine the action J remains constant, while the angle advances with the β-function,

$$\phi_x(s) = \phi_x(0) + \int_0^s \frac{\mathrm{d}s'}{\beta(s')} \tag{2.37}$$

which is depicted in figure 2.16. The transformation from the accelerator variables to the linear action J_x is given by,

$$J_x = \frac{1}{2\beta_x(s)} \left[x^2(s) + \left(\beta_x(s)x'(s) - \frac{\beta_x'(s)x(s)}{2} \right)^2 \right], \tag{2.38}$$

where $\beta_x'(s)$ is the rate in change in β_x with s. The transformation back to the

accelerator variables is given by [38],

$$\begin{aligned} x(s) &= \sqrt{2J_x\beta_x(s)}\cos(\phi_x) \\ x'(s) &= -\sqrt{2J_x\beta_x(s)}\left(\sin(\phi_x) - \frac{\beta_x'(s)}{2}\cos(\phi_x)\right). \end{aligned} \tag{2.39}$$

The action, $J_{x,y}$, is a property of a single particle and can be related to the emittance, $\varepsilon_{x,y}$, such that for a Gaussian distribution of particles in amplitude, the emittance is equal to the mean of the action for each particle in that distribution,

$$\varepsilon_{x,y} = \langle J_{x,y} \rangle \tag{2.40}$$

The angle can be further simplified through a further coordinate transformation $(\phi, J) \mapsto (\phi_1, J_1)$, where ϕ_1 is a uniformly advancing phase [38]. Only the angle variable changes in this transformation meaning that,

$$\begin{aligned} J_1 &= J \\ \phi_1 &= \phi + \frac{2\pi Q s}{C} - \int_0^s \frac{\mathrm{d}s'}{\beta(s')}, \end{aligned} \tag{2.41}$$

where C is the circumference of the accelerator. This allows a simplified Hamiltonian to be written,

$$H = \frac{2\pi Q}{C} J_1. \tag{2.42}$$

More generally this approach can be extended to include the non-linear motion of the machine to define a coordinate system so that the non-linear action, $\mathcal{I}$, remains constant with an angular advance, ψ [29, p. 96]. In general the normal form,

$$\mathcal{N} = \mathcal{A}\mathcal{M}\mathcal{A}^{-1} \tag{2.43}$$

is the simplest Lie transformation[2] from the one turn map $\mathcal{M}$, which describes the transformation in accelerator coordinates for one turn of the machine, where $\mathcal{A}$ describes the transformation between the coordinate systems so that,

$$I_x = \mathcal{A}^{-1}\left(\frac{x^2 + x'^2}{2}\right). \tag{2.44}$$

The process for determining $\mathcal{A}$ is normal form analysis. By determining $\mathcal{A}$ and calculating $\mathcal{M}$ the resonant driving terms (RDTs) of the lattice can be found.

Resonances

A resonance, in an accelerator, is a tendency for increased betatron motion at a given tune. Considering an arbitrary lattice in which there are a series of dipole errors, if there is an integer tune these errors will add on every turn. However, if there is a half-integer tune these errors will cancel every other turn. In a real lattice there are additional quadrupole errors, which for a half-integer tune will add on every turn. This argument continues where higher order magnet errors exist resonances will occur at given tunes. As the order of magnet error increases the impact of the resonance will decrease. In transverse variables there are two tunes which vary, Q_x and Q_y. In general the resonances can be described by,

$$(j-k)Q_x + (l-m)Q_y = n \tag{2.45}$$

where j, k, l, m and n are integers and the order of a resonance is given by,

$$\text{Resonance Order} = |j-k| + |l-m|. \tag{2.46}$$

The combinations of the tunes in the two planes form a web of tunes. The non-integer part of these tunes is shown in figure 2.17, in which an accelerators

[2]A transformation which is symplectic that conserves the phase space density.

working point would be chosen so that it avoids these resonance lines.

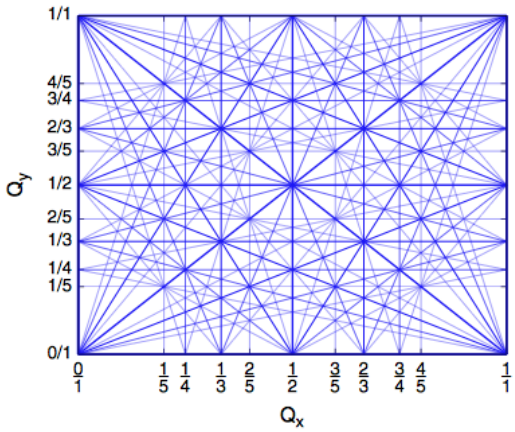

Figure 2.17: Tune diagram displaying all betatron resonances up to order 5 in the unitary square [39]

Coupling occurs when the three planes of motion can no longer be treated separately. Linear coupling, in particular, is generated by longitudinal magnetic fields or skew quadrupoles. As the motion is coupled, vertical dispersion and optics functions become distorted [40]. There are two types of linear coupling: linear difference resonance and linear sum resonance. The linear difference resonance occurs on the resonance line $Q_x - Q_y = n$, where n is an integer. The linear difference resonance constrains the sum of the two transverse emittances such that the total emittance does not grow, making it stable [32]. The linear sum resonance constrains the difference in transverse emittances allowing the total emittance to grow making it unstable [32]. Linear coupling leads the betatron tunes to approach each other such that they eventually become indistinguishable in measurement.

The strength of these various resonances are defined by the resonant driving terms (RDTs) which have varying amplitudes. The Hamiltonian description of

an accelerator in terms of RDTs is given by [41],

$$H = \sum_{jklm} h_{jklm} (2\mathcal{I}_x)^{\frac{j+k}{2}} (2\mathcal{I}_y)^{\frac{l+m}{2}} e^{-\imath[(j-k)(\psi_x+\psi_{x_0})+(l-m)(\psi_y+\psi_{y_0})]} \tag{2.47}$$

where ψ_{x_0} and ψ_{y_0} are the horizontal and vertical initial non-linear angles, ψ_x and ψ_y are the horizontal and vertical non-linear angles, and h_{jklm} is the amplitude of the resonance $(j-k, l-m)$. The resonance order, $|j-k|+|l-m|$ and resonance amplitude lead to varying changes in the transverse position of a particle.

Amplitude dependent tune shift

Chromaticity is the tune shift with change of momentum which can lead to instabilities as momentum changes move the tunes onto resonances. Tune shift can also vary with amplitude, a source of which is an octupolar magnetic field [42]. Consider the multipole expansion of a magnetic field in an accelerator,

$$B_y(x,y,s) + \imath B_x(x,y,s) = \sum_m [b_m(s) + \imath a_m(s)](x+\imath y)^{m-1}, \tag{2.48}$$

where b_m and a_m are the normal and skew multipole coefficients respectively. These multipole coefficients perturb the Hamiltonian away from the linear Hamiltonian of equation 2.42 by H_p,

$$H_p = \frac{q}{p_0} \Re \left[\sum_{m=3}^{\infty} \frac{1}{m} \left[b_m(s) + \imath a_m(s) \right] (x+\imath y)^m \right]. \tag{2.49}$$

For the case of a normal octupolar component where $m = 4$,

$$H_4 = \frac{q}{p_0} \frac{b_4(s)}{4} \left(x^4 - 6x^2y^2 + y^4 \right). \tag{2.50}$$

The tune shift is defined by,

$$\Delta Q_{x,y} = \frac{1}{2\pi} \oint \frac{\partial \langle H_4 \rangle}{\partial J_{x,y}} \, \mathrm{d}s, \tag{2.51}$$

where the Hamiltonian perturbation for the octupolar case in linear action-angle coordinates from the transformations given in equation 2.39 is given by,

$$H_4 = \frac{q}{p_0} \frac{b_4(s)}{4} \left[4J_x^2 \beta_x^2 \cos^4(\phi_x) + 4J_y^2 \beta_y^2 \cos^4(\phi_y) - 24 J_x J_y \beta_x \beta_y \cos^2(\phi_x) \cos^2(\phi_y) \right]. \tag{2.52}$$

Averaging over the angular terms, using the following results,

$$\begin{aligned} \langle \cos^2(\phi) \rangle &= \frac{1}{2\pi} \int_0^{2\pi} \cos^2(\phi) = \frac{1}{2}, \\ \langle \cos^4(\phi) \rangle &= \frac{1}{2\pi} \int_0^{2\pi} \cos^4(\phi) = \frac{3}{8}, \end{aligned} \tag{2.53}$$

allows the expression of the averaged Hamiltonian perturbation to be expressed,

$$\langle H_4 \rangle = \frac{q}{p_0} \frac{b_4(s)}{4} \left(\frac{3}{2} J_x^2 \beta_x^2 + \frac{3}{2} J_y^2 \beta_y^2 - 6 \beta_x \beta_y J_x J_y \right). \tag{2.54}$$

This leads to an amplitude dependent tune shift,

$$\begin{aligned} \Delta Q_x &= \frac{q}{p_0} \frac{3B_4}{8\pi} \left(\beta_x^2 J_x - 2 \beta_x \beta_y J_y \right), \\ \Delta Q_y &= \frac{q}{p_0} \frac{3B_4}{8\pi} \left(\beta_y^2 J_y - 2 \beta_x \beta_y J_x \right), \end{aligned} \tag{2.55}$$

where B_4 is the integrated normal octupolar strength. This tune shift shows explicitly that varying the amplitude leads to a change in tune, which could possibly lead to driving the tune of a particle on to a resonance, which could lead to unbounded motion and eventual loss on a restrictive aperture. For a real machine, if this amplitude detuning increases then the available dynamic aperture

in which bounded motion can occur decreases.

Frequency map analysis

A real accelerator with non-linearities can be described in the form of a Hamiltonian with the linear Hamiltonian H_0 and a non-linear perturbation H_1,

$$H = H_0 + \epsilon H_1 \tag{2.56}$$

where ϵ is a small parameter describing the amplitude of perturbation. The equations of motion for the linear Hamiltonian can be thought of as a set of orbits which are confined within an n dimensional tori. In the case where ϵ is zero such that the system is integrable there exists a one to one correspondence linking the tune Q, and action $\mathcal{I}$. This correspondence holds if the system is not degenerated (remains stable over the time period of evaluation) such that [43],

$$\det \left| \frac{\partial Q(\mathcal{I})}{\partial \mathcal{I}} \right| = \det \left| \frac{\partial^2 H_0(\mathcal{I})}{\partial \mathcal{I}^2} \right| \neq 0. \tag{2.57}$$

The frequency map F is a mapping from actions to frequencies,

$$F : (\mathcal{I}_1, \ldots, \mathcal{I}_n) \mapsto (Q_1, \ldots, Q_n). \tag{2.58}$$

For a fixed energy only $n-1$ actions are independent, leading to the frequency map,

$$F : (\mathcal{I}_1, \ldots, \mathcal{I}_{n-1}) \mapsto \left(\frac{Q_1}{Q_n}, \ldots, \frac{Q_{n-1}}{Q_n} \right) \tag{2.59}$$

where describing the system in terms of frequencies is equivalent to actions. Considering the simple 2D case of H_0 which gives a constant tune for each amplitude,

$$Q(\mathcal{I}) = Q_0 \tag{2.60}$$

where Q_0 is the reference tune.

When ϵ is small, such that the tori containing the orbits are deformed and not destroyed, the frequencies of the tori change. The family of tori describing stable orbits are parameterised by a set of frequencies. In the gaps of this set chaotic behaviour occurs (resonances). For the case of an accelerator these gaps form an interconnected web passing close to all points in phase space with varying amplitudes of resonance [44]. Diffusion is defined by the rate of transport of orbits between tori. This rate of transport of orbits between tori can also be seen as a measure of proximity to integrability i.e. a particle on a trajectory with a high level of diffusion will become quickly unbounded and therefore will be lost rapidly (Nekhoroshev theorem [45]). Such diffusion was first analysed for a real system by Laskar [46] who used it to analyse the chaotic nature of the Solar system.

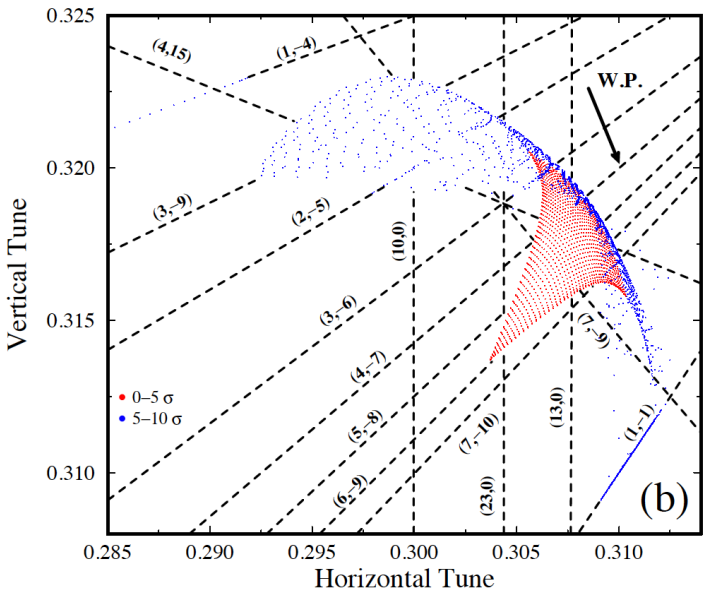

Figure 2.18: Frequency map analysis of the LHC [47], colour coded by initial amplitude greater (blue) and less (red) than 5σ, with head on and long range collisions.

An example of a frequency map is shown in figure 2.18 in which the resonance lines are overlaid on the frequency map. The resonance lines are denoted

$(j-k, l-m)$ as described in equation **??**.

A fold in a map occurs where the tune shift with amplitude is no longer positive. An example of a fold can be seen in figure 2.18 in the amplitude transition from less than 5σ to greater than 5σ. In order to determine the nature of a fold a torsion matrix is defined to describe the type of fold [48]. This torsion matrix is a generalised matrix describing tune shift with amplitude in the transverse variables, and is defined by

$$M = \frac{\partial \vec{Q}(\vec{\mathcal{I}})}{\partial \vec{\mathcal{I}}} = \begin{pmatrix} \frac{\partial Q_x}{\partial \mathcal{I}_x} & \frac{\partial Q_x}{\partial \mathcal{I}_y} \\ \frac{\partial Q_y}{\partial \mathcal{I}_x} & \frac{\partial Q_y}{\partial \mathcal{I}_y} \end{pmatrix} \tag{2.61}$$

where $\vec{Q}$ is the vector of transverse tunes and $\vec{\mathcal{I}}$ is the vector containing transverse actions. If the torsion matrix M is of a definite[3] quadratic form, finite time stability results exist, which do not persist in the case of non-definite[4] torsion [45, 48]. Non-definite torsion means that the quadratic form is also non-definite. For the case of non-definite torsion the quadratic form of M will indicate directions of fast escape, in which unbounded motion will occur. The inverse of the torsion matrix is defined,

$$M^{-1} = \frac{1}{\left(\frac{\partial Q_x}{\partial \mathcal{I}_x}\frac{\partial Q_y}{\partial \mathcal{I}_y} - \frac{\partial Q_x}{\partial \mathcal{I}_y}\frac{\partial Q_y}{\partial \mathcal{I}_x}\right)} \begin{pmatrix} \frac{\partial Q_y}{\partial \mathcal{I}_y} & -\frac{\partial Q_x}{\partial \mathcal{I}_y} \\ -\frac{\partial Q_y}{\partial \mathcal{I}_x} & \frac{\partial Q_x}{\partial \mathcal{I}_x} \end{pmatrix}. \tag{2.62}$$

If the inverse of the torsion matrix takes a quadratic form it will look like,

$$M^{-1} = \begin{pmatrix} a & c \\ c & b \end{pmatrix}. \tag{2.63}$$

[3]Definite = The sign remains constant over vector space.
[4]Non-definite = The sign varies over vector space.

For this to be true it must be the case that

$$\frac{\partial Q_x}{\partial \mathcal{I}_y} = \frac{\partial Q_y}{\partial \mathcal{I}_x}. \tag{2.64}$$

The vector $V = (x, y)$ are the possible directions of escape, if [48],

$$V^T M^{-1} V = ax^2 + 2cxy + by^2 = 0. \tag{2.65}$$

The discriminant in x is given by $\Delta = y^2(c^2 - ab) = -y^2 \det(M^{-1})$. The signature of torsion is defined by the determinant of the torsion matrix [48]. The signature of torsion indicates the type of transition the frequency map has with amplitude at a given point in frequency space. The interpretation of the signature of torsion comes from the resulting value of the discriminant Δ [48],

$$|M| \begin{cases} < 0 & \text{Torsion non-definite, } \Delta > 0 \rightarrow \text{Two possible directions of escape,} \\ 0 & \text{Fold,} \\ > 0 & \text{Torsion definite, } \Delta < 0 \rightarrow \text{No possible directions of escape.} \end{cases} \tag{2.66}$$

If torsion is said to be non-definite a particle at this point in phase space is more likely to undergo unbounded motion due to the existence of two possible directions for fast escape, in which diffusion is higher. In contrast, if torsion is said to be definite a particle at this point in phase space is less likely to undergo unbounded motion as there are no possible directions of escape and therefore the diffusion is lower. There are two types of fold: a single fold, in which there is one change in the sign of the signature of torsion, and a double fold in which there are two changes. Figure 2.19 shows the signature of torsion for these two types of fold found in a frequency map. The single fold ends in a region of non-definite torsion, so is less stable, while the double fold ends in a region of definite torsion

so is more stable.

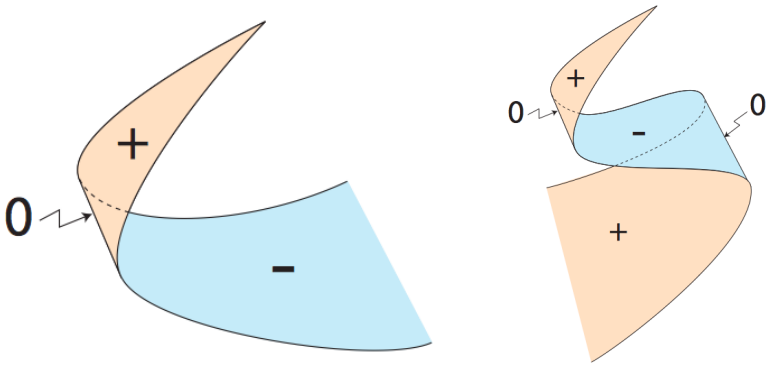

(a) (b)

Figure 2.19: The nature of folded frequency maps in terms of the signature of torsion. (a) Single fold and (b) double fold in map [48].

The fold in figure 2.18 can be seen to be a single fold which means that amplitudes beyond this fold are likely to form unbounded motion caused by resonances. An example of one of these destructive resonances is marked by (3,-6) in figure 2.18. In general, the frequency map allows loss mechanisms caused by chaotic motion to be studied. It indicates areas of phase space which are particularly vulnerable to unbounded motion from resonances.

Dynamic aperture

The dynamic aperture (DA) is defined by the region in phase space over which stable motion occurs [49]. Stable motion is defined as bounded quasi-periodic motion over a given time or number of turns, depending upon the choice of independent variable. This definition implies that DA is time dependent, which asymptotically will tend towards the chaotic boundary. The chaotic boundary is time independent and is defined as the boundary which separates bounded and unbounded motion. When defining the stability of a real machine the DA is measured for a particular number of turns or time. In a lepton machine, where radiation damping is important, this choice may be considerably lower than a

hadron machine of similar circumference, in which radiation damping is generally negligible.

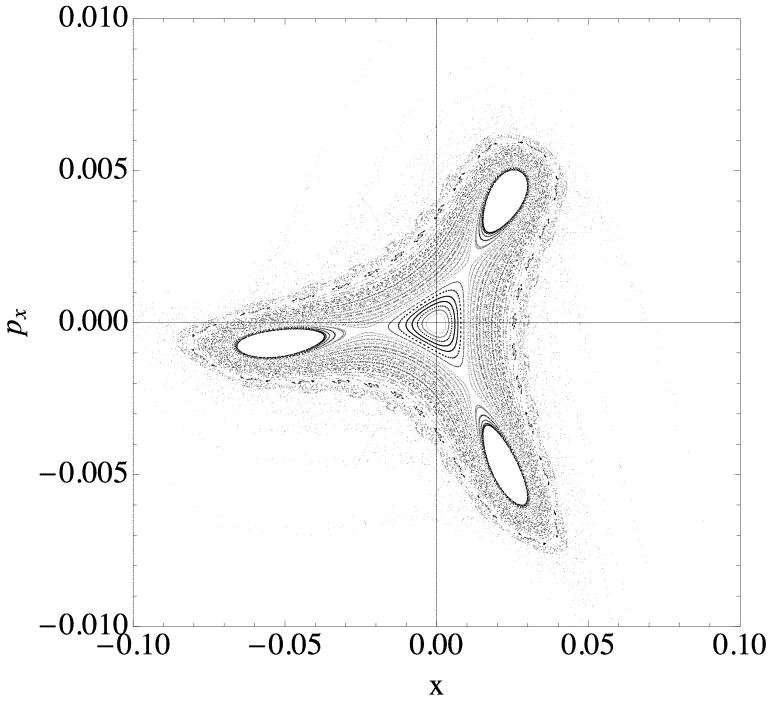

Figure 2.20: Phase space for a simple 2D model with a sextupole and octupole term showing the formation of stable islands.

By definition, the dynamic aperture does not contain all possible stable particles that remain within the physical aperture over the lifetime of the beam, as some exist in stable islands. This island formation is shown in figure 2.20. In a full six dimensional phase space this aperture is described by a six dimensional hypersphere centred on the closed orbit. For ease of scanning over the phase space to determine the dynamic aperture, action-angle coordinates can be used thus reducing the transverse phase space to be scanned from 4D to 2D. Similarly the longitudinal motion can be expressed in action-angle coordinates and be reduced from 2D to 1D. This reduction arises because in action-angle coordinates the action remains constant while the angle varies periodically, hence over the number of turns tracked all angles will be effectively scanned. Use of a search

method, for example a binary search, is not feasible to determine the dynamic aperture, for risk of converging on an island. A large scale scanning of the action phase space is required in order to determine dynamic aperture without the risk of converging on an island.

Long term tracking scans over various initial conditions, for up to 10^7 turns, to see if a particle is "lost" (goes beyond a physical aperture far greater than the mechanical aperture of the machine). For the LHC this is conducted using SixTrack [50]. This provides a direct measurement of the dynamic aperture. However, in order to determine the long term stability a relationship between the dynamic aperture and time is required [49]. This direct measurement is computationally intensive.

The chaotic boundary is defined where unbounded motion begins. There is some correlation between the chaotic boundary and dynamic aperture, although a particle can have unbounded and yet stable motion [51]. Short term tracking predictions make use of a fewer number of turns to determine the chaotic boundary, from as little as 10^3 turns. There are two methods available for such a calculation; the Lyapunov exponent [52] and the tune variation [53]. These methods are not often used for dynamic aperture calculations as they exclude initial conditions where a particle is chaotic yet physically stable (i.e. never lost), hence greatly underestimating the dynamic aperture.

2.3 HL-LHC

After 2022, it is intended to begin the third long shut down in order to upgrade the LHC's delivered luminosity to the experiments (see figure 2.8). To do this, the pileup (see section 2.2.2) needs to be kept fairly constant throughout a run, rather than degrading with time. In order to perform such a run a luminosity levelling scheme has been proposed [54], which will deliver a levelled peak luminosity of

5×10^{34} cm^{-2}s^{-1} with a virtual luminosity of 2×10^{35} cm^{-2}s^{-1}, which aims to provide an integrated luminosity of 250 fb^{-1} per year [55]. A schematic of this is shown in figure 2.21 in which the luminosity is given over the lifetime of a run. Over 12 years of operation this will equate to 3000 fb^{-1} of integrated luminosity, post upgrade, running with a centre of mass energy of 14 TeV. This would see a 10 fold increase in the integrated luminosity compared to the planned first ten years operation of the LHC [56]. The aim is to deliver this luminosity to the two low β^* experiments ATLAS and CMS, at IP1 and IP5 respectively.

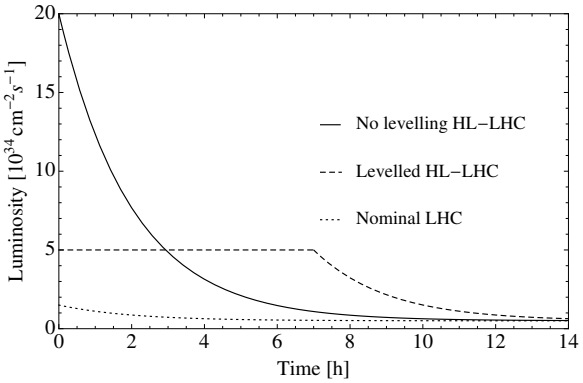

Figure 2.21: Example of luminosity levelling over one run (Schematic). [17]

The ATLAS [57] and CMS [58] collaborations, in 2012, presented the first results, with 5 standard deviations of significance, indicating the existence of the Standard Model Higgs boson at the LHC. The increased integrated luminosity would allow for greater accuracy of measurement to be made on the properties of this boson, as shown in figure 2.22. Beyond this an integrated luminosity of this magnitude allows for limits to be placed on the observation of rare processes, both in keeping with and beyond the standard model (e.g heavy stable charged particles and dark matter candidates [59]).

The HL-LHC upgrade requires a number of significant hardware changes to reach its goals, of increasing the luminosity and enabling operation with luminosity levelling. In order to reach this high luminosity goal the beam must be

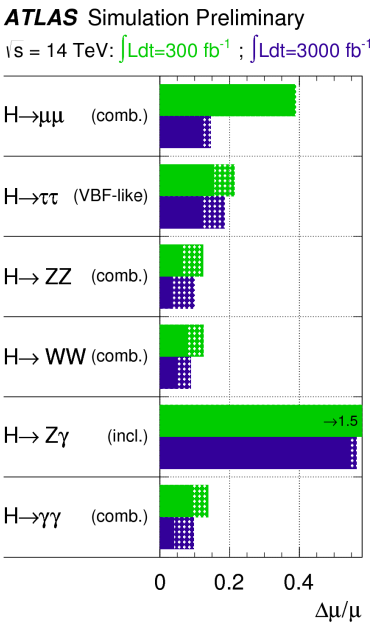

Figure 2.22: Improvement in relative uncertainty on the total signal strength μ for different Higgs final states, assuming the Standard Model Higgs boson has a mass of 125 GeV/c^2. "Comb." refers to combined measurements and "Incl." indicates inclusive analysis. The dotted regions indicate theory uncertainty. [60]

strongly squeezed at the IP and emittance reduced. This is currently limited by the injector chain, which impacts the emittance, and the optics and aperture restraints of the current LHC [61]. The aim is to upgrade the injector chain in long shutdown 2 leaving the upgrades to the LHC machine to long shutdown 3.

At the ultimate bunch intensity of 1.7×10^{11} protons the crossing angles which the nominal optics permit lead to a decreased dynamic aperture as a result of long range beam-beam interaction, where the reduced dynamic aperture leads to a greatly shortened lifetime. In the nominal LHC, without any beam-beam compensation, the minimum normalised crossing angle ϕ increases as a function of the bunch intensity N_b and bunch spacing T_{sep} with the approximate relation [47, 62],

$$\phi \approx \sqrt{\varepsilon}\beta^* \left(\frac{DA}{\sigma} + 3\sqrt{\frac{N_b}{1.05 \times 10^{11}} \frac{25\ ns}{T_{\text{sep}}} \frac{n_{LR}}{72}} \right), \tag{2.67}$$

where DA/σ is the required dynamic aperture and where the units are given in terms of the rms width of the bunch. n_{LR} is the number of long range beam-beam encounters. The dynamic aperture is nominally required to be greater than 6σ as this is the minimum physical aperture set by the collimation system in the LHC. With the ultimate bunch intensity, 25 ns time separation, β^* of 15 cm, and normalised emittance of 3.75 π mm mrad, the required crossing angle is approximately 300 μrad. In order to gain such a crossing angle it is necessary to increase the aperture and field strength of the final focussing triplet, this allows for a smaller β^* and a larger crossing angle. An increased crossing angle can be attained using inner triplet magnets with an aperture of 150 mm constructed with superconducting wires made from Nb_3Sn [63]; allowing for a peak field gradient of 150 T/m.

While this larger crossing angle permits for an increased dynamic aperture it leads to significant geometric loss in luminosity. The effect of this overlapping loss in luminosity is demonstrated in figure 2.15, in which the area of overlap decreases with increased crossing angle. The method proposed to overcome this loss in luminosity is a local crab cavity scheme [64, 63, 54]. The crab cavities generate a rotation of the bunch about its centre at the IP, correcting for the geometric losses from the crossing angle. Adjusting this angle means that the crab cavity scheme also presents a method in which to control these geometric losses, allowing luminosity levelling throughout a run in the machine. A novel approach to the optics called the "Achromatic Telescopic Squeezing" (ATS) scheme allows for further squeezing of the beam with limited alteration to the current LHC lattice.

2.3.1 Arc and insertion regions

The LHC can be broken down into two types of optical regions, the insertion regions (IR) and the arc regions, of which there is one of each for each octant. For the HL-LHC the insertion regions contain the experiments, some collimation, injection and beam dump systems. For the HL-LHC the IRs will undergo the greatest number of changes, while the arc regions will mostly go unchanged except for the addition of the new dispersion suppression collimation system [65]. In the HL-LHC the final focussing magnets and separation dipoles in IR1 and IR5 will be replaced to allow for an increased crossing angle and to allow for a greater squeezing of the β^* value.

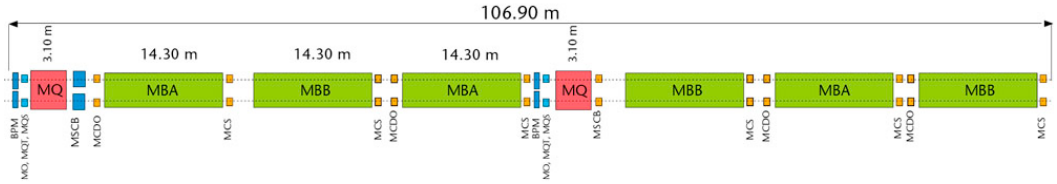

Figure 2.23: Schematic layout of one LHC arc cell [66]

Each arc in the LHC is made up of 23 cells and is 106.9 m long, as shown in figure 2.23. Each cell is made up of dipole bending magnets, quadrupole magnets and a series of correctors [16]. The two counter rotating beams are held in separate apertures throughout the arcs, separated by 194 mm. There are a number of different components making up the arc cell, as shown in figure 2.23:

- **MBA/MBB.**These are the two types of bending dipole magnet. MBA come equipped with a b_4/b_5 correction spool piece (MCDO) (Figure 2.24)
- **MQ.** Lattice quadrupole.
- **MO.** Landau octupole for damping the coherent oscillations caused by collective effects.

- **MQT.** Tuning quadrupole for independent control of the phase advance between the two beams.
- **MQS.** Skew quadrupole corrector magnets to correct for systematic a_2 errors in the main dipole magnets.
- **MSCB.** Combined lattice sextupole or skew sextupole and orbit corrector
- **BPM.** Beam position monitor.
- **MCS/MCDO.** The local sextupole corrector and local combined decapole and octupole correctors are also known as the spool pieces. These are small corrector magnets designed to compensate for the $b_{3,4,5}$ field components of the main dipoles which would impact linear chromaticity at the top centre of mass energy.

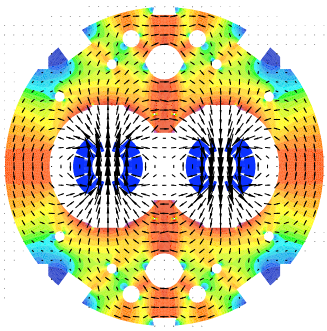

Figure 2.24: Magnet field in dipole magnets (MBA/MBB) [67]

The IRs at the time of writing were not finalised for the HL-LHC design and the optics discussed throughout this thesis are that of the SLHCv3.1b [68]. The IRs are all classed as long straight sections, with interaction points (IPs) at their centres. From the arcs the aperture remains split for the two beams entering the IR, combining into one aperture for the IP. IR1 and IR5 contain ATLAS and CMS respectively, and are the low-β insertion regions.

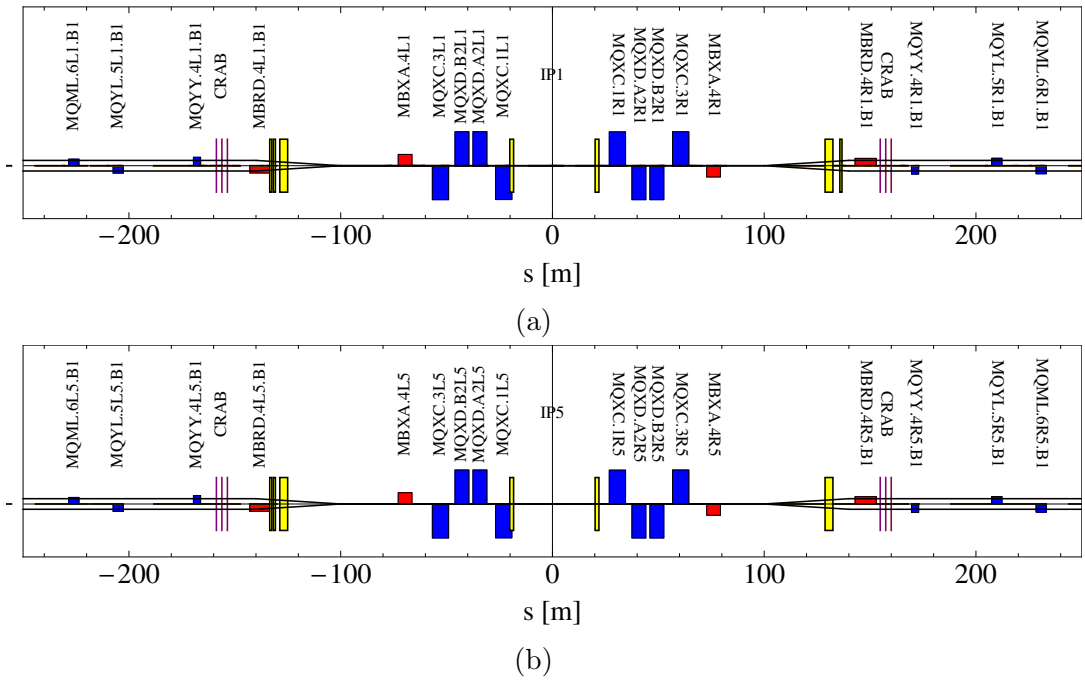

Figure 2.25: (a) IR1 and (b) IR5 schematics for SLHC v3.1b [68], beam 1. Includes quadrupoles (blue) and sextupoles (red) which are both relatively scaled with field strength, collimators (yellow) and crab cavities (magenta). Aperture shown to indicate separated and split regions, however, not to scale.

In figure 2.25 the basic layouts of IR1 and IR5 are shown, not all magnets are included. The following is a brief description of the key elements of the IR and their alternative naming [16]:

- **MQXC/MQXD (Q1,Q2A,Q2B,Q3).** These are the inner triplet magnets, as with the nominal LHC, for this optics layout the central magnet is split. In later optics layouts it is proposed to split all three magnets. They are superconducting and constructed of Nb_3Sn with a large aperture ($\approx$ 150 mm)

- **MBXA/MBRD (D1,D2).** This is a pair of separation/recombination dipoles which take the beams from a double to a single aperture. In the nominal machine D1 was a normal conducting magnet due to the large aperture requirements, however, as part of the upgrade this will become a

superconducting magnet.

- **CRAB.** This is the proposed location for the crab cavities in the optics. In this optical layout it was proposed that there should be six cavities either side of the IP, with three cavities per beam at each location, laid out in a staggered formation.

- **MQYY/MQYL/MQML (Q4,Q5,Q6).** These quadrupoles are superconducting and form the beginning of the matching section, which is key to the ATS scheme.

- **Collimation.** In the schematic two sets of collimation are shown either side of the IP. The set closest to the IP, the TAS absorber, protects the inner triplet magnets from particles leaving the IP. The second set, the TAN absorber, protects the split aperture magnets from neutrally charged particles coming from the IP.

- **IP.** At the time of writing there were two different proposed β^* configurations with a variety of properties which are still under consideration. There is a round beam proposal with β^* of 15 cm and flat beam of $\beta^*_{x,y}$ of 7.5/30 cm.

The luminosity levelling need not be controlled solely by crab cavities, as previously mentioned. Another possibility lies in the control of the β^*, instead of reducing the geometric loss from the crossing angle. This is done through a set of large corrector magnets just after Q4. Such a scheme has already been verified during a machine development run, in 2011, by applying a luminosity control to LHCb [69].

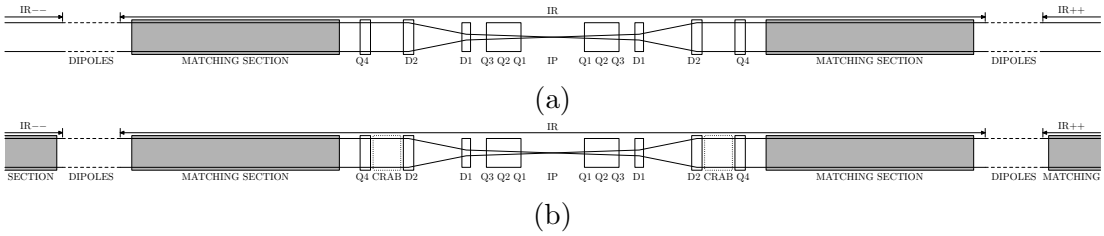

Figure 2.26: The low β^* insertion region layouts for the (a) nominal and (b) HL-LHC optics.

2.3.2 Achromatic Telescopic Squeezing scheme

The nominal LHC optics, shown in figure 2.26a, are limited by the mechanical acceptance of the matching section, the gradient limits of the quadrupoles in the insertion region (IR) and the strength limit of the arc sextupoles [61]. Sextupoles are the basic tool used to reduce the chromaticity in a lattice. The basis of the chromaticity correction scheme, to allow for a squeezed β^* at IP1 and IP5, is to allow correction to occur in the matching section of the IRs either side of the IR being corrected. For example, for IR1, the matching sections of IR8 and IR2 closest to IR1 are used to gain additional chromaticity correction, as shown in figure 2.26b.

Increased chromatic errors arise from the introduction of large aperture, higher strength quadrupoles close to the IP, required to squeeze the β^*. These lead to both significant linear and non-linear chromaticity which must be corrected for. The larger aperture and increased field strength of these quadrupoles, over the nominal LHC magnets, allow for a greater crossing angle to be attained which is needed to overcome the beam-beam interaction limit. There is a significant amount of beam-beam interaction, even with an increased crossing angle, which can be limited by orientating the crossing angles such that IP1 is vertical and IP5 horizontal relative to the plane of the HL-LHC ring. This is done so that the tune shift resulting from the beam-beam interaction does not occur in the same plane. It is proposed to build the final triplet (Q1, Q2, Q3) using the superconducting

material Nb_3Sn [70]. The Nb_3Sn allows the gradient of the magnets to operate at 150 T/m with an aperture of 150 mm [68].

Chromaticity is generally unwanted in an accelerator as it can lead to instabilities by pushing particles onto unstable resonances [71]. The primary instability is in the particle's transverse motion and is called the strong head-tail instability. It is dependent on the synchrotron motion and impedance resulting from the aperture of the machine. In order to correct for the chromaticity in the HL-LHC lattice large families of sextupoles are used which are contained in the matching sections at the edges of the IRs and in the arcs. These matching sections pre-exist in the nominal machine, however, their usage in the ATS scheme differs.

The ATS scheme creates a mismatch in the matching sections adjacent to the IR so that there are intentional errors in the β-function in these regions. These errors are used to increase the chromatic correction capabilities of the lattice to correct for the chromaticity arising from the strong focussing used to gain the ultra low β^* values at IP1 and IP5 [61]. In this case matching refers to gaining the desired β-function and phase advances at given points in the lattice. Initial matching of the sextupoles arises from the matching sections of IR1 and IR5 down to a certain β^*. Beyond this β^* the additional matching sections are required to reach the desired operational β^*. The adjacent matching sections are used to produce a mismatch in the optics which induces a beta-beating wave in the arcs adjacent to IR1 and IR5. A beta-beating wave refers to an error in the β-function which processes around the machine with twice the phase advance to the betatron phase advance. Around the arc sextupoles this phase advance is π for every $\pi/2$ betatron phase advance, such that the total amplitude of the β-function resulting from the induced errors peaks at every other sextupole. These sextupoles are powered in two families with every other sextupole connected to each other, requiring any change in magnet strength to be continuous across a

whole family. This beta-beating wave increases the efficiency of chromaticity correction due to all the sextupoles in one family gaining the same increase in β-function. This allows the current sextupole powering arrangement to overcome the strength limit of the arc sextupoles [61].

2.3.3 Crab crossing scheme

In 1988 Palmer [72] suggested, for linear colliders, the possibility of a crab crossing scheme as a way of recovering some of the luminosity lost by the geometric loss at the crossing angle. It was proposed to use an RF deflector (crab cavity) to deflect the front and back of the bunch in opposite directions so that at the IP they would cross head on, as shown in figure 2.27.

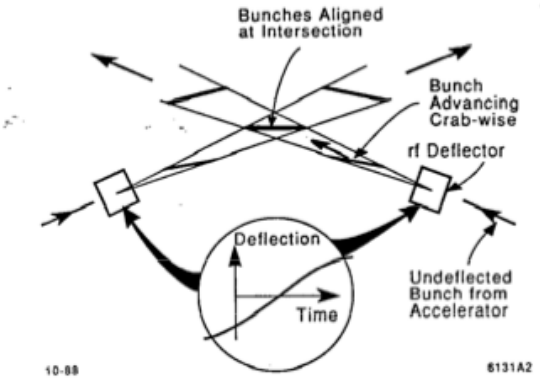

Figure 2.27: Crab crossing scheme at a linear collider as proposed by Palmer [72]

This was later extended to storage rings by Oide et al [64]. A local crab crossing scheme involves the introduction of cavities on each beam either side of the IP [54]. A "crab bump" occurs between two points either side of the IP with a π betatron phase advance between the two cavities in order to return the bunch to its original pre-crabbed state. At the initial point in the bump a transverse z dependent kick is applied to the bunch by a deflecting (aka. crab) cavity; this generates an effective angular momentum about the centre of the bunch. By the

time the bunch reaches the IP it will have rotated far enough to collide head on, thereby recovering the luminosity lost by the crossing angle. Between the crab cavity and the IP a betatron phase advance of $\pi/2$ occurs, hence from the IP the direction of bunch rotation reverses until it reaches the final crab cavity where the bunch returns to its original physical orientation. At this point a kick of the same phase as initially applied to the bunch is applied to close the "crab bump". This process is shown in figure 2.28. The ability to completely correct

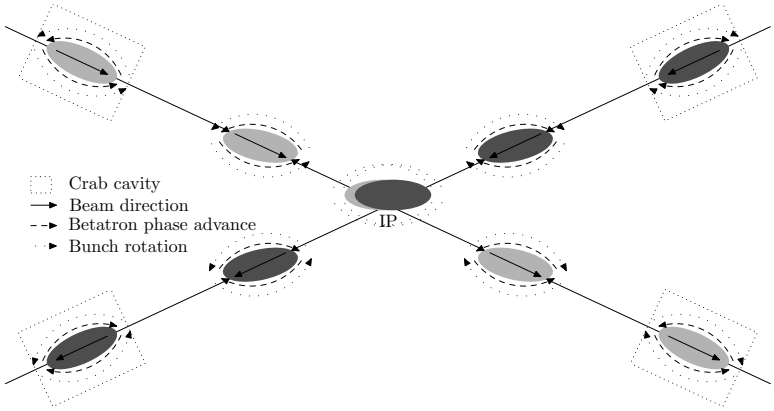

Figure 2.28: Bunch crossing with crossing angle and local crab cavity scheme

for these geometric losses with crab cavities leads to a maximum peak luminosity, however, this also leads to significant pileup for an experiment. This method of partially correcting these geometric losses using crab cavities is proposed in order to control the luminosity over the lifetime of a run.

The dependence of luminosity upon voltage can be calculated starting with an idealised crab cavity, for which the transverse momentum kick applied at any given longitudinal position z for a cavity with voltage V and frequency ω is given by,

$$\Delta p_x = \frac{qV}{cp_0} \sin\left(\frac{\omega z}{c}\right) \tag{2.68}$$

where the reference momentum is p_0. This can be reduced by the small angle

approximation to give an expression for the required voltage,

$$V = \frac{c^2 p_0}{q\omega}\frac{\Delta p_x}{z}. \tag{2.69}$$

The R matrix defines the linear transfer map through any number of accelerator elements such that between s_0 and s_1 the map for transverse variables is defined,

$$\begin{pmatrix} x(s_1) \\ p_x(s_1) \\ y(s_1) \\ p_y(s_1) \end{pmatrix} = \begin{pmatrix} \mathrm{R}_{11} & \mathrm{R}_{12} & \mathrm{R}_{13} & \mathrm{R}_{14} \\ \mathrm{R}_{21} & \mathrm{R}_{22} & \mathrm{R}_{23} & \mathrm{R}_{24} \\ \mathrm{R}_{31} & \mathrm{R}_{32} & \mathrm{R}_{33} & \mathrm{R}_{34} \\ \mathrm{R}_{41} & \mathrm{R}_{42} & \mathrm{R}_{43} & \mathrm{R}_{44} \end{pmatrix} \begin{pmatrix} x(s_0) \\ p_x(s_0) \\ y(s_0) \\ p_y(s_0) \end{pmatrix}, \tag{2.70}$$

where R_{ij} are the coefficients of the linear transfer map, and p_x and p_y are the transverse momenta. The longitudinal position in the bunch is designated z and defined as,

$$z = \frac{s}{\beta_0} - ct, \tag{2.71}$$

where t is time and β_0 is the reference speed as a fraction of the speed of light. The change in p_x with z can be expressed in terms of the crossing angle ϕ and the linear coefficient R_{12}, which gives the linear dependence of x at the IP on p_x at the crab cavity,

$$\frac{\Delta p_x}{z} \approx \frac{\Delta p_x}{\Delta x}\frac{\Delta x}{z} \approx \frac{\tan\left(\frac{\phi}{2}\right)}{\mathrm{R}_{12}}. \tag{2.72}$$

The R_{12} between the crab cavity and IP is related to the β-function by the following relation [73],

$$\mathrm{R}_{12} = \sqrt{\beta_x^* \beta_{x\mathrm{crab}}}\sin\left(\Delta\psi_{\mathrm{crab}}\right), \tag{2.73}$$

where $\Delta\psi_{\mathrm{crab}}$ is the betatron phase advance between the cavity and the IP, $\beta_{x\mathrm{crab}}$ and β_x^* are the horizontal β-function at the crab cavity and IP respectively. This

leads to the following voltage relation for the cavity before the IP [74],

$$V_1 = \frac{c^2 p_0 \tan\left(\frac{\phi}{2}\right)}{q\omega\sqrt{\beta_x^* \beta_{x\,\mathrm{crab}}}\sin\left(\Delta\psi_{\mathrm{crab}}\right)}. \tag{2.74}$$

The corresponding voltage of the cavity after the IP is dependent on the optics between the two cavities. The linear relation between the horizontal momenta across the two sets of cavities R_{22}, is given by,

$$V_2 = -R_{22} V_1, \tag{2.75}$$

with the stipulation that there is no relation between the initial horizontal momentum and the resulting horizontal displacement between the two sets of crab cavities,

$$R_{12} = 0, \tag{2.76}$$

to allow for complete correction of the crab kick. From equation 2.74, a relationship between the crossing angle ϕ and voltage V_1 can be found,

$$\tan\left(\frac{\phi}{2}\right) = \frac{V_1 q\omega}{c^2 p_0}\sqrt{\beta_x^* \beta_{x\,crab}}\sin(\Delta\psi_{\mathrm{crab}}). \tag{2.77}$$

Substituting this into equation 2.35 leads to a voltage dependence on luminosity,

$$\mathcal{L}(V_1) = \frac{N_1 N_2 f n_b}{4\pi\sigma_x\sigma_y}\frac{1}{\sqrt{1+\left(\frac{\sigma_s}{\sigma_x}\frac{V_1 q\omega}{c^2 p_0}\sqrt{\beta_x^* \beta_{x\,crab}}\sin(\Delta\psi_{\mathrm{crab}})\right)^2}} \tag{2.78}$$

allowing direct control of the luminosity from the crab cavities. This technique enables luminosity levelling to be performed. Correcting for the loss in luminosity due to the crossing angle by use of crab cavities is not the only technique to perform luminosity levelling, other techniques involve offsetting bunches [69, 54] and varying β^*.

2.4 Crab cavities

2.4.1 Introduction to RF cavities

Resonant cavities are approximately closed volumes within which electromagnetic resonant modes are excited. In general they consist of two openings for the beam to pass through, a hole through which the power is coupled to enable the resonances to form, and often couplers to dampen unwanted excited modes. The simplest cavity design is a pillbox, which can be further simplified to its closed form of a cylinder, as shown in figure 2.29.

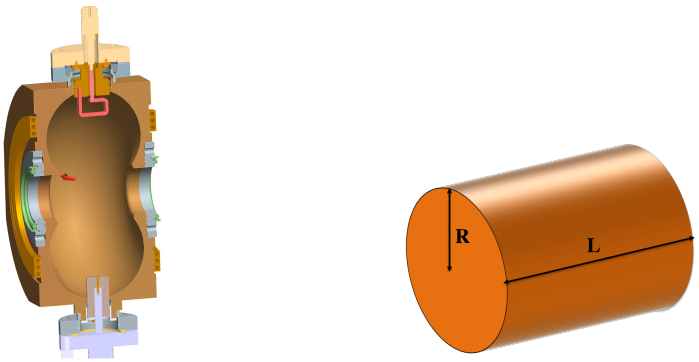

(a) (b)

Figure 2.29: Layout of pillbox cavity with (a) a real cavity from the EMMA accelerator [75] and (b) an idealised model.

The excited modes in a cavity are defined by their electromagnetic fields and associated frequencies. The only modes which can exist in a cavity are the eigenmodes found from the Helmholtz equation and the boundary conditions exerted by the cavity's structure. These boundary conditions prevent the existence, in the case of a conductive boundary, of parallel electric and perpendicular magnetic fields to the cavity's surface (defined by the surface vector $\vec{n}$), such that,

$$\vec{n} \times \vec{E} = 0, \qquad \vec{n} \cdot \vec{B} = 0. \tag{2.79}$$

The Helmholtz equation for the electric and magnetic fields is given by,

$$\nabla^2 \vec{E} + |\vec{k}|^2 \vec{E} = 0,$$
$$\nabla^2 \vec{B} + |\vec{k}|^2 \vec{B} = 0, \tag{2.80}$$

where $\vec{k}$ is the wavenumber of one eigenmode from a set of allowed eigenmodes defined by the boundary conditions on the internal surface of the cavity. In general, two types of mode exist in a resonant cavity of similar form to a pillbox.

1. **TE, Transverse Electric** where the electric field only has transverse components and the magnetic field is parallel to the axis, $E_z = 0$.

2. **TM, Transverse Magnetic** where the magnetic field only has transverse components and the electric field is parallel to the axis, $B_z = 0$.

A further type of mode can exist by inserting conductive structures into the volume of the cavity.

3. **TEM, Transverse Electric and Magnetic** where the electric and magnetic fields only have transverse components, $E_z = 0$ and $B_z = 0$.

The nomenclature for describing these eigenmodes is given by $\mathrm{A}_{\mathrm{mnp}}$ where A can be interchanged with TM, TE and TEM to describe the field components, the index m (for a pillbox cavity) describes the rotational symmetry, n describes the number of nodes in radial dependence and p describes the number of longitudinal nodes. For a TM mode the fields in the idealised cavity of length L and radius

R are given by [76],

$$E_z = E_0 \cos\left(\frac{p\pi z}{L}\right) J_m\left(\frac{u_{mn}\rho}{R}\right) \cos(m\phi) \tag{2.81}$$

$$E_\rho = -E_0 \frac{p\pi R}{L u_{mn}} \sin\left(\frac{p\pi z}{L}\right) J'_m\left(\frac{u_{mn}\rho}{R}\right) \cos(m\phi) \tag{2.82}$$

$$E_\phi = E_0 \frac{mp\pi R^2}{\rho L u_{mn}^2} \sin\left(\frac{p\pi z}{L}\right) J_m\left(\frac{u_{mn}\rho}{R}\right) \sin(m\phi) \tag{2.83}$$

$$B_z = 0 \tag{2.84}$$

$$B_\rho = \mathrm{i}E_0 \frac{m\mu_0\omega_{mnp}R^2}{\eta c\rho u_{mn}^2} \cos\left(\frac{p\pi z}{L}\right) J_m\left(\frac{u_{mn}\rho}{R}\right) \sin(m\phi) \tag{2.85}$$

$$B_\phi = \mathrm{i}E_0 \frac{\mu_0\omega_{mnp}R}{\eta c u_{mn}} \cos\left(\frac{p\pi z}{L}\right) J'_m\left(\frac{u_{mn}\rho}{R}\right) \cos(m\phi) \tag{2.86}$$

$$\gamma_{mn} = \frac{u_{mn}}{R} \qquad\qquad \omega_{mnp} = c\sqrt{\gamma_{mn}^2 + \left(\frac{p\pi}{L}\right)^2} \tag{2.87}$$

where η is the impedance in a vacuum ($\sqrt{(\mu_0/\varepsilon_0)}$), u_{mn} is the n^{th} root of $J_m(x)$, and $J'_m(x)$ is the first derivative with respect to x. In figure 2.30 the electric and magnetic fields of the TM_{010} mode are shown for a pillbox cavity.

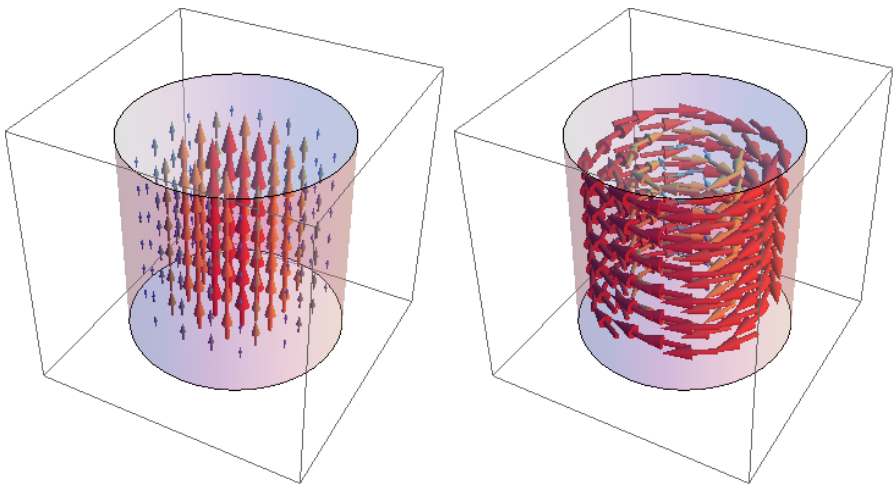

(a) (b)

Figure 2.30: (a) Electric and (b) magnetic fields of TM_{010} mode in a pillbox cavity.

When describing the quality of a cavity mode, in terms of its ability to act on a beam, the measure R/Q is used. The quality factor Q of the cavity is defined as the ratio of the stored energy to the energy lost in one radian of an oscillation [73]. The shunt impedance R_s, is defined by the ratio of the square of the energy gain to the loss rate. The ratio of these two quantities, the R/Q, relates the work done by the cavity on a particle to the energy stored in the cavity. A high R/Q indicates that a mode will do work efficiently on a particle as it passes through the cavity.

Beam loading occurs when a beam passes through a cavity and transfers energy into unwanted modes. The RF system, which drives the cavity's desired mode or operating mode, will also drive unwanted modes in the cavity. These unwanted modes are often referred to as Higher Order Modes (HOMs), as they often exist at higher frequencies than the operating mode. In some cases Lower Order Modes occur (LOMs), however, these only tend to occur for deflecting or crab cavities. Couplers are often added to RF cavities and are designed to resonate at the frequency of the HOMs which increases the power loss from these particular modes, resulting in a reduced R/Q value. In figure 2.31, the R/Q values for the various modes of the four rod crab cavity prototype design are shown. It can be seen that the R/Q value is significantly higher for the operating mode that the other modes. Many of the HOMs have the same spatial field distributions as the operating mode but at integer multiples of the operating frequency.

2.4.2 Crab cavities

Crab cavities, compared with accelerating cavities, provide a z dependent transverse kick rather than a z dependent longitudinal kick. The lowest frequency mode to operate in a pillbox cavity that provides this deflecting kick is given by a TM_{110} mode. The desired operating frequency for the HL-LHC is 400 MHz,

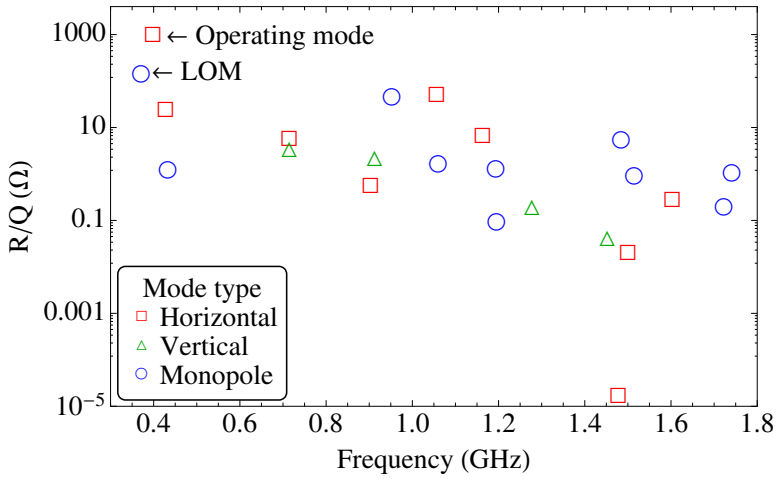

Figure 2.31: Modes of the four rod cavity; showing the Lower Order Mode, operating mode and Higher Order Modes [77].

which is chosen out of consideration of the bunch length in order to deliver a reasonably linear kick over the length of the bunch. From equation 2.87 this frequency would equate to a pillbox cavity with a radius of 610 mm.

Crab cavities are relatively new in colliders with the first implementation for crossing angle correction performed at the lepton collider KEKB in 2007 [78]. This crab cavity system has met with many operational issues linked to cavity breakdown, where the eigenmodes of the cavity fail due to sudden change in the boundary conditions caused by plasma emission from the surface of the cavity [79]. In KEKB a global crabbing scheme was used, in which the phase advance of the machine causes bunches to oscillate about their bunch centre as they travel around the machine, with the bunches reaching the desired angle for head on collision at the IP.

Crab cavities have never been tested in a hadron collider. They present many issues for a collider such as the HL-LHC where long term beam stability is important. In the initial studies for the HL-LHC two crabbing schemes were proposed; a global scheme and a local scheme, as shown in figure 2.32. The global scheme involved having crab cavities at IP4 which would cause the bunches to oscillate

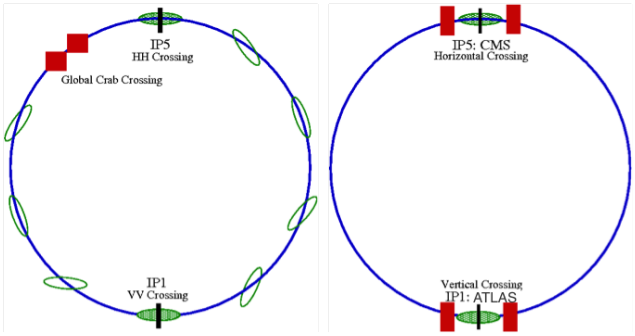

(a) (b)

Figure 2.32: (a) Global and (b) local crabbing schemes for the HL-LHC [80].

around the machine giving the correct tilt at each IP for the desired geometric correction. The global scheme allowed the use of elliptical cavities, similar to those used at KEKB, to perform the kick on the beam as there are no space constraints in having the cavities at IP4. The local scheme only applies this oscillation with phase advance locally across the IPs, with sets of cavities either side of the IP in order to cancel the oscillation. The local crab cavity scheme was chosen because of its flexibility, in that the scheme allows independent control of the IPs. It is anticipated that three cavities will be required for each beam, at each crabbing location in order to reach the desired voltage, for the SLHC v3.1b optics [68], required to completely overcome the geometric loss from the crossing angle.

2.4.3 Prototype crab cavity designs

There have been a number of proposed designs for the crab cavities in the HL-LHC with the shortlist of three potential designs, at the time of writing, shown in figure 2.33. The final shortlist of three potential crab cavity designs includes the four rod (4RCAV), quarter wave resonator (QWCAV) and the ridged wave guide (ODUCAV) cavities. The cavities have many space constraints which arise from having to fit side by side on two beam lines, within one cryostat, and

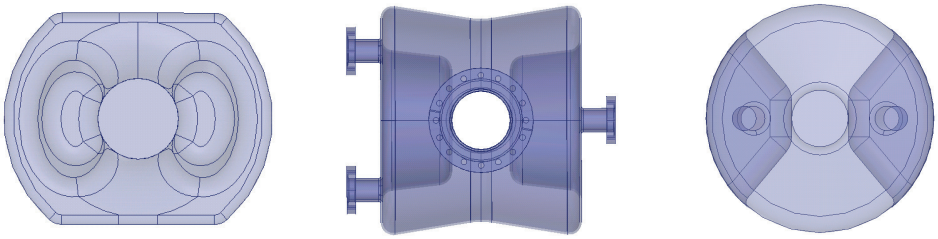

(a) (b) (c)

Figure 2.33: Proposed compact crab cavity designs. (a) Four rod cavity (Lancaster University/ CERN) [81] (b) Quarter wave resonator cavity (Brookhaven) [82] (c) Ridged wave guide cavity (ODU) [83]

longitudinally in the space between Q4 and D2 (see figure 2.25). The transverse beam separation is 194 mm at these locations, requiring the outer radius of the cavities to be limited to 150 mm. The length required to fit the three cavities, including couplers, is constrained to a maximum of 10 m [84].

In order to fit in this confined space, operate at a frequency of 400 MHz, and apply the correct voltage, unusual cavity geometries are required. The simplest cavity design of a pillbox, as previously discussed, would have a radius of 610 mm. For this reason a TM_{110} mode pillbox cavity can not be used for the crab cavities in the local crossing scheme whereas a TEM type resonator allows for more compact geometries of cavity. For TM mode cavities the frequency is dependent on the radius of the cavity, however, for a TEM type cavity this dependency is lost allowing for a cavity to have a very small transverse size.

The simplest design for a TEM type cavity is a quarter wave resonator [85]. This consists of a coaxial geometry with one end closed at a quarter of the wavelength from the resonator opening (Figure 2.34b). At resonance the high voltage is generated at the open end of the cavity and a transverse voltage is generated between that and the closed end of the cavity. The open end, which is at the bottom of the cavity, is where the RF power is inserted and the top is the closed

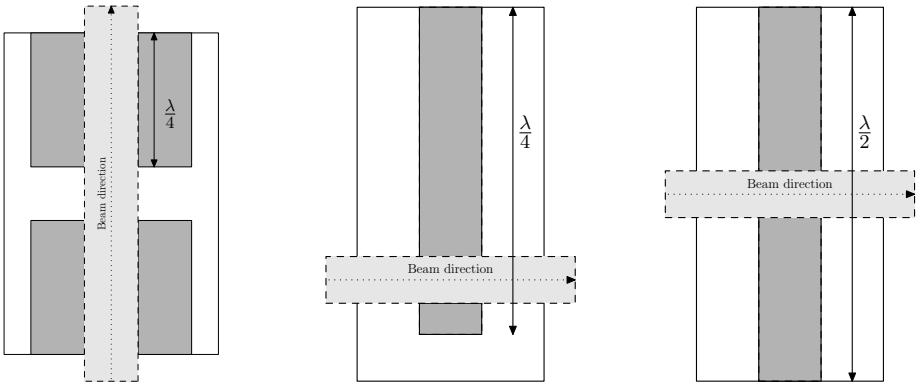

Figure 2.34: Basic form of coaxial geometry from which the (a) 4RCAV, (b) QWCAV, and (c) ODUCAV cavity designs are derived, where λ is the wavelength of the cavity.

end where the E field is reflected. The operating mode for deflection in the QWCAV is the lowest frequency eigenmode of the cavity. The higher order modes are at significantly higher frequencies than the fundamental mode which makes damping the cavity relatively simple compared with other designs. Geometrically the design is very compact between the closed end and the beam, allowing for the tight 194 mm beam separation.

The ODUCAV was originally based upon a half wave resonator design (Figure 2.34c). A half wave resonator is formed from two quarter wave resonators with both ends shorted and a length half that of the wavelength. The power is inputted half way up the cavity perpendicular to the beam line. The first eigenmode of such a resonator develops a potential between the upper and lower rods, leading to a cosine voltage distribution with zero voltage at the beam entrance and exit. This is an accelerating mode rather than the desired transverse deflecting mode. From this basic cavity design alterations can be made to produce a transverse deflecting mode. There are several ways to alter the half wave resonator to produce a deflecting mode; a spoke design by Li [86], and a parallel bar design based upon a pair of half wave resonators side by side with the deflecting

voltage formed between the two resonators [87]. In the plane perpendicular to the resonator the half wave resonator can be small. However, in the other plane the geometry is limited to half the wave length, meaning that the proposed designs will not fit when a crab cavity is orientated vertically. This was the reason for the development of the ODUCAV, as shown in figure 2.33c.

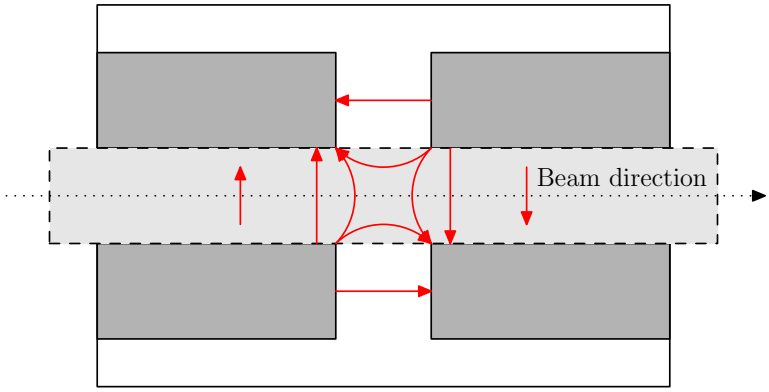

Figure 2.35: The operating mode of the four rod cavity showing the E field (red) around the tips of the rods [88].

The 4RCAV is based upon four quarter wave resonators arranged co-linearly about the beam axis, shown in figure 2.34a. The potential is developed between the tips of the rods leading to various resonant modes (shown in figure 2.31). The lowest order mode is an accelerating mode where the potential between the rods leads to an electric field parallel with the beam axis. This lower order mode requires significant damping in order to remove it. The operating mode resonates with rod tips with alternating polarity such that the electric field circulates around the four rod tips. Unlike the half wave and quarter wave designs this cavity's geometric constraint lies in its length, which causes less physical constraint, rather than in transverse dimensions. This length constraint consists of the length of each rod, $\lambda/4$, which dictates the cavity frequency and the separation between the rods, which is determined by the distance required to mitigate the electrical breakdown between the rods. This geometry allows the 4RCAV to be ultra compact [89]. This design already exists in a normal conducting context

for beam diagnostics at the Cornell electron recovery linac [90].

2.5 Single particle dynamics

In order to fully understand the behaviour of an accelerator an accurate and efficient model is required. For a high energy machine, the ability to calculate single particle trajectories through the machine is essential for its design and operation. The equations of motion for the Hamiltonian description of a given accelerator do not have a simple analytical result, hence a whole range of techniques are used to calculate approximate transformations around the machine in order to determine the trajectory of a particle. These techniques have to make compromises on the speed of calculation, numerical accuracy of the result and accuracy in the representation of the real machine in order for a trajectory to be calculated.

For a storage ring, such as the LHC, a significant performance goal is its integrated luminosity. The integrated luminosity is dependent upon the lattice, to allow for a large peak luminosity (see section 2.2.2), and the dynamic aperture, to allow for a long beam lifetime and significant current (see section 2.2.3). The beam lifetime and current are dependent upon the long term stability of the machine, which corresponds directly to particle losses on restrictive physical apertures e.g. collimators. Comparing such stability calculations for hadron machines, such as the LHC, requires a significantly greater number of turns to be tracked in order to define the dynamic aperture. This is significantly higher than for lepton machines, such as LEP, for which the processes of synchrotron radiation and damping lead to far more stable machines.

In order to find the dynamic aperture a Poincaré section from the tracking data is required. A Poincaré section describes the turn by turn behaviour of a particle as it passes a point periodically in the lattice. A Poincaré map projects a particle to its next position on the Poincaré section after one turn. There are

three techniques for generating such a map from a periodic accelerator, in order of slowest to fastest:

1. **Numerically integrate through the complete electromagnetic field map of the accelerator.**

   This technique is often preferred for cases of small accelerators in which the small variation of fields has significant impact upon the stability of the machine. Issues arise when a precise magnet strength is required in the lattice and the step size throughout the fields affects the convergence to this strength; this is particularly true for a hadron synchrotron where small errors scale considerably over many turns. This method is able to conserve the phase space volume and is therefore relatively numerically stable. The most significant issues with this technique are its computational and time inefficiencies; this method is very slow.

2. **Model each element as a single transformation and integrate through the lattice, element by element.**

   In general this is used for long term tracking of larger accelerators, for example LHC simulations, in the form of a kick code (e.g. SixTrack [91]), which describes each element as a set of momentum kicks separated by drifts. This is particularly reasonable for cases of magnets where the edge, or "fringe" field effects are small and many magnets have to be modelled. It is possible to further decompose the magnets into azimuthal modes called multipoles, with the integrated kicks of each multipole providing the description for any magnet. An extension to this method is the use of generating functions. A phase space conserving (or symplectic) transformation can be described by a generating function which ensures the phase conservation when integrating through the lattice. This method is computationally very fast and is particularly useful for cases of machines with many different magnets.

3. **Devise a single transformation representing one turn of the accelerator.**

   This technique requires integrating through the lattice, using either the first or second method without assigning the initial canonical variables on the Poincaré section. This generates a one turn map or Poincaré map from which the whole of phase space might be evaluated. One representation of this transformation is a Taylor map, these are Taylor series [92] representations formed by multiplying through the single element transfer maps using truncated power series algebra. Truncation of such a map, caused by the limitations of orders to which power series can be computed, generates significant errors in the numerical and model accuracy. Particular issues lie in the conservation of phase space volume, more formally described as symplectic error. Methods exist to fix this broken symplecticity in a Taylor map [93], however, these generate further complications. The typical approach to rectify this symplectic error is to factorise the Taylor map to give a transformation which has a corresponding generating function. This method has been used in the past to study large machines, for example the LHC [94, 95], but it is now avoided for long term tracking due to the symplecticity issues which lead to a broken phase space. The single transfer map, however, does allow the calculation of the normal form, closed orbit and many global properties of the lattice, hence it is still useful. Other representations of this one turn map can be considered such as Lie maps [93] or mixed variable generating functions [96].

The techniques used to make a Taylor map can be expanded to the construction of single element transformations rather than just those of the whole machine. This considerably improves the accuracy of the description of specific elements within an accelerator, thereby restricting the symplectic errors to originate in a

small number of elements rather than over the whole of the machine.

2.5.1 Accelerator Hamiltonian

A Hamiltonian, H, is a function which describes the total energy of a physical system in terms of a set of canonical variables. A Lagrangian, in a similar manner, is a function describing the dynamics of a physical system defined by the kinetic energy of the system minus its potential energy. The Lagrangian, $\mathcal{L}$, is expressed in terms of position and velocity rather than position and momentum. Two representations are linked by the Legendre transformation of the Lagrangian so that,

$$H(q_j, p_j; t) = \sum_i \dot{q}_i p_i - \mathcal{L}(q_j, \dot{q}_j; t) \tag{2.88}$$

where q is position, p is momentum, $\dot{q}$ is velocity and t is time, which is the independent variable. The time evolution of the system is defined by Hamilton's equations,

$$\frac{dp}{dt} = \frac{\partial H}{\partial q}, \tag{2.89}$$

$$\frac{dq}{dt} = -\frac{\partial H}{\partial p}. \tag{2.90}$$

For simple Hamiltonian systems, for example a pendulum, for which the Hamiltonian is separable into components with p and q dependence, directly applying Hamilton's equations is possible. Introducing mixed terms means that solving the equations of motion is no longer trivial.

All single particle dynamics calculations consider the motion of a charged particle through an electromagnetic field. This can be considered from a Newtonian or Hamiltonian perspective, where in the Hamiltonian case the particle is considered moving in a potential. Single particle dynamics ignores things such as collective effects, which are related to the interaction of the particles with

each other [30]. For many applications, to first order, these interactions are not considered. Defining the Hamiltonian of such a system begins with the relationship between energy E and mechanical momentum $\vec{P}$ of a particle given by the relation [97],

$$E^2 = m^2c^4 + \vec{P}^2c^2 \tag{2.91}$$

where m is the mass of the particle. In the case where no external forces are applied the Hamiltonian of a system H can be considered the total energy,

$$H = \sqrt{\vec{P}^2c^2 + m^2c^4}. \tag{2.92}$$

At this point it is important to clarify the difference between the mechanical and conjugate momenta, denoted $\vec{P}$ and $\vec{p}$ respectively. To describe the electromagnetic potential in which the particle is sited a scalar function ϕ and vector potential $\vec{A}$ are required; these are dependent on the position and time. In the presence of an electromagnetic field the conjugate and mechanical momenta are no longer equal and they are related to each other by the vector potential $\vec{A}$ [98]. This arises from the Lagrangian of a non-relativistic particle in an electromagnetic field,

$$\mathcal{L} = \frac{1}{2}m\dot{\vec{x}} \cdot \dot{\vec{x}} - q\phi + q\vec{A} \cdot \dot{\vec{x}}, \tag{2.93}$$

where q is the particle charge. The conjugate momentum is given by,

$$\vec{p} = \frac{\partial \mathcal{L}}{\partial \dot{\vec{x}}} = m\dot{\vec{x}} + q\vec{A} \tag{2.94}$$

which can be rearranged to,

$$\vec{P} = \vec{p} - q\vec{A}, \tag{2.95}$$

where $\vec{P}$ is the mechanical momentum and in the relativistic case is given by $\gamma m\dot{\vec{x}}$.

The Hamiltonian may now be expressed in terms of the conjugate momentum,

$$H(x, p_x, y, p_y, z, p_z; t) = \sqrt{(\vec{p} - q\vec{A})^2 c^2 + m^2 c^4} + q\phi. \tag{2.96}$$

In the form given in equation 2.96, the Hamiltonian is not particularly useful for describing an accelerator, where the lattice is defined in space and not time, hence a change of independent variable is convenient. The first step required is to change the independent variable from time t to path length s, via the principle of least action [99]. The action of a physical system $\mathcal{S}$ is defined as the integral of the Lagrangian between two instants in time. The Euler-Lagrange equations further define a path between these two instances in which the property of the action is a minimum such that,

$$\delta\mathcal{S} = \delta\left[\int_{t_0}^{t_1} \mathcal{L}\, dt\right] = 0. \tag{2.97}$$

Expressing the action in terms of the Hamiltonian using equation 2.88 takes the form,

$$\mathcal{S} = \int_{t_0}^{t_1} \left(p_x\dot{x} + p_y\dot{y} + p_z\dot{\tilde{z}} - H\right)\, dt \tag{2.98}$$

where the $\dot{x}$ is the first derivative of x with respect to t. Changing the independent variable to $\tilde{z}$, which is defined as the path length, changes the action to

$$\mathcal{S} = \int_{\tilde{z}_0}^{\tilde{z}_1} \left(p_x x' + p_y y' + p_z - Ht'\right)\, d\tilde{z} \tag{2.99}$$

where the x' is the first derivative of x with respect to $\tilde{z}$. From this it can be seen that the new set of canonical variables required for $\tilde{z}$ as the independent variable are given by,

$$(x, p_x) \qquad (y, p_y) \qquad (-t, H) \tag{2.100}$$

and the new Hamiltonian, $\tilde{H}$ equates to $-p_z$. Rearranging the Hamiltonian, H, given in equation 2.96 with energy E, and normalising with the reference momentum p_0 results in,

$$\tilde{H}(x, \tilde{p}_x, y, \tilde{p}_y, -t, E; \tilde{z}) = -\sqrt{\frac{(E - q\phi)^2}{p_0^2 c^2} - \frac{m^2 c^2}{p_0^2} - (\tilde{p}_x - a_x)^2 - (\tilde{p}_y - a_y)^2} - a_z \tag{2.101}$$

where E is the total energy, $\tilde{\vec{p}}$ is the normalised conjugate momentum, and $\vec{a} = q\vec{A}/p_0$. For a relativistic particle $E/p_0 \approx c$, showing that this Hamiltonian's sensitivity to energy variation is small. In order to increase this sensitivity a new pair of conjugate variables are introduced to replace $\tilde{z}$ and E. The longitudinal variable describing the energy deviation is given by,

$$\delta = \frac{E}{p_0 c} - \frac{1}{\beta_0}, \tag{2.102}$$

where β_0 is the speed of the reference particle as a fraction of c. A particle with reference energy will have a value of $\delta = 0$. The conjugate to δ is the relative longitudinal position of a particle relative to the reference particle,

$$z = \frac{\tilde{z}}{\beta_0} - ct. \tag{2.103}$$

A particle ahead of the reference particle has a positive $\tilde{z}$ value and behind has a negative value. By renaming the conjugate variables in order to simplify the expression of the Hamiltonian,

$$\tilde{H} \mapsto H \qquad \tilde{\vec{p}} \mapsto \vec{p} \qquad \tilde{z} \mapsto s$$

the accelerator Hamiltonian is defined,

$$H(x, p_x, y, p_y, z, \delta; s) = \frac{\delta}{\beta_0} - \sqrt{\left(\frac{1}{\beta_0} + \delta - \frac{q\phi}{p_0 c}\right)^2 - (p_x - a_x)^2 - (p_y - a_y)^2 - \frac{1}{\beta_0^2 \gamma_0^2}} - a_z. \tag{2.104}$$

In this accelerator Hamiltonian the independent variable is now the reference orbit position s, with the canonical transverse positions x and y, canonical transverse momenta p_x and p_y and longitudinal variables z and δ. In order to simplify this Hamiltonian further a gauge can be chosen which reduces the number of components of the electromagnetic potential required to describe the fields. One such gauge is named the Weyl gauge (or Hamiltonian gauge) and sets the scalar potential to zero, $\phi = 0$.

2.5.2 Symplecticity

A canonical transformation is a change in canonical coordinates that preserves the form of Hamilton's equations [100]. Symplecticity is the property that defines this preservation. If a transformation can be said to be symplectic then it must also be canonical. A canonical transformation is characterised by the generating function of the transformation [100, p. 144]. The generating function gives the relationship between the initial coordinates, final coordinates and the new Hamiltonian. Generating function theory states that if a given transformation is canonical then a generating function exists to describe it. This provides a direct method with which to test the symplecticity of a transformation. A direct calculation to obtain the corresponding generating function from a general transformation does not exist. Another method is then required to analytically determine whether the transformation is canonical, and therefore symplectic, this approach uses the symplectic condition [101].

In order to generalise the form of Hamilton's equations the antisymmetric

matrix $\mathbf{S}$ is introduced,

$$\mathbf{S} = \begin{pmatrix} \mathbf{s} & \mathbf{0} & \mathbf{0} \\ \mathbf{0} & \ddots & \mathbf{0} \\ \mathbf{0} & \mathbf{0} & \mathbf{s} \end{pmatrix}$$
$$\mathbf{s} = \begin{pmatrix} 0 & 1 \\ -1 & 0 \end{pmatrix}. \tag{2.105}$$

This matrix has the following properties,

$$\mathbf{S}^{-1} = \tilde{\mathbf{S}} = -\mathbf{S}, \qquad \mathbf{S}^2 = -\mathbf{I}, \qquad |\mathbf{S}| = 1. \tag{2.106}$$

Consider that a transformation can be written,

$$\mathbf{x} = \mathbf{x}(\mathbf{X}, s) \tag{2.107}$$

where $\mathbf{x}$ is the column matrix of initial conjugate variables and $\mathbf{X}$ is the resulting column matrix of conjugate variables. The inverted transformation is defined,

$$\mathbf{X} = \mathbf{X}(\mathbf{x}, s). \tag{2.108}$$

Using the $\mathbf{S}$ matrix Hamilton's equations can be expressed for the Hamiltonian $H(\mathbf{x}, s)$; in addition, if the transformation is canonical, a Hamiltonian $K(\mathbf{X}, s)$ will exist. This leads to the general forms of Hamilton's equations,

$$\mathbf{X}' = \mathbf{S}\frac{\partial K}{\partial \mathbf{X}} \qquad \mathbf{x}' = \mathbf{S}\frac{\partial H}{\partial \mathbf{x}}. \tag{2.109}$$

The total derivative of $\mathbf{X}$ with respect to s is,

$$\mathbf{X}' = \frac{\partial \mathbf{X}}{\partial \mathbf{x}}\mathbf{x}' + \frac{\partial \mathbf{X}}{\partial s}, \tag{2.110}$$

this can be further simplified by introducing the Jacobian, $\mathbf{J}$, defined,

$$\mathbf{J} = \frac{\partial \mathbf{X}}{\partial \mathbf{x}}. \tag{2.111}$$

Inserting equation 2.111 into equation 2.110 with the relations defined in equation 2.109 leads to,

$$\frac{\partial K}{\partial \mathbf{X}} = \tilde{\mathbf{S}} \left(\mathbf{J}\mathbf{S} \frac{\partial H}{\partial \mathbf{x}} + \frac{\partial \mathbf{X}}{\partial s} \right). \tag{2.112}$$

Using the Jacobian relation,

$$\frac{\partial K}{\partial \mathbf{x}} = \tilde{\mathbf{J}} \frac{\partial K}{\partial \mathbf{X}}, \tag{2.113}$$

allows for further simplification of equation 2.112 to,

$$\frac{\partial K}{\partial \mathbf{x}} = \tilde{\mathbf{J}}\tilde{\mathbf{S}}\mathbf{J}\mathbf{S} \frac{\partial H}{\partial \mathbf{x}} + \tilde{\mathbf{J}}\tilde{\mathbf{S}} \frac{\partial \mathbf{X}}{\partial s}. \tag{2.114}$$

This resulting matrix equation represents a set of $2N$ equations which take the form,

$$\frac{\partial K}{\partial x_j} = a_j + \sum_{k=1}^{2N} b_{jk} \frac{\partial H}{\partial x_k} \tag{2.115}$$

where $\mathbf{a}$ and $\mathbf{b}$ are,

$$\mathbf{a} = \tilde{\mathbf{J}}\tilde{\mathbf{S}} \frac{\partial \mathbf{X}}{\partial s} \qquad\qquad \mathbf{b} = \tilde{\mathbf{J}}\tilde{\mathbf{S}}\mathbf{J}\mathbf{S}. \tag{2.116}$$

If K is a Hamiltonian, it is also a scalar function, and hence takes the following condition,

$$\frac{\partial^2 K}{\partial x_i \partial x_j} = \frac{\partial^2 K}{\partial x_j \partial x_i} \tag{2.117}$$

Applying this to equation 2.115 leads to,

$$\left(\frac{\partial a_j}{\partial x_i} - \frac{\partial a_i}{\partial x_j} \right) + \sum_{k=1}^{2N} \left(\frac{\partial b_{jk}}{\partial x_i} - \frac{\partial b_{ik}}{\partial x_j} \right) \frac{\partial H}{\partial x_k} + e_{ij} = 0 \tag{2.118}$$

where e_{ij} is defined in terms of the Hamiltonian H such that,

$$e_{ij} = \sum_{k=1}^{2N} \left(b_{jk} \frac{\partial^2 H}{\partial x_i \partial x_k} - b_{ik} \frac{\partial^2 H}{\partial x_j \partial x_k} \right) \tag{2.119}$$

H and K must be scalar functions for any i and j hence,

- $\left(\frac{\partial a_j}{\partial x_i} - \frac{\partial a_i}{\partial x_j} \right)$ vanishes when summed over all i and j values.
- $\left(\frac{\partial b_{jk}}{\partial x_i} - \frac{\partial b_{ik}}{\partial x_j} \right)$ also vanishes for each k value when summed over all i and j values.
- This leaves $e_{ij} = 0$. Considering the cases where $i \neq j$ in the summation, there will exist two cases where $k = j$ and $k = i$,

  $$\left(b_{jj} \frac{\partial^2 H}{\partial x_i \partial x_j} - b_{ij} \frac{\partial^2 H}{\partial x_j^2} \right) \qquad \left(b_{ji} \frac{\partial^2 H}{\partial x_i^2} - b_{ii} \frac{\partial^2 H}{\partial x_j \partial x_i} \right)$$

  These are the only terms in which mixed derivatives appear, for them to disappear $b_{ii} = b_{jj}$, furthermore $b_{ij} = 0$ for all $i \neq j$.

This leaves the diagonal components of $\mathbf{b}$ which must be equal but not zero, which leads to $\mathbf{b} = \lambda \mathbf{I}$, where λ is a constant. From equation 2.116 the extended symplectic condition can be derived,

$$\begin{aligned} \tilde{\mathbf{J}}\tilde{\mathbf{S}}\mathbf{J}\mathbf{S} &= \lambda \mathbf{I} \\ \tilde{\mathbf{J}}\mathbf{S}\mathbf{J}\mathbf{S} &= \lambda \mathbf{S}^2 \\ \tilde{\mathbf{J}}\mathbf{S}\mathbf{J} &= \lambda \mathbf{S} \end{aligned} \tag{2.120}$$

This result determines whether a generating function exists for a given transformation, thereby removing the need to attempt to find one. This is especially useful for something like a Taylor map where there can be many terms making up the transformation. The symplectic condition is given by the case of $\lambda = 1$,

from which an error $\mathbf{E}$ can be defined,

$$\mathbf{E} = \tilde{\mathbf{J}}\mathbf{S}\mathbf{J} - \mathbf{S} \tag{2.121}$$

This gives a technique which analytically determines whether a transformation is canonical, and hence symplectic. It can also provide a measure of symplectic error of a given transformation. A further general property of a symplectic transformation is that [102],

$$\det(\mathbf{J}) = 1. \tag{2.122}$$

This can be shown by considering the Jacobian in terms of the Hamiltonian. From Hamilton's equations, the Jacobian describing the transformation over a small time step Δt is given by,

$$\mathbf{J} = \begin{pmatrix} 1 + \frac{\partial^2 H}{\partial q\, \partial p}\Delta t & -\frac{\partial^2 H}{\partial q^2}\Delta t \\ \frac{\partial^2 H}{\partial p^2}\Delta t & 1 - \frac{\partial^2 H}{\partial q\, \partial p}\Delta t \end{pmatrix} + \mathcal{O}(\Delta t^2), \tag{2.123}$$

$$\det(\mathbf{J}) = 1. \tag{2.124}$$

Unlike $\mathbf{E}$, which is in the form of a matrix, $\det(\mathbf{J})$ provides a scalar value of error. However, $\det(\mathbf{J})$ does not determine if the transformation is canonical.

A further property of these canonical transformations is that every result from an initial condition is unique. This property arises from the theory of differential equations [103, 101]. Consider the case of a volume of phase space filled with points of various initial conditions such that all points have an infinitely small gap between their neighbouring points. Applying a canonical transformation to each of these points for a small time step leads to a new resulting condition. Given that the initial conditions were all unique the corresponding results must be unique. As the points are restricted to their own unique trajectory the gaps between them must remain conserved. This leads to Liouville's theorem which

states:

> "In any system governed by a Hamiltonian, the density of system points surrounding a particular system point in phase space must remain constant as the independent variable evolves." [101, 104]

2.5.3 Numerical integration methods

Numerical integration is used when there is an inability to find a closed form expression for an integral. It is common for a Hamiltonian system not to have a closed form expression for the equations of motion but instead for numerical integration to be applied in order to determine the evolution of the system with the independent variable.

Classification of integration methods

Numerical integration comes in two forms: explicit and implicit. An integration step starts from the current value of the independent variable, s_0, and goes to the future step, $s_0 + \Delta s$, over which the conjugate variables change. The explicit approach evaluates the Hamiltonian from the current conjugate variables, at s_0. The implicit approach finds a solution to a set of equations determining both the current and future conjugate variable values, at s_0 and $s_0 + \Delta s$ respectively; this might be done using a numerical method such as the Newton-Raphson method.

The first form of integration to consider is the first order explicit Euler method. The order of an integrator is defined by the truncation of the following Taylor expansion,

$$p(s + \Delta s) = p(s) + \Delta s \; \dot{p}(s) + \frac{1}{2}\Delta s^2 \; \ddot{p}(s) + \ldots \tag{2.125}$$

where $\dot{p}$ and $\ddot{p}$ are the first and second order differentiation of p with respect to s, and the order is defined by the highest order of differentiation. From the expansion, the first order explicit method (Forward Euler) is given by the following

steps,

$$\textbf{1: } q(s+\Delta s) = q(s) + \Delta s\ p(s), \tag{2.126}$$

$$\textbf{2: } p(s+\Delta s) = p(s) + \Delta s\ \dot{p}(s), \tag{2.127}$$

where p and q are the conjugate momenta and position. From Hamilton's equations (equation 2.89), Forward Euler in terms of the Hamiltonian is given by,

$$\textbf{1: } q(s+\Delta s) = q(s) + \Delta s\ p(s), \tag{2.128}$$

$$\textbf{2: } p(s+\Delta s) = p(s) - \Delta s\ \nabla_q H\left[q(s), p(s); s\right]. \tag{2.129}$$

The implicit case for the Euler method (Backward Euler) requires using a numerical method to determine the future values of the canonical variables,

$$\textbf{1: } q(s+\Delta s) = q(s) + \Delta s\ p(s+\Delta s), \tag{2.130}$$

$$\textbf{2: } p(s+\Delta s) = p(s) - \Delta s\ \nabla_q H\left[q(s) + \Delta s\ p(s+\Delta s), p(s+\Delta s); s+\Delta s\right]. \tag{2.131}$$

The second step can be performed by numerically solving,

$$p(s+\Delta s) = p(s) - \Delta s\ \nabla H_q\left[q(s) + \Delta s\ p(s+\Delta s), p(s+\Delta s); s+\Delta s\right], \tag{2.132}$$

using a method such as the Newton-Raphson method, where the function $f(p(s+\Delta s))$ is,

$$\begin{aligned} f\left[p(s+\Delta s)\right] =& p(s+\Delta s) - p(s) \\ &+ \Delta s \nabla_q H\left[q(s) + \Delta s\ p(s+\Delta s, p(s+\Delta s); s+\Delta s\right]. \end{aligned} \tag{2.133}$$

The value of $p(s+\Delta s)$ for which $f\left[p(s+\Delta s)\right]=0$ can be found using the method,

$$\begin{aligned} p_{n+1} =& p_n - \frac{f(p_n)}{f'(p_n)}, \\ p_n =& p_{n+1}, \end{aligned} \tag{2.134}$$

where p_n converges on the solution. The forward and backward Euler methods are both non-symplectic which means that as the system evolves the phase space density is no longer conserved. The semi-implicit Euler method, however, is globally symplectic and is given by,

$$\textbf{1:}\ q(s+\Delta s) = q(s) + \Delta s\ p(s+\Delta s), \tag{2.135}$$

$$\textbf{2:}\ p(s+\Delta s) = p(s) - \Delta s\ \nabla_q H\left[q(s), p(s); s\right]. \tag{2.136}$$

Locally the semi-implicit method exhibits oscillations in the phase space area. To consider the properties of these three Euler integration methods the Hamiltonian of a non-linear pendulum is considered,

$$H(q,p;t) = \frac{1}{2}p^2 - \cos(q). \tag{2.137}$$

The phase space area conservation is a property of a symplectic transformation. In figure 2.36 the phase space and phase space area are shown; they are calculated using the aforementioned Euler integration methods implemented using Mathematica [105]. It can be seen that globally the phase space area of the semi-implicit method remains conserved. The explicit method undergoes an increase in phase space area over time, equating to an energy growth and outward spiralling trajectory. In contrast the implicit method decreases in phase space area over time, equating to energy loss and inward spiralling trajectory.

The order of integration is increased by taking the next term in the series given

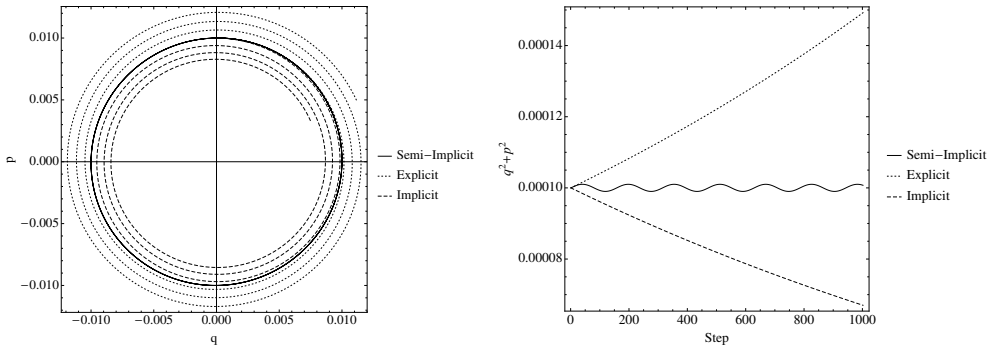

(a) (b)

Figure 2.36: (a) The position and momentum and (b) phase space area over 1000 turns with $\Delta s = 0.02$ using Euler (First order) methods.

in equation 2.125. The second order semi implicit integration (Velocity-Verlet) is given by,

$$\textbf{1:}\ q(s+\Delta s) = q(s) + \Delta s\ p(s) - \frac{1}{2}\Delta s^2\ \nabla_q H\left[q(s), p(s); s\right], \tag{2.138}$$

$$\textbf{2:}\ p(s+\Delta s) = p(s) + \frac{\Delta s}{2}\left\{\nabla_q H\left[q(s), p(s); s\right] + \nabla_q H\left[q(s) + \Delta s\ p(s), p(s); s+\Delta s\right]\right\}. \tag{2.139}$$

In figure 2.37 it can be seen that both semi-implicit methods undergo oscillatory errors. The magnitude and frequency decreases with the order of integration.

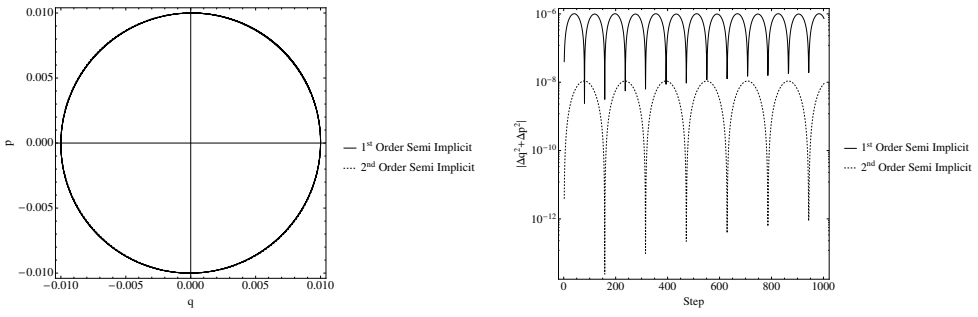

(a) (b)

Figure 2.37: (a) The position and momentum and (b) the phase space error over 1000 turns with $\Delta s = 0.02$, comparing first and second order semi implicit methods.

In summary, non-symplectic integration methods lead to a loss in the preservation of phase space. Furthermore, with increased order of integration there is a decreased local phase space area error.

Extending and expanding the accelerator Hamiltonian

The integration order and the method are both important considerations in calculating the transformation generated by a Hamiltonian. In order to integrate the accelerator Hamiltonian an approach is required to deal with the mixed terms in the Hamiltonian. An implicit method is computationally more intensive due to the need to numerically find the future canonical variable values. The semi-implicit method requires the Hamiltonian to be separable, with no mixed momentum and position terms, such that it is directly solvable with Hamilton's equations; this excludes it from being used with the accelerator Hamiltonian. Therefore, an explicit symplectic method is required for the accelerator Hamiltonian. For a Hamiltonian of the form,

$$H = T(\vec{p}) + V(\vec{q}) \tag{2.140}$$

the momentum and spatial dependent components are separable. This work was originally performed by Ruth [106] and allows for symplectic integration of accelerator components for which $a_x = a_y = 0$. For cases in which these are non-zero, where the transverse magnetic field varies longitudinally, the Hamiltonian takes the following form [107],

$$H = T\left[\vec{p} - \vec{a}(\vec{q}, s)\right] + V(\vec{q}, s). \tag{2.141}$$

In order to develop an integrator for an s dependent Hamiltonian an extension of the phase space is required in order for s to become a canonical variable rather

than just an independent variable. When integrating through a vector potential which is s dependent, such as that of a real magnet, the Hamiltonian phase space can be extended to include (s, p_s) with a new independent variable σ, where $d\sigma = ds$ [108]. This leads to the extended accelerator Hamiltonian,

$$\begin{aligned} &H(x, p_x, y, p_y, z, \delta, s, p_s; \sigma) \\ &= \frac{\delta}{\beta_0} - \sqrt{\left(\frac{1}{\beta_0} + \delta - \frac{q\phi}{p_0 c}\right)^2 - (p_x - a_x)^2 - (p_y - a_y)^2 - \frac{1}{\beta_0^2 \gamma_0^2}} - a_z + p_s, \end{aligned} \tag{2.142}$$

where $\vec{a} = \vec{a}(x, y, z, s; \sigma)$. There are two main difficulties when finding the equations of motion from such a Hamiltonian. The first is that, unlike the case of the pendulum, it is not directly solvable using Hamilton's equations, and the second arises from the complexity caused by the square root. The first difficulty arises from the mixed terms containing both momentum and position dependence. The series expansion,

$$\sqrt{a^2 - x^2} \approx a - \frac{x^2}{2a} \tag{2.143}$$

to second order, allows the second difficulty to be removed. This expansion is called the paraxial approximation and is valid in cases where $p_x/p_s \ll 1$. This expresses the Hamiltonian to second order in transverse canonical variables:

$$\begin{aligned} H = &- \left(\frac{1}{\beta_0} + \delta\right) + \frac{1}{2\beta_0^2\gamma_0^2}\left(\frac{1}{\beta_0} + \delta\right)^{-1} + \frac{\delta}{\beta_0} + \frac{(p_x - a_x)^2}{2\left(\frac{1}{\beta_0} + \delta\right)} + \frac{(p_y - a_y)^2}{2\left(\frac{1}{\beta_0} + \delta\right)} \\ &- a_z + p_s. \end{aligned} \tag{2.144}$$

From this Hamiltonian there are mixed terms originating from the transverse vector potential terms, but with the use of Lie transformations an explicit integrator can be produced.

Lie transformations

In order to find the transformations resulting from the paraxial approximation of the extended phase space Hamiltonian Lie algebra must first be introduced. A Lie operator $:H:$ for any function $H(q,p;s)$ is defined [109],

$$:H:\equiv[H,\circ]=\frac{\partial g}{\partial q}\frac{\partial}{\partial p}-\frac{\partial g}{\partial p}\frac{\partial}{\partial q} \tag{2.145}$$

where $\circ$ is the canonical variable being operated on. Hamilton's equations in Lie operator form are given by,

$$\frac{\mathrm{d}x}{\mathrm{d}\sigma}=-:H:x. \tag{2.146}$$

The evolution of variable x in the independent variable σ can be written as,

$$x(\sigma_0+\Delta\sigma)=e^{-:H:\Delta\sigma}x(\sigma_0). \tag{2.147}$$

In the exponential form this operation is defined by the Taylor expansion,

$$e^{-\Delta\sigma:H:}=1-\Delta\sigma:H:+\frac{\Delta\sigma^2}{2}:H:H:-\frac{\Delta\sigma^3}{3!}:H:H:H:+\ldots \tag{2.148}$$

This operation $e^{:H:}$ is called a Lie transformation. The properties of this transformation allow for an appropriate integrator to be developed. The following rules apply to Lie transformations:

1. The series expression for a Lie transformation with generator x is,

$$e^{:H:}x=x+[H,x]+\frac{1}{2}[H,[H,x]]+\ldots \tag{2.149}$$

2. The Lie transformation of the product of two functions is,

$$e^{:H:}(xy)=(e^{:H:}x)(e^{:H:}y). \tag{2.150}$$

3. The Lie transformation of a function operating on a function is,

$$e^{:H:}x(y) = x(e^{:H:}y). \tag{2.151}$$

4. The Lie transformation of a Poisson bracket is,

$$e^{:H:}[x, y] = [e^{:H:}x, e^{:H:}y]. \tag{2.152}$$

5. The Lie transformation of a Lie transformation with generator x is,

$$e^{:e^{:H:}x:} = e^{:H:}e^{:x:}e^{-:H:}. \tag{2.153}$$

Lie transformations also provide a way in which the Hamiltonian can be split into parts. From the Baker-Campbell-Hausdoff formula (BCH) the combination of two Lie transformations might be expressed as [110]

$$e^{:A:}e^{:B:} = e^{:C:} \tag{2.154}$$

where,

$$C = A + B + \frac{1}{2}[A, B] + \frac{1}{12}[A, [A, B]] + \frac{1}{12}[B, [B, A]] + \dots \tag{2.155}$$

The Zassenhaus formula comes from the BCH and is needed to be able to factorize a Lie transformation whose generator is expressed as a sum;

$$e^{-\Delta\sigma:A+B:} = e^{-\Delta\sigma:A:}e^{-\Delta\sigma:B:}e^{\frac{\Delta\sigma^2}{2}:[A,B]:}e^{-\frac{\Delta\sigma^3}{6}(2:[B,[A,B]]:+:[A,[A,B]]:)}\dots \tag{2.156}$$

Considering the simple case in which $H = H_1 + H_2$, using BCH this might be expressed as,

$$e^{-\Delta\sigma:H_1:}e^{-\Delta\sigma:H_2:} = e^{-\Delta\sigma:H_1+H_2-\frac{\Delta\sigma}{2}[H_1,H_2]+\ldots:} \tag{2.157}$$

$$= e^{-\Delta\sigma:H_1+H_2+O(\Delta\sigma):}. \tag{2.158}$$

This concatenation of maps leaves errors of $\Delta\sigma^2$, in order to gain a higher order map a different form of this concatenation is required. Therefore by further splitting H_1 the following can be derived,

$$e^{-d_1\Delta\sigma:H_1:}e^{-\Delta\sigma:H_2:}e^{-d_2\Delta\sigma:H_1:} = e^{-d_1\Delta\sigma:H_1:}e^{-\Delta\sigma:d_2H_1+H_2-\frac{1}{2}d_2L[H_1,H_2]+\ldots:} \tag{2.159}$$

$$= e^{-\Delta\sigma:(d_1+d_2)H_1+H_2-\frac{1}{2}(d_1-d_2)L[H_1,H_2]+\ldots:}. \tag{2.160}$$

From the choice of $d_1 = d_2 = \frac{1}{2}$ a second order splitting can be formed,

$$e^{-\frac{\Delta\sigma}{2}:H_1:}e^{-\Delta\sigma:H_2:}e^{-\frac{\Delta\sigma}{2}:H_1:} = e^{-\Delta\sigma:H_1+H_2+O(\Delta\sigma^2):}. \tag{2.161}$$

Using similar methods developed by Yoshida even higher order concatenation of maps can be performed [111].

Splitting of the Hamiltonian

From the accelerator Hamiltonian H, the transfer map over a path length $\Delta\sigma$ is given by [107],

$$\mathcal{M}(\Delta\sigma) = e^{-\Delta\sigma:H:}. \tag{2.162}$$

The Hamiltonian H, in its paraxial form, can be split into four components. This is chosen to simplify the splits to two components which are only dependent on either momentum or spatial components (H_1 and H_4). The remaining two components, formed of mixed variables, can be reduced to a solvable form by

using Lie methods.

$$H_1(\delta, p_s; \sigma) = -\left(\frac{1}{\beta_0} + \delta\right) + \frac{1}{2\beta_0^2\gamma_0^2}\left(\frac{1}{\beta_0} + \delta\right)^{-1} + \frac{\delta}{\beta_0} + p_s, \quad (2.163)$$

$$H_2(x, y, z, s, p_x, \delta; \sigma) = \frac{(p_x - a_x)^2}{2\left(\frac{1}{\beta_0} + \delta\right)}, \quad (2.164)$$

$$H_3(x, y, z, s, p_y, \delta; \sigma) = \frac{(p_y - a_y)^2}{2\left(\frac{1}{\beta_0} + \delta\right)}, \quad (2.165)$$

$$H_4(x, y, z, s; \sigma) = -a_z. \quad (2.166)$$

From this splitting the transfer map is written,

$$\mathcal{M}(\Delta\sigma) = e^{-\Delta\sigma:H_1+H_2+H_3+H_4:}. \quad (2.167)$$

Using a second order splitting the full transfer map is given by,

$$\begin{aligned}
e^{-\Delta\sigma:H_1+H_2+H_3+H_4:} &= e^{-\frac{\Delta\sigma}{2}:H_1+H_2+H_3:}e^{-\Delta\sigma:H_4:}e^{-\frac{\Delta\sigma}{2}:H_1+H_2+H_3:} \\
&= e^{-\frac{\Delta\sigma}{4}:H_1+H_2:}e^{-\frac{\Delta\sigma}{2}:H_3:}e^{-\frac{\Delta\sigma}{4}:H_1+H_2:}e^{-\Delta\sigma:H_4:}e^{-\frac{\Delta\sigma}{4}:H_1+H_2:}e^{-\frac{\Delta\sigma}{2}:H_3:}e^{-\frac{\Delta\sigma}{4}:H_1+H_2:} \\
&= e^{-\frac{\Delta\sigma}{8}:H_1:}e^{-\frac{\Delta\sigma}{4}:H_2:}e^{-\frac{\Delta\sigma}{8}:H_1:}e^{-\frac{\Delta\sigma}{2}:H_3:}e^{-\frac{\Delta\sigma}{8}:H_1:}e^{-\frac{\Delta\sigma}{4}:H_2:}e^{-\frac{\Delta\sigma}{8}:H_1:} \\
&\quad e^{-\Delta\sigma:H_4:}e^{-\frac{\Delta\sigma}{8}:H_1:}e^{-\frac{\Delta\sigma}{4}:H_2:}e^{-\frac{\Delta\sigma}{8}:H_1:}e^{-\frac{\Delta\sigma}{2}:H_3:}e^{-\frac{\Delta\sigma}{8}:H_1:}e^{-\frac{\Delta\sigma}{4}:H_2:}e^{-\frac{\Delta\sigma}{8}:H_1:}. \quad (2.168)
\end{aligned}$$

This splitting is not unique and is dependent upon the choice of order $H_{1,2,3,4}$, however the result of the transfer map is the same for all cases. This splitting only describes a second order integrator; however from this splitting higher order integrators can be constructed [111]. A fourth order integrator $\mathcal{M}_4(\Delta\sigma)$ can be constructed from the second order integrator $\mathcal{M}_2(\Delta\sigma)$,

$$\mathcal{M}_4(\Delta\sigma) = \mathcal{M}_2(c_1\Delta\sigma) \circ \mathcal{M}_2(c_0\Delta\sigma) \circ \mathcal{M}_2(c_1\Delta\sigma), \quad (2.169)$$

where the constants c_1 and c_2 are defined [111],

$$c_0 = \frac{-2^{\frac{1}{3}}}{2 - 2^{\frac{1}{3}}} \qquad\qquad c_1 = \frac{1}{2 - 2^{\frac{1}{3}}}. \tag{2.170}$$

Beyond this even higher order integrators can be formulated in a similar manner with this kind of splitting.

Evaluation of the transfer map

The transformations resulting from H_1 and H_4 can be directly calculated from the Lie transformation due to the lack of any mixed terms,

$$e^{-\Delta\sigma:H_1:}\begin{pmatrix} x \\ p_x \\ y \\ p_y \\ z \\ \delta \\ s \\ p_s \end{pmatrix} \mapsto \begin{pmatrix} x \\ p_x \\ y \\ p_y \\ z + \Delta s\left(\frac{1}{\beta_0} - 1 - \frac{1}{2\beta_0^2\gamma_0^2\left(\frac{1}{\beta_0}+\delta\right)^2}\right) \\ \delta \\ s + \Delta s \\ p_s \end{pmatrix} \tag{2.171}$$

$$e^{-\Delta\sigma:H_4:}\begin{pmatrix} x \\ p_x \\ y \\ p_y \\ z \\ \delta \\ s \\ p_s \end{pmatrix} \mapsto \begin{pmatrix} x \\ p_x + \Delta s \frac{\partial a_s}{\partial x} \\ y \\ p_y + \Delta s \frac{\partial a_s}{\partial y} \\ z \\ \delta + \Delta s \frac{\partial a_s}{\partial z} \\ s \\ p_s \end{pmatrix}. \tag{2.172}$$

where $\Delta\sigma = \Delta s$ in the conveniently chosen independent variable. In order to evaluate transformations with mixed variables the equations 2.151 and 2.153 are required. Starting with H_2 as a function of a new dummy momentum $\tilde{p}_x$ and using equation 2.150,

$$\tilde{H}_2(\tilde{p}_x) = \frac{\tilde{p}_x^2}{2\left(\frac{1}{\beta_0} + \delta\right)} \tag{2.173}$$

$$\begin{aligned} e^{:I_x:}\tilde{H}_2(p_x) &= \tilde{H}_2(e^{:I_x:}p_x) \\ &= \tilde{H}_2(p_x - a_x) \equiv H_2 \end{aligned} \tag{2.174}$$

where the identity of I_x is,

$$e^{:I_x:}p_x \mapsto p_x - a_x \tag{2.175}$$

which leads to this definition for I_x,

$$\begin{aligned} p_x - a_x &= p_x - \frac{\partial I_x}{\partial x} \\ \frac{\partial I_x}{\partial x} &= a_x \\ I_x &= \int_0^x a_x(x, y, z, s)\ dx. \end{aligned} \tag{2.176}$$

Using equation 2.149 this can be extended to,

$$e^{:I_x:}e^{-\Delta\sigma:\tilde{H}_2(p_x):}e^{-:I_x} = e^{\Delta\sigma:H_2:}. \tag{2.177}$$

The transformation for H_2 is given by the following maps,

$$e^{:I_x:}\begin{pmatrix} x \\ p_x \\ y \\ p_y \\ z \\ \delta \\ s \\ p_s \end{pmatrix} \mapsto \begin{pmatrix} x \\ p_x - a_x \\ y \\ p_y - \int_0^x \frac{\partial}{\partial y} a_x(x,y,z,s)\ dx \\ z \\ \delta - \int_0^x \frac{\partial}{\partial z} a_x(x,y,z,s)\ dx \\ s \\ p_s \end{pmatrix} \tag{2.178}$$

$$e^{-\Delta\sigma:\tilde{H}_2:}\begin{pmatrix} x \\ p_x \\ y \\ p_y \\ z \\ \delta \\ s \\ p_s \end{pmatrix} \mapsto \begin{pmatrix} x + \Delta s \frac{p_x}{\left(\frac{1}{\beta_0}+\delta\right)} \\ p_x \\ y \\ p_y \\ z - \Delta s \frac{p_x^2}{2\left(\frac{1}{\beta_0}+\delta\right)^2} \\ \delta \\ s \\ p_s \end{pmatrix}. \tag{2.179}$$

The maps for H_3 are calculated in an identical manner. This gives the definition for all the operations performed by each component of the integrator described by the concatenation of operations in equation 2.168. This symplectic integrator

is the necessary tool required to completely evaluate the dynamics of an element with an s dependent field, without needing to assume the rigid bunch and axial approximations i.e. no momentum change and constant x and y through the cavity.

2.5.4 Kick codes

Kick codes were developed out of a need to track particles numerically through very large lattices, for many turns, with the need to remain symplectic. The formalism of a kick code arises from applying approximations to the accelerator Hamiltonian,

$$H(x,p_x,y,p_y,z,\delta;s)=\frac{\delta}{\beta_0}-\sqrt{\left(\frac{1}{\beta_0}+\delta-\frac{q\phi}{p_0c}\right)^2-(p_x-a_x)^2-(p_y-a_y)^2-\frac{1}{\beta_0^2\gamma_0^2}}-a_z, \tag{2.180}$$

where in this case s is an independent variable. If the thin lens approximation is applicable to all accelerator elements the Hamiltonian does not need to be extended to include s as a canonical variable, as was seen in section 2.5.3. In this approximation it is also assumed that there are only transverse magnetic fields, hence in the Hamiltonian gauge the vector potential components a_x and a_y go to zero, thereby greatly simplifying the Hamiltonian. This allows the Hamiltonian to be split into two components,

$$H_{\text{drift}}(p_x,p_y,\delta;s)=\frac{\delta}{\beta_0}-\sqrt{\left(\frac{1}{\beta_0}+\delta-\frac{q\phi}{p_0c}\right)^2-p_x^2-p_y^2-\frac{1}{\beta_0^2\gamma_0^2}}, \tag{2.181}$$

$$H_{\text{kick}}(x,y,z;s)=-a_z, \tag{2.182}$$

where the choice of $a_z(x,y,z)$ describes the integrated kicks resulting from the elements in the lattice. The choice of the order of splitting allows for better representation of stronger magnets; these higher order splittings were exploited

in the code TEAPOT [112]. SixTrack [113] is another example of a kick code and is used for much of the analysis of the HL-LHC. For all kick codes the integrator is both symplectic and fast, and therefore ideal for long term tracking studies.

2.5.5 Taylor maps

A Taylor map is a representation of a transfer map in the form of a set of Taylor series expressed as functions of the initial variables. These Taylor maps are truncated in order to allow them to be evaluated quickly. Taylor maps are constructed using a differential (or truncated power series) algebra. This type of library allows starting variables to be declared symbolically rather than numerically and for algebraic operations to be performed on them. The library can often be contained and handled within an accelerator code, e.g SixTrack [91] and MADX [114], or as standalone software e.g COSY INFINITY [115].

Taylor maps have been seen in many guises in the accelerator field, more typically for use in one turn maps describing the whole machine in the form of a set of Taylor series. Studies were carried out for the LHC in the past [116] and it was concluded that the use of a one turn map at large amplitudes presented significant errors in the calculation of the dynamic aperture for long term tracking [117]. The issue encountered was that the magnitude of the symplectic error resulting from the truncation of the maps meant that over the number of iterations required for a dynamic aperture study, the difference between tracked particles compared with a direct integration scheme was significant. To overcome the errors associated with directly calculated one turn maps, symplectification schemes were introduced which sought to factorise the Taylor map into a transformation with a corresponding generating function [118]. However, in the process of symplectifying the maps non linear terms were altered along with the detailed dynamics contained within the maps, resulting in the creation of an unrealistic symplectic

representation. Therefore in order to conserve symplecticity, the development of numerical tracking methods is still focussed on kick code development rather than more complex methods.

Taylor maps still have their uses when calculating global properties such as the tune, chromaticity, dispersion and closed orbit. From these properties the global coordinate system, relative to the closed orbit, can be found and normal form analysis performed, whereby a transformation of variables is conducted such that the Poincaré map of the new variables appears as a pure rotation. Calculations such as these are carried out by SixTrack [113].

2.6 Conclusion

In this chapter the reason for the luminosity upgrade to the LHC has been presented and it has been shown that crab cavities serve a role in delivering increased luminosity. In addition to this the need for compact crab cavities has been shown and the resulting exotic cavity designs presented. Understanding the impact of such cavity designs in the complexity of such a large machine is not trivial with non-linear components leading to chaotic motion.

Taylor maps and kick codes form the two options when performing long term tracking through large accelerator lattices. Kick codes allow for a symplectic integration through the machine, however, they prevent the inclusion of an s dependent Hamiltonian. The use of a single element Taylor maps constructed to describe the precise dynamics of a crab cavity allows some possible insight into the dynamics of a crab cavity and its impact on the dynamic aperture of the whole machine. This insight comes in the form of the separation of the various dependencies on the initial conditions of the transfer map which would not be shown with direct numerical integration.

The tools developed in this chapter are used in the rest of the thesis to develop

new models for crab cavities and fringe fields in order that they can studied in the context of the stability of the HL-LHC.

Chapter 3

Single element Taylor maps

In chapter 2 it was seen that the non-linear dynamics can lead to chaotic motion in an accelerator and possible losses of particles. It is therefore important to consider the non-linear dynamics of a new element being introduced into a machine like the LHC. In order to consider this a model of the crab cavities must be constructed. Single element Taylor maps allow the precise dynamics of a single accelerator element to be contained in a form which is both computationally fast and physically correct. They provide a benchmark from which to compare models with simplified dynamics.

A model of the crab cavity operating mode is constructed by first fitting the electric field to a solution of the Helmholtz equation. This provides an analytical field description which in combination with a truncated power series algebra library, and a symplectic integrator enables the production of a Taylor map of the cavity.

One downside of a Taylor map, as discussed in section 2.5.5, is that symplectic errors are introduced from the power series truncation. An evaluation of this error is presented from the single evaluation of a Taylor map and from the multiple evaluations used in long term tracking.

In this chapter the implementation of a field fitting method is presented which

allows an analytical vector potential to be calculated for a real cavity, with application to a real crab cavity shown for the first time. A parallelised differential algebra library is also introduced and demonstrated in the creation of extended variable Taylor maps. The first implementation of a Taylor map within a kick code is presented with studies of symplectic error made.

3.1 Field fitting of standing wave RF cavities

This section explores methods to analytically express the electric field of a standing wave RF cavity in the form of a power series in the transverse variables of x and y at positions in s. This gives a complete analytic representation of the vector potential from which a Taylor map of the dynamics can be produced. The basis of the method comes from [119, 120]. In this section three different forms of the electric field are discussed:

1. *Interpolated* field refers to the field directly interpolated from meshed field data.

2. *Fitted* field refers to an analytical description which is an exact solution to the Helmholtz equation in cylindrical coordinates.

3. *Taylor* field refers to the *fitted* field in the form of a truncated power series in cartesian coordinates.

3.1.1 Implementation of the fitting method and study of the four rod cavity

The electric field contained within the vacuum of a powered RF cavity satisfies the homogeneous wave equation,

$$\nabla^2 \vec{E} - \frac{1}{c^2}\frac{\partial^2 \vec{E}}{\partial t^2} = 0. \tag{3.1}$$

For a standing wave cavity it is assumed that the $\vec{E}$ field's time dependence is harmonic, and hence the spatial and time dependent field components are separable,

$$\vec{E}(\mathbf{r}, t) = \sum_l \vec{E}^{(l)}(\mathbf{r}) e^{-\mathrm{i}(\omega_l t + \Phi_l)}, \tag{3.2}$$

where ω_l and Φ_l are the frequency and phase of the harmonic time dependence respectively, for a given mode l. The spatial component of the field obeys the vector Helmholtz equation,

$$\nabla^2 \vec{E}^{(l)} + k_l^2 \vec{E}^{(l)} = 0, \tag{3.3}$$

where $k_l \equiv \omega_l / c$. The fields can be related to the vector potential through the expressions

$$\vec{E} = -\frac{\partial \vec{A}}{\partial t}, \tag{3.4}$$

$$\vec{B} = \nabla \times A. \tag{3.5}$$

A gauge is chosen to relate the electromagnetic field to the scalar φ and vector potential $\vec{A}$ such that $\varphi = 0$. For standing wave modes the vector potential $\vec{A}$ is

only dependent on the spatial mode of the electric field $\vec{E}^{(l)}$, such that,

$$\vec{A} = \sum_l -\frac{\mathrm{i}}{\omega_l}\vec{E}^{(l)} e^{-\mathrm{i}(\omega_l t + \Phi_l)}. \tag{3.6}$$

This removes the necessity to consider the $\vec{B}$ field to calculate the vector potential. The solutions to the Helmholtz equation in cylindrical coordinates can be written as [119] [1], where the radial electric field has the form,

$$\begin{aligned} E_r(\mathbf{r}) = \int_{-\infty}^{\infty} \frac{dk}{\sqrt{2\pi}} e^{\mathrm{i}kz} \left(\frac{-\mathrm{i}k}{\kappa_l}\right) (\tilde{e}_0 R_1(k,\rho) + \\ \sum_{n=1}^{\infty} \left[\left(\tilde{e}_n(k) R_{n+1}(k,\rho) + \tilde{\beta}_n(k) \frac{R_n(k,\rho)}{\kappa_l \rho} \right) \cos(n\phi) \right. \\ \left. + \left(\tilde{f}_n(k) R_{n+1}(k,\rho) + \tilde{\alpha}_n(k) \frac{R_n(k,\rho)}{\kappa_l \rho} \right) \sin(n\phi) \right] \Bigg), \end{aligned} \tag{3.7}$$

the azimuthal electric field takes the form,

$$\begin{aligned} E_\phi(\mathbf{r}) = \int_{-\infty}^{\infty} \frac{dk}{\sqrt{2\pi}} e^{\mathrm{i}kz} \left(\frac{\mathrm{i}k}{\kappa_l}\right) \Big(\tilde{f}_0 R_1(k,\rho) + \\ \sum_{n=1}^{\infty} \left[\left(\tilde{f}_n(k) R_{n+1}(k,\rho) + \tilde{\alpha}_n(k) \left(\frac{R_n(k,\rho)}{\kappa_l \rho} - \frac{1}{n} R_{n-1}(k,\rho) \right) \right) \cos(n\phi) \right. \\ \left. + \left(\tilde{e}_n(k) R_{n+1}(k,\rho) + \tilde{\beta}_n(k) \left(\frac{R_n(k,\rho)}{\kappa_l \rho} - \frac{1}{n} R_{n-1}(k,\rho) \right) \right) \sin(n\phi) \right] \Bigg), \end{aligned} \tag{3.8}$$

and the longitudinal electric field takes the form,

$$\begin{aligned} E_z(\mathbf{r}) = \int_{-\infty}^{\infty} \frac{dk}{\sqrt{2\pi}} e^{\mathrm{i}kz} \left(\tilde{e}_0(k) R_0(k,\rho) + \right. \\ \left. \sum_{n=1}^{\infty} \left[\tilde{e}_n(k) R_n(k,\rho) \cos(n\phi) + \tilde{f}_n(k) R_n(k,\rho) \sin(n\phi) \right] \right). \end{aligned} \tag{3.9}$$

[1] For the remainder of this section the superscript (l) is dropped, discussing only the spatial component of a given mode.

The radial function R_n consists of a regular and modified Bessel function,

$$R_n(k,\rho) = \begin{cases} J_n(\kappa_l(k)\rho) & \text{If } \mathrm{sgn}(k^2 - k_l^2) < 0, \\ I_n(\kappa_l(k)\rho) & \text{Otherwise.} \end{cases} \tag{3.10}$$

k_l is the wavenumber for the given mode in the cavity and n is the order of the Bessel function. For the prototype crab cavity designs the operating mode has a frequency of approximately $\omega \approx 2\pi \times 400$ MHz, leading to a wavenumber of approximately $k_l \approx 8.34$ m^{-1}. The function κ_l is defined,

$$\kappa_l(k)^2 = |k^2 - k_l^2|. \tag{3.11}$$

The series of functions $\tilde{e}_n$, $\tilde{f}_n$, $\tilde{\alpha}_n$ and $\tilde{\beta}_n$ are calculated from the field values on the surface of a cylinder of radius R. The resulting analytical field is valid for $\rho < R$. The field data used to populate the surface of the cylinder comes from the eigenmode solution of the cavity geometry which corresponds with the operating mode produced using the finite element solver, HFSS [121]. The field data is produced on a specially defined cylindrical mesh [122] of radius $R = 20$ mm with 16 azimuthal points and steps of 2 mm in s through the centre of the cavity, as shown in figure 3.1a. A special mesh was created such that nodes of the tetrahedra created by the finite element solver would lie on the the surface of a cyclinder. By doing this it removes the necessity to interpolate between nodes in order to populate the field values for the field fitting. From the field data Fourier transforms are performed resulting in the harmonic functions of the spatial component of the fields. The *interpolated* field is an interpolation over a 1 mm Cartesian mesh of field data produced to allow for validation of the fitting. By fitting the fields to this exact solution to the Helmholtz equation, error resulting from the finite element solver is damped. This means that while the fields from the solver may not exactly be a valid Helmholtz solution, the

analytical fields will be. However, not all errors will be removed as some will be attributed to valid components of the Helmholtz solution [119, 123].

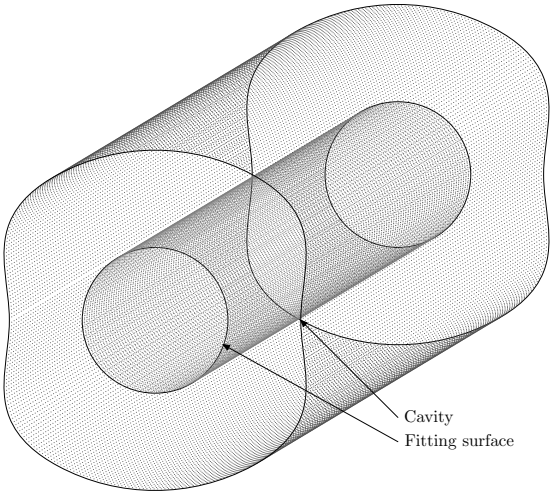

(a)

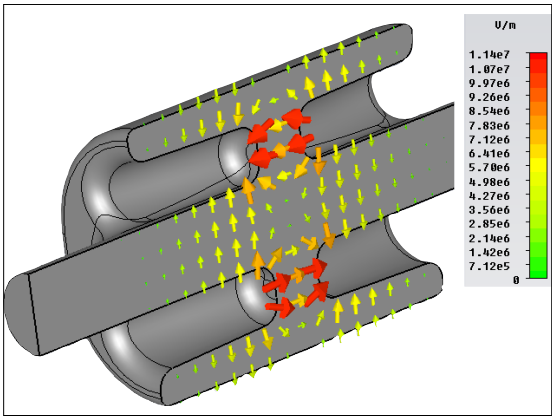

(b)

Figure 3.1: (a) Field fitting surface through cavity (b) four rod crab cavity showing peak E field of the operating mode [89].

From the field data, Fourier transforms are performed to give the harmonic modes of the fields. $\tilde{e}_n(k)$ is defined for $n \in \{0, 1, 2, ...\}$ in terms of the longitudinal electric field,

$$\tilde{e}_n(k) = \frac{1}{R_n(k,R)} \int_{-\infty}^{\infty} \frac{ds}{\sqrt{2\pi}} e^{-iks} \int_{-\infty}^{\infty} \frac{d\phi}{\pi} \cos(n\phi) E_z(R, \phi, s). \tag{3.12}$$

$\tilde{f}_n(k)$ is similarly defined for $n \in \{1, 2, ...\}$;

$$\tilde{f}_n(k) = \frac{1}{R_n(k,R)} \int_{-\infty}^{\infty} \frac{ds}{\sqrt{2\pi}} e^{-\mathrm{i}ks} \int_{-\infty}^{\infty} \frac{d\phi}{\pi} \sin(n\phi) E_z(R, \phi, s), \tag{3.13}$$

$\tilde{f}_0(k)$ requires the azimuthal component of the electric field such that

$$\tilde{f}_0(k) = \frac{\kappa_l}{\mathrm{i}k} \frac{1}{R_1(k,R)} \int_{-\infty}^{\infty} \frac{ds}{\sqrt{2\pi}} e^{-\mathrm{i}ks} \int_{-\infty}^{\infty} \frac{d\phi}{\pi} E_\phi(R, \phi, s). \tag{3.14}$$

$\tilde{\alpha}_n(k)$ is defined for $n \in \{1, 2, ...\}$

$$\tilde{\alpha}_n(k) = \frac{\kappa_l R}{R_n(k,R)} \left[\mathrm{i}\frac{\kappa_l}{k} \left(\int_{-\infty}^{\infty} \frac{d\phi}{\pi} \sin(n\phi) E_\rho(R, \phi, s) \right) - \tilde{f}_m(k) R_{n+1}(k,R) \right], \tag{3.15}$$

$\tilde{\beta}_n(k)$ is defined for $n \in \{1, 2, ...\}$;

$$\tilde{\beta}_n(k) = \frac{\kappa_l R}{R_n(k,R)} \left[\mathrm{i}\frac{\kappa_l}{k} \left(\int_{-\infty}^{\infty} \frac{d\phi}{\pi} \cos(n\phi) E_\rho(R, \phi, s) \right) - \tilde{e}_n(k) R_{n+1}(k,R) \right], \tag{3.16}$$

however $\tilde{\alpha}_0(k) = \tilde{\beta}_0(k) \equiv 0$. An example of the analysis is shown here for the 4 rod cavity design [89]. This cavity has two transverse planes of symmetry which are shown in figure 3.1b.

The harmonic functions are calculated using a parallelised `c++` code which uses bilinear interpolation of the E field data on the surface of the cylinder. The bilinear interpolation method uses the regular grid created by the field data, as shown in figure 3.2. To calculate a desired value $\vec{E}(s, \phi)$ at longitudinal position s and angle ϕ surrounded by known values $\vec{E}_A(s_1, \phi_2)$, $\vec{E}_B(s_2, \phi_2)$, $\vec{E}_C(s_1, \phi_1)$ and

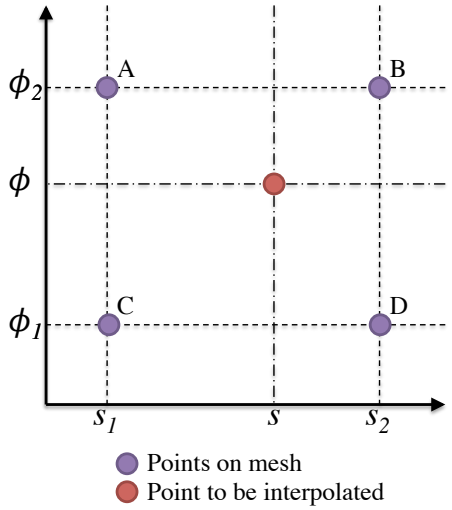

Figure 3.2: Bilinear interpolation method

$\vec{E}_D(s_2, \phi_1)$ the following relation is used,

$$\begin{aligned}\vec{E}(s,\phi) \approx & \frac{1}{(s_1 - s_2)(\phi_2 - \phi_1)} \\ & \Big(\vec{E}_A(s_2 - s)(\phi - \phi_1) + \vec{E}_B(s - s_1)(\phi - \phi_1) \\ & + \vec{E}_C(s_2 - s)(\phi_2 - \phi) + \vec{E}_D(s - s_1)(\phi_2 - \phi)\Big) . \end{aligned} \tag{3.17}$$

From this bilinear interpolation the azimuthal integration in ϕ and then the longitudinal integration in s are performed using the midpoint method. The use of bilinear interpolation does not improve the integration beyond that of the midpoint method, but it does simplify the implementation of the fitting method. In order to go beyond the midpoint method a higher order interpolation could be used, e.g. a spline interpolation. Like the bilinear interpolation, these higher order methods would not hold to Maxwell's equations for interpolated points.

The resulting harmonic functions are expressed in discrete steps of k over a range of ± 400 m^{-1} in steps of 0.2 m^{-1}, up to an order of $n = 8$. In figure 3.3, the error in fitting performed with different step sizes in k is shown. It can be

seen that the peak error reduces with step size, however, it is also shown that the sensitivity to noise where field is low increases with step size. This implies that there is no definite convergence in the analytical field for the case where the field data does not exactly correspond to a solution to the Helmholtz equation.

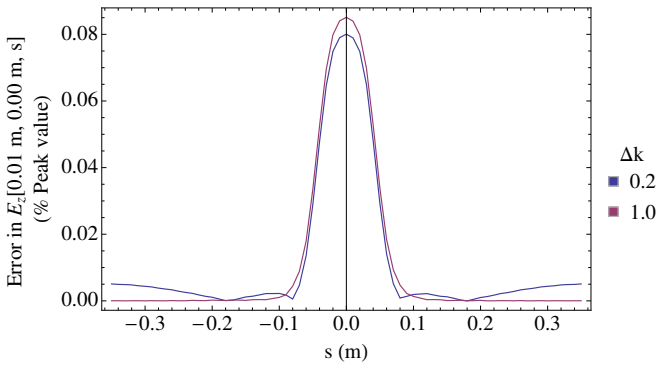

Figure 3.3: Converge of the analytical E_z field with the step size of the harmonic functions. The error is normalised to the peak field.

The planes of symmetry lead to an absence in skew longitudinal field components and only odd values for the index n. The first symmetry condition,

$$E_z(r, \phi, z) = E_z(r, -\phi, z), \tag{3.18}$$

determines that $f_n(k)$ must be equal to zero in order for E_z to be an even function. The second symmetry condition is given by,

$$E_z(r, \phi, z) = -E_z(r, \phi + \pi, z). \tag{3.19}$$

where,

$$E_z(r,\phi,z) = \int_{-\infty}^{\infty} \frac{dk}{\sqrt{2\pi}} e^{\mathrm{i}kz} \left(\tilde{e}_0(k) R_0(k,\rho) + \sum_{n=1}^{\infty} \tilde{e}_n(k) R_n(k,\rho) \cos(n\phi) \right)$$
$$E_z(r,\phi+\pi,z) = \int_{-\infty}^{\infty} \frac{dk}{\sqrt{2\pi}} e^{\mathrm{i}kz} \times \left(\tilde{e}_0(k) R_0(k,\rho) + \sum_{n=1}^{\infty} \tilde{e}_n(k) R_n(k,\rho) \cos(n\pi) \cos(n\phi) \right). \tag{3.20}$$

For this condition to be true it is required that $\cos(n\pi) = -1$ which is only true for odd values of n.

From the field fitting it was apparent that $f_n(k)$ was not equal to zero. This is a result of the Fourier decomposition method only dampening noise from the field data rather than totally removing it. This, combined with the errors from the numerical integration, generates a small additional skew component in the fitted field. Integrating the total kick applied to a particle from $\tilde{e}_1$ and $\tilde{f}_1$ allows an effective rotation of the cavity to be calculated, which equates to approximately 10 μrad.

The electric field in the cavity is dominated by the longitudinal "dipole" field component (the $n = 1$ term in equation 3.9) which is observed in the $\tilde{e}_1$ harmonic function, shown in figure 3.4a. Although $\tilde{e}_5$ is of similar magnitude to $\tilde{e}_1$, in terms of contribution to the field these are scaled by the radial function and hence $\tilde{e}_5$ is a small component of the field.

The radial dependencies corresponding to the $\tilde{e}$ functions in figure 3.4 are shown in figure 3.5. As k increases, $\tilde{e}_n(k)$ decreases at a faster rate than $R_n(k,R)$ increases. This effect leads to greater sensitivity to $\tilde{e}_n(k)$ at smaller values of k. In figure 3.6 this effect is shown for the case of $\tilde{e}_1(k) \cdot R_1(k, 0.02\ m)$ which tends to zero with increasing k.

A coordinate transformation from the fields given by the harmonic functions

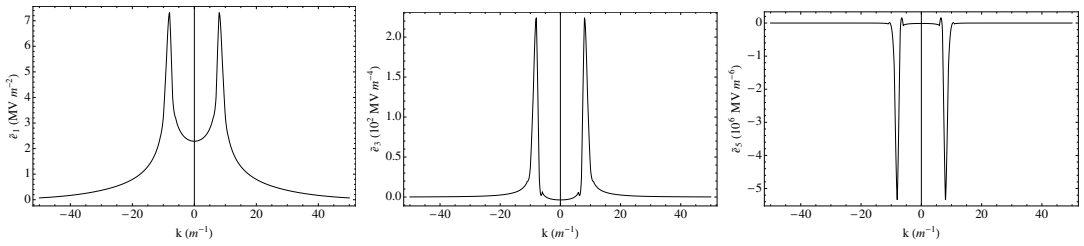

(a) (b) (c)

Figure 3.4: The $\tilde{e}$ functions, (a) $\tilde{e}_1(k)$, (b) $\tilde{e}_3(k)$, and (c) $\tilde{e}_5(k)$ for the four rod cavity which form the largest contribution to the longitudinal component of the electric field.

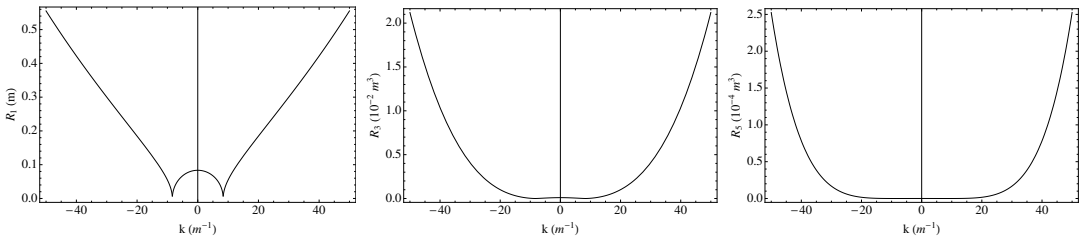

(a) (b) (c)

Figure 3.5: The radial functions (a) $R_1(k)$, (b) $R_3(k)$, and (c) $R_5(k)$ which correspond to the $\tilde{e}$ functions in figure 3.4, evaluated at $R = 20$ mm.

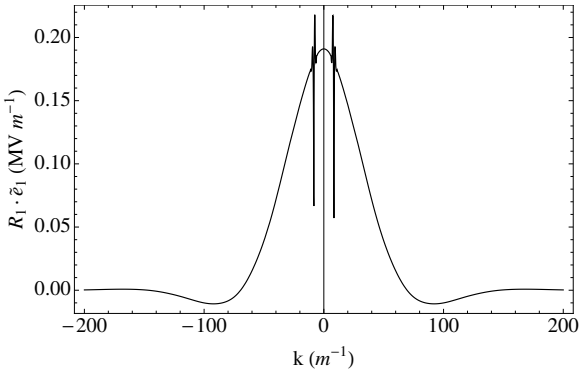

Figure 3.6: Scaling of $\tilde{e}_1$ with the radial function $R_1(k, 0.02\ m)$.

(given in equations 3.7, 3.8 and 3.9), which are dependent on ρ and ϕ (*fitted*), is required in order to produce a Taylor map. Firstly it is necessary to transform the fields to the same spatial coordinates as the accelerator Hamiltonian given in equation 2.104 i.e. Cartesian coordinates. It is then necessary to put these Cartesian fields into the form of a power series using a Taylor series expansion such that they are compatible with a truncated power series library in order to produce a Taylor map. This Taylor series expansion of the Cartesian fields is performed in Mathematica [105] and produces the *Taylor* analytic field. The Cartesian coordinate form of the field is expressed in terms of generalised gradients [124, 119], which are a set of functions dependent on longitudinal position s, azimuthal index n and radial index m. There are six sets of functions, where the longitudinal normal $C_{zc}^{(l)}$ and skew $C_{zs}^{(l)}$ functions are defined [119],

$$C_{zc}(s,n,m) = \int_{-\infty}^{\infty} \frac{\mathrm{d}k}{\sqrt{2\pi}} e^{\mathrm{i}ks} \mathrm{sgn}(k^2 - k_l^2)^m \kappa_l(k)^{n+2m} \tilde{e}_n(k) \tag{3.21}$$

$$C_{zs}(s,n,m) = \int_{-\infty}^{\infty} \frac{\mathrm{d}k}{\sqrt{2\pi}} e^{\mathrm{i}ks} \mathrm{sgn}(k^2 - k_l^2)^m \kappa_l(k)^{n+2m} \tilde{f}_n(k), \tag{3.22}$$

azimuthal normal $C_{\phi c}^{(l)}$ and skew $C_{\phi s}^{(l)}$ functions are defined,

$$\begin{aligned} C_{\phi c}(s,n,m) = \int_{-\infty}^{\infty} \frac{\mathrm{d}k}{\sqrt{2\pi}} e^{\mathrm{i}ks} \left(\frac{\mathrm{i}k}{\kappa_l}\right) \mathrm{sgn}(k^2 - k_l^2)^m \kappa_l(k)^{n-1+2m} \\ \times \left(m\ \mathrm{sgn}(k^2 - k_l^2) \tilde{f}_n(k) - \frac{n+2m}{2n} \tilde{\alpha}_n(k) \right) \end{aligned} \tag{3.23}$$

$$\begin{aligned} C_{\phi s}(s,n,m) = \int_{-\infty}^{\infty} \frac{\mathrm{d}k}{\sqrt{2\pi}} e^{\mathrm{i}ks} \left(\frac{\mathrm{i}k}{\kappa_l}\right) \mathrm{sgn}(k^2 - k_l^2)^m \kappa_l(k)^{n-1+2m} \\ \times \left(m\ \mathrm{sgn}(k^2 - k_l^2) \tilde{e}_n(k) - \frac{n+2m}{2n} \tilde{\beta}_n(k) \right), \end{aligned} \tag{3.24}$$

and radial normal $C_{\rho c}^{(l)}$ and skew $C_{\rho s}^{(l)}$ functions are defined,

$$C_{\rho c}(s,n,m) = \int_{-\infty}^{\infty} \frac{\mathrm{d}k}{\sqrt{2\pi}} e^{\mathrm{i}ks} \left(\frac{-\mathrm{i}k}{\kappa_l}\right) \mathrm{sgn}(k^2-k_l^2)^m \kappa_l(k)^{n-1+2m} \times \left(m\,\mathrm{sgn}(k^2-k_l^2)\tilde{e}_n(k) + \frac{1}{2}\tilde{\beta}_n(k)\right) \tag{3.25}$$

$$C_{\rho s}(s,n,m) = \int_{-\infty}^{\infty} \frac{\mathrm{d}k}{\sqrt{2\pi}} e^{\mathrm{i}ks} \left(\frac{-\mathrm{i}k}{\kappa_l}\right) \mathrm{sgn}(k^2-k_l^2)^m \kappa_l(k)^{n-1+2m} \times \left(m\,\mathrm{sgn}(k^2-k_l^2)\tilde{f}_n(k) + \frac{1}{2}\tilde{\alpha}_n(k)\right). \tag{3.26}$$

The cylindrical fields in terms of the generalised gradients are given by [119],

$$E_\rho(\rho,\phi,s) = \sum_{m=0}^{\infty}\sum_{n=1}^{\infty} \frac{(\rho/2)^{n-1+2m}}{m!(n+m)!} \left[C_{\rho c}(s,n,m)\cos(n\phi) + C_{\rho s}(s,n,m)\sin(n\phi)\right] \tag{3.27}$$

$$E_\phi(\rho,\phi,s) = \sum_{m=0}^{\infty}\sum_{n=1}^{\infty} \frac{(\rho/2)^{n-1+2m}}{m!(n+m)!} \left[C_{\phi c}(s,n,m)\cos(n\phi) - C_{\phi s}(s,n,m)\sin(n\phi)\right] \tag{3.28}$$

$$E_\phi(\rho,\phi,s) = \sum_{m=0}^{\infty}\sum_{n=1}^{\infty} \frac{(\rho/2)^{n+2m}}{m!(n+m)!} \left[C_{zc}(s,n,m)\cos(n\phi) + C_{zs}(s,n,m)\sin(n\phi)\right]. \tag{3.29}$$

The E_ϕ and E_ρ are related to E_x and E_y by the following relations,

$$E_x = E_\rho\cos(\phi) - E_\phi\sin(\phi) \tag{3.30}$$

$$E_y = E_\rho\sin(\phi) + E_\phi\cos(\phi). \tag{3.31}$$

To obtain the $\vec{E}$ fields in Cartesian coordinates the following transformations are also required,

$$\rho^2 \to x^2+y^2, \quad \rho^n\cos(n\phi) \to \Re[(x+\mathrm{i}y)^n], \quad \rho^n\sin(n\phi) \to \Im[(x+\mathrm{i}y)^n]. \tag{3.32}$$

The Cartesian E fields in terms of these generalised gradients are given by,

$$E_x(x,y,s) = \sum_{m=0}^{M}\sum_{n=1}^{N} \frac{(x^2+y^2)^{m-1}}{2^{n+2m-1}m!(n+m)!} \left[\left(\Re[(x+\mathrm{i}y)^n C_{\rho c}^{(l)}(s,n,m)] + \Im[(x+\mathrm{i}y)^n C_{\rho s}^{(l)}(s,n,m)]\right) x - \left(\Re[(x+\mathrm{i}y)^n C_{\phi c}^{(l)}(s,n,m)] - \Im[(x+\mathrm{i}y)^n C_{\phi s}^{(l)}(s,n,m)]\right) y\right], \quad (3.33)$$

$$E_y(x,y,s) = \sum_{m=0}^{M}\sum_{n=1}^{N} \frac{(x^2+y^2)^{m-1}}{2^{n+2m-1}m!(n+m)!} \left[\left(\Re[(x+\mathrm{i}y)^n C_{\rho c}^{(l)}(s,n,m)] + \Im[(x+\mathrm{i}y)^n C_{\rho s}^{(l)}(s,n,m)]\right) y + \left(\Re[(x+\mathrm{i}y)^n C_{\phi c}^{(l)}(s,n,m)] - \Im[(x+\mathrm{i}y)^n C_{\phi s}^{(l)}(s,n,m)]\right) x\right], \quad (3.34)$$

$$E_z(x,y,s) = \sum_{m=0}^{M}\sum_{n=1}^{N} \frac{(x^2+y^2)^{m}}{2^{n+2m}m!(n+m)!} \left(\Re[(x+\mathrm{i}y)^n C_{zc}^{(l)}(s,n,m)] + \Im[(x+\mathrm{i}y)^n C_{zs}^{(l)}(s,n,m)]\right). \quad (3.35)$$

The methods used to construct these analytical fields are summarised in figure 3.7, with the intermediate transformations and functions to describe the fields.

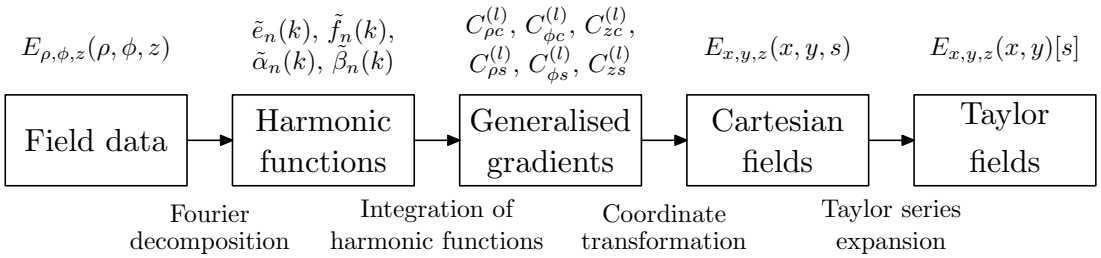

Figure 3.7: Summary of the method used to construct the analytical fields for Taylor map production from the field data.

The *Taylor* analytical field was truncated to include all the terms up to and including fifth order for each position in s. This order was chosen due to the uncertainty in the $n = 7$ component observed in another study [125]. The uncertainty of $n = 7$ arises from the choice to fit over 16 angles azimuthally. From this

choice the Nyquist critical frequency [126] is reached at $n = 8$ at which higher order n terms greater than eight fold back on lower terms to contribute to their values. The results from this final step are shown in figure 3.8 compared with *interpolated* field data directly from the eigenmode solver.

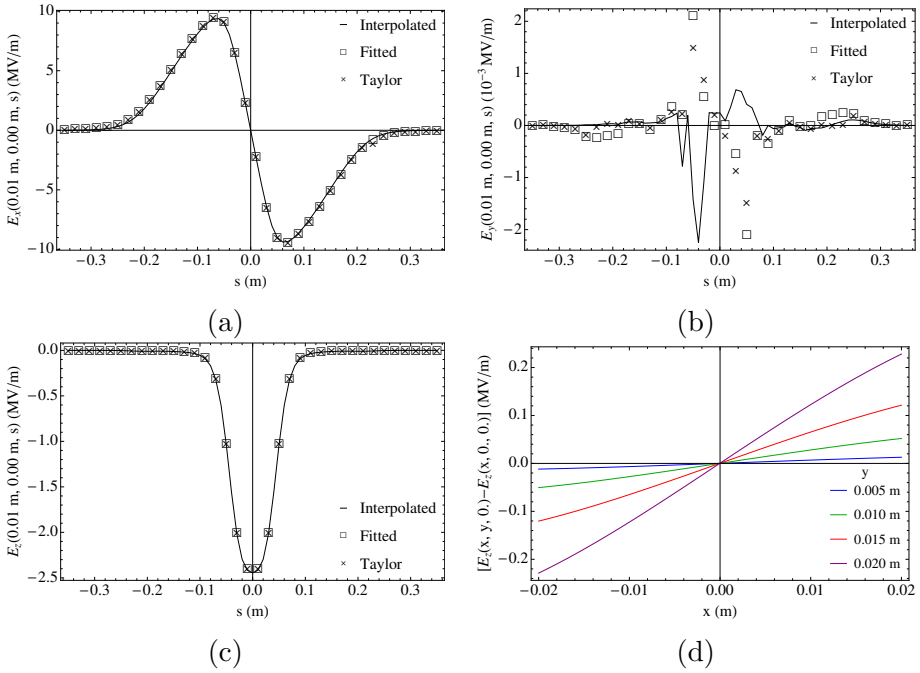

Figure 3.8: E fields with varying s at $x = 0.01$ m and $y = 0.$ m. (a) E_x, (b) E_y and (c) E_z. The *interpolated* mesh fields and *fitted* and *Taylor* analytical representations are shown. (d) E_z transverse variation in x and y away from from variation at $y = 0$ m from *Taylor* field.

E_x and E_z are the largest components of the $\vec{E}$ field in the operating mode of the crab cavity; in the horizontal crab cavity orientation. The distribution of the fields arises from the position of the tips of the rods, as discussed in section 2.4.3. The E_z field is shown to peak between the rods, longitudinally, while the E_x field peaks at the tips of the rods. The E_y component is a consequence of mesh noise, the result of which can be seen in figure 3.8a. The apparent smoothness of the *fitted* and *Taylor* E_y field arises from the fitting method damping non-Maxwellian components of the fields on to the general solution of the Helmholtz equation. The transverse variation in the E_z field beyond the dipole distribution at the centre

of the cavity is shown in figure 3.8d. This shows that there are components of the E_z field with radial dependencies beyond a linear ρ dependence.

To study the variation in the field with radius requires the use of the generalised gradients. In figure 3.9 the field components are plotted in terms of their radial dependencies with constant x and y. It can be seen that for a field component, with a radial power given by $n+2m$, it is made up of an increasing number of terms, with differing azimuthal dependencies, n. This effect can be clearly seen for the ρ^3 dependent component of the field, which for $x = 10$ mm is dominated by the $n = 1$ term, while for $y = 10$ mm the $n = 3$ is most significant.

The errors introduced at the two stages in the fitting process are shown in Fig. 3.10 and 3.11, in comparison to the meshed field data. The difference in the E_z field between the *fitted* and *interpolated* fields is of order 0.3% of the peak E_z field. The step expressing the field in the *Taylor* analytical form from the *fitted* increases the fitting error by 0.01%.

The $\vec{E}$ field error between the *Taylor* and *interpolated* field, with radial position in x, is shown in figure 3.11. The error is normalised, to the peak field value, at the given x value along the whole length of the cavity. The error in E_x and E_z is relatively stable at $\approx 2\%$ and $\approx 0.3\%$ respectively. The E_y field has significant errors due to the peak field values being close to zero.

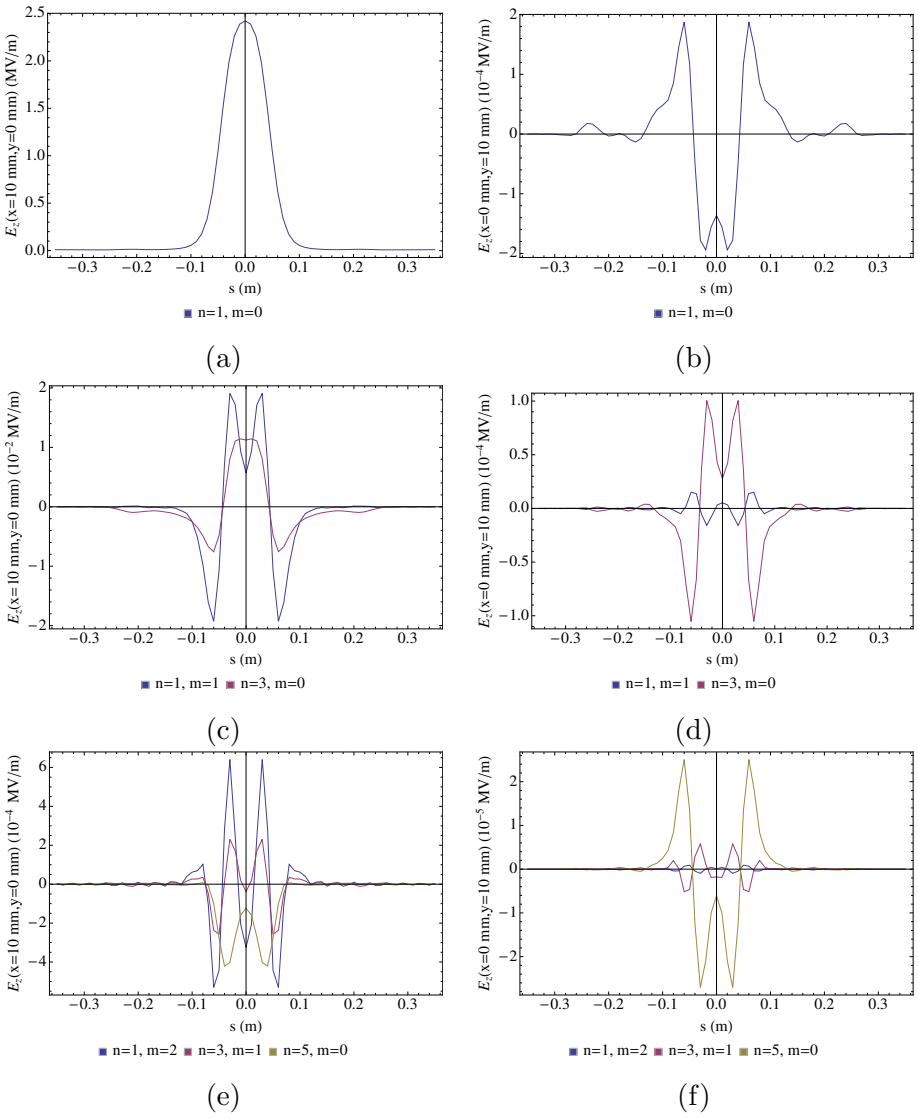

Figure 3.9: Contributions from various generalised gradients to E_z with radial dependencies (a,b) ρ, (c,d) ρ^3 and (e,f) ρ^5. Evaluated at (a,c,e) $(x, y) = (10, 0)$ mm, (b,d,f) $(x, y) = (0, 10)$ mm.

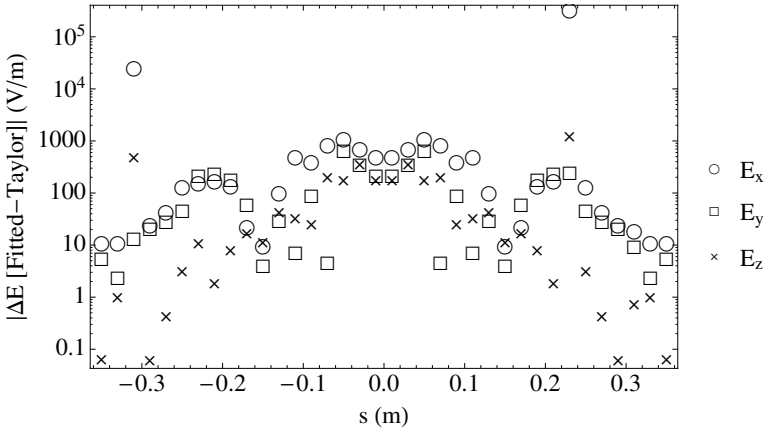

Figure 3.10: Difference between *Taylor* analytical and *fitted* analytical fields with varying s at $x = 0.01$ m and $y = 0.$ m.

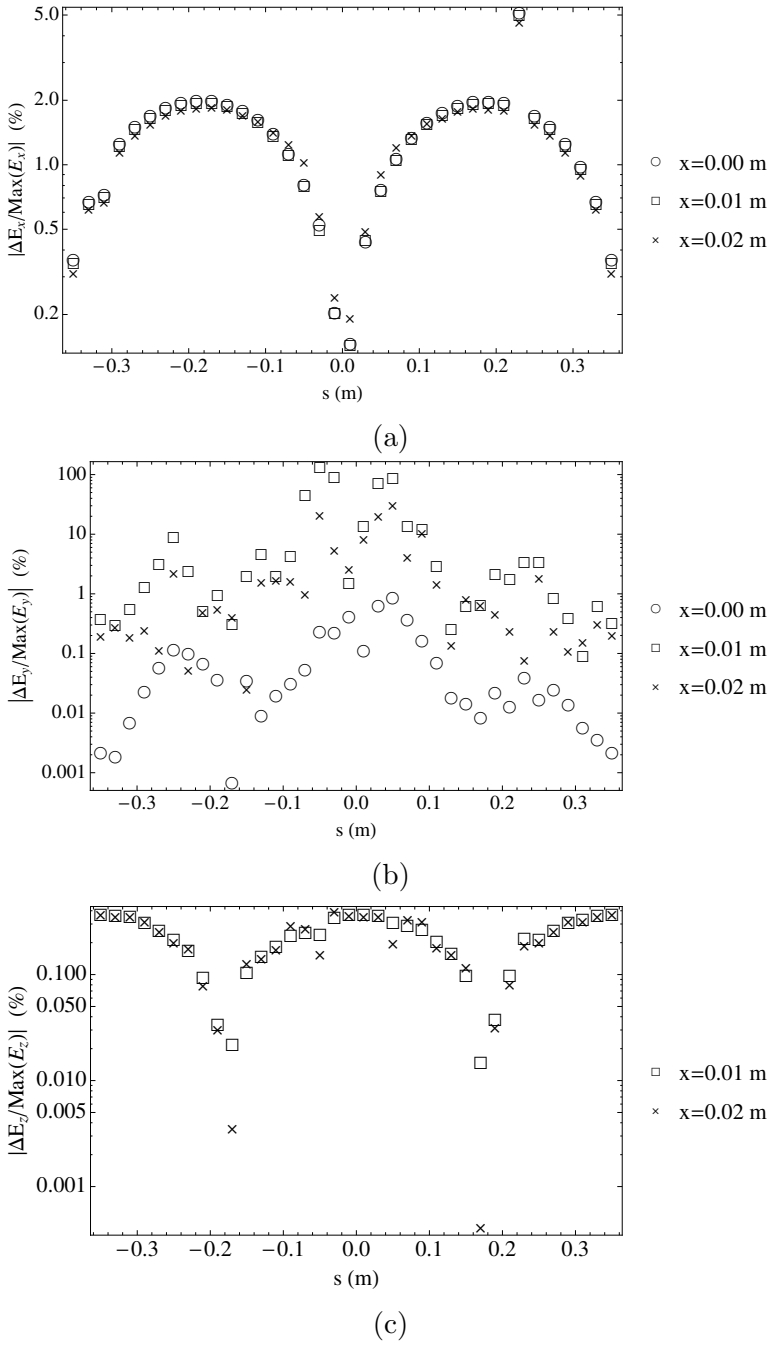

Figure 3.11: E fitting error with varying x for the (a) E_x, (b) E_y, and (c) E_z components of the field. Absolute difference between *interpolated* and *Taylor* fitted fields as function of s normalised to the maximum field value.

3.1.2 Quarter wave cavity and ridge wave cavity analyses

This field fitting was applied to two additional cavity designs proposed for the HL-LHC. These are the quarter wave cavity designed by Brookhaven (QWCAV) [127] and the ridge wave cavity designed by Old Dominium University and Stanford (ODUCAV) [87]. Figure 3.12 shows the central plane for both cavities. They exhibit similar symmetries to the 4RCAV, removing skew components from the field variation. The field fitting for these cavities was carried out with the cavities orientated with a horizontal kick. Therefore E_y should be expected to be small.

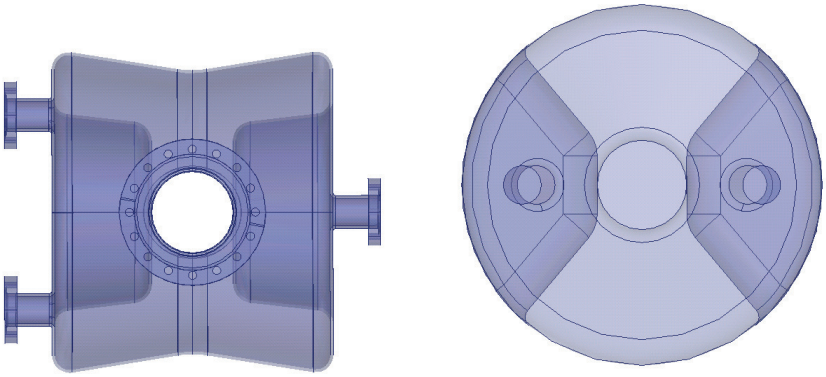

(a) (b)

Figure 3.12: x-y plane for (a) QWCAV and (b) ODUCAV transparent from end of cavity [127, 87].

Rather than the double peak transverse field seen in the 4RCAV the QWCAV exhibits a singular broad peak. In a similar manner to the 4RCAV there exists a small skew component for the QWCAV which is a result of the meshing noise and numerical integration. This is particularly evident in figure 3.13e where a significant E_y component error is shown to increase with radius.

There are many similarities in the geometry of the ODUCAV and QWCAV, with the resulting E_x field component almost identical in longitudinal variation, as shown in figure 3.14a. This is similar for E_z, however, the magnitude of the peak for the ODUCAV is lower than that seen in the QWCAV. The field fitting

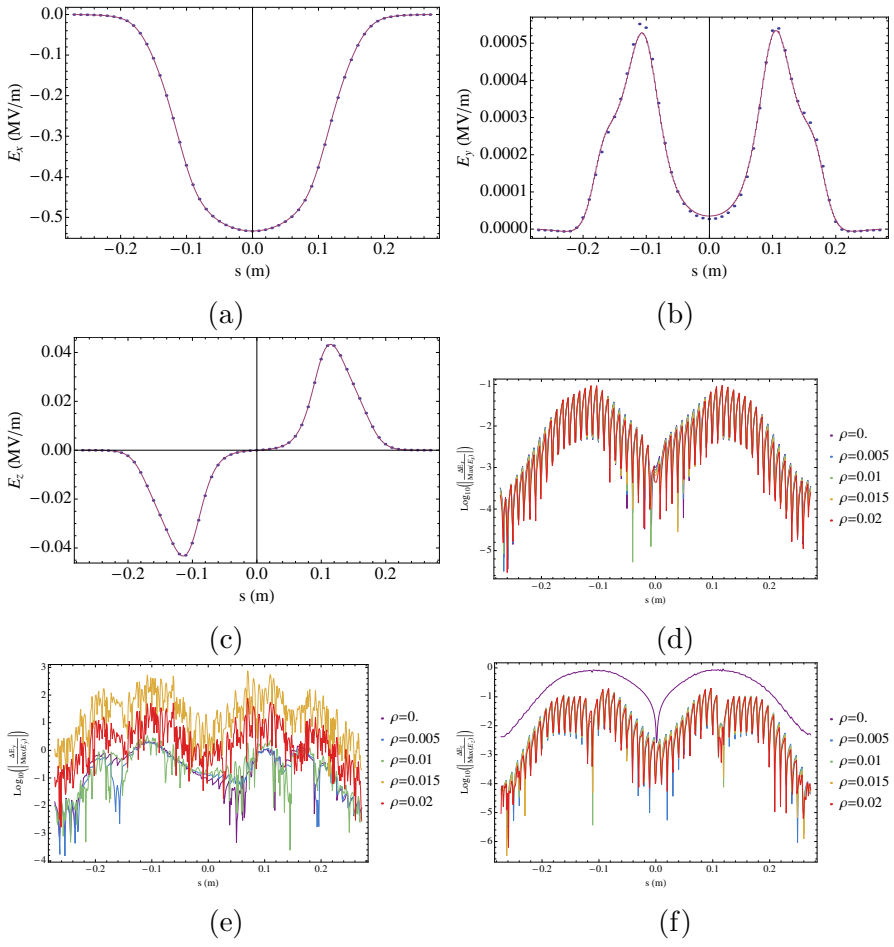

Figure 3.13: Fitted fields for the QWCAV comparing the *interpolated* and *fitted* (a,d) E_x, (b,e) E_y, and (c,f) E_z components of the field. (a,b,c) Comparison of the *interpolated* (line) and *fitted* (dotted) fields. (d,e,f) Residual of the *fitted* fields evaluated at $y = 0$.

for the ODUCAV and QWCAV were carried out using the same code with the same numerical integration settings for the Fourier analysis, which means that the errors for both are of similar order.

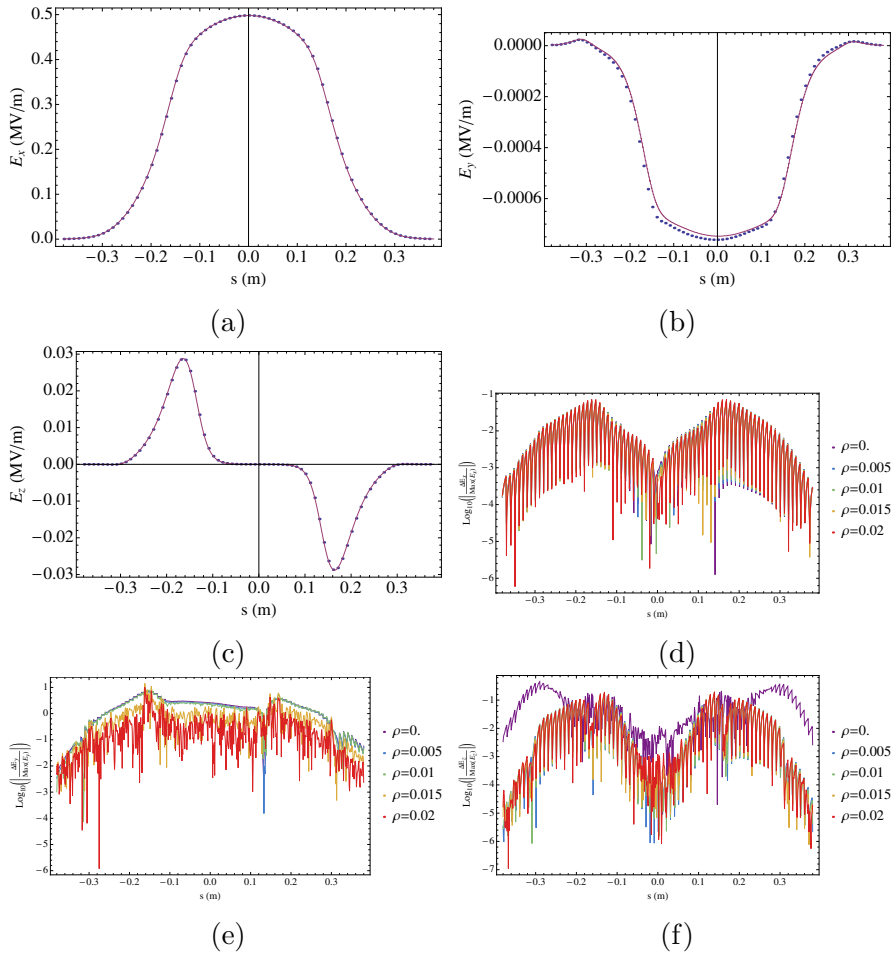

Figure 3.14: Fitted fields for the ODUCAV comparing the *interpolated* and *fitted* (a,d) E_x, (b,e) E_y, and (c,f) E_z components of the field. (a,b,c) Comparison of the *interpolated* (line) and *fitted* (dotted) fields. (d,e,f) Residual of the *fitted* fields evaluated at $y = 0$.

3.1.3 Conclusion

The fitting method has been presented and applied to all three cavity prototype designs. This is the first time that such an analysis was performed on TEM type cavities with previous studies only considering simple pillbox like geometries [120, 119]. The field data has been used to provide a continuous description of the fields expressed as a power series in x and y. It has been shown that the fitted field, for the 4RCAV 2011 design, exhibits a maximum error of 0.3% at $x = 0.02$ m in the E_z component. It has also been shown that there are visible harmonic field components in the 4RCAV cavity beyond those of the dipole component. This would suggest that whatever model is used it would need to go beyond that of a simple kick model [128, 129, 74].

3.2 Differential algebra

Differential algebra, also known as truncated power series algebra (TPSA), has a large variety of applications with many different available codes. In accelerator physics COSY INFINITY [115] is a popular choice of TPSA code, though there are many other alternatives e.g. PTC [130]. The purpose of a TPSA code is to apply multiple operations on an initial set of variables and express the result without assigning the initial variables. Many of the codes originate from the development of the Superconducting Super Collider [131], with the desire to simulate the whole ring as a one turn map using differential algebra. The programming language of choice was `F77` which lacks the modern memory management features, object-orientation and parallelisation capabilities open to newer languages such as `c++`. A truncated power series lends itself to a very object orientated style of programming.

One of the most powerful components of the `c++` programming language is the

standard template library (STL) [132]. This is a highly optimised library based around class templates that allow you to have dynamically controllable arrays of any desired class type, including user defined classes. In the traditional memory model of a code such as COSY, a series S is defined in size by its order n_o and the number of variables n_v such that,

$$S(x_j) = \sum_{i}^{\frac{(n_v+n_o)!}{n_v!n_o!}} c_i \prod_{j}^{n_v} x_j^{\epsilon_{ij}}, \tag{3.36}$$

where x_j is a vector of size n_v of the unassigned initial variables, c_i is the coefficient of a term in the series with the n_v exponents ϵ_{ij}. The number of terms in the series increases quickly with order, for example for a series with six variables of up to tenth order there are,

$$\frac{(n_v + n_o)!}{n_v!n_o!} = 8008 \,\text{coefficients}. \tag{3.37}$$

To efficiently store these large arrays of coefficients the most common method used is to put the coefficients c_i in a large array of double precision numbers. For precompiled software such as COSY, where only static memory allocation is allowed, this has to be performed by setting the array to a very large size and only partially using this allocated memory; in terms of memory usage this is rather inefficient. The STL allows for dynamic and static memory allocation of arrays. Static array sizing is computationally more efficient when copying TPSA; copying a succinct array is obviously more time efficient than copying an array which is unnecessarily large. The other major component of memory management is the system to access coefficients in the array corresponding to a specific array of exponents. The STL has a template type called map, which creates an elegant solution to this access problem. A map element is made up of a key, which is a unique identifier, which in this case is the vector of integers

holding the exponents, and a corresponding mapped value which in this case is the array address where the coefficient is held. It might appear more logical for this map to hold the corresponding coefficient, however, using the array address has the benefit of allowing sparse array techniques, in which only filled values are considered, to be applied. The use of the maps is shown in figure 3.15. In the code there exists one master map of addresses, which is static and is from where the addresses are copied. For each TPSA object there is a dynamic map containing the filled addresses of the coefficients in the static vector array. This removes the necessity of iterating over the whole static array of coefficients when performing operations.

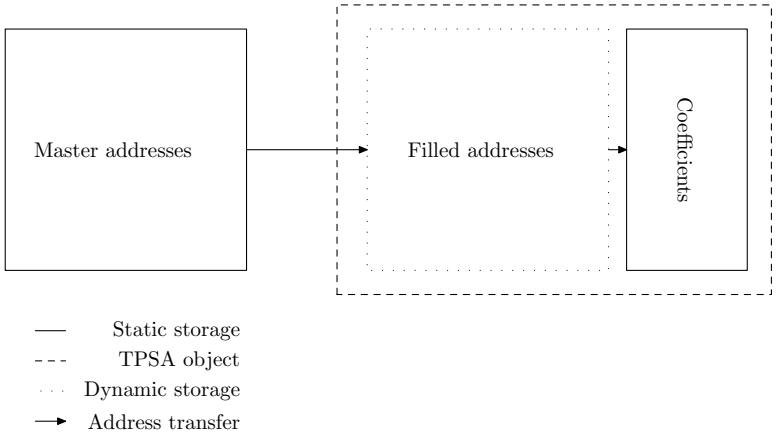

Figure 3.15: The memory address management for new TPSA code.

One advantage of using a truncated power series (TPS) representation is that many algebraic operations can be applied. The use of the memory management method discussed prior is to allow a highly optimised set of operations, thereby removing unnecessary computations. An STL template object can be iterated over which means that only the filled array is read instead of all the possible series elements. Addition and subtraction are the computationally simplest operations with the number of computations performed scaling linearly with the number of power series variables. The addition operation is shown in algorithm 1, with the

subtraction operation defined in a similar manner.

```
input  : TPS object A, TPS object B
output: TPS object C
C:=A for Filled elements in B ,i do
|  C[i]=C[i]+B[i]
end
```

Algorithm 1: Addition

The addition and subtraction operations do not create additional terms in the power series from those present in the initial two series. In contrast, multiplication can create additional terms in the series and hence the operation is required to remove higher order terms and take into account that multiple computations can lead to results with the same exponents. The multiplication algorithm, shown in algorithm 2, requires access to the master addresses to find the address of the coefficient of new terms formed in the multiplication. The multiplication operation removes information contained in the two original series through the truncation formed by the "if" statement. If this truncation did not exist then the number of terms would increase upon each operation, increasing the computation time and memory usage.

```
input  : TPS object A, TPS object B
output: TPS object C
for Filled elements in B ,i do
|  for Filled elements in A ,j do
|  |  if Sum(A[j].Exponents+B[i].Exponents)⩽ n_o then
|  |  |  k:=GetAddress[A[j].Exponents+B[i].Exponents)]
|  |  |  C[k]:=C[k]+A[j]×B[i]
|  |  end
|  end
end
```

Algorithm 2: Multiplication

Many mathematical operations can be reduced to a Taylor series allowing

them to be expressed in terms of multiplication, addition and subtraction operations. These operations all have limitations requiring a significant constant component to the truncated power series. The sine and cosine functions applied to a truncated power series C are given by,

$$\cos(C) = \sum_{k=0}^{n_o/2} \frac{(-1)^k C^{2k}}{(2k)!} \tag{3.38}$$

$$\sin(C) = \sum_{k=0}^{(n_o-1)/2} \frac{(-1)^k C^{2k+1}}{(1+2k)!}. \tag{3.39}$$

In the event that C has a constant term a,

$$C(x_i) = B(x_i) + a, \tag{3.40}$$

it is necessary to extend the cosine and sine function definitions in order to avoid unnecessary rounding errors caused by large constant terms. This is performed using the following,

$$\cos(C) = \cos(B)\cos(a) - \sin(B)\sin(a) \tag{3.41}$$

$$\sin(C) = \cos(B)\sin(a) + \cos(a)\sin(B) \tag{3.42}$$

where the $\cos(B)$ and $\sin(B)$ functions are as described in equation 3.38 and 3.39. The following operations are also included in the code for truncated power series with constant terms only,

$$\frac{1}{C} = \sum_{k=0}^{n_0} \frac{B^k}{(-a)^k a} \tag{3.43}$$

$$\sqrt{C} = \sum_{k=0}^{n_0} a^k B^{\frac{1}{2}-k} \binom{\frac{1}{2}}{k}. \tag{3.44}$$

One advantage of a truncated power series over a numerical value are the

possibilities to perform algebraic differentiation and integration. The algorithms 3 and 4 show the methods used to implement these operations. They use very similar methods to that of addition in that they iterate over one loop, however they lose terms due to truncation.

input : TPS object **A**, Exponent index **D**
output: TPS object **C**

for Filled elements in **A** , i **do**
  if Sum(**A**[i].Exponent+(**A**[i].Exponent[**D**]+=1))$\leqslant n_o$ **then**
    j:=GetAddress(**A**[i].Exponent+(**A**[i].Exponent[**D**]+=1))
    C[j]:=**A**[i].Exponent[**D**]$\times$**A**[i]
  end
end

Algorithm 3: Differentiation

input : TPS object **A**, Exponent index **D**
output: TPS object **C**

for Filled elements in **A** , i **do**
  if Sum(**A**[i].Exponent+(**A**[i].Exponent[**D**]-=1))$\geqslant 0$ **then**
    j:=GetAddress(**A**[i].Exponent+(**A**[i].Exponent[**D**]-=1))
    C[j]:=$\frac{1}{\mathbf{A}[\mathrm{i}].\mathrm{Exponent}[\mathbf{D}]+1}\times$**A**[i]
  end
end

Algorithm 4: Integration

The presented methods were implemented and a benchmark performed with COSY. The benchmarks comparing all the TPSA operations of both codes resulted in exact agreement. In figure 3.16 one such test is shown for the result of $\cos(2x+1)$.

A further test was performed with a 2D Gaussian defined,

$$f(x,y) = \frac{1}{2\pi\sigma_x\sigma_y} e^{-\frac{1}{2}\left(\frac{x^2}{\sigma_x^2}+\frac{y^2}{\sigma_y^2}\right)}, \tag{3.45}$$

which was evaluated both numerically and with a power series computed to 20^{th} order. This order limit is defined by the size of the integer which is formed during

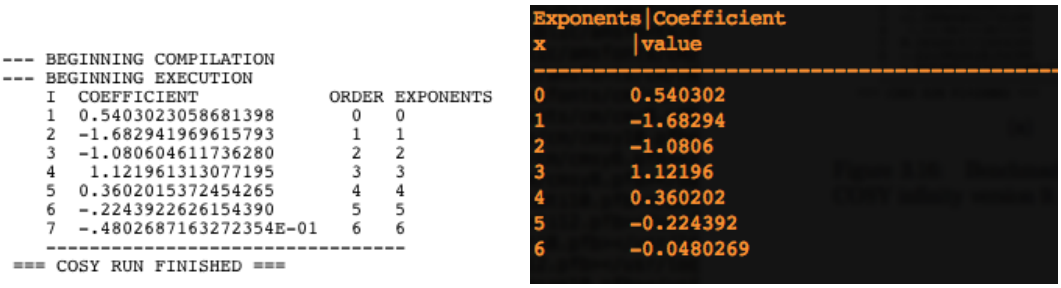

(a) (b)

Figure 3.16: Benchmark of truncated power series codes for $\cos(2x+1)$. (a) COSY infinity version 9 [133]. (b) New code.

the factorial operation used to compute the exponential. Over the range depicted in figure 3.17 there is agreement ranging from double precision to 10^{-6} % at the extremities of the range. This ability to compute power series to higher orders

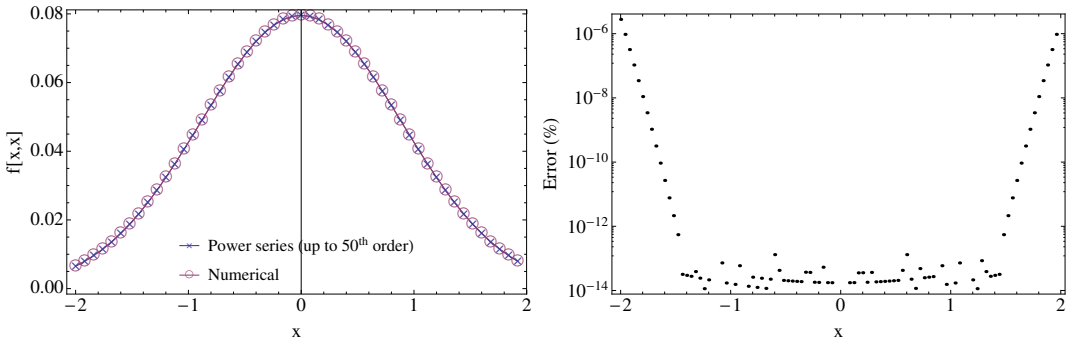

(a) (b)

Figure 3.17: Test of truncated power series code using a double Gaussian function, where $\sigma_x = 1$ and $\sigma_y = 2$, using power series and numerical evaluation. (a) Comparison of evaluation. (b) Error in power series calculation.

beyond the limitation of COSY INFINITY allowed the computation of Taylor maps with the number of variables extended beyond the six canonical variables.

3.3 Taylor map

A Taylor map expresses the relationship between the initial and final state variables in the form of a set of truncated power series, in this case for six variables,

$$\begin{pmatrix} x_1^f \\ x_2^f \\ x_3^f \\ x_4^f \\ x_5^f \\ x_6^f \end{pmatrix} = \begin{pmatrix} f_1(x_1^i,\ldots,x_6^i) \\ f_2(x_1^i,\ldots,x_6^i) \\ f_3(x_1^i,\ldots,x_6^i) \\ f_4(x_1^i,\ldots,x_6^i) \\ f_5(x_1^i,\ldots,x_6^i) \\ f_6(x_1^i,\ldots,x_6^i) \end{pmatrix}, \tag{3.46}$$

where $f_k(x_1^i,\ldots,x_6^i)$ is a truncated power series. For a six variable Taylor map in which $\vec{i}$ are the exponents and A is the coefficient of a given term in the series,

$$f_k(x_1^i,\ldots,x_6^i) = \sum_{i_1,\ldots,i_6=0}^{\sum_j^6 i_j=\text{Order}} A_{k,i_1,\ldots,i_6} \prod_{j=1}^{6} (x_j^i)^{i_j}. \tag{3.47}$$

The order of a Taylor map is determined by the largest total power of any term in the series. To calculate a Taylor map the numerical integration must be carried out using a differential algebra library. The second order explicit integrator, described in section 2.5, is then used to integrate through the Taylor series vector potential with calculus operations performed directly upon the individual terms of the vector potential series. This means that the integration is carried out with unassigned initial variables. For this study COSY infinity [133] was used up to and including eighth order. This order is chosen such that the five orders from the spatial component of the field and an additional three for the time component can be included. The Taylor maps must be normalised and phase corrected to set the correct voltage kick and desired phase required to rotate the bunch about its centre (crabbing phase). In order to determine the correct phase a second order

map was calculated and the zero order momentum kick term then extracted; from this a binary search was used to minimise the momentum kick at $z = 0$ to 10^{-20} rad. The second order map is computed because a minimum order of two is required in order to represent the first term of the vector potential representing the dipole field, axz, where a is a constant. The correct voltage normalisation is then calculated by a similar binary search to match the linear z dependence of p_x, $p_x(z)$, with the corresponding analytical map term,

$$p_x(z) = \frac{e_0 V}{c p_0} \frac{\omega}{c}, \tag{3.48}$$

where e_0 is the charge on a electron, V is the voltage, ω is the frequency, p_0 is the reference momentum, minimising the error to 14 significant figures. This normalisation is necessary due to the longitudinal variation in the kicks. Otherwise it is impossible to analytically calculate the required phase and corresponding voltage to correctly match the desired dynamics of the cavity.

The chosen step size used for the integration was 0.01 m, giving 70 steps through the cavity. This choice gives an error at the level of $10^{-7}\%$ of the peak p_x kick. The choice of step size was determined from exploratory studies looking to balance the computing time and precision of the Taylor maps. The step size also coincides with the step size of the mesh from which the field data was produced. The variation of momentum kick as a function of step size is shown in figure 3.18, indicating that the variation rapidly decreases with step size. A further reduction by a factor of two in step size does not equate to any further gain in the error reduction. Beyond 0.01 m the momentum error is no longer asymptotic but instead sensitive to the limits of the original mesh.

The Taylor map contains non-linear terms which are beyond the simple map

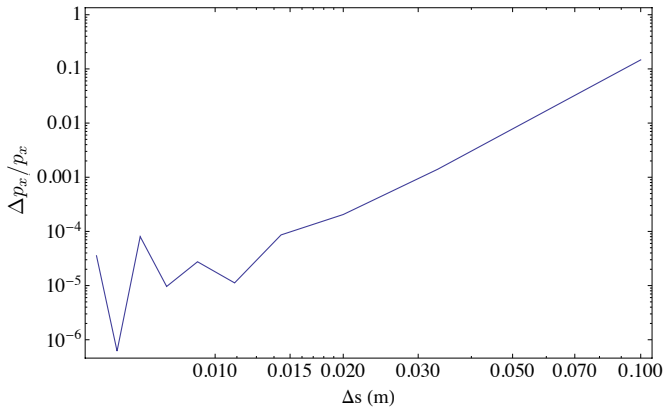

Figure 3.18: Convergence of integration. Final p_x error produced with WFR integration with varying step size compared with integration with step size 0.5 mm. Initial conditions $(x, p_x, y, p_y, \delta) = 0.$, $z = 0.01$

shown in equation 3.49. These non-linearities arise from two sources: the transverse field dependency and the longitudinal field dependency. The longitudinal field dependency leads to a particle experiencing multiple kicks as it passes through the cavity. In order to understand the properties contained within a Taylor map it is important to consider the trajectories of individual particles through the element.

Considering the 4RCAV, figures 3.19a and 3.19b show that longitudinal variation in the kick results in a net offset in x for the $z = 0$ case. Figure 3.19d shows that the p_y kick is approximately 10^5 times smaller than that of the p_x kick. Figure 3.19f shows that for a particle at $z = 0.01$ m, the net transverse momentum kick varies both radially and azimuthally. The plot shows a maximum variation of 2% at 20 mm radius. The magnitude of this variation is a result of the compact geometry of the cavity close to the beam axis. This transverse variation has already been seen in the higher order field components in figure 3.9.

Figure 3.20 shows trajectories through the fields using a numerical integration and TPSA integration truncated to eighth order. There is a difference of $5 \times 10^{-4}\%$ in the total integrated p_x kick resulting from the truncation in the TPSA integration. The trajectories in x and y appear to be more affected by the truncation than the transverse momenta, with x experiencing a final difference of 2%. The energy variation δ results in a final difference of 0.3%.

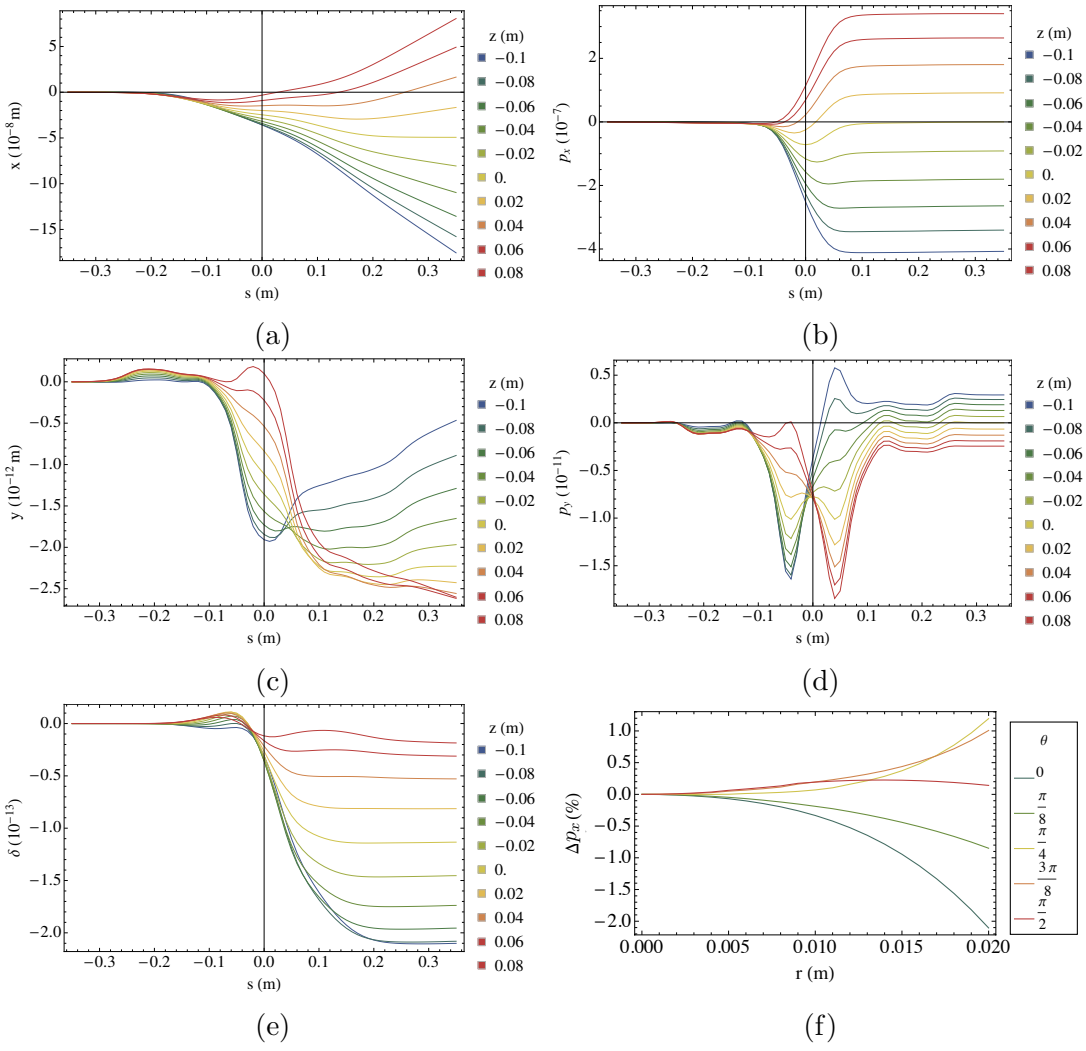

Figure 3.19: Trajectories and transverse non-linearities for the horizontally orientated 4RCAV at the crabbing phase, normalised to 3.83833 MV [134]. Trajectory in (a) x, (b) p_x, (c) y, (d) p_y, and (e) δ for various z values. (f) The variation in p_x as a percentage of the on axis value with respect to the initial radial r and azimuthal θ position. Initially $z = 0.01$ m.

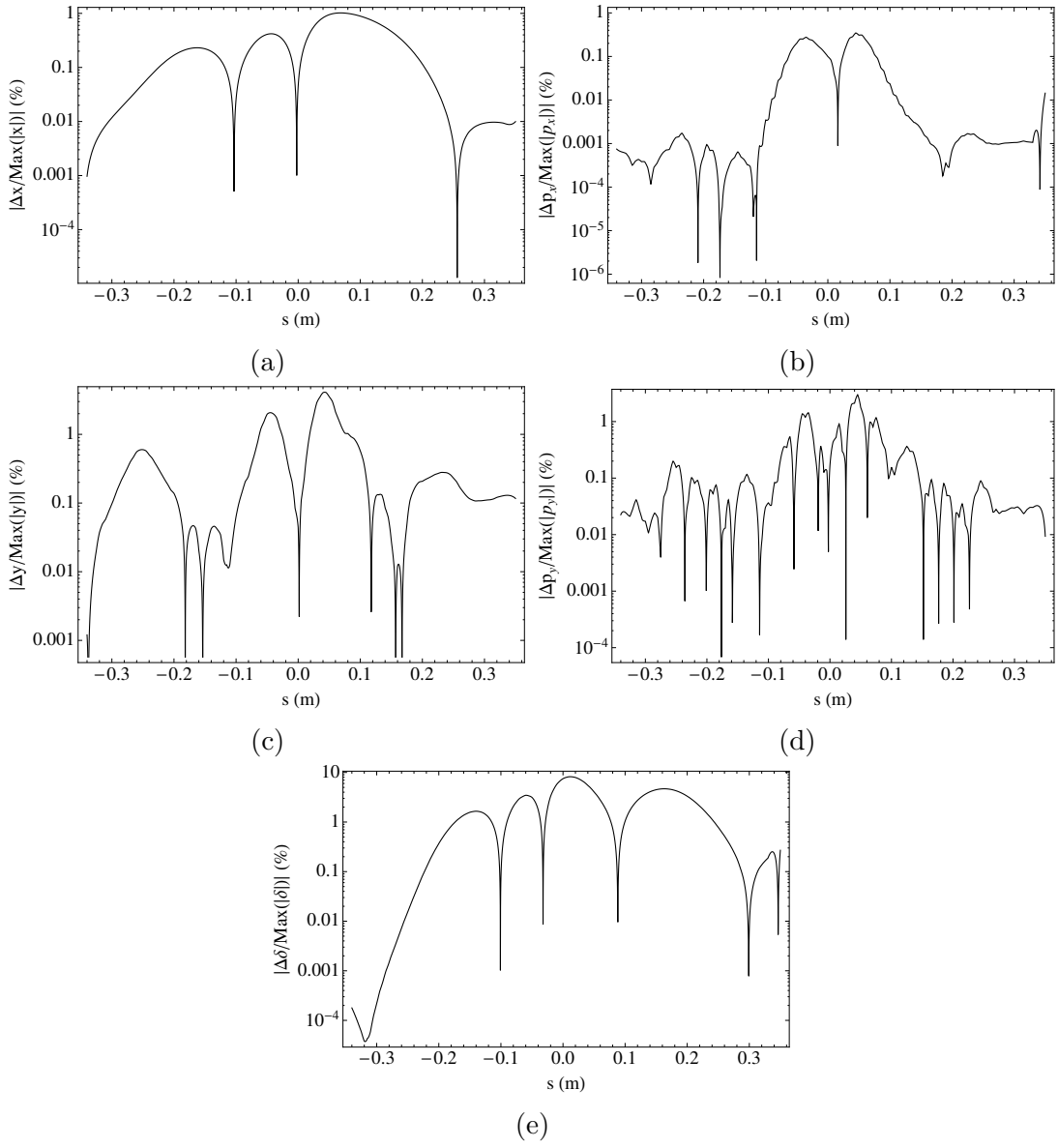

Figure 3.20: Trajectory error resulting from integration with truncated power series normalised to the maximum value over the trajectory. For variables (a) x, (b) p_x, (c) y, (d) p_y, and (e) δ. Initial condition $z = 0.1$ m, normalised to 3.83833 MV.

The R matrix describes the linear components of the Taylor map. The analytical R matrix for a horizontal crab cavity is,

$$\begin{pmatrix} x \\ p_x \\ y \\ p_y \\ z \\ \delta \end{pmatrix} \mapsto \begin{pmatrix} 1 & l & 0 & 0 & \frac{l}{2}\frac{qV}{cp_0}\frac{\omega}{c} & 0 \\ 0 & 1 & 0 & 0 & \frac{qV}{cp_0}\frac{\omega}{c} & 0 \\ 0 & 0 & 1 & l & 0 & 0 \\ 0 & 0 & 0 & 1 & 0 & 0 \\ 0 & 0 & 0 & 0 & 1 & \frac{1}{\gamma_0^2\beta_0^2} \\ \frac{qV}{cp_0}\frac{\omega}{c} & \frac{l}{2}\frac{qV}{cp_0}\frac{\omega}{c} & 0 & 0 & 0 & 1 \end{pmatrix} \begin{pmatrix} x \\ p_x \\ y \\ p_y \\ z \\ \delta \end{pmatrix}, \tag{3.49}$$

where l is the cavity length, ω the cavity frequency and V the cavity voltage. This R matrix of the crab cavity is very similar to that of a drift. The additional terms present for a crab cavity are the z dependent transverse terms which are required to rotate the bunch about its centre. In table 3.1 the linear R matrix terms R_{15} and R_{25}, from the 4RCAV Taylor map, are in agreement with the analytical model to 3 significant figures. The presence of a constant x term indicates that there is an additional phase offset between the z dependences of x and p_x, which was also observed in figure 3.19.

Linear Term	Drift-Kick-Drift	4 Rod Taylor map
Constant x	0.	-2.021×10^{-8}
R_{15}	4.127×10^{-6}	4.127×10^{-6}
R_{16}	0.	2.021×10^{-8}
R_{25}	1.197×10^{-5}	1.197×10^{-5}

Table 3.1: Linear map terms comparing the simple kick model with the four rod cavity Taylor map.

In figure 3.21 a number of R matrix terms are evaluated for the cavity at various phases. This shows that there are other terms, similar to the constant x term, which are non synchronous with the R_{25} transverse kick term. These

non synchronous terms occur as a result of the multiple kicks experienced by a charged particle passing through the cavity. Figure 3.19 shows that there are multiple changes in the momentum p_x trajectory resulting from multiple kicks in the cavity. Between these kicks the particle has time to move transversely which means that even if the integrated kick is zero there may have been more time spent with an overall momentum in one particular direction. This effect allows for the non-synchronous terms to form.

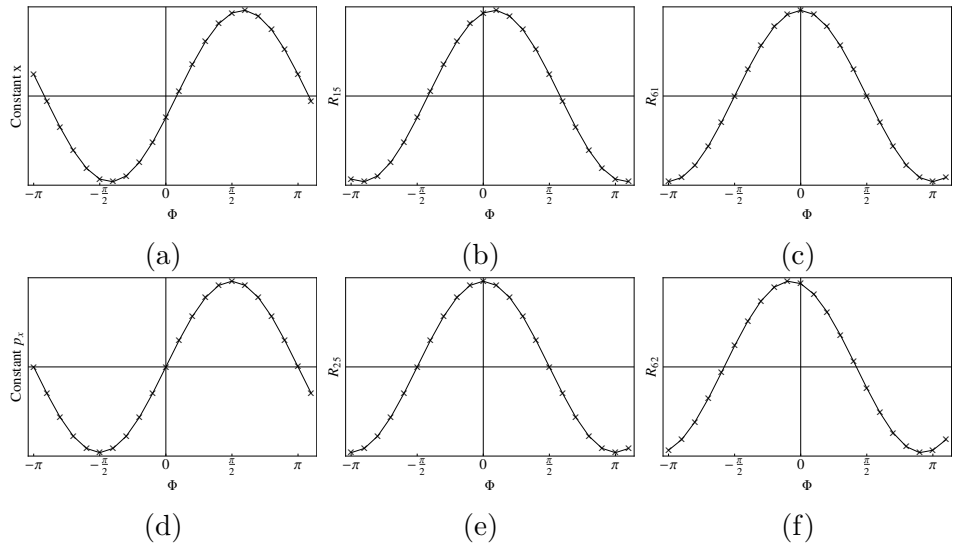

Figure 3.21: Phase dependence of the (a) constant x, (b) R_{15}, (c) R_{61}, (d) constant y, (e) R_{25}, and (f) R_{62} linear map terms for the 4RCAV evaluated at discrete phases using the TPSA library. The crabbing phase is at $\Phi = 0$.

Beyond the linear terms of the map, contained in the R matrix, there are higher order terms. These result from the higher order radial and azimuthal components of the field (shown in section 3.1), the non rigid trajectory of the particle through the cavity (shown in figure 3.19), and the higher order terms of the expansion of the time component, $\sin(kz)$. In the production of Taylor maps, for use in long term tracking, the maps were calculated to eighth order with six variables, giving 3003 terms for each Taylor series in the Taylor map. Many of these series terms contribute very little to a particle within the aperture of the cavity, with their contribution at the level of machine precision. In order

to evaluate the contribution of each term to an actual particle, a scoring system is used to rank the terms. The score is given by,

$$\text{score} = |\text{coefficient} \times (0.01\text{ m})^{O_x+O_y+O_z} \times 0.0001^{O_{p_x}+O_{p_y}+O_\delta}| \tag{3.50}$$

where O_n is the power to which a given variable n is raised. This scoring simply gives an order of magnitude to the maxima of initial variables from a particle in a stable position on the edge of a bunch. The values of 0.01 m and 0.0001 for the spatial and momentum values were chosen from the order of magnitude of the maximum absolute values of a single particle's position at large amplitude. This information was taken from tracking data at the face of each cavity in the lattice over 10^5 turns. The effect of small changes to these weighting values makes little change in the top ranked 50 terms of the Taylor series. Table 3.2 shows the ranked top 10 terms for each Taylor series in the Taylor map. Most of these terms are non-linear. Of these top 10 terms there are a number of particular note; the zero order term in x is ranked third showing significance to the transverse variation in the final x value, and the sum of the exponents of the x and y dependencies for the transverse kick p_x are even, while odd for δ, resulting from the dominant higher order transverse field components.

In figure 3.22 a number of the dominant non-linear terms are plotted against phase. It can be seen for both the third and fifth order momentum terms that the absolute peak coefficient value coincides with the crabbing phase. In contrast, the spatial terms, as seen previously for the linear case, are non synchronous with the momentum terms; in fact figure 3.22a shows that they are not even in phase with each other. This is a result of the multiple non-linear kicks contained in the full dynamic description of the crab cavity.

Rank \ Series	x	p_x	y	p_y	z	δ
1	x	p_x	y	p_y	z	δ
2	p_x	z	p_y	xyz	const.	x
3	const.	x^2y^2z	$p_y\delta$	xy^3z	p_y^2	xz^2
4	z	x^2z	xy	x^3yz	p_x^2	p_x
5	$p_x\delta$	y^2z	x^3y	x^3y^3z	p_x	xy^2
6	x^2	z^3	xz^3	xp_y	δ	x^3y^2
7	x^2y^2	x^4z	xyz	x^5yz	p_xz	x^3
8	z^2	y^4z	xy^3z	x^2p_xy	$p_y^2\delta$	xy^4
9	y^2	x^2y^4z	x^3yz	xy^2p_y	$p_x^2\delta$	x^5
10	x^2y^2z	x^4y^2z	x^3y^3z	p_xy	p_xyp_y	x^3y^4

Table 3.2: Ranked terms of the Taylor map showing terms with greatest impact on dynamics for particles with $|(x, y, z)| \approx 0.01$ m and $|(p_x, p_y, \delta)| = 10^{-4}$

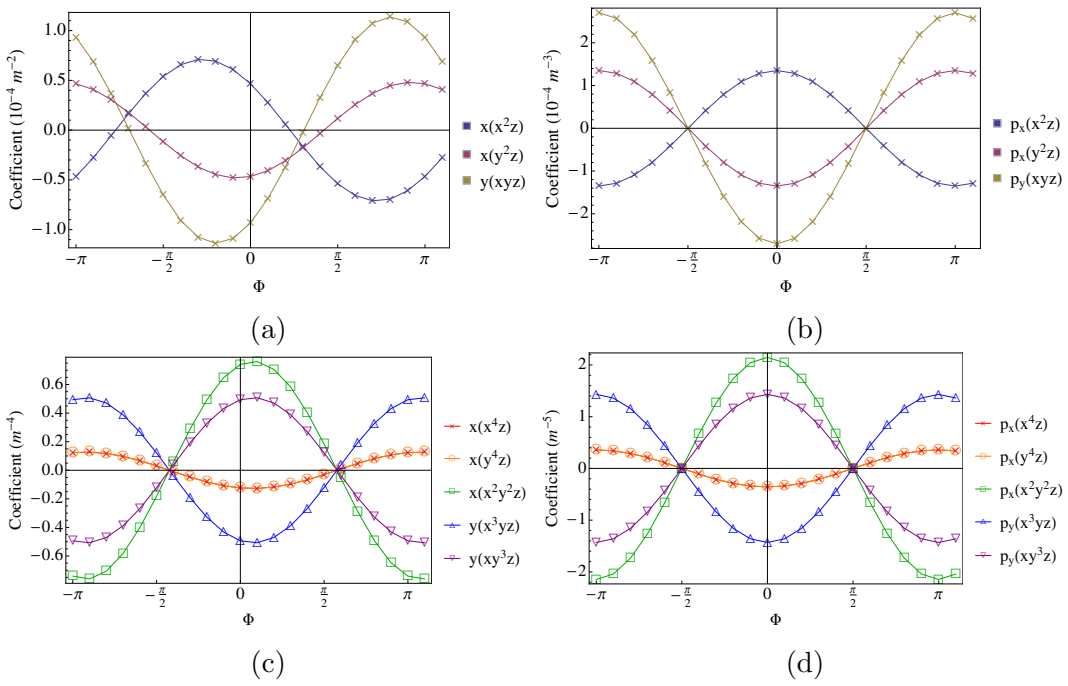

Figure 3.22: Phase dependence of (a) third order spatial, (b) third order momentum, (c) fifth order spatial, and (d) fifth order momentum non-linear terms for the 4RCAV evaluated at discrete phases using the TPSA library. Operating mode at crabbing phase, normalised to 4.155 MV.

Taylor maps and Numerical precision

In single particle dynamics some of the greatest limitations of tracking for larger numbers of turns lie with the numerical precision of numbers stored on a computer. The result of a function can be represented either symbolically or numerically. The simplest method of expressing a symbolic result is in the form of a power series. Computers store 64 bit double precision numbers in the following manner [135],

$$\mathbf{value} = (-1)^{\mathbf{sign}}(1 + \sum_{i=1}^{52} \mathbf{fraction}_{-i} 2^{-i}) \times 2^{\mathbf{exponent}-1023} \tag{3.51}$$

where one bit is assigned to the **sign**, 11 bits to the **exponent** and 52 bits for the **fraction**. This then stores a number with up to 15 decimal places of precision. This limit in precision leads to rounding errors in computation particularly when adding numbers. Considering a power series in one dimension is stored as,

$$\mathbf{value} = \sum_{i=0}^{\mathbf{order}} c_i \times x^i, \tag{3.52}$$

where c_i and x^i are double precision numbers some rounding error will occur in its evaluation. This is true whether considering a Taylor map representation or numerical integration, thereby making all transformations effectively non-symplectic when considering evaluation using a computer.

Extended Taylor maps

To increase the capabilities of a Taylor map, additional non-canonical variables, that are constants of the vector potential, can be added. This would allow, for example, a simulation in which the voltage changes on each turn to be computed using Taylor maps. For this study the extended variable considered was a voltage

scaling factor. The total crabbing voltage required from the three cavities is of order 10 MV. It was therefore decided that an extended variable V_{scale} would be defined as a fraction of 3 MV,

$$V_{\text{scale}} = \frac{V}{3 \text{ MV}}, \tag{3.53}$$

where V is the voltage in MV. In the TPSA this is implemented as a power series variable that acts as a normalisation factor on the vector potential. A Taylor map is calculated to 11^{th} order with seven variables. Six variable maps based on the canonical variables are produced for a set of V_{scale} values by summing the terms with common canonical variable exponents. In figure 3.23 it is shown that there is a non-linear scaling of the map with voltage of order $10^{-10}\%$ which is either a result of a physical effect or just the error in the convergence of the maps.

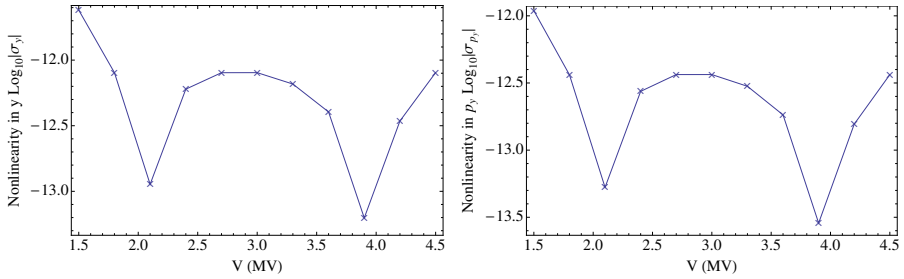

(a) (b)

Figure 3.23: Nonlinearity in (a) y and (b) p_y with V introduced by scaling the voltage with a 7 variable Taylor map. Initial variables (0.02,0,0,0,0.05,0). Cavity orientated vertically.

Symplectic error

The symplectic error is introduced in the Taylor maps through the loss of numerical precision provided by the truncated power series. The integration method, while theoretically symplectic, is only symplectic to the precision of the numerical storage whether as a power series or a real number. This level of symplecticity

can be analysed by evaluating the Jacobian of the Taylor map. The Jacobian of a map is defined by [136],

$$J(\vec{x}^i) = \begin{pmatrix} \frac{\partial x_1^f}{\partial x_1^i} & \cdots & \frac{\partial x_1^f}{\partial x_6^i} \\ \vdots & \ddots & \vdots \\ \frac{\partial x_6^f}{\partial x_1^i} & \cdots & \frac{\partial x_6^f}{\partial x_6^i} \end{pmatrix}, \tag{3.54}$$

where $\vec{x}^i$ and $\vec{x}^f$ are the initial and final canonical variables. From the symplectic condition, the symplectic error is given by the coefficients of the matrix E defined,

$$E(\vec{x}^i) = \tilde{J}(\vec{x}^i) \cdot S \cdot J(\vec{x}^i) - S, \tag{3.55}$$

as shown in section 2.5.2. The resulting symplectic error is shown in figure 3.24 for varying initial conditions. The coefficients peak at 10^{-7}, with very little change in the error once the order is above four, due to the contribution of higher order power series terms being smaller than the symplectic error of lower order terms. Figure 3.24b also shows that the maximum coefficient of the matrix E does not always decrease with order which is caused by significant higher order terms that have greater impact than those of lower orders when evaluated at a given point in the phase space.

Furthermore, considering the matrix $E(\vec{x}^i)$ as a function of the initial conditions, the maximum symplectic error over the hypersphere of the 6D phase space bounded by the dynamic aperture can be found. Scanning the value of E over the phase space ranges, as determined by the 6D tracking at large amplitude, given by $(x, y) = [-0.02, 0.02]$ m, $(p_x, p_y) = [-0.0001, 0.0001]$, $z = [-0.1, 0.1]$ m and $\delta = [-0.0001, 0.0001]$, gives a position independent measurement of the symplectic error. For the eighth order 4.155 MV map for the 4RCAV cavity this is given by 6.05×10^{-13}. For a symplectic map expressed to double precision one might

expect rounding errors to lead to an error of order 1×10^{-15}. This Taylor map has an error significantly greater than the error resulting from double precision rounding errors which suggests that the symplectic error would have a visible effect in the numerical tracking at a faster rate than that of symplectic tracking with double precision numbers. The point at which this occurs cannot be verified from a single evaluation of the symplectic error.

Reduced coefficient Taylor map

Truncating Taylor maps by order means that even with a 8^{th} order map each variable can have a power series with up to 3003 variables. Computationally using this full 8^{th} order map is slow in comparison to using a multipole method. In addition numerical noise is generated from the evaluation of the Taylor map from the addition of many very small numbers produced by higher order terms. Ordering the terms of a Taylor series by contribution to the final value instead of by power series order would allow a truncation which conserved more dynamics for fewer terms within the phase space over which the Taylor map must be valid for. Ranking these components would then provide a method of truncation based on a term's impact on the dynamics, instead of truncating based on power order. The two questions arising from this method relate to how does the symplectic error scale with the number of terms, and how many terms are needed to reproduce approximately the complete map. The coefficient scoring is carried out by,

$$\text{score} = \left|\text{Coefficient} \times (0.01\text{ m})^{O_x+O_y+O_z} \times 0.0001^{O_{px}+O_{py}+O_\delta}\right|, \tag{3.56}$$

The values of 0.01 m and 0.0001 for the spatial and momentum values respectively were taken from the order of magnitude of the maximum absolute values of a single particle's position at large amplitude. This information was taken from tracking data at the face of each cavity in the lattice over 10^5 turns.

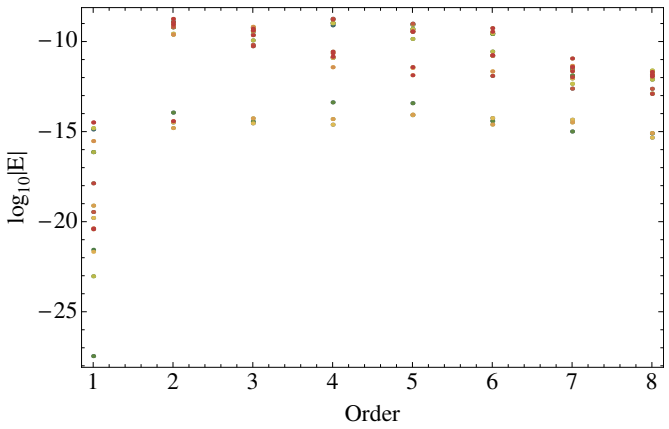

(a)

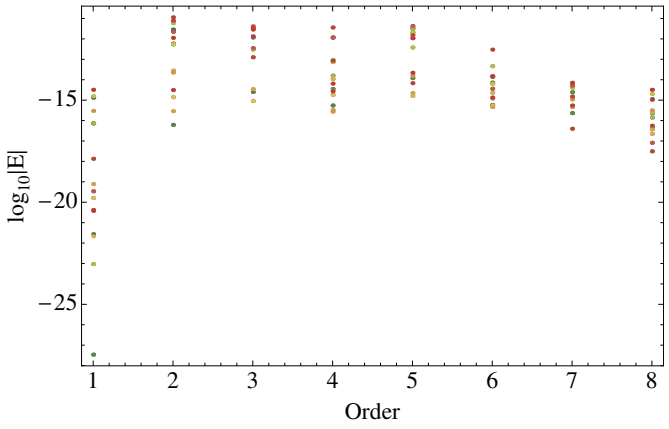

(b)

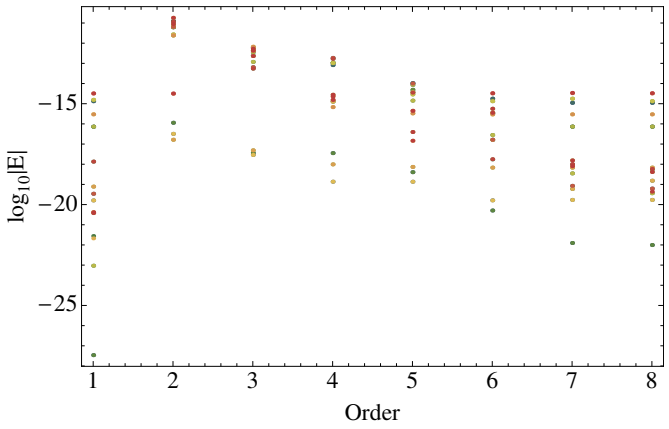

(c)

Figure 3.24: Symplectic error of the 4RCAV Taylor map evaluated at (a) $(x, y, z) = 0.01$ and $(p_x, p_y, \delta) = 0.01$, (b) $(x, y, z) = 0.01$ and $(p_x, p_y, \delta) = 0.0001$, and (c) $(x, y, z) = 0.001$ and $(p_x, p_y, \delta) = 0.001$. Taylor map normalised to a voltage of 4.155 MV.

The reduced coefficient map (RCM) is produced from the full eighth order Taylor map previously discussed. The standard Taylor map method in figure 3.25a shows that for the first 8 orders there are still highly contributing terms contained at higher orders. Contrasting this by taking a RCM in figure 3.25b it can be seen that far fewer terms are needed as insignificant terms are removed making it a far more efficient method in terms of number of computations.

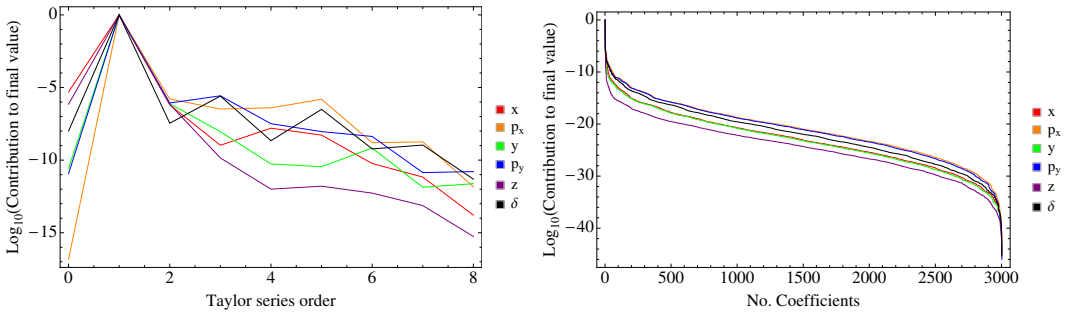

(a) (b)

Figure 3.25: Contribution to the final value from (a) all the terms of a given power series order, and (b) individual ranked terms. Map evaluated at $(x, y, z) = 0.01$ and $(p_x, p_y, \delta) = 0.0001$

The RCM method removes the less significant terms from the Taylor map which allows a control on the level of symplectic error; the symplectic error increases with the reduction of the Taylor map. In figure 3.26 the resulting variation in symplectic error and deviation in the Jacobian with coefficient reduction is shown. The Jacobian describes both the linear matrix, J, and its determinant, of the equations of motion evaluated at some instance [136]. The determinant of the Jacobian gives a measure of the growth of the phase space density, which for a conserved symplectic system is equal to unity. Both plots show that after 500 terms there is very little variation in the error and that the amplitude of the Jacobian error is at 10^{-15}. This error is the minimum error associated with a complete map and is at the level of machine precision. This levelling off of the error is expected as the precision of the largest contributing term will become

the limiting factor in decreasing the error. This effect is caused by the precision limit on a Taylor map being lower than that of a double precision number, as discussed in section 3.3.

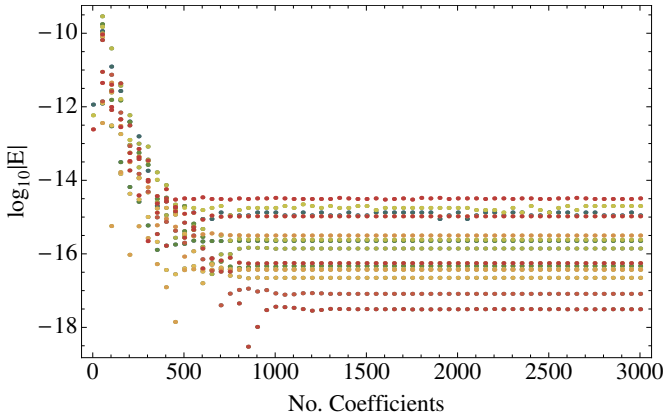

(a)

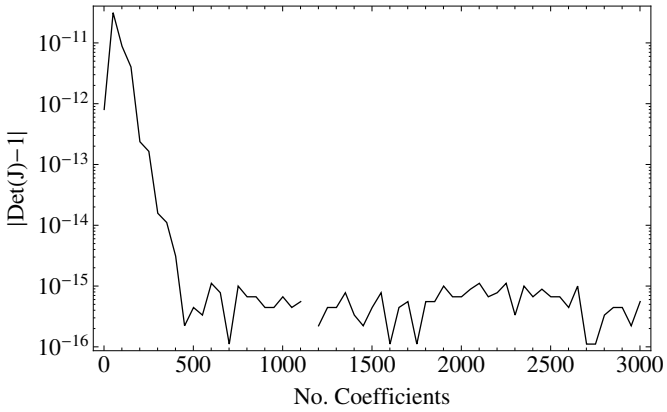

(b)

Figure 3.26: (a) Symplectic error and (b) Jacobian error as a function of ranked coefficient evaluated at (x, y, z)=0.01 m and (p_x, p_y, δ)=0.0001 for cavity normalised to 4.155 MV

Implementation of Taylor maps into a thin lens tracking code

In a thin lens tracking code, such as SixTrack [128], the elements in the lattice are described by a series of kicks and drift spaces as discussed in section 2.5.4. However, in a Taylor map the kicks and drift spaces are combined into one element, which means that a Taylor map in its "standard" form would not be able

to be applied directly. In order to overcome this, each element has an additional set of Taylor maps called anti-drifts. These are constructed using the same integration program used to produce the Taylor maps in reverse for half the length of the cavity with a zero potential. In the tracking code this anti-drift is applied either side of each cavity Taylor map, leading to an effectively thin element with a momentum change and orbit offset, shown in the schematic in figure 3.27. In terms of technical detail, within SixTrack, the element is both constructed for numerical integration and TPSA integration through the lattice. The Taylor maps are stored as a long list in a file external to the tracking file and then read into the code at the beginning of a run. When evaluated for either integration type, the array containing the Taylor map terms is iterated over to apply the transformation.

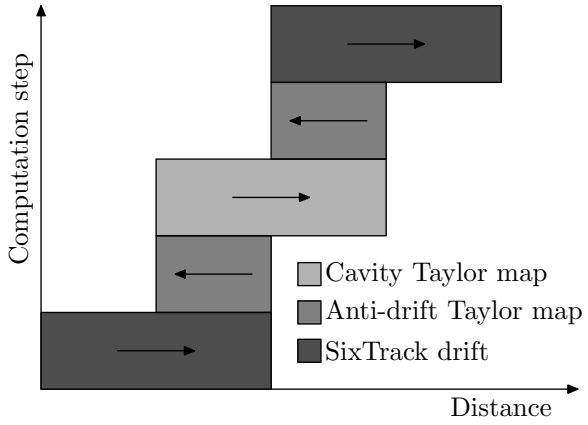

Figure 3.27: Implementation of a Taylor map element in a thin lens tracking code.

3.4 Symplecticity of a Taylor map in long term tracking

In order to simulate the crab cavities it is possible to integrate through the cavity fields either numerically, in situ within the tracking code, or with truncated power series, to form high order single element Taylor maps. For long term tracking, computationally, the Taylor maps are faster. However, their symplecticity has caused hesitation in using them to describe a single element. Just as with the impact of rounding errors [137], the truncation of a single element map will cause an error at every single pass through the map during tracking. The question then posed is not, "Is there an error?" but rather, "Do the gains made from using the single element Taylor map, i.e. the precision in dynamics far outweighs the effect of the symplectic error introduced?". The thin lens model used to describe a crab cavity is called an RF multipole which gives time dependent multipole kicks [138], and provides a symplectic model with a simpler description of the dynamics compared with those contained in the Taylor maps.

For this study the thin lens model [138] was replaced with Taylor maps for the 4RCAV cavity design [89]. The magnitude of symplectic error was controlled using the reduced coefficient Taylor map method; by reducing the number of terms, the symplectic error increases. A single particle tracking is performed using SixTrack [91] at a large amplitude (close to the dynamic aperture) and the cumulative symplectic error is evaluated. A symplectic numerical integration of the fields was implemented in SixTrack and used to bench mark against the tracking with the Taylor maps. This provides a control from which to evaluate the impact of symplectic error in terms of the physical tracking and the growth in symplectic error. A full dynamic aperture study was not deemed feasible with such an integrator due to the long computation time required.

In section 3.3 the single element symplectic errors were shown. However, these do not provide a direct correlation to the errors associated with long term tracking at large amplitudes. At large amplitudes the amplitude will be turn dependent which will change the symplectic error added on each turn hence a linear relation cannot simply be considered in terms of the overall multiple turn symplectic error.

For 100,000 turns the phase space at IP3 was recorded for a single particle at a large, but stable, amplitude (a particle at this amplitude is not lost after 100,000 turns of tracking). This amplitude equates to 16 times the root mean square beam width (16σ) which is within the upper 25% of the dynamic aperture. The tracking is performed using various models of the crab cavity; a thin lens model, various truncated Taylor maps and a numerical integration through the fields. Figure 3.28 shows the linear action calculated from tracking data in accelerator coordinates using equation 2.39 plotted with turn number. It can be seen that the linear action varies over a wide range of values indicating that the motion is very non-linear. Considering the moving average of the linear action it can be seen that this varies far more slowly than the linear action with turn. This averaged linear action is a more stable measurement, and hence is considered as a reasonable way in which to compare the different models in terms of tracking.

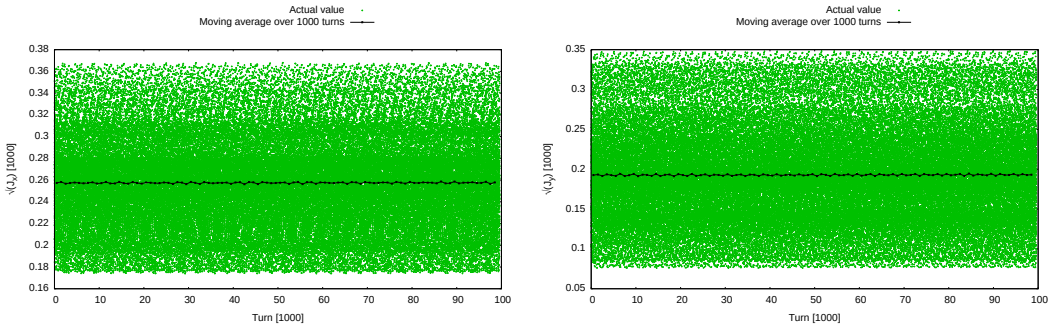

(a) (b)

Figure 3.28: Linear action with turn for numerical integrator with moving average and action (a) J_x and (b) J_y values.

In figure 3.29 the Taylor maps and RF multipole model are compared with the numerical integrator. It can be seen that the variation compared with the numerical integrator is up to the order of 1% of the moving average after 10^5 turns. The differences between the Taylor map model and RF multipole are similar suggesting that either the overall dynamics has limited sensitivity to the crab cavity model choice, in terms of variation in averaged linear action with turn, or that the models have a good level of agreement. A dynamic aperture result would confirm which is true.

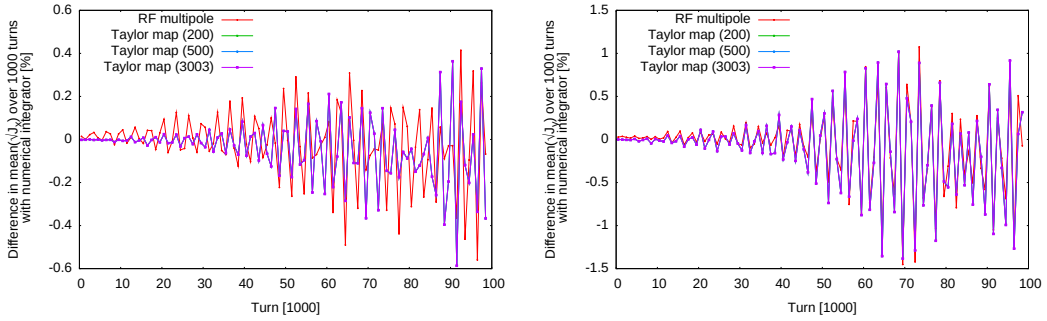

(a) (b)

Figure 3.29: Moving average of linear action with turn for numerical integrator compared with other cavity models for (a) J_x and (b) J_y.

Irrespective of the method used for tracking, whether using an algebraically symplectic kick model or a Taylor map, some level of numerical error will occur. This may be purely due to round off error from the machine's numerical precision [137] or the truncation errors associated with Taylor maps. In order to consider Taylor maps for long term tracking the loss in symplecticity must be deemed acceptable relative to the additional changes in dynamics which the Taylor map achieves compared to an alternative symplectic model. In order to evaluate the symplectic error over a large number of turns, 10^5 turns are tracked, with the cumulative symplectic and Jacobian errors calculated from the tracking data at each Taylor map element. From this data the Jacobian matrices are calculated from the individual Taylor maps and multiplied together in order to

calculate the total errors from the Taylor maps. The symplectic and Jacobian errors are not calculated for every element in the machine as it is assumed that the contribution is greatest from the Taylor maps.

The cumulative Jacobian error, shown in figure 3.30, is evaluated at an amplitude close to the dynamic aperture, in a very chaotic region. It can be seen that with a reduced number of coefficients there is an increased Jacobian error. However the difference between 500 and 3003 coefficients is very small compared with that of 200 coefficients at this point in phase space. It can be concluded that for this point in phase space the increase in number of terms beyond ≈500 does not equate to a significant reduction in the cumulative symplectic error. It is evident, however, that in terms of tracking there are differences. These may arise from numerical precision limitations, as discussed in section 3.3, or removal of physics, through truncation, relevant to this point in phase space.

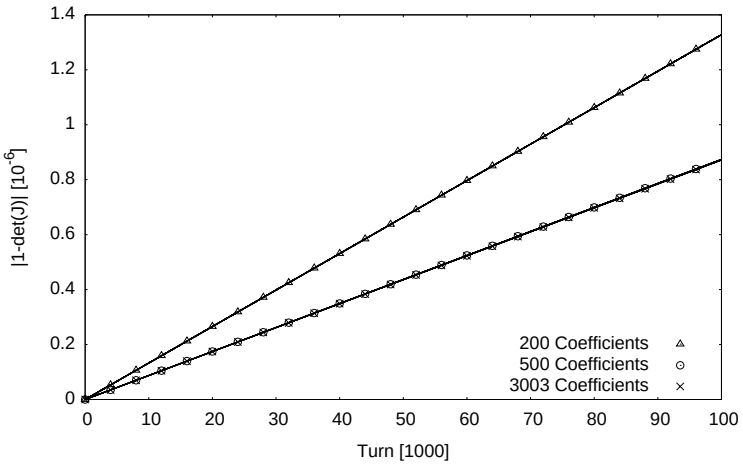

Figure 3.30: Jacobian error from all Taylor maps in SixTrack model with varying number of coefficients in units of $|1 - \det(J)|$.

In figure 3.31 the cumulative symplectic error can be seen to behave in a similar manner to the Jacobian error. A few symplectic error matrix coefficients dominate, with almost linear growth with each turn. These larger terms have almost identical values for the 500 and 3003 coefficient cases suggesting that the

error is caused by the numerical precision resulting from a common significant term or terms rather than through truncation of series terms.

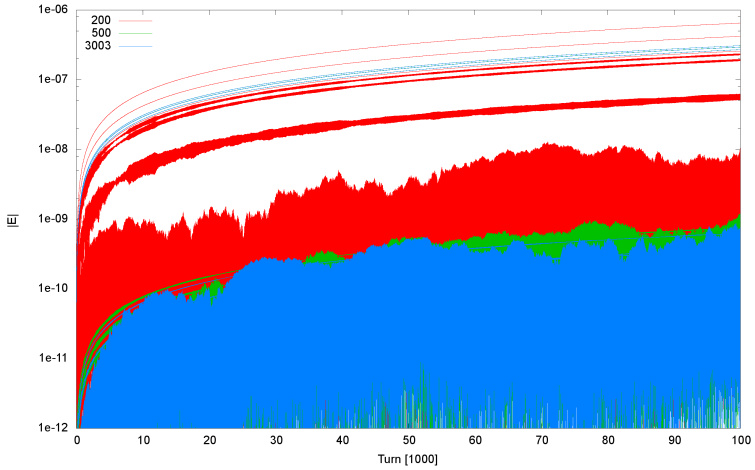

Figure 3.31: Cumulative symplectic error matrix coefficients, from all Taylor maps in SixTrack model, with varying number of coefficients.

While these methods show the amount of symplectic error at a given point in phase space, they do not determine the suitability over the whole of the phase space when considering long term tracking. It was shown in section 3.3 that the errors in tracking with Taylor maps would be significant due to the maximum symplectic errors of the single maps. The dynamic aperture is defined by the boundary of a closed volume formed by the lowest amplitude particles lost after 10^5 turns. The requirement on numerical precision is that close to this boundary the error in tracking does not exceed the steps in which amplitude is scanned. However, determining this tolerance is not a trivial task and was beyond the scope of this study. The chaotic nature of particles close to the dynamic aperture creates added complication, where small differences in the tracking could lead to significant differences in the final amplitude. This principle is used in the chaotic boundary calculation of the Lyapunov exponent [139]. The only true determination of the suitability of a Taylor map for dynamic aperture studies is to have exact agreement with a symplectic model.

3.5 Conclusion

A method for fitting the electric field to a set of analytical functions has been presented and successfully applied to the three prototype crab cavity designs. From these fitted fields an integration was performed using a truncated power series library to produce a Taylor map to describe the dynamics of the cavity. From these Taylor maps the cavity dynamics has been shown to exhibit strong nonlinear terms resulting from the transverse variation of the fields. Furthermore, through this Taylor map approach, it has been shown that the phase dependences of the spatial terms are not synchronous with the phase dependences of the momentum terms, as a result of longitudinal variations in the fields. A new truncated power series algebra library has also been described and applied to create Taylor maps with variables beyond that of the six canonical variables.

The symplecticity of the Taylor maps has been studied and it has been shown that there is evident symplectic error which increases cumulatively with turn. However, studying a single point in phase space has been inconclusive in determining the suitability of using Taylor maps for dynamic aperture studies. One proposed method is to seek agreement in dynamic aperture results between the Taylor map and symplectic cavity models. The dynamic aperture defines a boundary outside of the chaotic boundary at which particles remain stable after a given number of turns. By being chaotic the particles are sensitive to their initial conditions, hence having a close dynamic aperture between two different models would suggest a very small perturbation in the dynamics of the accelerator relative to the sensitivity to initial conditions. In order to create a symplectic model approximations upon the dynamics of the cavity must be applied. A Taylor map will contain both additional dynamics and symplectic error beyond a symplectic model. If there is a good agreement between a symplectic model and a Taylor map in terms of the resulting dynamic aperture this would indicate that the

impact of the additional dynamics and symplectic error are within the level of agreement of the two dynamic apertures.

Chapter 4

Symplectic cavity models

From the previous chapter it was seen that there was uncertainty surrounding the use of non symplectic models, such as single element Taylor maps, for long term tracking. However, the Taylor map provides the most complete picture of the dynamics of the cavity, thereby giving a reference point from which to choose a symplectic model. In this chapter thin kick models of the style by Ripken *et al.* [128] are considered. The distinct advantage of such models over Taylor maps is that they are symplectic. However, as already shown in section 3.3, Taylor maps contain the dynamics resulting from the longitudinal variation in the fields which can not be included in thin models. As a result it would be impossible to have a thin model which exactly agreed with the Taylor map.

In this chapter a series of symplectic cavity models in the rigid bunch and axial approximations are described, i.e. no momentum change and constant x and y through the cavity. Two pre-existing models which apply further approximations are described, these being the simple kick model and RF multipole kick model. Furthermore, a new model is introduced, the generalised RF multipole kick model, by generalising the thin model to a full solution of the Helmholtz equation. From these symplectic models comparisons are made to the dynamics described by the Taylor map.

4.1 Thin cavity models

In order to form a thin cavity model the s dependence of the vector potential must first be removed. In order to do this the Hamiltonian needs to be averaged in s over the length of the cavity, however a number of approximations are required in order to do this. By taking the rigid bunch and axial approximations (i.e. no momentum change and constant x and y) an exactly symplectic model can be produced. The extended accelerator Hamiltonian in the paraxial approximation is given in equation 2.144,

$$H = -\left(\frac{1}{\beta_0}+\delta\right)+\frac{1}{2\beta_0^2\gamma_0^2}\left(\frac{1}{\beta_0}+\delta\right)^{-1}+\frac{\delta}{\beta_0}+\frac{\left[p_x-a_x(x[s],y[s],z[s],s)\right]^2}{2\left(\frac{1}{\beta_0}+\delta\right)} + \frac{\left[p_y-a_y(x[s],y[s],z[s],s)\right]^2}{2\left(\frac{1}{\beta_0}+\delta\right)}-a_z(x[s],y[s],z[s],s)+p_s \tag{4.1}$$

where the normalised vector potential $\vec{a}$ is dependent on x, y and z (which are dependent on s), and s. Averaging over the length of the cavity leads to,

$$\langle H\rangle = \frac{1}{L}\int_0^L H(x,p_x,y,p_y,z,\delta,s,p_s)\,\mathrm{d}s, \tag{4.2}$$

however, given that x, p_x, y, p_y ,z and δ all vary with s this becomes difficult to evaluate. The rigid bunch approximation states that the momentum variables p are constant with time over the length of the cavity from Hamilton's equations this means that the Hamiltonian does not vary with position variables q,

$$\frac{\mathrm{d}p}{\mathrm{d}t} = -\frac{\partial H}{\partial q} = 0. \tag{4.3}$$

This means that only p_x, p_y and δ are effected by the kick of the cavity. The axial approximation states that the position variables q are constant over the length of

the cavity which leads to,

$$\frac{\mathrm{d}q}{\mathrm{d}t} = \frac{\partial H}{\partial p} = 0. \tag{4.4}$$

This means that the trajectory is independent of p_x, p_y and δ. These two assumptions reduce the averaged Hamiltonian to,

$$\langle H \rangle = \frac{1}{L} \int_0^L H(s, p_s)\, \mathrm{d}s, \tag{4.5}$$

where p_s is a constant, which results in,

$$\begin{aligned}\langle H \rangle = &- \left(\frac{1}{\beta_0} + \delta\right) + \frac{1}{2\beta_0^2\gamma_0^2}\left(\frac{1}{\beta_0} + \delta\right)^{-1} + \frac{\delta}{\beta_0} \\ &+ \frac{1}{L}\int_0^L \frac{\left[p_x - a_x(x,y,z,s)\right]^2}{2\left(\frac{1}{\beta_0} + \delta\right)}\, \mathrm{d}s + \frac{1}{L}\int_0^L \frac{\left[p_y - a_y(x,y,z,s)\right]^2}{2\left(\frac{1}{\beta_0} + \delta\right)}\, \mathrm{d}s \\ &- \frac{1}{L}\int_0^L a_z(x,y,z,s)\, \mathrm{d}s. \end{aligned} \tag{4.6}$$

The Panofsky-Wenzel theorem [140] assumes these rigid bunch and axial approximations and can be used to show that the kicks from the transverse vector potential terms cancel over the integrated length of the cavity. From Newton's second law of dynamics, and the Lorentz force law, the normalised momentum change from an electromagnetic field on a rigid particle is given by [140],

$$\Delta p_\perp = \frac{q}{p_0 v} \int_0^L \vec{E}_\perp + (\vec{v} \times \vec{B})_\perp \, ds. \tag{4.7}$$

From Maxwell's equations the $\vec{E}$ and $\vec{B}$ fields can be expressed in terms of the magnetic vector potential $\vec{A}$ such that,

$$\vec{B} = \nabla \times \vec{A}, \qquad\qquad \vec{E} = -\frac{\partial \vec{A}}{\partial t}, \tag{4.8}$$

leading to the expression,

$$\Delta p_\perp = \frac{q}{p_0 v}\int_0^L -\frac{\partial \vec{A}_\perp}{\partial t} + (\vec{v}\times\nabla\times\vec{A})_\perp \, ds. \tag{4.9}$$

By applying the vector calculus identity,

$$\vec{v}\times(\nabla\times\vec{A}_\perp) = \nabla(\vec{v}\cdot\vec{A}_\perp) - (\vec{v}\cdot\nabla)\vec{A}_\perp, \tag{4.10}$$

the curl terms can be removed from equation 4.9 to give [140],

$$\Delta\vec{p}_\perp = -\frac{q}{p_0 v}\int_0^L \left[\left(\frac{\partial}{\partial t} + \vec{v}\cdot\nabla\right)\vec{A}_\perp - \nabla_\perp(\vec{v}\cdot\vec{A})\right] \, ds. \tag{4.11}$$

In the relativistic limit where $\vec{v}\to c\hat{s}$, such that the velocity is assumed constant, the following simplifications can be made,

$$\frac{1}{v}\nabla_\perp(\vec{v}\cdot\vec{A}) = \nabla_\perp A_z, \tag{4.12}$$

$$\frac{1}{v}\left(\frac{\partial}{\partial t} + \vec{v}\cdot\nabla\right)\vec{A}_\perp = \frac{1}{c}\frac{\partial\vec{A}_\perp}{\partial t} = \frac{\partial}{\partial s}\vec{A}_\perp. \tag{4.13}$$

From these simplifications the change in momentum is given by [140],

$$\Delta\vec{p}_\perp = \frac{q}{p_0}\left[\vec{A}_\perp(s=0) - \vec{A}_\perp(s=L)\right] + \frac{q}{p_0}\int_0^L \nabla_\perp A_z \, ds. \tag{4.14}$$

The locations for s equal to zero and L equate to field free regions. Therefore, the kicks resulting from the transverse vector potential can be seen to cancel. This assumption means that this thin cavity model can only be applied over the whole length of the cavity and prevents a cavity being split into slices as is often considered for magnets [141]. This reduces the Hamiltonian in the rigid bunch

approximation to,

$$\langle H \rangle = -\left(\frac{1}{\beta_0} + \delta\right) + \frac{1}{2\beta_0^2\gamma_0^2}\left(\frac{1}{\beta_0} + \delta\right)^{-1} + \frac{p_x^2}{2\left(\frac{1}{\beta_0} + \delta\right)} + \frac{p_y^2}{2\left(\frac{1}{\beta_0} + \delta\right)} + \frac{\delta}{\beta_0} - \frac{1}{L}\int_0^L a_z(x, y, z, s)\ \mathrm{d}s \tag{4.15}$$

From the rigid bunch approximation then the Hamiltonian can be split such that,

$$\langle H \rangle = H_{\text{drift}}(p_x, p_y, \delta) + H_{\text{kick}}(x, y, z), \tag{4.16}$$

where H_{drift} is given by,

$$H_{\text{drift}}(p_x, p_y, \delta) = -\left(\frac{1}{\beta_0} + \delta\right) + \frac{1}{2\beta_0^2\gamma_0^2}\left(\frac{1}{\beta_0} + \delta\right)^{-1} + \frac{p_x^2}{2\left(\frac{1}{\beta_0} + \delta\right)} + \frac{p_y^2}{2\left(\frac{1}{\beta_0} + \delta\right)} + \frac{\delta}{\beta_0}, \tag{4.17}$$

and H_{kick},

$$H_{\text{kick}}(x, y, z) = -\frac{1}{L}\int_0^L a_z(x, y, z, s)\ \mathrm{d}s. \tag{4.18}$$

Both Hamiltonian components are solvable with Hamilton's equations and therefore they result in symplectic transformations. For H_{kick} in general the transformation is given by,

$$\Delta p_x = \frac{\partial}{\partial x}\int_0^L a_z(x, y, z, s)\ \mathrm{d}s, \tag{4.19}$$

$$\Delta p_y = \frac{\partial}{\partial y}\int_0^L a_z(x, y, z, s)\ \mathrm{d}s, \tag{4.20}$$

$$\Delta \delta = \frac{\partial}{\partial z}\int_0^L a_z(x, y, z, s)\ \mathrm{d}s. \tag{4.21}$$

The removal of a_x and a_y terms mean that H_{drift} no longer needs to be in a paraxial form, such that,

$$H_{\text{drift}}(p_x, p_y, \delta) = \frac{\delta}{\beta_0} - \sqrt{\left(\frac{1}{\beta_0} + \delta\right)^2 - p_x^2 - p_y^2 - \frac{1}{\beta_0^2\gamma_0^2}}. \tag{4.22}$$

Symplectic transformations exist for this Hamiltonian of the drift and can be found in [128, 142].

From the rigid bunch and axial approximations two further assumptions can be applied to the averaged a_z to further simplify the crab cavity model. In this section three variants of the thin crab cavity model are introduced. In its most general form a_z is a solution to the Helmholtz equation, as discussed in section 3.1. This leads to the generalised RF multipole kick model which is introduced in section 4.1.3. The first approximation to this general form is that in the ultra-relativistic limit, the transverse dependence of the work done on a particle is a solution to the Laplace equation [143]. This limit reduces the integrated a_z to a multipole expansion. This results in the RF multipole kick model which is introduced in section 4.1.2. The second approximation is to only consider the component of the multipole expansion that is dominant in the cavity. For example, for the crab cavity this would be the dipole component. This leads to the simple kick model shown in section 4.1.1. A summary of the different models is shown in figure 4.1.

4.1.1 Simple kick model

For most accelerators the model describing cavities is limited to a simple thin kick model [74, 128, 129]. These do not contain explicit information about the dynamics of a specific cavity design and typically either consider a uniform acceleration or transverse kick [119, 120]. The simplest model for a crab cavity comes

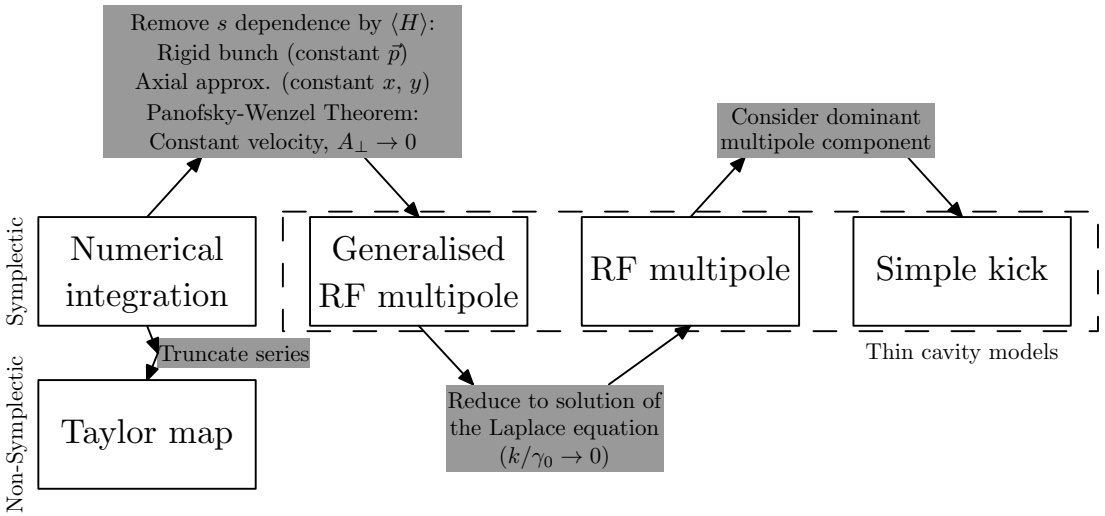

Figure 4.1: Assumptions made in the construction of crab cavity models.

from the following kick Hamiltonian,

$$H_{\text{kick}} = \frac{qV(s)}{p_0} x \sin\left(\frac{\omega z}{c} + \Phi\right), \tag{4.23}$$

where q is the charge of the particle, V is the cavity deflecting voltage in the horizontal plane, Φ is the cavity phase relative to the reference particle and ω is the cavity frequency. The s dependence creates difficulties in handling and solving the equations of motion, leading to methods such as those used to compute the single element Taylor maps. By taking the thin lens approximation for $V(s)$,

$$V(s) = V(s_0)\ \Delta s\ \delta(s - s_0), \tag{4.24}$$

such issues can be avoided. The Hamiltonian kick component, by integration over the length of the cavity, can be reduced to,

$$H_{\text{kick}} = \frac{qV}{p_0} x \sin\left(\frac{\omega z}{c} + \Phi\right). \tag{4.25}$$

The effective length of the cavity is then treated as drift space. By applying Hamilton's equations directly to this kick Hamiltonian the following symplectic transfer map describing the kick of the cavity is derived,

$$p_x \mapsto p_x + \frac{qV}{p_0} \sin\left(\frac{\omega z}{c} + \Phi\right), \tag{4.26}$$

$$p_y \mapsto p_y, \tag{4.27}$$

$$\delta \mapsto \delta + \frac{qV}{p_0} \frac{\omega x}{c} \cos\left(\frac{\omega z}{c} + \Phi\right). \tag{4.28}$$

From this transformation it can be seen that this model exhibits a z dependent transverse kick, and an x and z dependent change in δ because of symplecticity. This model is good in the limit that the transverse dependencies of the kick can be neglected. If this were not the case a model including these dependencies would be required. It has already been shown that this is not the case in figure 3.19 in which a transverse kick dependence beyond the dipole kick was observed.

4.1.2 RF multipole kick model

The RF multipole kick model (RFM) is named after the corresponding multipoles used to express azimuthal components of magnetic fields [144, 138]. The azimuthal decomposition of static magnet fields was sought to be applied also to RF cavities. The RFM model provides a leading order description of the transverse dependencies of the kick.

The first assumption comes about by considering the spatial dependencies of the transverse kicks which do most work on a particle as it passes through the cavity. The work done to a particle traversing the cavity needs to be found as a function of x and y, which has been previously derived in [143]. A function describing the work done (or voltage) V is needed from the cavity $\vec{E}$ field. The

$\vec{E}$ field in a cavity is described in general by the wave equation,

$$\nabla^2 \vec{E} - \frac{1}{c^2}\frac{\partial^2 \vec{E}}{\partial t^2} = 0, \tag{4.29}$$

where c is the speed of light and t is time. From the axial and rigid bunch approximations the energy transferred to the particle from the cavity field is given by [143],

$$qV(x,y) = q\int_a^b E_z(x,y,s)\, ds, \tag{4.30}$$

where q is the particle charge, a and b are the start and end locations in the longitudinal position s. The Laplacian operator applied to the potential is given by,

$$\nabla^2 V \equiv \frac{\partial^2 V}{\partial x^2} + \frac{\partial^2 V}{\partial y^2}, \tag{4.31}$$

where V is only dependent on x and y. Expanding the Laplace operator in the wave equation in equation 4.29, considering only the E_z component, leads to [143],

$$\frac{\partial^2 E_z}{\partial x^2} + \frac{\partial^2 E_z}{\partial y^2} + \frac{\partial^2 E_z}{\partial s^2} - \frac{1}{c^2}\frac{\partial^2 E_z}{\partial t^2} = 0. \tag{4.32}$$

Rearranging this and integrating over the length of the cavity results in,

$$\int_a^b \left(\frac{\partial^2 E_z}{\partial x^2} + \frac{\partial^2 E_z}{\partial y^2}\right) ds = \int_a^b \left(\frac{1}{c^2}\frac{\partial^2 E_z}{\partial t^2} - \frac{\partial^2 E_z}{\partial s^2}\right) ds. \tag{4.33}$$

The left hand side of equation 4.33 is identical to equation 4.31 hence,

$$\nabla_\perp^2 V = \int_a^b \nabla_\perp^2 E_z\, ds = \int_a^b \left(\frac{1}{c^2}\frac{\partial^2 E_z}{\partial t^2} - \frac{\partial^2 E_z}{\partial s^2}\right) ds. \tag{4.34}$$

The E_z field component takes the form of a function $f[s, t(s)]$ which has a total

differential of the form,

$$\int \frac{\partial f}{\partial s}\, ds = f - \int \frac{\partial f}{\partial t}\frac{dt}{ds}\, ds + \text{const.} \tag{4.35}$$

Applying this first to $\partial E_z/\partial s$ allows the simplification of equation 4.34 to [143],

$$\nabla^2 V = -\frac{\partial E_z}{\partial s}\Big|_a^b + \int_a^b \left(\frac{1}{c^2}\frac{\partial^2 E_z}{\partial t^2} + \frac{1}{\beta c}\frac{\partial^2 E_z}{\partial s \partial t}\right) ds \tag{4.36}$$

where β is the velocity as a fraction of c. Applying equation 4.35 to $\partial E_z/\partial t$ allows further simplification to,

$$\nabla_\perp^2 V = \left(-\frac{\partial \vec{E}}{\partial s} + \frac{1}{\beta c}\frac{\partial \vec{E}}{\partial t}\right)\Big|_a^b + \int_a^b \frac{1}{(\beta_0\gamma_0 c)^2}\frac{\partial^2 \vec{E}}{\partial t^2}\, ds \tag{4.37}$$

From equation 4.30 this can be arranged to a form close to that of the wave equation,

$$\nabla_\perp^2 V + \frac{1}{(\beta_0\gamma_0 c)^2}\frac{\partial^2 V}{\partial t^2} = \left(-\frac{\partial E_z}{\partial s} + \frac{1}{\beta c}\frac{\partial E_z}{\partial t}\right)\Big|_{a,t_a}^{b,t_a+\frac{(b-a)}{\beta c}} \tag{4.38}$$

where t_a is the time at point a. Defining a and b as the position at the entrance and exit of the cavity, which are field free regions, leads the right hand side of equation 4.38 to go to zero leaving,

$$\nabla_\perp^2 V + \frac{1}{(\beta_0\gamma_0 c)^2}\frac{\partial^2 V}{\partial t^2} = 0. \tag{4.39}$$

Equation 4.39 can be simplified if the time component of the field is harmonic with frequency ω and wavenumber $k = \omega/\beta c$,

$$\nabla_\perp^2 V - \left(\frac{k}{\gamma_0}\right)^2 V = 0, \tag{4.40}$$

where in the limit $k/\gamma_0 \to 0$ this reduces to the Laplace equation. This gives an expression for V from the form of the $\vec{E}$ field in the cavity. This is important as it defines the transverse dependency of the work done on a particle as it passes through the cavity. In order to reach this function the rigid bunch and axial approximations were applied.

Given that V is defined in terms of E_z in equation 4.30, in this limit, the spatial component $E_z^{(l)}$, defined in equation 3.2, takes the form of a general solution to the Laplace equation,

$$\int_a^b E_z^{(l)}(\rho, \phi, s)\, ds = E_0 \sum_{n=0}^{\infty} c_n \rho^n e^{\mathrm{i}n\phi}. \tag{4.41}$$

c_n is a series of complex coefficients describing the field, E_0 is a normalisation factor, ρ is radius and ϕ is the azimuthal position. The direct relation between the vector potential and electric field arising from Maxwell's equations,

$$\vec{A} = \frac{\mathrm{i}}{\omega}\vec{E}, \tag{4.42}$$

leads to the integrated vector potential,

$$\int_0^L A_z\, ds = e^{\mathrm{i}(k_l z + \Phi_l)} \int_0^L A_z^{(l)}\, ds = e^{\mathrm{i}(k_l z + \Phi_l)} \sum_{n=1}^{N} \frac{\rho^n}{n} \left(b_n^{(l)} \cos(n\phi) + a_n^{(l)} \sin(n\phi) \right). \tag{4.43}$$

$a_n^{(l)}$ and $b_n^{(l)}$ are the skew and normal RF-multipole coefficients of a spatial component of a particular standing wave mode, and $A_z^{(l)}$ is the spatial component of the longitudinal vector potential. In [138] the multipole coefficients are complex to include the phase dependency as their argument. However, to keep with the formalism described in chapter 3 the convention is chosen that they are real numbers with an additional term Φ_l used to describe the phase. Using the transformations given in equation 3.32 the integrated vector potential can be expressed in

Cartesian coordinates,

$$\int_0^L A_z \, ds = e^{\mathrm{i}(k_l z + \Phi_l)} \sum_{n=1}^{N} \frac{1}{n} \left\{ b_n^{(l)} \Re[(x + \mathrm{i}y)^n] + a_n^{(l)} \Im[(x + \mathrm{i}y)^n] \right\}. \tag{4.44}$$

From the kick Hamiltonian,

$$H_{\text{kick}}(x, y, z) = -\frac{q}{p_0} \frac{1}{L} \int_0^L A_z \, ds, \tag{4.45}$$

by applying Hamilton's equations the following symplectic transformation is derived [138],

$$p_x \mapsto p_x + \frac{q}{p_0} \sin(k_l z + \Phi_l) \sum_{n=1}^{N} \Re\left[\left(b_n^{(l)} + \mathrm{i} a_n^{(l)} \right) (x + \mathrm{i}y)^{n-1} \right], \tag{4.46}$$

$$p_y \mapsto p_y - \frac{q}{p_0} \sin(k_l z + \Phi_l) \sum_{n=1}^{N} \Im\left[\left(b_n^{(l)} + \mathrm{i} a_n^{(l)} \right) (x + \mathrm{i}y)^{n-1} \right], \tag{4.47}$$

$$\delta \mapsto \delta + \frac{q}{p_0} k_l \cos(k_l z + \Phi_l) \sum_{n=1}^{N} \frac{1}{n} \Re\left[\left(b_n^{(l)} + \mathrm{i} a_n^{(l)} \right) (x + \mathrm{i}y)^{n} \right]. \tag{4.48}$$

This map goes beyond the simple kick model seen in equation 4.26 by including a transverse kick dependency, while still including the rigid bunch and axial approximations. However, this model is only valid in the high γ_0 limit where additional terms present in the solution to the Helmholtz equation can be neglected. Below this limit additional terms which are present in the solution to the Helmholtz equation will contribute.

4.1.3 Generalised RF multipole kick model

The generalised RF multipole kick model takes the rigid bunch and axial approximations and makes no further assumptions in its construction. The integrated a_z description comes from the general solution to the Helmholtz equation given

in equation 3.9. From the form of the fitted $E_z^{(l)}$ in equation 3.9 [119], in terms of the generalised gradients in equation 3.33 (which are directly calculable from the field surface data), in Cartesian coordinates the integrated A_z is given by,

$$\begin{aligned}\int_0^L A_z\ ds &= \sum_l \frac{\mathrm{i}}{\omega_l} e^{-\mathrm{i}(k_l z+\Phi_l)} \int_0^L e^{\mathrm{i}k_l s} E_z^{(l)}\ ds \\ &= \sum_l \frac{\mathrm{i}}{\omega_l} e^{-\mathrm{i}(k_l z+\Phi_l)} \sum_{m=0}^{M}\sum_{n=1}^{N} \frac{1}{2^{n+2m} m!(n+m)!}(x^2+y^2)^m \\ &\quad \Big\{ \Re\left[(x+\mathrm{i}y)^n\right] \int_0^L e^{\mathrm{i}k_l s} C_{zc}^{(l)}(s,n,m)\ ds \\ &\quad + \Im\left[(x+\mathrm{i}y)^n\right] \int_0^L e^{\mathrm{i}k_l s} C_{zs}^{(l)}(s,n,m)\ ds \Big\}, \end{aligned} \tag{4.49}$$

for multiple standing modes. From the kick Hamiltonian defined in equation 4.45 the following equations of motion are found using Hamilton's equations,[1]

$$\begin{aligned} p_x \mapsto p_x + \frac{q}{p_0} \sin\left(\frac{\omega z}{c}+\Phi\right) &\sum_{m=0}^{M}\sum_{n=1}^{N} \\ &\Big\{ (x^2+y^2)^m \left(\Re\left[(x+\mathrm{i}y)^{n-1}\right] b_{n,m} + \Im\left[(x+\mathrm{i}y)^{n-1}\right] a_{n,m} \right) \\ &+ 2\frac{m}{n} x (x^2+y^2)^{m-1} \left(\Re\left[(x+\mathrm{i}y)^n\right] b_{n,m} + \Im\left[(x+\mathrm{i}y)^n\right] a_{n,m} \right) \Big\}, \end{aligned} \tag{4.50}$$

$$\begin{aligned} p_y \mapsto p_y - \frac{q}{p_0} \sin\left(\frac{\omega z}{c}+\Phi\right) &\sum_{m=0}^{M}\sum_{n=1}^{N} \\ &\Big\{ (x^2+y^2)^m \left(\Im\left[(x+\mathrm{i}y)^{n-1}\right] b_{n,m} + \Re\left[(x+\mathrm{i}y)^{n-1}\right] a_{n,m} \right) \\ &+ 2\frac{m}{n} y (x^2+y^2)^{m-1} \left(\Re\left[(x+\mathrm{i}y)^n\right] b_{n,m} + \Im\left[(x+\mathrm{i}y)^n\right] a_{n,m} \right) \Big\}, \end{aligned} \tag{4.51}$$

[1] Suppressing the superscript (l) and assuming a singular standing mode.

$$\delta \mapsto \delta + \frac{q}{p_0}\frac{\omega}{c}\cos\left(\frac{\omega z}{c}+\Phi\right)\sum_{m=0}^{M}\sum_{n=1}^{N}\frac{1}{n}(x^2+y^2)^m$$
$$\left(\Re\left[(x+\mathrm{i}y)^n\right]b_{n,m}+\Im\left[(x+\mathrm{i}y)^n\right]a_{n,m}\right). \tag{4.52}$$

The generalised multipole coefficients are defined by,

$$b_{n,m} = \Re\left[\frac{\mathrm{i}n}{\omega}\frac{1}{2^{n+2m}m!(n+m)!}\int_0^L e^{\mathrm{i}\frac{\omega s}{c}}C_{zc}(s,n,m)\ ds\right], \tag{4.53}$$
$$a_{n,m} = \Re\left[\frac{\mathrm{i}n}{\omega}\frac{1}{2^{n+2m}m!(n+m)!}\int_0^L e^{\mathrm{i}\frac{\omega s}{c}}C_{zs}(s,n,m)\ ds\right], \tag{4.54}$$

The generalised multipole coefficients $b_{n,m}$ are directly related to the multipole coefficients b_n such that $b_{n,0} \equiv b_n$. This model provides a description of the cavity dynamics with only the rigid bunch and axial approximations applied. This model is applicable for cases where the ultra-relativistic limit is no longer valid such that the additional terms in the solution to the Helmholtz equation are important and where the rigid bunch and axial approximations hold.

4.2 RF multipole coefficient calculations

The RF multipole coefficients were calculated directly from field maps of the various cavity designs. There are several methods used to do this [138], with each method starting from the eigenmode solution for the cavity operating mode, calculated using the frequency domain finite element code HFSS [121]. A precise Fourier decomposition of the fields required a regular meshing upon the surface of a cylinder. This avoids non-Maxwellian interpolation between the automatically assigned mesh nodes, which would be the default for HFSS. Instead the nodes of the solution are forced to lie regularly upon the cylinder. Figure 4.2 shows the mesh, which is constructed from a series of tetrahedra whose nodes lie on the surface of three cylinders, used to perform this eigenmode solution [122].

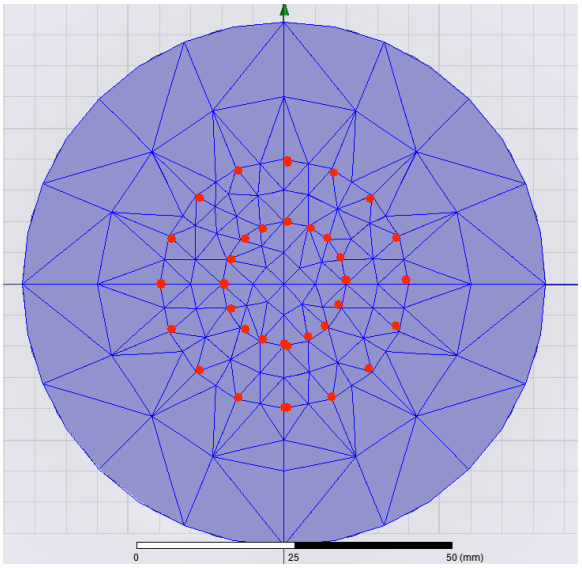

Figure 4.2: Meshing used to construct azimuthal decomposition constructed in HFSS [121] with equiradial mesh points lying on coaxial polyhedrons [122].

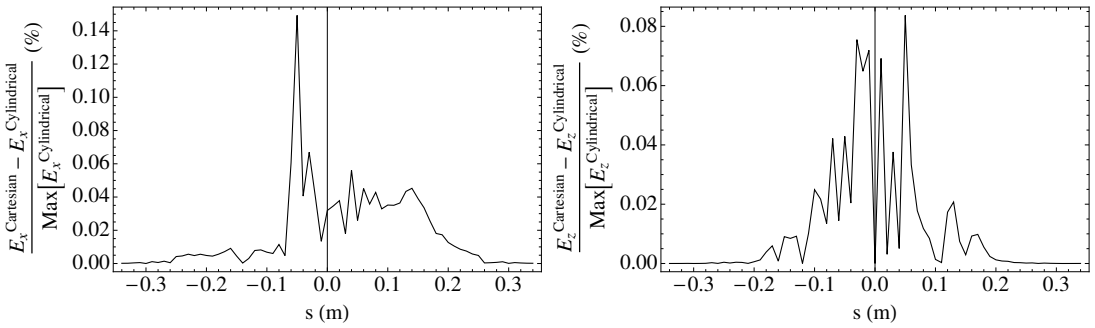

(a) (b)

Figure 4.3: Mesh error from interpolating the fields on a Cartesian mesh compared with the exact cylindrical meshing method. Absolute error in (a) E_x and (b) E_z field components at $x = 20$ mm and $y = 0$ mm.

It was found that there were significant errors introduced if this method was not used. Figure 4.3 shows the resulting error from interpolating from a Cartesian mesh compared with the fields on a Cylindrical mesh. It can be seen that there errors of order 0.1% in the E_z field introduced from this interpolation. The meshes used produced cylinders at radii of 10 mm and 20 mm respectively, with 16 uniformly separated azimuthal points in steps of 2 mm down the length of the cavity. For each mesh point the $\vec{E}$ and $\vec{B}$ fields were extracted, and from these the multipole coefficients calculated.

4.2.1 Lorentz Force multipole calculation

The Lorentz force multipole calculation makes use of electric and magnetic field data to calculate RF-multipole coefficients. Starting from the general Lorentz force expression, the transverse force is given by,

$$\vec{F}_\perp = q\left(\vec{E}_\perp + c(\hat{s} \times \vec{B})\right), \tag{4.55}$$

where $\hat{s}$ is the unit vector in the reference orbit direction and $\vec{E}$ and $\vec{B}$ are the electric and magnetic fields respectively. From Newton's second law, assuming that ds/dt is constant, the force can be expressed as the rate in change in momentum with position s,

$$\vec{F} = \frac{\mathrm{d}\vec{P}}{\mathrm{d}t} \approx \frac{1}{c}\frac{\mathrm{d}\vec{P}}{\mathrm{d}s}. \tag{4.56}$$

The normalised momentum kick $\vec{p}$, normalised to the reference momentum p_0, can be found from the force by integrating over the length of the cavity L,

$$\Delta\vec{p}_\perp = \frac{1}{p_0 c}\int_0^L \vec{F}_\perp \,\mathrm{d}s. \tag{4.57}$$

From the integrated vector potential in the high γ_0 limit, described by equation 4.39, the transverse momentum change can be directly calculated from Hamilton's equations in polar coordinates,

$$\begin{aligned}\Delta\vec{p}_\perp(\rho,\phi) &= e^{\mathrm{i}(k_l z+\Phi_l)}\frac{q}{p_0}\int_0^L \nabla_\perp A_z^{(l)}\,\mathrm{d}s \\ &= e^{\mathrm{i}(k_l z+\Phi_l)}\frac{q}{p_0}\int_0^L \begin{pmatrix} \frac{\partial A_z^{(l)}}{\partial\rho}\hat{\rho} \\ \frac{1}{\rho}\frac{\partial A_z^{(l)}}{\partial\phi}\hat{\phi} \end{pmatrix}\,\mathrm{d}s, \end{aligned} \tag{4.58}$$

where $A_z^{(l)}$ in the high γ_0 limit, from equation 4.44, is given by,

$$\int_0^L A_z^{(l)}\,\mathrm{d}s = \sum_{n=1}^{N}\frac{\rho^n}{n}\left(b_n^{(l)}\cos(n\phi)+a_n^{(l)}\sin(n\phi)\right). \tag{4.59}$$

This leads to a transverse momentum change of,

$$\Delta\vec{p}_\perp(\rho,\phi) = e^{\mathrm{i}(k_l z+\Phi_l)}\frac{q}{p_0}\sum_{n=1}^{N}\rho^{n-1}\begin{pmatrix} (b_n^{(l)}\cos(n\phi)+a_n^{(l)}\sin(n\phi))\hat{\rho} \\ (a_n^{(l)}\cos(n\phi)-b_n^{(l)}\sin(n\phi))\hat{\phi} \end{pmatrix}. \tag{4.60}$$

From this relation the following expression can be found by equating the radial component of momentum in equations 4.57 and 4.60,

$$\frac{1}{c}\int_0^L F_\rho\,\mathrm{d}s = e^{\mathrm{i}(k_l z+\Phi_l)}q\sum_{n=1}^{N}\rho^{n-1}\left(b_n^{(l)}\cos(n\phi)+a_n^{(l)}\sin(n\phi)\right). \tag{4.61}$$

The spatial component of the force $\vec{F}^{(l)}$ is defined by $\vec{F}=\sum_l \vec{F}^{(l)}\cdot e^{\mathrm{i}(kz+\Phi)}$ and can be directly calculated from the fields given by HFSS using the Lorentz force equation in equation 4.55. The spatial component of the right hand side of equation 4.61 takes the form of a Fourier series given by,

$$f(\phi) = \frac{1}{qc}\int_0^L F_\rho^{(l)}\,\mathrm{d}s = \sum_{n=1}^{N}\rho^{n-1}\left(b_n^{(l)}\cos(n\phi)+a_n^{(l)}\sin(n\phi)\right). \tag{4.62}$$

Multiplying $f(\phi)$ by $\cos(p\phi)$, where p is an integer, and integrating over one full period in ϕ results in,

$$\int_{-\pi}^{\pi} f(\phi)\cos(p\phi)\ \mathrm{d}\phi = \sum_{n=1}^{N} \rho^{n-1} a_n^{(l)} \int_{-\pi}^{\pi} \cos(p\phi)\sin(n\phi)\ \mathrm{d}\phi + \sum_{n=1}^{N} \rho^{n-1} b_n^{(l)} \int_{-\pi}^{\pi} \cos(p\phi)\cos(n\phi)\ \mathrm{d}\phi. \tag{4.63}$$

The only non-vanishing terms on the right hand side occur when $p = n$ so,

$$\int_{-\pi}^{\pi} f(\phi)\cos(n\phi)\ \mathrm{d}\phi = \rho^{n-1} b_n^{(l)} \pi. \tag{4.64}$$

In a similar way $f(\phi)$ can be multiplied by $\sin(p\phi)$ resulting in a relation for $a_n^{(l)}$,

$$\int_{-\pi}^{\pi} f(\phi)\sin(n\phi)\ \mathrm{d}\phi = \rho^{n-1} a_n^{(l)} \pi. \tag{4.65}$$

Using $f(\phi)$ defined by the Lorentz force in equation 4.62 the multipole coefficients can be calculated using,

$$a_n^{(l)} = \Re\left\{ \frac{1}{qc}\frac{1}{\pi} \int_{-\pi}^{\pi} \frac{1}{\rho^{n-1}} \sin(n\phi) \int_0^L F_\rho^{(l)}(\rho,\phi,s)\ \mathrm{d}s\ \mathrm{d}\phi \right\}, \tag{4.66}$$

$$b_n^{(l)} = \Re\left\{ \frac{1}{qc}\frac{1}{\pi} \int_{-\pi}^{\pi} \frac{1}{\rho^{n-1}} \cos(n\phi) \int_0^L F_\rho^{(l)}(\rho,\phi,s)\ \mathrm{d}s\ \mathrm{d}\phi \right\}. \tag{4.67}$$

4.2.2 Panofsky-Wenzel multipole calculation

The Panofsky-Wenzel theorem [140] is a useful relationship between transverse kicks and the electric field, allowing calculation of the multipole coefficients from only the longitudinal electric field component. Equation 4.14 states that,

$$\Delta\vec{p}_\perp = \frac{q}{p_0}\left[\vec{A}_\perp(s=0) - \vec{A}_\perp(s=L)\right] + \frac{q}{p_0}\int_0^L \nabla_\perp A_z\ \mathrm{d}s. \tag{4.68}$$

With some manipulation, assuming that field free regions are at the edges of the integrable region $[0, L]$, the momentum change can be expressed in terms of E_z only,

$$\begin{aligned}\Delta\vec{p}_\perp =& \frac{q}{p_0}\int_0^L \nabla_\perp A_z \,\mathrm{d}s \\ =& \frac{\mathrm{i}q}{\omega p_0} e^{-\mathrm{i}(k_l z+\Phi_l)} \int_0^L e^{\mathrm{i}k_l s}\nabla_\perp E_z^{(l)} \,\mathrm{d}s. \end{aligned} \tag{4.69}$$

The E_z field is separable into spatial and time components, as discussed in section 3.1, such that $E_z = \sum_l E_z^{(l)} \cdot e^{\mathrm{i}(k_l z+\Phi_l)}$. From equations 4.60 and 4.69 the following relation can found,

$$\frac{\mathrm{i}q}{\omega_l}\int_0^L e^{\mathrm{i}k_l s}\frac{\partial E_z^{(l)}}{\partial\rho}\,\mathrm{d}s = q\sum_{n=1}^{N}\rho^{n-1}\left(b_n^{(l)}\cos(n\phi)+a_n^{(l)}\sin(n\phi)\right), \tag{4.70}$$

from which a new function $f(\phi)$ is defined,

$$f(\phi) = \frac{\mathrm{i}}{\omega_l}\int_0^L e^{\mathrm{i}k_l s}E_z^{(l)}\,\mathrm{d}s = \sum_{n=1}^{N}\frac{1}{n}\rho^n\left(b_n^{(l)}\cos(n\phi)+a_n^{(l)}\sin(n\phi)\right). \tag{4.71}$$

By similar arguments used to find the coefficients of the Fourier series $f(\phi)$ in section 4.2.1 the multipole coefficients are given by,

$$a_n^{(l)} = \frac{1}{\pi}\frac{1}{\rho^n}\int_{-\pi}^{\pi} f(\phi)\sin(n\phi)\,\mathrm{d}\phi, \tag{4.72}$$

$$b_n^{(l)} = \frac{1}{\pi}\frac{1}{\rho^n}\int_{-\pi}^{\pi} f(\phi)\cos(n\phi)\,\mathrm{d}\phi. \tag{4.73}$$

From the definition of $f(\phi)$ in terms of E_z given in equation 4.71 the multipole coefficients can be calculated using,

$$a_n^{(l)} = \Re\left\{\frac{\mathrm{i}n}{\omega}\frac{1}{\pi}\int_{-\pi}^{\pi}\frac{1}{\rho^n}\sin(n\phi)\int_0^L e^{\mathrm{i}k_l s}E_z^{(l)}(\rho,\phi,s)\ \mathrm{d}s\ \mathrm{d}\phi\right\} \tag{4.74}$$

$$b_n^{(l)} = \Re\left\{\frac{\mathrm{i}n}{\omega}\frac{1}{\pi}\int_{-\pi}^{\pi}\frac{1}{\rho^n}\cos(n\phi)\int_0^L e^{\mathrm{i}k_l s}E_z^{(l)}(\rho,\phi,s)\ \mathrm{d}s\ \mathrm{d}\phi\right\}. \tag{4.75}$$

This method requires the eigenmode solver to solve the fields beyond the beam pipe cutoff of the operating mode such that the vector potential is zero at the limits of integration.

4.2.3 Helmholtz decomposition

The field fitting method can be extended to calculate generalised multipole coefficients from the harmonic functions $\tilde{e}_n(k)$ and $\tilde{f}_n(k)$ defined in equations 3.12 and 3.13 respectively. Starting from the generalised multipole coefficients defined in equations 4.53 and 4.54,

$$b_{n,m} = \Re\left[\frac{\mathrm{i}n}{\omega}\frac{1}{2^{n+2m}m!(n+m)!}\int_0^L e^{\mathrm{i}\frac{\omega s}{c}}C_{zc}(s,n,m)\ \mathrm{d}s\right] \tag{4.76}$$

$$a_{n,m} = \Re\left[\frac{\mathrm{i}n}{\omega}\frac{1}{2^{n+2m}m!(n+m)!}\int_0^L e^{\mathrm{i}\frac{\omega s}{c}}C_{zs}(s,n,m)\ \mathrm{d}s\right], \tag{4.77}$$

the generalised multipoles are expressed in terms of generalised gradients defined in equation 3.21. The generalised gradients in terms of $\tilde{e}_n(k)$ and $\tilde{f}_n(k)$ are given by,

$$C_{zc}(s,n,m) = \int_{-\infty}^{\infty}\frac{\mathrm{d}k}{\sqrt{2\pi}}e^{\mathrm{i}ks}\mathrm{sgn}(k^2-k_l^2)^m\kappa_l(k)^{n+2m}\tilde{e}_n(k) \tag{4.78}$$

$$C_{zs}(s,n,m) = \int_{-\infty}^{\infty}\frac{\mathrm{d}k}{\sqrt{2\pi}}e^{\mathrm{i}ks}\mathrm{sgn}(k^2-k_l^2)^m\kappa_l(k)^{n+2m}\tilde{f}_n(k). \tag{4.79}$$

As previously stated, given that the generalised multipoles of the form $b_{n,0}$ are equal to the regular multipoles this method provides a further way to calculate the regular multipoles.

4.2.4 Multipole results

The results of the various multipole calculations applied to the different cavities is summarised in table 4.1; in which it can be seen that there are apparent variations between the methods. The most significant of these differences occurs with the Helmholtz decomposition and arises from the use of Bessel functions in computing the harmonic functions by forcing the fields to form an exact solution to the Helmholtz equation. For example, in the 4RCAV 2011 cavity this leads to a difference of approximately 1% in the b_3 value at 20 mm. Comparing the two direct methods, the Lorentz force and Panofsky-Wenzel decomposition, there can be seen at 0.5% difference in the 20 mm results for b_3 of the QWCAV 2011 cavity. Further variations arise between all three methods from the mesh noise and the error introduced in the Fourier decomposition through the limited number of angular bins. Examples of this can be seen in the non-zero b_2 and b_4 values for all cavities with two planes of transverse symmetry i.e. all but the QWCAV 2011 cavity.

Considering the actual multipole values of the various cavity designs it can be seen that only for the QWCAV 2011 design are there significant b_2 and b_4 components. This arises from the cavity only having one plane of transverse symmetry. The maximum b_3 component of the 2012 designs can be found in the ODUCAV 2012 design which is approximately 4.5 T/m. Comparatively the minimum b_3 of the 2012 designs is the QWCAV closely followed by the 4RCAV, both with approximately 1 T/m.

Cavity	Multipole	Lorentz method		Panofsky-Wenzel		Helmholtz
	coefficient	10 mm	20 mm	10 mm	20 mm	20 mm
	b_2	−0.02	−0.03	−0.02	−0.03	−0.06
4RCAV 2011	b_3	898	898	896	898	906
	b_4	24	−7	−5	39	−2
	b_2	−0.06	−0.05	−0.06	−0.06	−0.10
4RCAV 2012	b_3	1160	1159	1161	1162	1156
	b_4	−4	100	65	27	57
	b_2	−0.04	−0.04	−0.04	−0.06	−0.08
ODUCAV 2011	b_3	3198	3199	3196	3198	3194
	b_4	−239	−52	323	−96	−57
	b_2	0.01	0.00	0.00	0.01	0.01
ODUCAV 2012	b_3	4511	4511	4495	4495	4518
	b_4	−4	−7	−21	7	10
	b_2	111.42	111.40	111.43	111.48	113.06
QWCAV 2011	b_3	1266	1267	1256	1260	1279
	b_4	1776	1776	1400	1836	2102
	b_2	0.29	0.29	0.29	0.29	0.24
QWCAV 2012	b_3	1073	1073	1077	1078	1073
	b_4	50	67	6	64	22

Table 4.1: Values of the multipole RF kick coefficients for the crab cavity prototypes at nominal deflecting voltage: V_{cc}=10 MV in units of $\mathrm{mT/m}^{n-2}$. Calculated using the Lorentz force, Panofsky-Wenzel and Helmholtz decomposition methods at a radius of either 10 mm or 20 mm.

4.3 Comparing thin models with the Taylor map

The terms of the Taylor map can be directly compared to the three cavity models described in sections 4.1.1, 4.1.2 and 4.1.3.

Considering the simple thin kick model, as described in section 4.1.1, a comparison with the Taylor map has already been made in section 3.3 in table 3.1. It was shown that there was good agreement in the p_x and p_y dependencies upon the canonical variables. However, averaging over the Hamiltonian leads to the removal of additional terms in the spatial functions resulting from the longitudinal kick variation of the cavity. This longitudinal kick variation was observed in the numerical integration through the cavity shown in figure 3.19. In this figure it was shown that additional displacement arose from the time integrated momentum being different between the positive and negative transverse kicks. Furthermore it was shown in table 4.1 that higher order multipoles do exist indicating the limitations of this model.

The RF multipole kick model, as described in section 4.1.2, can be directly compared with the Taylor map. In applying a Taylor expansion to the transverse kick terms described in equation 4.46, it is possible to match terms with those of the Taylor map. The transverse kicks of the RF multipole kick model are given by,

$$p_x \mapsto p_x + \frac{q}{p_0}\sin\left(k_l z + \Phi_l\right)\sum_{n=1}^{N}\Re\left[\left(b_n^{(l)} + \mathrm{i}a_n^{(l)}\right)(x+\mathrm{i}y)^{n-1}\right], \tag{4.80}$$

$$p_y \mapsto p_y - \frac{q}{p_0}\sin\left(k_l z + \Phi_l\right)\sum_{n=1}^{N}\Im\left[\left(b_n^{(l)} + \mathrm{i}a_n^{(l)}\right)(x+\mathrm{i}y)^{n-1}\right]. \tag{4.81}$$

The nominal phase for a crab cavity is $\Phi_l = 0$. By using the Taylor series of a

sine function,

$$\sin(x) = \sum_{n=0}^{\infty} \frac{(-1)^n}{(2n+1)!} x^{2n+1}, \tag{4.82}$$

the Taylor series expansions for equations 4.80 and 4.81 are given by,

$$p_x \mapsto p_x + b_1 \frac{q}{p_0}\frac{\omega}{c} z + b_2 \frac{q}{p_0}\frac{\omega}{c} xz + b_3 \frac{q}{p_0}\frac{\omega}{c} x^2 z - b_3 \frac{q}{p_0}\frac{\omega}{c} y^2 z + \ldots \tag{4.83}$$

$$p_y \mapsto p_y - b_2 \frac{q}{p_0}\frac{\omega}{c} yz - b_3 \frac{q}{p_0}\frac{\omega}{c} 2xyz + b_3 \frac{q}{p_0}\frac{\omega}{c} y^3 z + \ldots \tag{4.84}$$

From this expansion equivalent terms can be directly compared with the Taylor map. From the coefficients of these terms an equivalent multipole coefficient can be calculated. For example, from the first multipole term in equation 4.83 the equivalent b_1 can be calculated such that,

$$b_1 = \frac{cp_0}{q\omega} p_x(z), \tag{4.85}$$

where $p_x(z)$ is the Taylor map term referring to the z dependence of p_x. A first comparison made use of the p_x terms with the highest power in x and first order dependence in z. However, these are not unique terms from which to extract the multipole coefficients. In table 4.2 the results of this comparison show that to three significant figures the dominant multipoles (b_1, b_3 and b_5) agree between the multipole calculation and Taylor map terms. This would imply a significant agreement between the Taylor map model and the RF multipole model. However, there are some differences present, for example for b_3 there is a 0.07% difference, suggesting that there is not absolute agreement in the p_x and p_y descriptions of the two models.

Multipole coefficient	Terms used	Taylor map	RF multipole
b_1	$p_x(z)$	$3.333 \times 10^{+1}$	$3.333 \times 10^{+1}$
b_2	$p_x(xz)$	7.362×10^{-2}	7.386×10^{-2}
a_2	$p_x(yz)$	-3.308×10^{-2}	-3.313×10^{-2}
b_3	$p_x(x^2z)$	$9.055 \times 10^{+2}$	$9.062 \times 10^{+2}$
a_3	$p_x(xyz)$	-1.845×10^{0}	-0.917×10^{-1}
b_4	$p_x(x^3z)$	3.078×10^{0}	$2.565 \times 10^{+0}$
a_4	$p_x(x^2yz)$	$6.106 \times 10^{+2}$	$2.033 \times 10^{+2}$
b_5	$p_x(x^4z)$	$-2.395 \times 10^{+6}$	$-2.399 \times 10^{+6}$
a_5	$p_x(x^3yz)$	$-5.949 \times 10^{+4}$	$-1.485 \times 10^{+4}$

Table 4.2: Comparison of multipole coefficients derived from Taylor map terms and the RF multipole calculation using the Helmholtz decomposition at 20 mm result. Coefficients in units of mT/m^{n-2} at 10 MV.

Table 4.3 shows the extension of this study to consider all the Taylor map terms containing b_3 with a first order dependence in z. It can be seen that the result of $p_x(x^2z)$ differs to that of $p_x(y^2z)$ and $p_y(xyz)$. This further indicates that there is not absolute agreement in the p_x and p_y descriptions of the two models.

Multipole coefficient	Terms used	Taylor map	RF multipole
b_3	$p_x(x^2z)$	$9.055 \times 10^{+2}$	$9.062 \times 10^{+2}$
b_3	$p_x(y^2z)$	$9.061 \times 10^{+2}$	$9.062 \times 10^{+2}$
b_3	$p_y(xyz)$	$9.061 \times 10^{+2}$	$9.062 \times 10^{+2}$

Table 4.3: Comparison of b_3 derived from Taylor map terms and the RF multipole calculation using the Helmholtz decomposition at 20 mm result. Coefficients in units of mT/m at 10 MV.

Although table 4.2 shows reasonable agreement between the Taylor map and the RF multipole kick model it is evident that there are definite differences. From the generalised RF multipole kick model (as presented in section 4.1.3) a similar

Taylor expansion can be made to express the transverse kicks in the form of a Taylor series. In this expansion there is no longer a one to one correlation between multipole coefficients and Taylor map terms and hence a series of simultaneous equations must be solved in order to calculate the effective multipoles. For example, there are three terms in which the $b_{3,0}$ generalised multipole coefficient appears,

$$\begin{aligned} p_x(x^2z) &= \frac{q}{p_0}\frac{\omega}{c}\left(b_{3,0} + 3b_{1,1}\right), \\ p_x(y^2z) &= -\frac{q}{p_0}\frac{\omega}{c}\left(b_{3,0} - b_{1,1}\right), \\ p_y(xyz) &= -\frac{q}{p_0}\frac{\omega}{c}2\left(b_{3,0} + b_{1,1}\right), \end{aligned} \tag{4.86}$$

where $p_x(x^2z)$ is the Taylor map term corresponding to the x^2z dependence of p_x. Equation 4.86 indicates that the value of b_3 calculated in table 4.2 is in fact equal to $b_{3,0} + 3b_{1,1}$. In table 4.4 the results of this method for a number of generalised RF multipole coefficients is shown and compared with the coefficients calculated using the generalised gradients from equation 4.53. It can be seen that there is good agreement in the $b_{n,0}$ terms and that from the scaled values they contribute approximately 1% of the dipole kick at $x = 20$ mm. The higher order terms ($b_{1,1}$, $b_{1,2}$ and $b_{3,1}$) contribute at the level of 0.001% of the dipole kick. It can be seen that that for the $b_{1,1}$, $b_{1,2}$ and $b_{3,1}$ coefficients that the values between the Taylor map and Helmholtz decomposition are completely different. This indicates that the generalised RF multipole kick model does not correctly describe the beyond RF multipole kick model dynamics for the p_x and p_y transformations contained within the Taylor map.

Considering the case of $b_{3,0}$ terms, there are three Taylor map terms containing $b_{3,0}$; shown in equations 4.86. Comparing the solutions using the different arrangements of these simultaneous equations, shown in table 4.5, the relation

	Terms used	Taylor map		Helmholtz decomposition	
		Value	Scaled [10^{-4}]	Value	Scaled [10^{-4}]
$b_{1,0}$	$p_x(z)$	33.333	10000.0007	33.333	10000.000
$b_{1,1}$	$p_x(x^2z)$, $p_x(y^2z)$	-0.146	-0.017	-0.438	-0.052
$b_{1,2}$	$p_x(x^4z)$, $p_x(y^4z)$, $p_y(x^3yz)$	668.523	0.032	-123.657	-0.006
$b_{3,0}$	$p_x(x^2z)$, $p_x(y^2z)$	905.977	108.717	906.178	108.741
$b_{3,1}$	$p_x(x^4z)$, $p_x(y^4z)$, $p_y(x^3yz)$	-121.248	-0.006	-221.112	-0.011
$b_{5,0}$	$p_x(x^4z)$, $p_x(y^4z)$, $p_y(x^3yz)$	-2.399×10^6	-115.152	-2.399×10^6	-115.152

Table 4.4: Generalised multipole coefficients calculated from the Taylor map and Helmholtz decomposition. Coefficients in units of $\mathrm{mT/m}^{n+2m-2}$ for $b_{n,m}$, normalised to 10 MV. Where the scaled value is given by $(b_{n,m}/b_{1,0}) \times (20\ \mathrm{mm})^{n+2m-2}$

between the Taylor map and generalised multipoles is no longer so clear. This suggests that there are other physical effects that feature in the Taylor map at the same level of impact as the generalised RF multipoles where $m > 0$ for $b_{n,m}$. Therefore the application of generalised RF multipoles for the HL-LHC case appears inappropriate in that there is ambiguity with the Taylor maps at the level of the additional dynamics which they would provide.

	Terms used	Taylor map	Scaled [10^{-4}]
$b_{1,1}$	$p_x(x^2z)$, $p_x(y^2z)$	-0.146	-0.018
$b_{3,0}$	$p_x(x^2z)$, $p_x(y^2z)$	905.977	108.717
$b_{1,1}$	$p_x(x^2z)$, $p_y(xyz)$	-0.293	-0.035
$b_{3,0}$	$p_x(x^2z)$, $p_y(xyz)$	906.415	108.770
$b_{1,1}$	$p_x(y^2z)$, $p_y(xyz)$	-9.720×10^{-8}	-1.166×10^{-8}
$b_{3,0}$	$p_x(y^2z)$, $p_y(xyz)$	906.123	108.735

Table 4.5: Variation in generalised multipole coefficients calculated from the Taylor map. Coefficients in units of $\mathrm{mT/m}^{n+2m-2}$ for $b_{n,m}$, normalised to 10 MV. Where the scaled value is given by $(b_{n,m}/b_{1,0}) \times (20\ \mathrm{mm})^{n+2m-2}$

4.4 Conclusion

The symplectic thin models remove the need to consider the impact of symplectic error making them a preferred option over Taylor maps to model the crab cavities

for long term tracking. Three different thin models have been shown with various assumptions leading to varying levels of model complexity. Methods to calculate the multipole coefficients which parametrise these models directly from the fields by assuming the rigid bunch and axial approximations have also been shown. It has been shown that between the different methods there is a difference of approximately 1% in the multipole values. It has also been shown that the RF multipole kick model changes the kicks by approximately 1% of the total kick from the simple kick model at $x = 20$ mm. Furthermore, it has been shown that the additional terms of the generalised RF multipole kick model change the kicks by approximately 0.001% of the total kick from the simple kick model at $x = 20$ mm.

Taylor maps have been used as a cross check with these thin models by using a technique to extract the multipole values from them. It has been shown that there is reasonable agreement between the Taylor map and RF multipole method for the descriptions of the x and y dependence on p_x and p_y with a 0.07% disagreement in the b_3 value for the 4RCAV 2011 design, between the Taylor map and Helmholtz decomposition values. A more complex description of the p_x and p_y dependence on x and y is required to describe that which is contained within the Taylor map. The generalised RF multipole kick model did not provide a suitable description for the beyond RF multipole description found in the Taylor map. It can be concluded that of the available symplectic models the RF multipole kick model is the most practical choice of crab cavity model.

Chapter 5

Dynamic aperture with crab cavities in the HL-LHC

Chapter 2 showed that non-linearities can lead to chaotic motion in an accelerator, with some of this chaotic motion leading to unstable motion in which particles become lost on restrictive apertures. Chapters 3 and 4 showed that the crab cavity itself exhibits non-linear dynamics. In this chapter these two findings are combined to consider the impact of the crab cavities on the HL-LHC.

Dynamic aperture provides a means to understand the impact of non-linear behaviour upon the stability of an accelerator, as discussed in section 2.2.3. A further tool available to study the non-linear behaviour of an accelerator is frequency map analysis, also discussed in section 2.2.3, which considers the mechanisms underlying any non-linear behaviour. In this chapter these two methods are used to consider the impact of the crab cavities.

In chapters 3 and 4 a variety of models of the crab cavity were introduced. Three models of the crab cavities are used in this chapter. The two symplectic thin lens models considered for use in these studies are the simple kick model (section 4.1.1) and the RF multipole kick model (section 4.1.2). The Taylor maps were shown to contain dynamics beyond these simple kick models, however, they

also exhibited symplectic errors. The Taylor maps continue to be used as a model of the crab cavities in this chapter.

In this chapter, section 5.1 details the HL-LHC model created in SixTrack [145] within which the crab cavities are installed. In sections 5.2.1 and 5.2.2 the techniques of dynamic aperture and frequency map analysis are used to consider the impact of the crab cavities, modelled using the simple kick model, on the HL-LHC. In section 5.2.3 the impact of the transverse dependence of the crab cavity kick on the HL-LHC is investigated using the three different cavity models. This section seeks to answer the question over which components of the crab cavity dynamics are important when studying long stability in the HL-LHC.

5.1 SixTrack

SixTrack is a suite of programs used to perform single particle tracking, in particular for dynamic aperture studies [145]. It uses a 6D thin lens tracking algorithm [128] for all the accelerator elements, with a symplectic treatment of synchrotron motion [50]. This creates a numerically stable model of the HL-LHC which neglects any dynamics beyond that of the thin lens approximation. In these dynamic aperture studies magnet multipole errors are included, and a series of points in transverse action phase space are evaluated to determine the dynamic aperture.

5.1.1 Lattice input and magnet errors

The lattice used for these studies was the SLHC v3.1b lattice [68]. This uses the ATS scheme [146], as previously discussed in section 2.3, with inner triplet quadrupole magnets which have an aperture of 150 mm. From this lattice sequence, for these studies, a β^* of 15 cm with round beams was considered at the

two low-β IPs (IP1, IP5) and β^* of 10 m at IP2 and IP8. The corresponding unperturbed betatron tune for Q_{x0} and Q_{y0} were set to 62.31 and 60.32 respectively.

The lattice input begins in the form of thick elements, which have associated lengths. This can not be made directly into a thin element lattice due to the need to preserve optical parameters (e.g. tune, chromaticity, β-function etc.). Figure 5.1 shows the β-function around the whole of the lattice. The lattice undergoes a series of matching routines to preserve the twiss parameters and tune advances around the ring. This is performed using matching routines built into the accelerator design program MADX [114], which performs the numerical search of parameters required to convert from the thick to the thin lattice whilst preserving the optical properties of the ring.

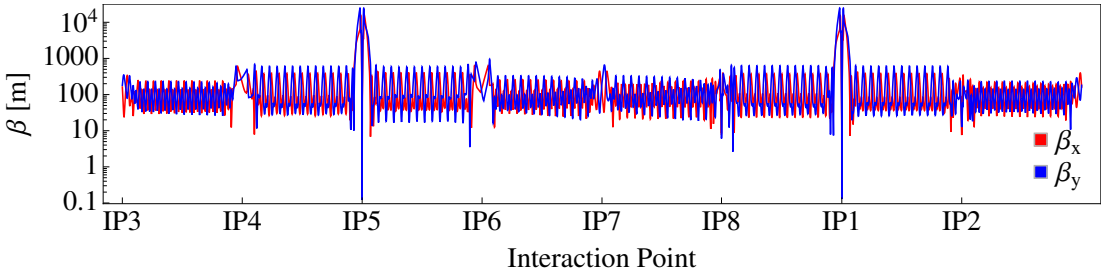

Figure 5.1: β-function around the complete SLHC v3.1b lattice [68].

In MADX kicker magnets at $z = 1\sigma_z$ of the bunch length are used instead of crab cavities. The voltages for the cavities are determined from the linear optics across the crab bump, given by the relations in equation 2.74 and 2.75, and calculated using the dipole kicker magnets placed between D2 and Q4 (see figure 2.26b). When using the Taylor maps the elements are added later by directly replacing each crab cavity element in the SixTrack lattice input files with sets of anti-drifts and Taylor maps. The matching and addition of crab cavities produces a thin lens lattice with crab cavities.

Magnet field errors are applied in the form of magnetic multipoles up to the

15^{th} order multipole. Estimates of errors arising from measurements and uncertainty are applied to the bending arc dipoles and the arc quadrupoles. Simulated estimates of errors for the inner triplet quadrupoles (Q1, Q2, Q3), separation dipoles (D1, D2), and matching quadrupoles (Q4, Q5) also exist. However, at the time of writing these errors remained under study and therefore were not used. A set of 60 different combinations of the errors in the bending arc dipoles and the arc quadrupoles were used to create 60 variants of the lattice. These 60 combinations were produced using a program called WISE [147], which incorporates all known uncertainties in the magnet error measurements. Many of the magnet error measurements of the superconducting magnets were only performed in warm conditions with low currents leading to an uncertainty in the magnet errors under operational conditions. A small set of these magnets were also measured in cold conditions with operational current. A linear model was assumed and fitted to these few cases in order to provide an estimation of the magnet errors for all the magnets under operational conditions [148, 149]. In WISE it is also assumed that the measured multipole magnet errors will form a Gaussian distribution from which magnet error values can be randomly chosen for each lattice variation. 60 random variants of the lattice, calculated using 60 seeds, are deemed sufficient from dynamic aperture considerations to gain a 95% certainty in the dynamic aperture [150]. The 60 seeds are common to all of the dynamic aperture simulations studied. Correction magnets are applied to remove any orbit distortion introduced by the magnet errors using matching routines. Further adjustments of the correction magnets are performed in order to recover the nominal optical parameters lost through the magnet errors. From this final set of matched thin lattices 60 sets of SixTrack input files are created.

5.1.2 Tracking

From the lattice files, computed with MADX, numerical tracking is performed using SixTrack. The tracking study begins with two one turn map calculations [50], from which the β-function values, chromaticity, tune and closed orbit are calculated and normal form analysis performed. The closed orbit is the point in phase space where it is assumed the orbit remains constant and stable, and is the reference point from which the dynamic aperture is defined. The closed orbit, defined by a single point in phase space X_0, can be found directly from the one turn map $\mathcal{M}$ by solving,

$$X_0 = \mathcal{M}(X_0). \tag{5.1}$$

The transverse phase space is scanned about the closed orbit using action-angle variables. This is broken down in terms of the ratio between horizontal and vertical actions defined by,

$$\theta = \arctan\left(\frac{I_y}{I_x}\right), \tag{5.2}$$

where I_x and I_y are the non-linear action, with θ scanned linearly across $0^\circ < \theta < 90^\circ$. It is only necessary to scan across initial action and not the corresponding initial angle due to the periodicity of a stable orbit in the non-linear action-angle phase space [145]. Amplitude is measured in units of σ where 1σ is the transverse RMS value of an assumed Gaussian shaped bunch. The range of amplitudes over which the dynamic aperture is scanned is user defined in SixTrack. In these studies the amplitude range is broken down into blocks of 2σ, over which 30 particles are tracked, and evenly distributed in amplitude over the 2σ step. For these cases only beam one in a clockwise direction is considered, it is assumed that the dynamic aperture of beam two would be identical. However, this is not the case in the real machine which has differing magnet errors.

The dynamic aperture is the greatest surviving averaged amplitude for 10^5 turns; given that the rotation frequency of the LHC is 11 KHz this is equivalent to 9 seconds of beam time. With this number of turns it is considered that the result is convergent on the dynamic aperture within the other uncertainties of the calculation [145] (where beam-beam interaction is not considered). This number of turns is considered the standard in terms of LHC dynamic aperture studies. This choice partially arises from computational considerations as the change in dynamic aperture with turn rapidly decreases with turn number hence for a considerable increase in computation time little will be gained. It is considered that the safety margin at collision for the dynamic aperture at 10^5 turns should be double the aperture of the collimation system which is 6σ [151]. From the phase space averaged amplitudes $\langle x - x_0 \rangle$ and $\langle y - y_0 \rangle$, which are averaged over 10^5 turns, where (x_0,y_0) is the position of the closed orbit, the dynamic aperture is defined by,

$$\mathrm{DA}[\sigma] = \sqrt{\left(\frac{\langle x - x_0 \rangle}{\sqrt{\frac{\epsilon^*}{\beta_0 \gamma_0} \beta_x}} \right)^2 + \left(\frac{\langle y - y_0 \rangle}{\sqrt{\frac{\epsilon^*}{\beta_0 \gamma_0} \beta_y}} \right)^2} \tag{5.3}$$

in units of 1 σ where $\epsilon^* = 3.75$ mm mrad is the normalised emittance, β_0 and γ_0 are relativistic factors, $\beta_{x,y}$ are the β functions at the point of measurement. The minimum dynamic aperture is defined by the minimum value at each angle in phase space over the 60 lattice variations.

5.1.3 SixTrack uncertainties

Many considerations are included in the determination of the dynamic aperture using the method outlined in the previous sections. However, there are some uncertainties which remain unaccounted for in its calculation. These uncertainties in SixTrack calculations can be split into 3 classes; scanning of the phase space, numerical tracking through the machine and lattice uncertainty.

The finite step size in phase space angle θ generates an uncertainty in the minimum dynamic aperture value due to the unknown behaviour of the dynamic aperture between these θ values. The magnitude of this variation is dependent upon the lattice and step size. The number of angles used for crab cavity studies was increased from 5 to 19 angles, this leads to an uncertainty in the minimum dynamic aperture of 0.5σ [152], as shown in figure 5.2. To reduce this uncertainty further would have required a significant increase in the number of computations.

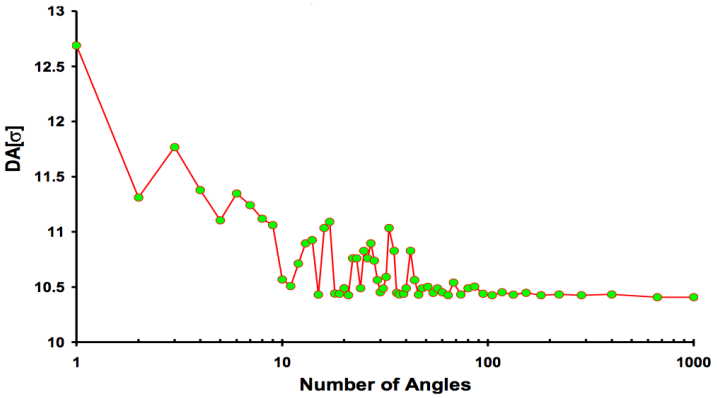

Figure 5.2: Minimum dynamic aperture as a function of number of phase space angles [152].

The finite step size in amplitude brings about an uncertainty on the dynamic aperture. Close to the chaotic boundary stable islands form which are not included in the hypersphere of the dynamic aperture. If the amplitude step size is too large it is possible that a stable island will be included in the measurement of dynamic aperture. In [153] a study was performed which it observed that there was no impact on the dynamic aperture from changing the step size from $(2/30)\sigma$ to $(0.5/30)\sigma$. For this reason $(2/30)\sigma$ is chosen as the step size over which the amplitude is varied.

The numerical tracking through the machine has two uncertainties: the numerical stability of the tracking and the physics included in the simulation. In

order to retain numerical stability SixTrack's integration methods are symplectic. This symplecticity is achieved by applying the thin lens approximation to the accelerator Hamiltonian [128]. However, the resulting transformations introduce unphysical non-Maxwellian fields, e.g. the instantaneous field drop off at the edge of a magnet [154]. In [95] additional tune shift with amplitude was observed as a result of the inclusion of fringe fields into the nominal LHC model. A more physically correct, computationally slower [141], thick quadrupole model can be used instead of a series of thin lens quadrupoles to model a quadrupole in SixTrack. In [141] it was found that this thick model lead to a maximum variation in the minimum dynamic aperture across 60 lattice variations of approximately 4% between the two models for the nominal LHC lattice. A further physical uncertainty lies in the modelling of the beam-beam effect which is very complex and hard to calculate [34]. A number of approximations can be made in order to simplify the computations and avoid large multi-particle simulations. Numerical uncertainties are introduced in long term tracking studies from rounding errors produced by using numbers of finite precision [137]. These prevent very long term tracking ($> 10^7$ turns) over which any extremely slow loss mechanisms might also be observed [49].

The final type of uncertainty is that of lattice uncertainty. The errors in the real magnets installed in the machine will differ depending on whether the magnetic field components were measured under warm or cold conditions, or at low or high current [148, 149]. A linear model was made between warm magnetic multipole coefficients and cold (1.9 K) coefficients. Due to the time constraints only a small number of magnets were measured for both warm and cold conditions, with the rest only measured in warm conditions, with their cold magnet errors calculated using the linear model. This leads to an uncertainty in the magnet error tables. An attempt to account for this is made by having 60 lattice variants which

then defines the dynamic aperture as a range of values. Taking the minimum of this range results in a worst case scenario based upon these 60 variants. For a tolerance study, such as looking at the worst possible impact from the crab cavities, this minimum dynamic aperture is the best measurement to consider. Further uncertainties are introduced into the magnet error tables through errors in the measurement methods. The magnetic hysteresis due to the iron yoke and persistent currents in superconducting magnets lead to further uncertainties in the magnet fields [155]. Only some hysteresis induced errors are taken into account in the magnet error tables leading to further uncertainty.

5.2 Dynamic aperture studies

The introduction of crab cavities presents many unknowns into the long term stability of the machine. Preliminary studies performed [74] focussed on both a local and global crab crossing scheme. However, these studies were only carried out using the simple kick model and used an old version of the lattice layout.

These studies were performed using the SLHCv3.1b [68] optics with crab cavities. From the available magnet errors only the arc dipole and arc quadrupole multipole errors were included. Beam one (in a clockwise direction) was studied at collision, with a beam energy of 7 TeV and with beam crossing at IP1, IP2, IP8 and IP5. The simulations did not consider beam-beam interaction as this was known to dominate the dynamic aperture and make it difficult to disentangle any effects of the crab cavities. Furthermore, beam-beam would have required longer simulations. The simulations were performed with synchrotron oscillations using a momentum offset of 3/4 of the bucket half-height, which was chosen to be consistent with previous calculations and to allow potential sensitivity to chromatic and synchro-betatron effects [153].

The main focus of these dynamic aperture studies has been on the non-linear

transverse kick which is a result of the compact geometry of the cavity designs. In previous work performed using the RF multipole kick model [156] it was found that the introduction of a b_2 RF multipole component to the transverse kick led to a tune shift in the horizontal-horizontal crossing case which had a detrimental effect on the dynamic aperture. This discovery led to a redesign of the QWCAV to remove the asymmetric geometry introduced by the quarter wave resonator, leading to a geometry resembling a half wave resonator. This study illustrated the importance of understanding the non-linear transverse kick of the crab cavities.

In addition to the effect of the non-linear transverse kick there are other areas of interest regarding the dynamics associated with the crab cavities including: The linear kick, RF noise related to the power system, beam loading of non operating modes and geometric misalignment in the cryostat. The linear transverse kick of the crab cavity is studied along with the voltage error using the simple thin crab cavity model presented in section 4.1. Furthermore using this model an understanding of the resonance mechanisms caused by the crab cavities is considered using frequency map analysis. Studies on the impact of RF noise, geometric misalignments and beam-loading are beyond the scope of these studies.

5.2.1 Impact of the simple thin crab cavity model

The initial dynamic aperture studies used the simple kick model, described by the transformation in equation 4.26, to consider the impact of the time dependent dipole kick. The crab cavities were modelled as 3 individual cavities with a separation of 2 cavity lengths between each cavity kick. The voltages were calculated using MADX [114] as described in section 5.1.1. The calculated voltages for the cavities are shown in table 5.1.

Figure 5.3 shows the dynamic aperture result of applying these voltages to the crab cavities in the lattice. It shows an insignificant change in the minimum of the

	Cavity voltage (MV)	
	Left	Right
IP1 (Vertical crossing)	4.07233	3.83833
IP5 (Horizontal crossing)	3.81933	4.15500

Table 5.1: Cavity voltages (MV) for the Horizontal-Vertical crossing scheme for optics SLHCv3.1b beam 1 clockwise direction, based on 3 cavities at each crabbing location.

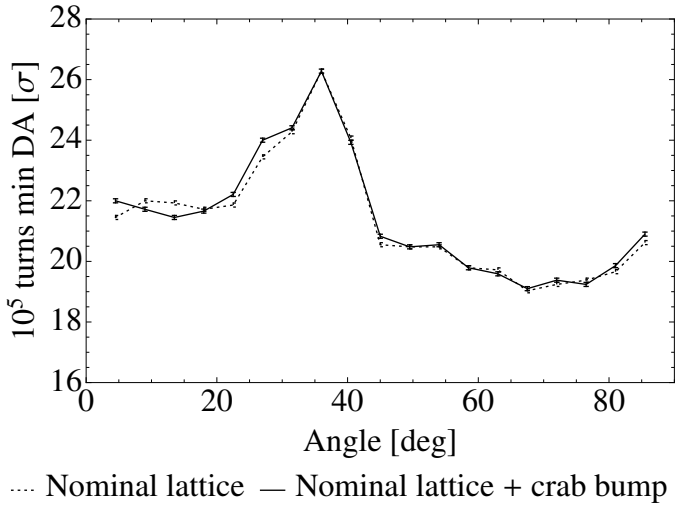

Figure 5.3: Impact of the addition of a closed crab bump on the minimum dynamic aperture determined from 60 variants of the lattice.

minimum dynamic aperture, which is at the order of the steps in amplitude, with an overall maximum difference of less than 0.5σ. While the minimum dynamic aperture provides a method to determine the worst case boundary of machine stability it does not indicate the mechanisms leading to any instabilities.

An operational consideration with the crab cavities is the impact of voltage error. In [157] it is stated that the low level RF systems in the LHC should be able to control the voltage jitter to within 0.1% of the total voltage. Such voltage jitter would break the closure of the crab bump, leading to possible head-tail oscillations of the bunch around the machine. This was studied using the simple

thin kick model. The case of varying the total voltage of the crab cavities left of IP1 up to 1% was considered. Figure 5.4 shows the impact of breaking the crab bump, with voltage error, upon the minimum dynamic aperture. There is no visible detrimental effect within the anticipated performance of the low level RF system; with the maximum variation across phase space being less than 0.5σ.

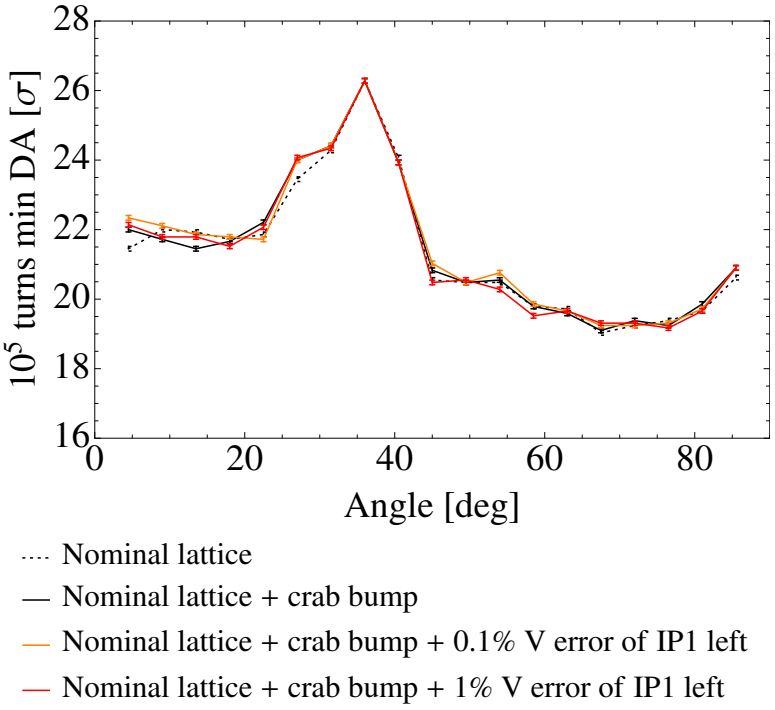

Figure 5.4: Impact of a voltage error to the cavities left of IP1 on the dynamic aperture performed using 60 variants of the lattice.

5.2.2 Resonance studies using the simple thin kick model

It was proposed in [158] that non zero dispersion at crab cavities, in a circular collider, leads to synchro-betatron resonances formed from a closed crab bump, without the effect of any beam-beam interaction. The arguments made in [158] are for a simpler case (a singular crab bump which is symmetric such that the voltages are identical either side of the IP), however it provides a motivation

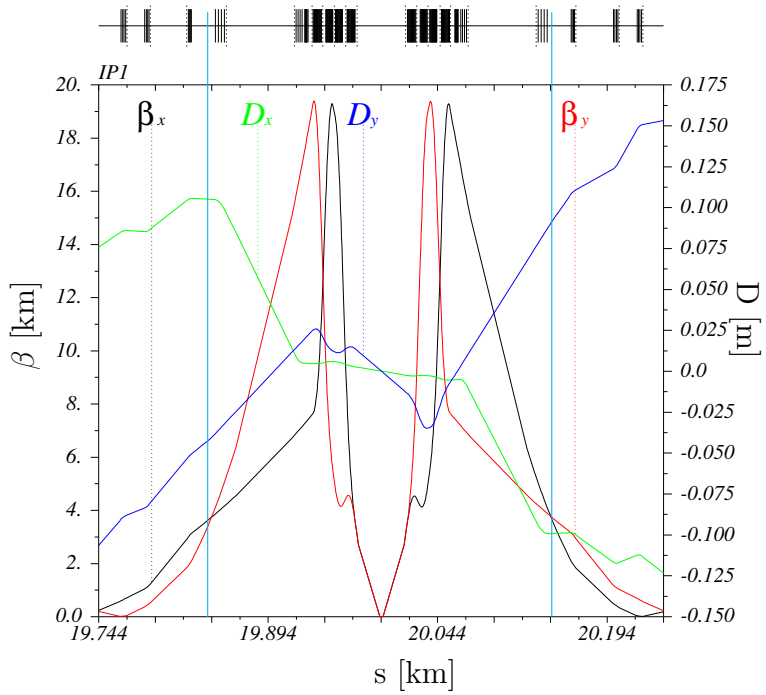

Figure 5.5: The dispersion D, and β functions about IP1, with crab cavities located about 19.83 km and 20.15 km (marked with blue vertical lines), for the bare lattice.

to investigate whether or not the closed crab bump leads to synchro-betatron resonances for the SLHC v3.1b optics. In figure 5.5 the dispersion about IP1 is shown to be non zero at the crab cavity locations. This generated interest in whether such synchro-betatron resonances formed in these optics as a result of the crab cavities. For these resonance studies the nominal lattice (without magnetic errors) was considered, for the cases with and without the crab bump; the resulting dynamic aperture is shown in figure 5.6.

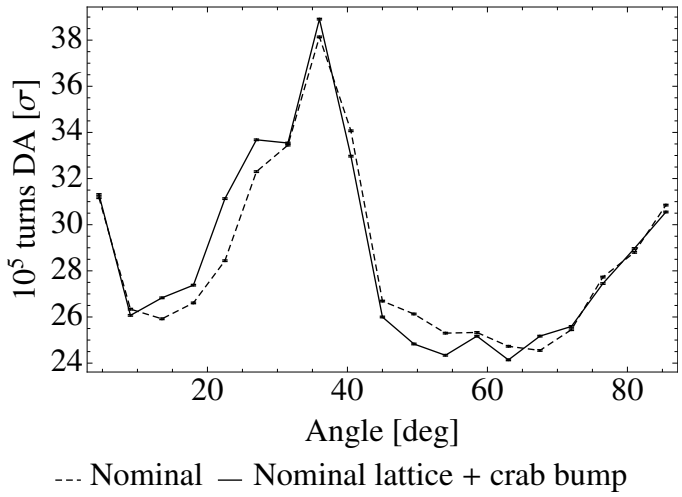

Figure 5.6: Impact of the addition of a closed crab bump on the dynamic aperture performed with an magnet error free lattice.

In order to consider the resonances associated with the lattice it is useful to consider the chaotic motion they generate. A useful tool when considering the chaotic motion of a particle is the diffusion rate, which measures the rate of change in tune. The tunes are calculated from 2000 turns of tracking data using SUSSIX [159], with a Hanning window filter [160] applied to the BPM data to increase the sensitivity of the tune measurement [53, 161]. SUSSIX produces a high precision tune measurement by performing a spectral decomposition of tracking data [159]. From SUSSIX the transverse and longitudinal tunes, Q_x, Q_y and Q_s are calculated and averaged over 10 BPMs to reduce any statistical error

in the tune measurement. The conventional measurement of diffusion rate comes from the difference in tune measurements arising from the first and second half of the tracking data,

$$D = \log_{10}\left(\frac{\sqrt{\Delta Q_x^2 + \Delta Q_y^2 + \Delta Q_s^2}}{N}\right), \tag{5.4}$$

where N is the number of turns ($N = 4000$) and $\Delta Q_{x,y,s}$ are the change in tune between the first 2000 and second 2000 turns.

Amplitude maps consider the diffusion rate as a function of the transverse amplitudes. The amplitude maps in figures 5.7a and 5.7b show the diffusion rates across the amplitude phase space for the cases with and without crab cavities respectively. They show very similar features in the distribution of diffusion with some regions of increased diffusion for amplitudes less than 10σ for the lattice with crab cavities. In figures 5.7c and 5.7d the region in which the linear difference resonance is encountered is highlighted i.e. $Q_x - Q_y = 0$. This is found by filtering the amplitude map for cases where $|Q_x - Q_y| < 10^{-4}$. The dynamic aperture is overlaid on these results, and it can be seen that in this region of linear difference coupling that there is a significant increase in stability compared with the rest of the phase space. Physically the linear difference coupling resonance is stable because it leads to an exchange of emittance in the transverse planes which are constrained such that [32, p. 625],

$$\varepsilon_x + \varepsilon_y = \text{const.} \tag{5.5}$$

Particles on this resonance can still be lost when other resonances cross the linear difference resonance, as shown in the tune diagram in figure 2.17. Other resonances lead to beam instability as they do not impose such a constraint on the emittance [32]. This region of linear coupling at its lower boundary is bounded

by a fold in frequency space; similar to that shown in figure 2.18 as discussed in section 2.2.3.

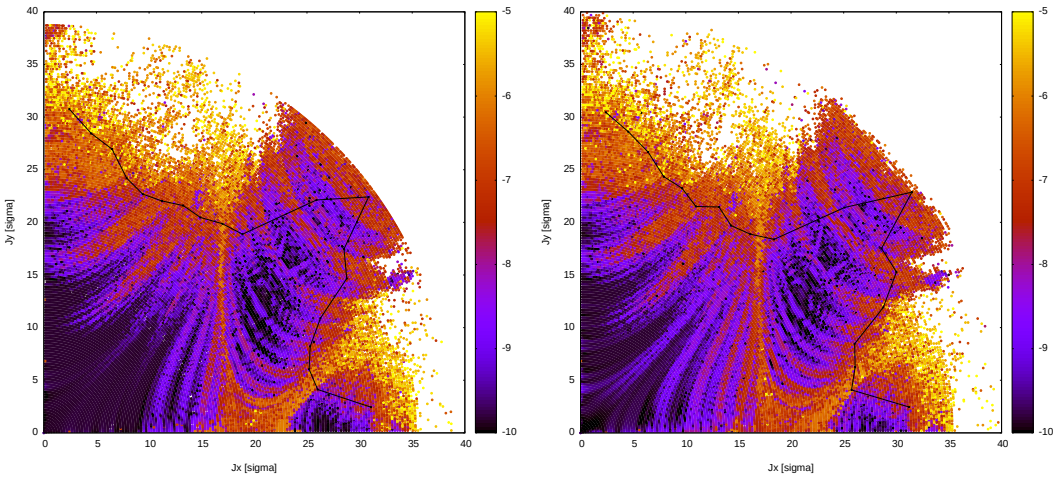

(a) (b)

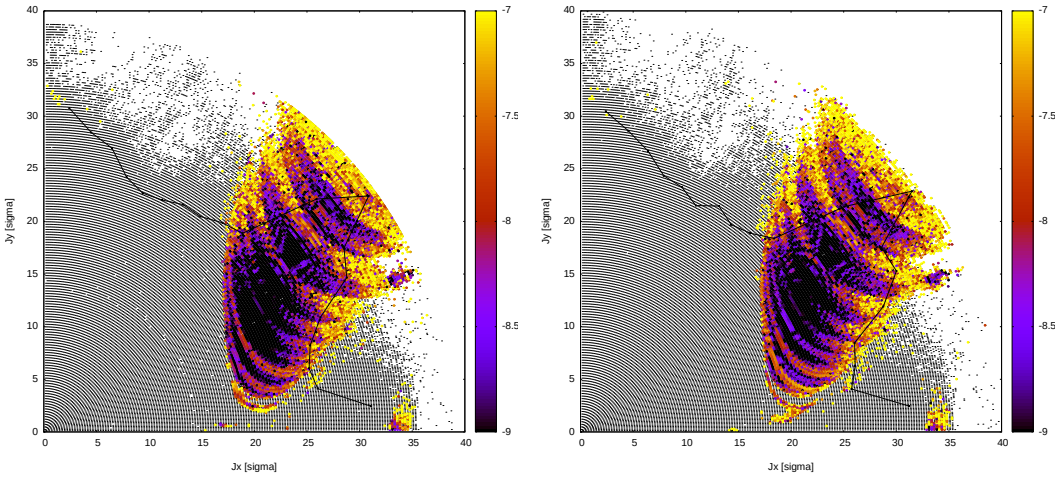

(c) (d)

Figure 5.7: Amplitudes maps with diffusion with dynamic aperture overlaid (black line) for (a) nominal SLHCv3.1b no errors, (b) nominal SLHCv3.1b no errors with crab cavities, (c) nominal SLHCv3.1b no errors with transverse linear coupling highlighted, and (d) nominal SLHCv3.1b no errors with crab cavities with transverse linear coupling highlighted.

Frequency map analysis (FMA) is a numerical tool typically intended for 4D systems in which betatron resonances are studied (see section 2.2.3) [53]. FMA considers the chaotic motion of a particle starting at a given point in phase space in terms of its tune. It has already been shown that amplitude dependent tune shift can occur in section 2.2.3 and this mechanism leads to the formation of the frequency map. As the frequency map expands with amplitude, away from the working point, particles will encounter resonances, some of which will lead to unbounded motion.

Previous studies [48, 47] for the LHC have only considered 4D motion; thereby seeking to keep the particle energy constant in tracking. Inclusion of synchrotron motion and crab cavities requires the technique to be extended to consider a full 6D system, in which the canonical variables z and δ are included. In order to do this a new time dependent method of the frequency map analysis was developed. Time is no longer an independent variable in the resulting extended frequency space. Synchrotron motion will couple with the betatron motion such that synchro-betatron resonances will occur. This means that the measured betatron tunes will undergo an additional time dependence beyond that associated with diffusion associated with the synchrotron motion. This means that the frequency map must be time dependent. This technique was developed for this study, based upon the idea of using a moving time window to calculate the tunes at different turns. A total of ten BPMs were placed with approximately equal separation about the machine. The 2000 turn window is shifted by a single turn and the measurement is then repeated, producing a total of 2000 averaged tune measurements from a total of 4000 turns of tracking data.

Figure 5.8 shows the frequency map for one instance in time, for the lattice with crab cavities. In the figure two folded regions are highlighted [48]. In figure 5.10 it can be observed that these are folds in that they exhibit high levels of

diffusion with resonances formed either side them. A fold in the frequency map occurs when the betatron tune no longer increases with transverse amplitude in either plane, but instead folds in on itself. These folded regions often lead to unbounded motion [48] and were studied in order to understand the stability associated with the linear difference resonance observed in figure 5.7d. The region with the linear difference resonance, shown in figure 5.7, occurs after the fold shown in the red region. The green fold transitions onto a different set of resonances.

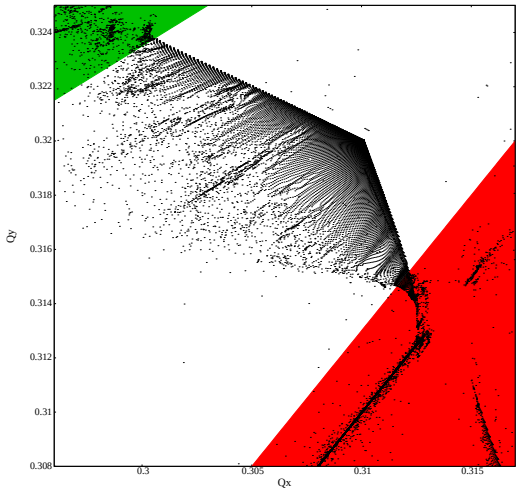

Figure 5.8: Regions indicating folds in the frequency map, leading to resonances. Frequency map with crab cavities taken from turn 1.

In order to determine the nature of a fold a torsion matrix can be found to describe the type of fold [48], as described in section 2.2.3. This torsion matrix, for this study, is determined by creating multidimensional interpolations of variation of Q_x and Q_y with J_x and J_y using Mathematica [105]. From these functions the torsion matrix can be directly evaluated for any point in amplitude space. Furthermore, since the corresponding point is known in frequency space the The signature of torsion indicates the type of transition the frequency map has with amplitude at a given point in frequency space and is given by the determinant of

the torsion matrix. In regions of the frequency map where the signature of torsion is less than zero the torsion is said to be non-definite. This means that there is a greater likelihood of unbounded motion through strong resonances [48]. From the interpolated torsion in amplitude space, given that corresponding frequencies are known, the sign of torsion as a function of frequency can plotted. Figure 5.9b shows the signature of torsion over the red fold region seen in figure 5.8. The transition in torsion and folding with amplitude are shown, exhibiting the properties of a double fold, as shown in figure 2.19b. Particles beyond the double fold are less vulnerable to unbounded motion caused by strong resonances compared with those beyond the single fold. This means that the dynamic aperture in this region, in which there is a linear difference resonance, is comparatively larger than that found beyond the other fold (figure 5.13). This then explains the peak observed in the dynamic aperture found in the region of amplitude space where linear coupling occurs.

In order to visualise the time dependent frequency map animations were produced. In figure 5.10 a series of frames from the animated frequency maps are shown for the two lattices. The frames chosen exhibit fast, turn by turn, changes in the tune of a point, which in amplitude space lies on the dynamic aperture, moving from the linear difference resonance to the folded region. There are significant changes in this region of frequency space in the turn by turn measurements, for both cases. Over the entire time period the point moves between the linear difference resonance and other resonances erratically. This motion does not fit with the traditional diffusion measurement, which would miss such turn by turn effects. This motion is chaotic and could easily cause issues for the traditional measurement of diffusion. Such motion has been considered previously in [37] where it was described as tune wandering, and is associated with particles which are slowly lost. This observation from a time dependent frequency map approach

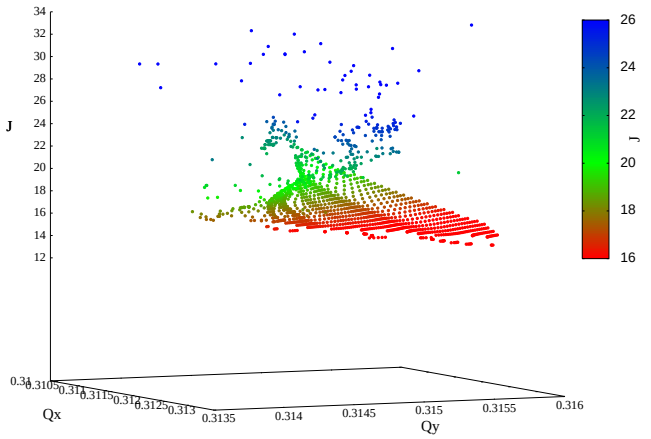

(a)

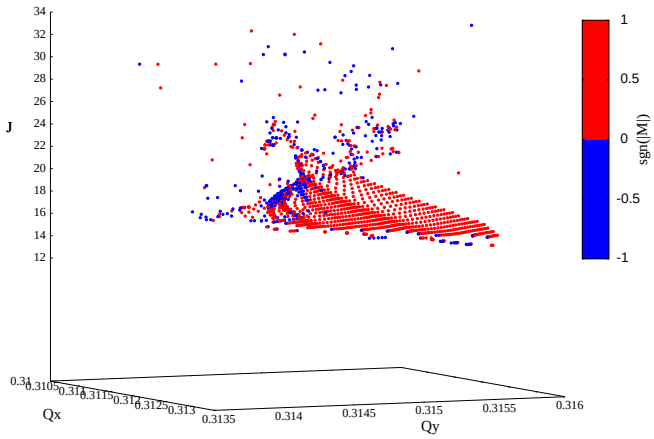

(b)

Figure 5.9: (a) Amplitude (J) dependence across tune space in the region of the fold. (b) Properties of the fold showing transition from definite → non-definite → definite torsion with amplitude.

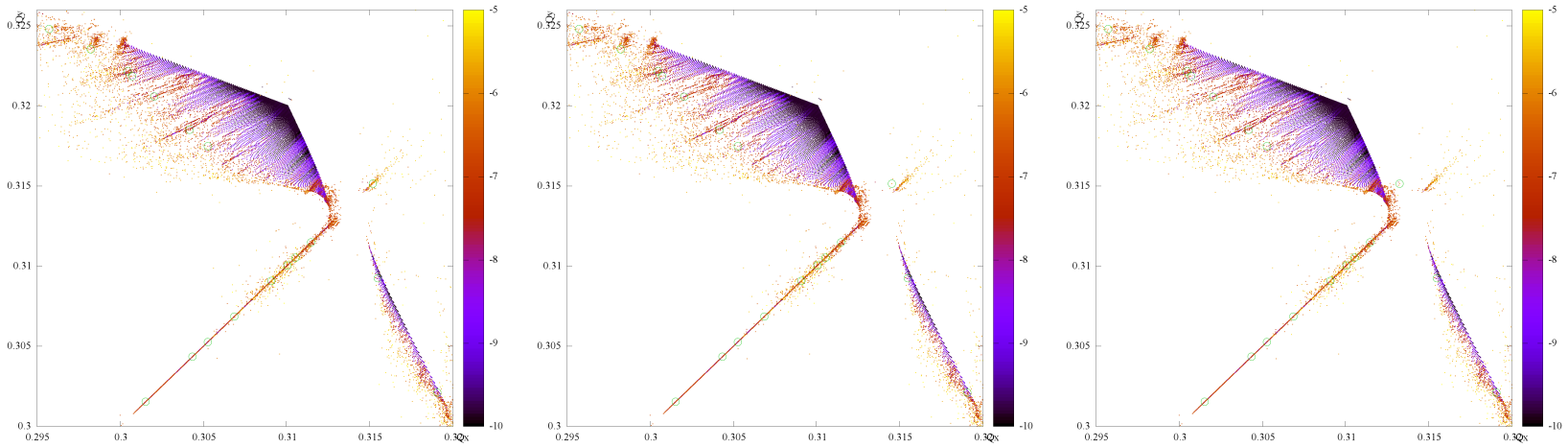

(a) Turn 46 / NOM (b) Turn 47 / NOM (c) Turn 48 / NOM

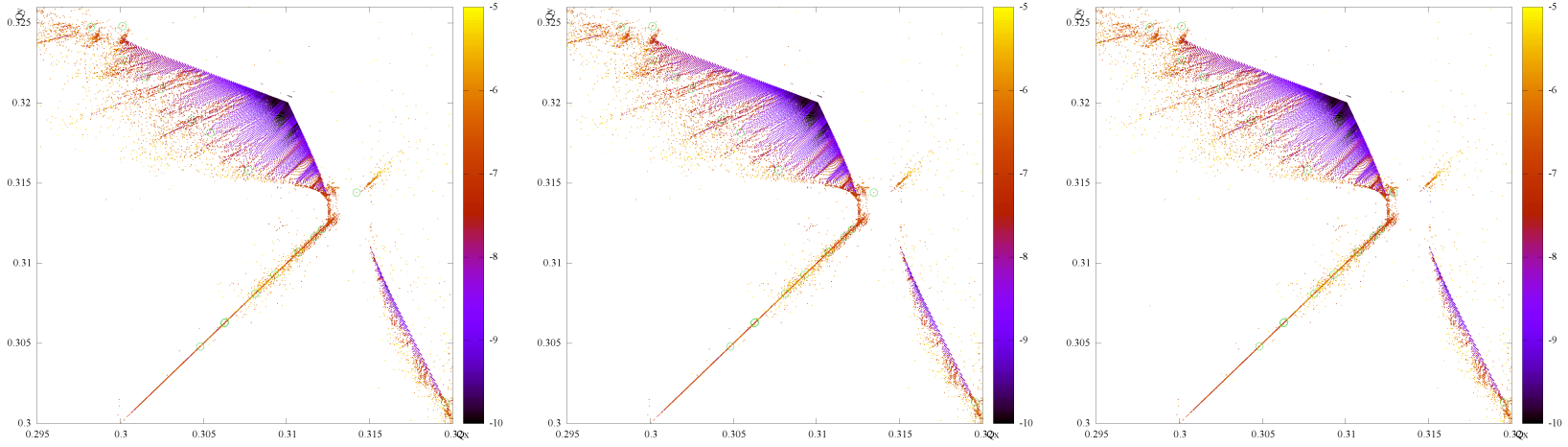

(d) Turn 500 / CC (e) Turn 501 / CC (f) Turn 502 / CC

Figure 5.10: Frames of the time dependent frequency map for (a,b,c) Nominal SLHC v3.1b no errors [NOM] (d,e,f) Nominal SLHC v3.1b no errors with crab cavities [CC]. Points on the dynamic aperture marked with green circles.

presents a new method by which to investigate this behaviour. Further investigation into tune wandering, however, is beyond the scope of this thesis. This tune wandering behaviour inhibits the use of diffusion as a direct measurement for dynamic aperture.

In order to investigate how this resonance wandering impacts the dynamic aperture two variations in the diffusion measurement were considered. The conventional diffusion measurement, as in equation 5.4, is designated D[first-last]. This approach appears to miss any effects that result from variation between measurements observed in figure 5.10. A second proposed method, designated D[max-min], uses the maximum and minimum values across the range of measurements, instead of the first and last, to consider the maximum variation in the tunes.

The amplitude ratio, $\theta = 36°$, was considered first as it coincides with the peak of the dynamic aperture in figure 5.6. A study at this ratio was performed plotting the diffusion variation with amplitude for the two diffusion measurements. The result of this evaluation is shown in figures 5.11a and 5.11b for the lattice without and with crab cavities respectively. Firstly, comparing the two lattices it is apparent that there is an increased diffusive peak at 12σ in the presence of crab cavities. Furthermore, the D[max-min] peak on the fold is reduced in the presence of crab cavities. These differences do suggest that the crab cavities do impact the non-linear dynamics of the lattice, however, these observations are at amplitudes well below the dynamic aperture of the this error free lattice. This does not rule out seeing an effect with increased errors in the lattice.

Comparing the two diffusion measurements in figures 5.11a and 5.11b, the greatest difference can be seen in the peak around 21σ. At this peak there is a strong disagreement between the D[max-min] and D[first-last] values. This difference arises from the increased sensitivity of the D[max-min] measurement to

chaotic motion in the region with non-definite torsion. The D[max-min] measurement does not appear to reveal new peaks in diffusivity. However, it does amplify the diffusion between resonances. Furthermore it can be seen that the dynamic aperture does not correlate with the first strong diffusive peak, at the amplitude at which the frequency map folds. This result is in agreement with the signature of torsion study which suggested that the stability arose from the frequency map transitioning from a double fold onto the linear difference resonance.

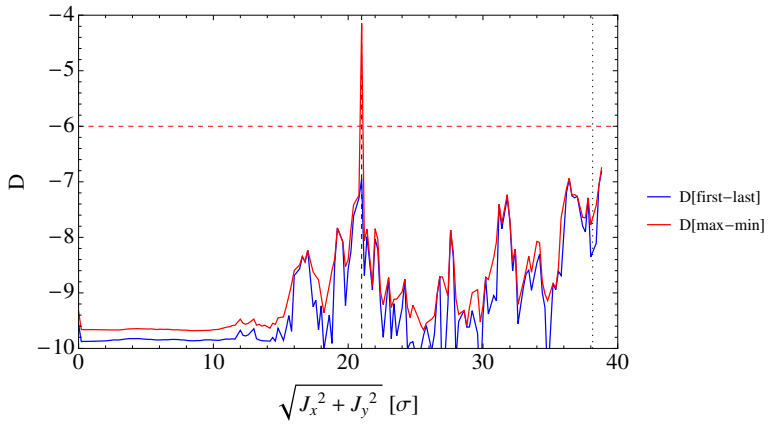

(a) 36°

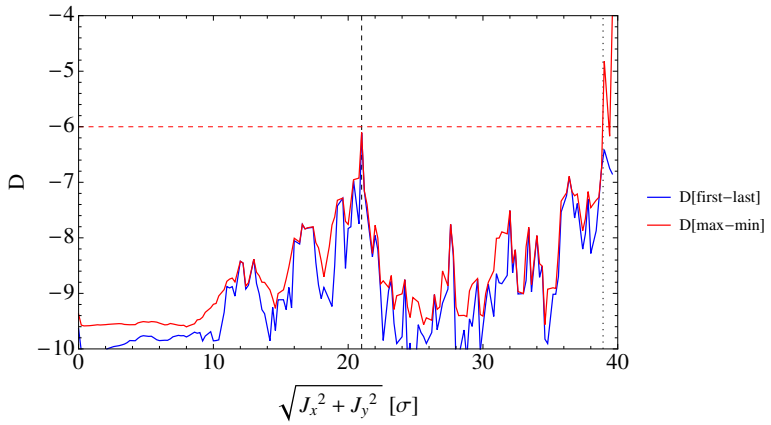

(b) 36° with crab cavities

Figure 5.11: The variation in diffusion with amplitude at 36°. Transition to linear difference resonance (black, dashed vertical line), dynamic aperture (black, dotted vertical line) and diffusion cut off (red, dashed horizontal line). Nominal SLHCv3.1b no errors.

In contrast, a ratio of 72° was chosen because the amplitude at which the

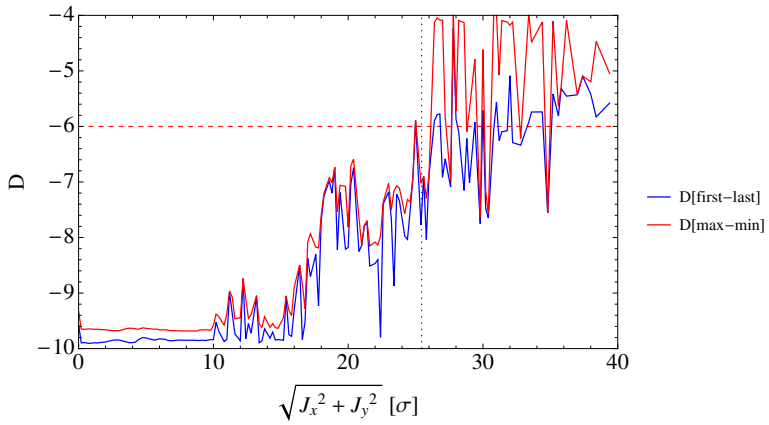

(a) 72°

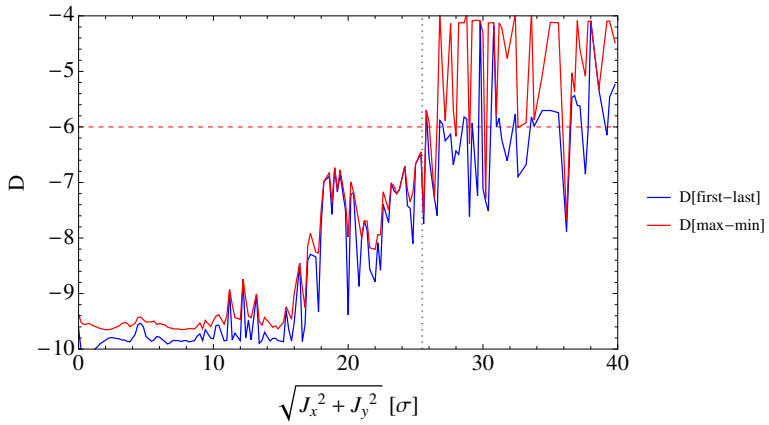

(b) 72° with crab cavities

Figure 5.12: The variation in diffusion with amplitude at 72°. Transition to linear difference resonance (black, dashed vertical line), dynamic aperture (black, dotted vertical line) and diffusion cut off (red, dashed horizontal line). Nominal SLHCv3.1b no errors.

dynamic aperture occurs does not correspond to a folded region. The results of this ratio can be seen in figures 5.12a and 5.12b, showing a similar pattern of peaks caused by resonances. However, for this case the dynamic aperture coincides with a diffusive peak indicating that the corresponding resonance leads to the unbounded motion that defines the dynamic aperture at this ratio.

In figures 5.12a and 5.12b the resonance peak crosses a boundary of D[first-last] > -6 for the first time with increasing amplitude at the location of the dynamic aperture. For the 36° cases the dynamic aperture is at a point at which the diffusion measurement is much lower than this diffusion boundary, suggesting that for this angular case there is no correlation between diffusion and dynamic aperture. In previous studies [47] it was observed that there was some relation between dynamic aperture and diffusion. This study suggests that this relationship is only true in regions of amplitude space in which the frequency space has not folded.

To further investigate the relationship between diffusion and dynamic aperture a diffusive aperture is defined by the point at which the diffusion first exceeds -6. This value was chosen from figures 5.12a and 5.12b by the point at which the dynamic aperture crosses the diffusion with amplitude line. Figure 5.13 shows the amplitude diffusion map for the regions beyond the two folds. The diffusive aperture, defined by the two diffusion measurements, and the dynamic aperture are overlaid. The D[max-min] defined diffusive aperture exhibits greater deviation from the dynamic aperture as it is more sensitive to the chaotic motion exhibited between the two folds of the double fold. This correlates with the large amount of resonance wandering exhibited in this region of phase space. The D[first-last] defined diffusive aperture has a closer agreement with the dynamic aperture as it is less sensitive to the resonance wandering that occurs between the folds of the

double fold. However, it is apparent that these two diffusive aperture measurements do not serve as a replacement for the dynamic aperture.

This frequency map study shows a new method to consider a 6D system. This study has shown increased diffusion resulting from the crab cavities at amplitudes well below that of the dynamic aperture of the error free nominal lattice. While these differences do not show visible impact on the dynamic aperture of the error free lattice they do not rule out an effect being observed in future lattice models with magnet errors. Further insight has been made into the dynamics of the SLHCv3.1b lattice. Through the time dependent map the process of resonance wandering has been observed. Using a single frame of the animated frequency map enabled the study of the nature of the folded regions and has shown that there is a double folded region which transitions onto the linear difference resonance which leads to a peak in the dynamic aperture. Furthermore, through this study it has been shown that tune shift is not a direct measurement of machine stability and that its relationship to dynamic aperture is dependent on the presence of folds in the frequency map.

5.2.3 Impact of the transverse dependence in the cavity model

Section 4.3 showed that the RF multipole kick model changed the kicks by approximately 1% of the total kick from that of the simple kick model at $x = 20$ mm. In figure 5.3 it was shown that the crab bump caused a small variation in the dynamic aperture, with no significant drop in the minimum of the minimum dynamic aperture. Studying the dynamic aperture with the RF multipoles kick model generates an understanding of the importance of the x and y dependence on p_x and p_y. Considering the 2012 cavity designs, in figure 5.14, the variation in the RF multipole values between the cavity designs leads to a small variation

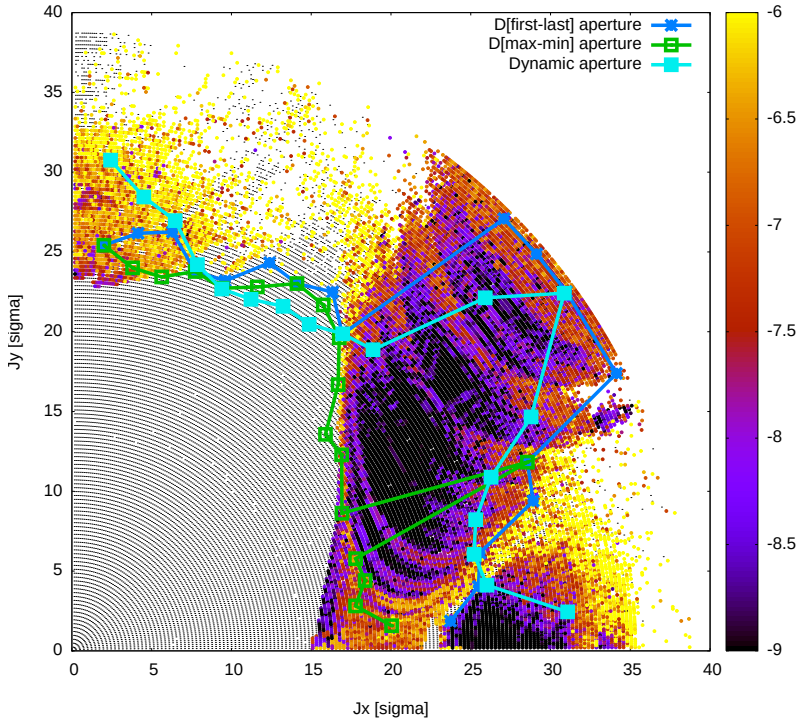

(a)

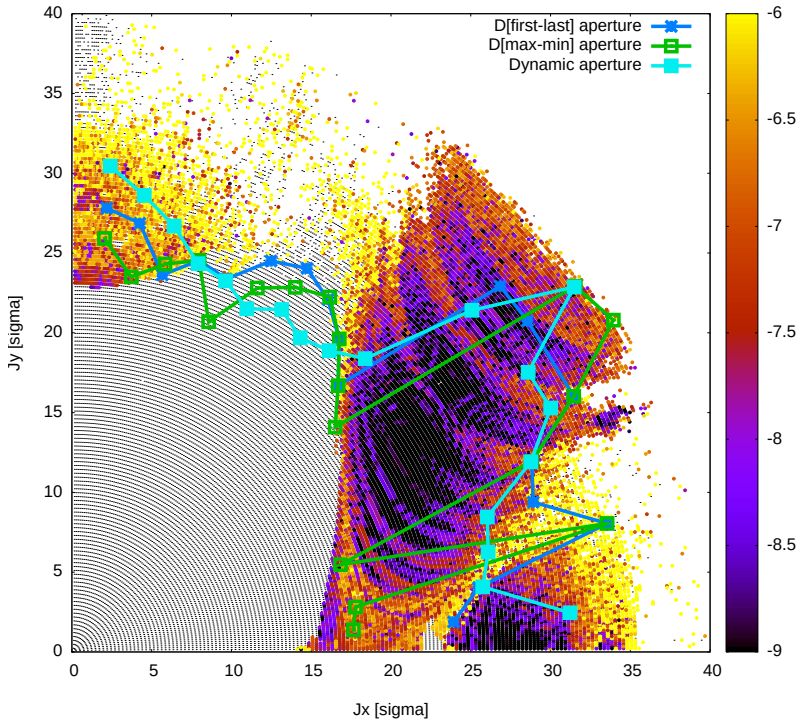

(b)

Figure 5.13: Variation in D[first-last] across regions on and beyond folds, with diffusive aperture and dynamic aperture overlaid. (a) Nominal SLHCv3.1b no errors, and (b) nominal SLHCv3.1b no errors with crab cavities.

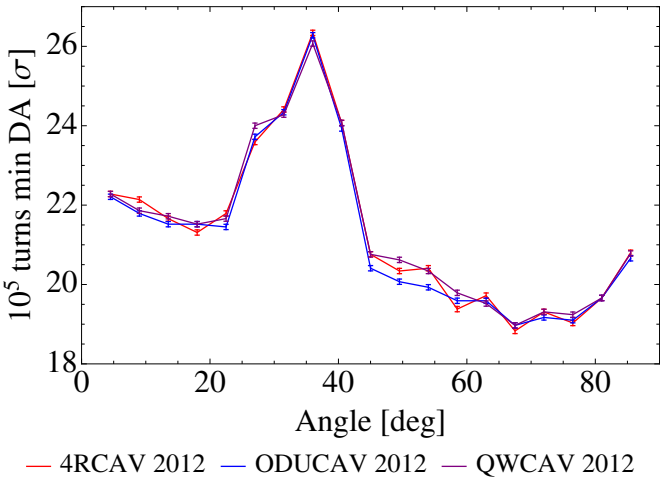

Figure 5.14: Minimum dynamic aperture for 2012 designs with RF multipoles, coefficients calculated using PW @ 20 mm (Up to b_5), and crab bump performed using 60 variants of arc magnet errors. H-V crossing.

in the minimum dynamic aperture. These cavity designs all have two transverse planes of symmetry and hence only the b_1, b_3 and b_5 components were considered. The additional variation in minimum dynamic aperture brought about by the transverse spatial dependence of the kick is of a similar order of magnitude to that introduced by the crab cavity bump in terms of its impact on the minimum dynamic aperture. It can be seen that the variation in dynamic aperture across the phase space is a maximum of 0.5σ between the different designs.

From the symplectic error studies in section 3.4 no methods were shown to imply the impact of symplectic error on the dynamic aperture calculation. In figure 5.15 the use of 200 and 500 coefficient reduced coefficient maps (RCM) are presented showing that there is a maximum deviation of 0.34σ. This maximum deviation occurs in the region of phase space at which the dynamic aperture lies on a fold. This region exhibits particularly chaotic motion, from figure 5.13b, and appears particularly sensitive to symplectic error.

In Fig. 5.16 the dynamic aperture is presented for four different cavity models.

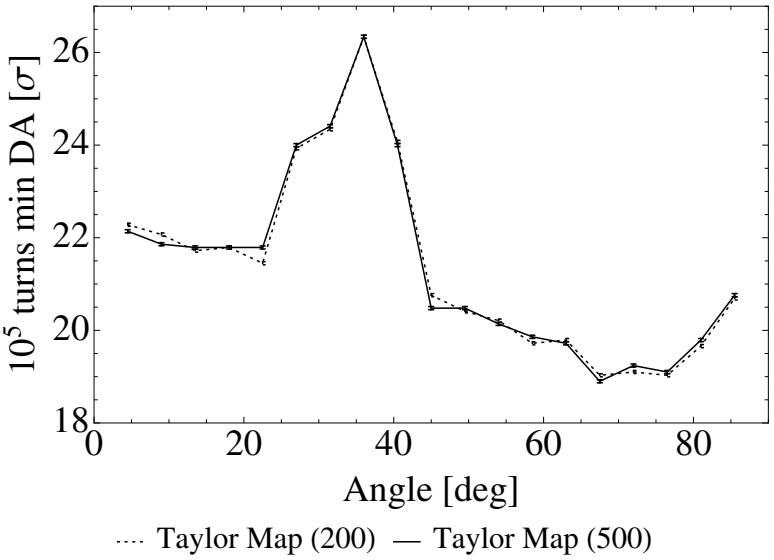

Figure 5.15: Impact of symplectic error on the minimum dynamic aperture determined from 60 variations of the lattice.

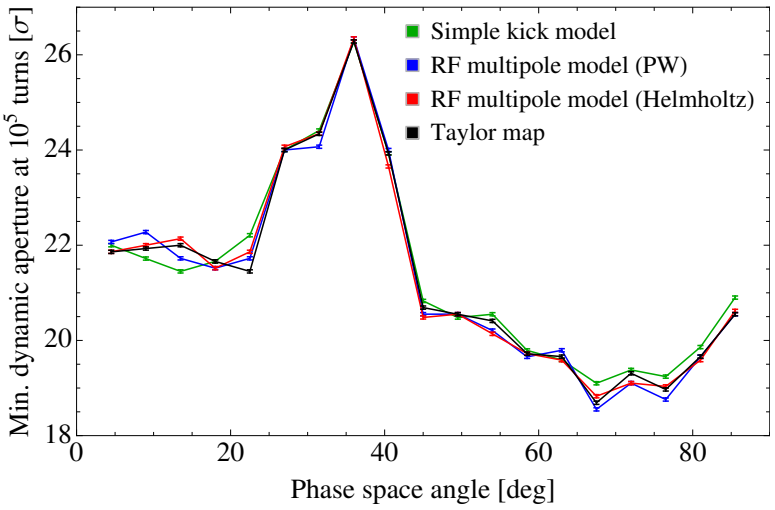

Figure 5.16: Impact of different crab cavity models on the minimum dynamic aperture after 10^5 turns. Comparing the 500 coefficient Taylor map with the RF multipole kick model (using multipoles calculated using the Helmholtz and PW decompositions), and the simple kick model.

The Taylor map used was a RCM with 500 coefficients per series, this is compared with three different thin lens models: The simple kick model considers only the kick from b_1, the RF multipole kick model from HD multipoles (RFM-HD) and RF multipole kick model from PW multipoles (RFM-PW). Comparing the difference between the Taylor map and RFM-HD there is a maximum difference of 0.4 σ. This difference arises from a combination of symplectic error and additional dynamics as observed in Tab. 4.4. The largest difference occurs at 22.5° which correlates with the maximum difference observed in figure 5.15 resulting from sensitivity of the dynamic aperture to the fold. By contrast comparing the simple kick model with the Taylor map there is a maximum difference of 0.8 σ. Even though symplectic error is present this indicates that the RFM-HD is a closer approximation to the dynamics of the cavity relevant to the HL-LHC than the simple kick model. The contributions to the difference between these models from symplectic error and additional dynamics, however, are unknown. Furthermore there is a maximum difference between the RFM-PW and RFM-HD models of 0.4 σ. This suggests that the sensitivity to additional dynamics and symplectic error is similar to that of the sensitivity to the multipole calculation. This would indicate that the RF multipole kick model gives a good approximation to the crab cavity dynamics relevant to the HL-LHC given the tolerances in the calculation of the multipole coefficients.

5.3 Conclusion

In this chapter the impact of the crab cavities on the HL-LHC dynamic aperture has been studied. These studies were performed using the kick code SixTrack. An initial study was performed to investigate the impact of the simple kick model on the dynamic aperture in which it was seen to vary the minimum dynamic aperture across phase space by up to 0.5σ. Furthermore, it was shown that

within the range of the voltage jitter from the low level RF system the minimum dynamic aperture variation remained within 0.5σ.

A study was performed to investigate any resonances associated with crab cavities. A small change in the diffusion variation with amplitude was observed, however, this had no direct consequence on the dynamic aperture for the case considered as it occurred at an amplitude well below that of the dynamic aperture. There were no visible additional resonances in the frequency map resulting from crab cavities suggesting that for the nominal lattice no additional loss mechanisms were introduced. This indicates why the impact of crab cavities on the dynamic aperture is so small. Investigating the optics with a new 6D frequency map technique showed the presence of resonance wandering occurring in a double folded region. It was also shown that the peak in the dynamic aperture arose from the stability of this double folded region's transition on to the linear difference resonance.

The transverse spatially dependent kicks from the different crab cavity designs were shown to have an effect of less than 1σ across the distribution of the minimum dynamic aperture. Taylor maps have been successfully applied in the calculation of dynamic aperture and have been used to show that the RF multipole description is a significant improvement to the simple kick model in describing the crab cavity dynamics relevant to the HL-LHC. The uncertainty from symplectic error and additional dynamics has not prevented the Taylor maps from indicating the relevance of the additional terms contained in the RF multipole kick model, compared with those of the simple kick model. However, there is some ambiguity over whether the difference between the models is dominated by symplectic error or additional dynamics. The difference between two different RF multipole calculations, arising from the sensitivity to errors from the finite element solver, led to a variation in the dynamic aperture of up to 0.4σ. This

difference is the largest uncertainty in the model for a specific cavity design with respect to its impact on the dynamic aperture.

Chapter 6

Developing an inner triplet fringe field model for the HL-LHC

In this chapter the second question posed in chapter 1 into whether the fringe fields of the inner triplet magnets cause significant variation in the stability of the current model of the HL-LHC is considered. From the tools used to develop models for crab cavities in chapters 3 and 4, models of the fringe fields of the Inner Triplet (IT) quadrupole magnets about IP1 and IP5 can also be developed. Fringe fields are a feature of an accelerator magnet resulting from the end windings and transition to a field free region. Typically the longitudinal fall off of a magnetic field in the fringe field region can be described using an Enge function [162, 133]. However, this is not the complete picture. As with the models developed for the crab cavity the fringe field models must fit within a kick code model of the HL-LHC.

In this chapter, in section 6.1 the need for a fringe field model is motivated. In section 6.2 a model for the fringe fields which fits into the current HL-LHC model is proposed and its limitations studied. Finally, in section 6.3 a first dynamic aperture with a fringe field model is performed.

6.1 Motivation

The ATS optics scheme, described in section 2.3.2, requires large aperture quadrupole magnets for the final focussing IT in IR1 and IR5. A large aperture of 150 mm is required to enable a large crossing angle of 300 μrad [163] in order to reduce the effect of beam-beam interaction, as discussed in section 2.3.

Figure 6.1: Hard edge magnet model; Real magnet field (red) and hard edge model (black).

In the kick code model of the HL-LHC a hard edge magnet model is used to describe the longitudinal distribution of the magnetic fields, as shown in figure 6.1. A physical motivation for considering a fringe field model arises when the assumptions used in the derivation of this hard edge model fail. Maxwell's equations for a magnetic field in a current and electric field free region are given by,

$$\nabla \times \vec{B} = 0, \tag{6.1}$$

$$\nabla \cdot \vec{B} = 0. \tag{6.2}$$

Expressing equation 6.1 in terms of the vector potential A leads to,

$$\begin{aligned} \nabla \times \vec{B} &= \nabla \times \nabla \times \vec{A} \\ &= \nabla(\nabla \cdot \vec{A}) - \nabla^2 \vec{A} \\ &= -\nabla^2 \vec{A}. \end{aligned} \tag{6.3}$$

In section 4.1 it was shown that in the axial and rigid bunch approximations the kick Hamiltonian is described by the normalised longitudinal component of the vector potential a_z. Applying the axial approximation, which assumes x and y are constant with time,

$$\frac{dx}{dt} = v_x = 0, \qquad \frac{dy}{dt} = v_y = 0, \tag{6.4}$$

to the Lorentz force,

$$\begin{aligned} \vec{F}_\perp &= \left(e_0 \vec{v} \times \vec{B}\right)_\perp \\ &= -v_z B_y \hat{x} + v_z B_x \hat{y}, \end{aligned} \tag{6.5}$$

means that B_z is neglected; therefore, a_x and a_y can also be neglected. From equation 6.3, the normalised longitudinal component of the vector potential is given by the solution to,

$$\nabla^2 a_z(x, y, s) \equiv \frac{\partial^2 a_z}{\partial x^2} + \frac{\partial^2 a_z}{\partial y^2} + \frac{\partial^2 a_z}{\partial s^2} = 0. \tag{6.6}$$

The hard edge limit assumes that the magnetic field is constant in longitudinal position s which leads to,

$$\nabla^2 a_z(x, y) \equiv \frac{\partial^2 a_z}{\partial x^2} + \frac{\partial^2 a_z}{\partial y^2} = 0. \tag{6.7}$$

From the vector potential the transverse magnetic fields are given by,

$$\vec{B}_\perp = \frac{e_0}{p_0} \nabla \times a_z, \tag{6.8}$$

so that,

$$\frac{p_0}{e_0}B_x = \frac{\partial a_z}{\partial y} \qquad\qquad \frac{p_0}{e_0}B_y = -\frac{\partial a_z}{\partial x}. \tag{6.9}$$

Substituting equation 6.9 into equation 6.7 results in,

$$-\frac{\partial B_y}{\partial x} + \frac{\partial B_x}{\partial y} = 0. \tag{6.10}$$

The conventional notation for the solution of equation 6.10 is given by [31],

$$B_y + \mathrm{i}B_x = B_0 \sum_{n=1}^{\infty} (b_n + \mathrm{i}a_n) \left(\frac{x + \mathrm{i}y}{R_0}\right)^{n-1}, \tag{6.11}$$

where B_0 and R_0 are a reference field strength and reference radius, and b_n and a_n are the normal and skew multipole coefficients. Further discussion of these multipoles can be found in section 2.2.1. These approximations no longer hold in a fringe field in which the transverse magnetic field varies longitudinally. Furthermore, in this fringe field region it is possible that B_z cannot be neglected as a B_z field must exist at the boundary to the field free region [164, 154]. This gives physical motivation to study the impact of the fringe fields.

The HL-LHC inner triplet magnets (MQXF) have apertures of 150 mm, as shown in figure 6.2, and at collision the β-functions are increased to around 20 km. In the nominal machine the equivalent magnets (MQXA) have an aperture of 70 mm and β-functions at collision of around 4 km. In studies of the fringe fields of these MQXA magnets [95] significant tune variation and increased amplitude dependent tune shift were observed in simulation. It was observed that the horizontal tune shifted by 2% and that there was a ten-fold increase in the ε_x^2 dependence of Q_x [95][1]. Furthermore, in studies performed on the LHC there is non-linear coupling which remains unaccounted for in the current model, with

[1] ε_x in this case refers to the single particle emittance.

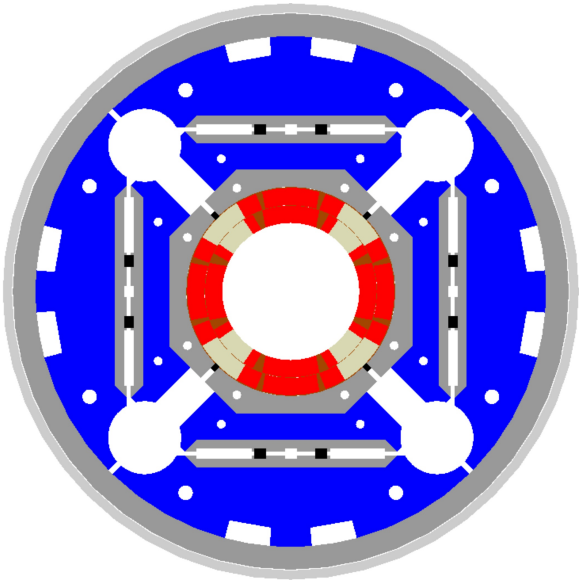

Figure 6.2: Cross-section of inner triplet magnet (MQXF) design for HL-LHC with aperture of 150 mm and gradient 140 T/m [165].

fringe fields a candidate for explaining this [166]. Comparing the HL-LHC case with the studied nominal LHC [95], the MQXF magnets have considerably larger fields, the lattice has greater β-functions and there is increased sensitivity to the fringe fields generated by the phase advances required for the ATS scheme [154].

In summary, the hard edge model is independent of s which means that it neglects any effects present in a real magnet at the boundary with the field free region. Furthermore, previous studies of the inner triplet fringe fields in the nominal LHC observed significant increase in tune shift with amplitude [95]. The effect of the fringe fields is anticipated to be worse for the HL-LHC than the nominal LHC so it was considered important to investigate the effects of these fringe fields. From the tools used to develop and study the crab cavity models a model is sought to study the impact of fringe fields of the IT magnets on the stability of the HL-LHC lattice.

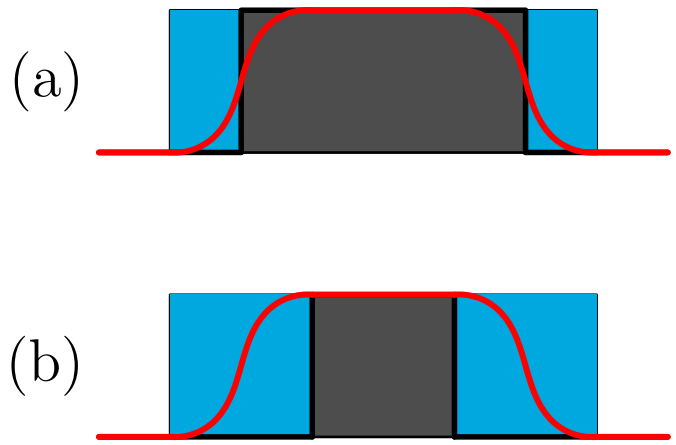

Figure 6.3: Separation options of magnet fringe fields. Real transverse magnetic field (red), region covered by hard edge model (grey), and region covered by fringe field model (blue).

.

6.2 Modelling the inner triplet fringe field

The first technical requirement imposed on the model of the fringe field is that it is an isolated mathematical representation which is separate from the core of the magnet (region over which the magnetic field is constant in s), which remains described by a hard edge model. This isolation is required in order to prevent disruption to the current matching and correction routines. Two choices are available in this separation of fringe fields from the central magnet and are shown in figure 6.3. Option (a) keeps the hard edge model as already implemented for previous LHC studies and any additional beam dynamic effects from the fringe fields are lumped onto the end of the hard edge model. However, this approach ignores any variation in the quadrupole component of the transverse field as the whole of the quadrupole field is contained within the hard edge description. Option (b) reduces the length of the hard edge model to only include the physically flat region of the quadrupole component. This allows the whole of the fringe field to be considered in the model, including the variation in the quadrupole component. Option (b) would appear to be the best option in terms of inclusion of all

properties of the fringe fields because it allows for the inclusion of the variation of the quadrupole component of the field.

A second technical requirement imposed on the model is that it must work with the current magnet error definition [31]. This is defined by the hard edge magnet of option (a) from the summed multipole errors which are calculated using a 2D[2] finite element solver. The multipole errors are calculated on a model assuming a magnet of infinite length. This means that any additional multipole errors associated with the fringe fields are neglected. This means only option (a) can be considered with the multipole errors from the fringe fields and any additional dynamics to be lumped on to the ends. These technical restraints neglect any effect from the variation in quadrupole field which will alter the β-function and phase advance, as seen previously [167]. In [167] it was observed for the SLHCv3.1b optics that there was a beta-beat of up to 11% generated by the longitudinal variation in the quadrupole field compared with that of the hard edge model.

From the crab cavity studies, in chapters 3 and 4, four possible approaches were considered when developing a new model.

1. **Simple kick model:** This model is computed from a split Hamiltonian representation which leads to a symplectic approach. The model is independent of the element design and arises from physical considerations. An example of this for fringe fields is the leading order model developed in [164].

2. **Parameterised kick model:** This model is computed from a split Hamiltonian representation which leads to a symplectic model. This model would make greater consideration of the details of a specific design. Similarly to the generalised RF multipole kick model in section 4.1.3, which was developed from [119], a model might be generated for the fringe fields from [123].

[2]In the x-y plane.

3. **Numerical integration:** Integration of a real field map using a symplectic integration scheme; e.g. the WFR integrator [107]. However, this approach is computationally very slow for long term tracking.

4. **Single element Taylor map models:** Integration of a real field map using a symplectic integration scheme such as the WFR integrator [107]. To increase the speed of this approach a Taylor map is produced rather than direct numerical integration. However, this approach leads to symplectic errors. An approach to avoid these symplectic errors using mixed variable generating functions was proposed in [96], however, it is anticipated such approaches would be computationally too slow for long term tracking.

Modelling the fringe fields with option (3), Taylor maps, or (4), numerical integration, could allow the inclusion of the full dynamics resulting from all components of the magnetic field. However, from the technical constraints, the quadrupole component of the field must be removed from the magnetic field of the fringe field as it is already contained in the hard edge model. This means that any effects arising from the path through fringe field would be incorrect due to the absence of the quadrupole field component. For this reason options (3) and (4) are ruled out. This leaves options (1) and (2), which are both kick models.

There are two physical effects generated in a fringe field which differ from those of the hard edge model: the impact of the longitudinal component of the magnetic field generated at the boundary to the field free region, and the additional transverse magnetic field components resulting from the Laplace equation in three rather than two dimensions. In order to make use of pre-existing work [123, 154, 164] and to keep the two physical effects separate a fringe field model composed of two components was considered. Removal of the b_2 multipole component from the transverse fields means that any simulated trajectory

through the fringe field will be incorrect. Therefore, the impact of changes in momentum from the magnetic field on the trajectory can no longer be considered on a particle as it passes through the fringe field model. The paraxial approximation of the accelerator Hamiltonian from equation 2.144 is given by,

$$H = -\left(\frac{1}{\beta_0}+\delta\right) + \frac{1}{2\beta_0^2\gamma_0^2}\left(\frac{1}{\beta_0}+\delta\right)^{-1} + \frac{\delta}{\beta_0} + \frac{(p_x-a_x)^2}{2\left(\frac{1}{\beta_0}+\delta\right)} + \frac{(p_y-a_y)^2}{2\left(\frac{1}{\beta_0}+\delta\right)} - a_z + p_s. \tag{6.12}$$

This can be split such that,

$$H_{\text{drift}} = -\left(\frac{1}{\beta_0}+\delta\right) + \frac{1}{2\beta_0^2\gamma_0^2}\left(\frac{1}{\beta_0}+\delta\right)^{-1} + \frac{\delta}{\beta_0} + \frac{p_x^2+p_y^2}{2\left(\frac{1}{\beta_0}+\delta\right)} + p_s \tag{6.13}$$

$$H_{\text{transverse}} = -a_z \tag{6.14}$$

$$H_{\text{longitudinal}} = \frac{(p_x-a_x)^2-p_x^2}{2\left(\frac{1}{\beta_0}+\delta\right)} + \frac{(p_y-a_y)^2-p_y^2}{2\left(\frac{1}{\beta_0}+\delta\right)} \tag{6.15}$$

From this splitting a first order symplectic map can be formed to describe the fringe field; at the entrance face to a magnet this is given by,

$$\mathcal{M}_{\text{entrance}} = e^{:H_{\text{drift}}:} e^{:H_{\text{transverse}}:} e^{:H_{\text{longitudinal}}:}, \tag{6.16}$$

at the exit face this is given by,

$$\mathcal{M}_{\text{exit}} = e^{:H_{\text{longitudinal}}:} e^{:H_{\text{transverse}}:} e^{:H_{\text{drift}}:}. \tag{6.17}$$

In this splitting, from the paraxial approximation, two separate models can be considered to describe the dynamics of the transverse and longitudinal components of the magnetic fields.

6.2.1 Modelling the transverse magnetic fields

The fringe field model component to describe the transverse magnetic fields starts from the work in [123, 124]. A field fitting was performed, in a similar manner to that of the crab cavities, of the fringe fields of the inner triplet magnets, by Dalena *et al.* [123, 124, 168]. The resulting fitted fields were provided by Dalena in the form of a power series in x and y up to a total order of 20, as a function of s with the corresponding raw field data from which the field fitting was performed.

The aim of this model component is to take this field fitting and develop a kick model which uses a physically correct description of the dynamics resulting from the transverse magnetic fields.

The fitting method used is shown in [123]. The method starts by assuming fields inside the magnet are in a current free region, hence the magnetic field $\vec{B}$ can be described by a scalar function ψ. From Maxwell's equations, $\vec{B}$ is also divergence free hence the scalar potential must obey the Laplace equation,

$$\nabla^2 A_z = 0, \tag{6.18}$$

as shown in equation 6.3. In cylindrical coordinates the general solution to the Laplace equation is given by [123],

$$\psi(\rho, \phi, s) = \sum_{n=0}^{\infty} \int_{-\infty}^{\infty} dk \; I_n(k\rho) e^{\mathrm{i}ks} \left[G_{n,s}(k) \sin(n\phi) + G_{n,c}(k) \cos(n\phi) \right]. \tag{6.19}$$

where $G_{n,s}(k)$ and $G_{n,c}(k)$ are the normal and skew harmonic functions to be defined and I_n is a modified Bessel function. By the same convention as chapter 3 the index n is the azimuthal index and m is the radial index. Using the Taylor expansion of I_n the scalar function ψ can be expressed in the form of a multipole

expansion,

$$\psi(\rho,\phi,s)=\sum_{n=0}^{\infty}\left[\psi_{n,s}(\rho,s)\sin(n\phi)+\psi(n,c)\cos(n\phi)\right] \tag{6.20}$$

where $\psi_{n,(s,c)}$ are defined,

$$\psi_{n,s}(\rho,s)=\sum_{m=0}^{\infty}\frac{(-1)^m n!}{2^{2m}m!(n+m)!}C_{n,s}^{[2m]}(s)\rho^{2m+n}, \tag{6.21}$$

$$\psi_{n,c}(\rho,s)=\sum_{m=0}^{\infty}\frac{(-1)^m n!}{2^{2m}m!(n+m)!}C_{n,c}^{[2m]}(s)\rho^{2m+n}. \tag{6.22}$$

The functions $C_{n,s}^{[m]}(s)$ and $C_{n,c}^{[m]}(s)$ are the normal and skew generalised gradients defined [123],

$$C_{n,s}^{[m]}(s)=\frac{\mathrm{i}^m}{2^n n!}\int_{-\infty}^{\infty}\mathrm{d}k\; e^{\mathrm{i}ks}k^{n+m}G_{m,s}, \tag{6.23}$$

$$C_{n,c}^{[m]}(s)=\frac{\mathrm{i}^m}{2^n n!}\int_{-\infty}^{\infty}\mathrm{d}k\; e^{\mathrm{i}ks}k^{n+m}G_{m,c}. \tag{6.24}$$

In Cartesian coordinates, using the transformations in equation 3.32, the scalar function in terms of the generalised gradients is,

$$\begin{aligned}\psi(x,y,s)=&\sum_{m=0}^{\infty}\sum_{n=0}^{\infty}\frac{(-1)^m n!\left(x^2+y^2\right)^m}{2^{2m}m!(m+n)!}\left[C_{n,s}^{[2m]}(s)\Im\{(x+\mathrm{i}y)^n\}\right.\\&\left.+C_{n,c}^{[2m]}(s)\Re\{(x+\mathrm{i}y)^n\}\right].\end{aligned} \tag{6.25}$$

To find an expression in terms of the vector potential $\vec{A}$ a solution must be found from the equation $\nabla\times\vec{A}=\nabla\psi$. The expression for A_z is given by [123],

$$\begin{aligned}A_z(x,y,s)=&\sum_{m=0}^{\infty}\sum_{n=0}^{\infty}\frac{(-1)^m n!\left(x^2+y^2\right)^m}{2^{2m}m!(m+n)!}\left[C_{n,c}^{[2m]}(s)\Im\{(x+\mathrm{i}y)^n\}\right.\\&\left.-C_{n,s}^{[2m]}(s)\Re\{(x+\mathrm{i}y)^n\}\right].\end{aligned} \tag{6.26}$$

The generalised gradients were calculated from the radial component of the magnetic field B_ρ at a given radius R such that [123],

$$C^{[m]}_{n,(c,s)}(s) = \frac{\mathrm{i}^m}{2^n n!}\int_{-\infty}^{\infty} \mathrm{d}k\; e^{\mathrm{i}ks} k^{n+m-1} \frac{\tilde{b}_{n,(c,s)}(R,k)}{I'_n(kR)}, \tag{6.27}$$

$$\tilde{b}_{n,s} = \frac{1}{2\pi^2}\int_0^{2\pi} \mathrm{d}\phi\; \sin(n\phi) \int_{-\infty}^{\infty} \mathrm{d}s\; e^{-\mathrm{i}ks} B_\rho(R,\phi,s), \tag{6.28}$$

$$\tilde{b}_{n,c} = \frac{1}{2\pi^2}\int_0^{2\pi} \mathrm{d}\phi\; \cos(n\phi) \int_{-\infty}^{\infty} \mathrm{d}s\; e^{-\mathrm{i}ks} B_\rho(R,\phi,s). \tag{6.29}$$

From the fitting data provided the radial terms of $C^{[m]}_{2,s}$ are shown in figure 6.4. One property of the generalised gradients is that,

$$C^{[m]}_{n,(c,s)}(s) = \mathrm{d}^m C^{[0]}_{n,(c,s)}(s)/\mathrm{d}s^m, \tag{6.30}$$

which means that in a region where the generalised gradients are constant with s all generalised gradients for $m > 0$ will be zero. This can be seen in figure 6.4 where terms with $m > 0$ go to zero at the boundaries of the fringe field. In figure 6.4b $C^{[2]}_{2,s}$ is calculated both from the field fitting and from equation 6.30 using an interpolation function of $C^{[0]}_{2,s}$ created in Mathematica [105]. It was found that this approach of only using the fitted $C^{[0]}_{2,s}$ to calculate $C^{[2]}_{2,s}$ provides a reasonable agreement with the fitting result. However, it could be conceived that an Enge function be fitted to $C^{[0]}_{2,s}$ in order to determine the generalised gradients for $m > 0$ as a cross check of the fitting.

The results from the field fitting are shown in figure 6.5. It can be seen that at a radius of 50 mm there is a peak error in the transverse fields of order 0.3% of the B_x value found at the exit face of the magnet core. Furthermore, there is a peak error in the longitudinal field component of order 1%. These errors are very high considering that in [123] a peak error of 2×10^{-3}% was achieved. This would suggest that this field fitting could be further improved. From the experience of

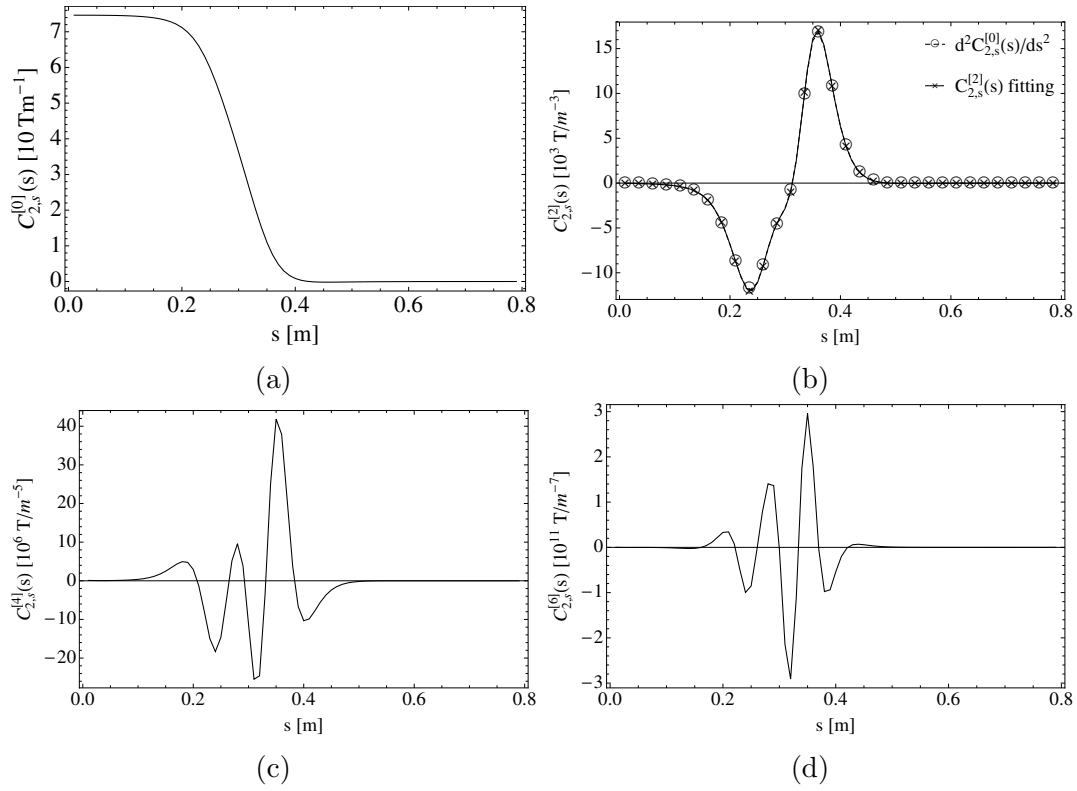

Figure 6.4: Generalised gradients of the fitted fringe fields, normalised to the magnet strength of MQXC.1R1, (a) $C_{2,s}^{[0]}$, (b) $C_{2,s}^{[2]}$, (c) $C_{2,s}^{[4]}$, and (d) $C_{2,s}^{[6]}$.

fitting the crab cavities in section 4.2 and the discussions in [123] it is possible that some of this error arises from the Cartesian mesh used to output the fields from the Eigenmode solver, which could be improved by going to a cylindrical mesh similar to that seen in figure 4.2. Furthermore, it is possible that in the provided fitting too lower truncation occurred of the generalised gradients, which could be improved by including generalised gradients of increased m and n.

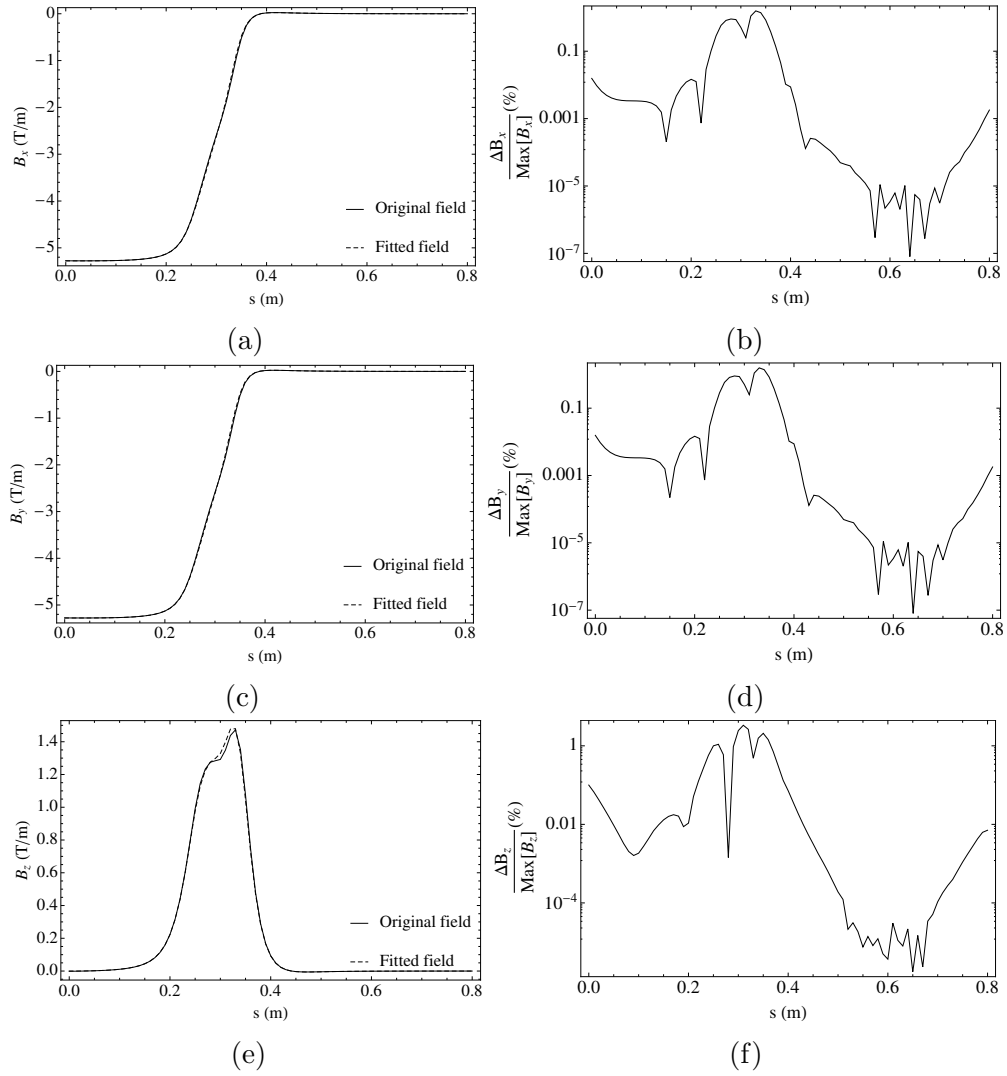

Figure 6.5: Results of the field fitting of fringe fields normalised to the magnet strength of MQXC.1R1 evaluated at $\phi = 45°$ and $\rho = 50$ mm [168]. s is the distance from the exit face of the magnet core. (a,c,e) Fitted fields compared with original fields from field data. (b,d,e) Residuals of the field fitting at this point in phase space.

Analogously to the generalised RF multipole kick model (equation 4.50) such a model can be formulated for magnets whose fields vary longitudinally. From the generalised gradients, generalised multipole coefficients are defined,

$$b_{n,m} = \Re\left\{\frac{(-1)^m n!}{2^{2m} m!(n+m)!}\int_0^L C_{n,s}^{[2m]}(s)\ ds\right\}, \tag{6.31}$$

$$a_{n,m} = \Re\left\{\frac{(-1)^m n!}{2^{2m} m!(n+m)!}\int_0^L C_{n,c}^{[2m]}(s)\ ds\right\}. \tag{6.32}$$

A consequence of equation 6.30 is that for $m > 0$ the sign of the multipole coefficient will change at the exit face of the magnet, compared to the entrance face. From equation 6.26 a kick Hamiltonian can be written to describe the transverse magnetic fields in the fringe field region,

$$\begin{aligned} H_{\text{transverse}} =& -\frac{q}{p_0}\int_0^L A_z\ ds \\ =& -\frac{q}{p_0}\sum_{m=0}^{\infty}\sum_{n=0}^{\infty}\left(x^2+y^2\right)^m\left[a_{n,m}\Im\left\{(x+\imath y)^n\right\} - b_{n,m}\Re\left\{(x+\imath y)^n\right\}\right]. \end{aligned} \tag{6.33}$$

From Hamilton's equations the symplectic momentum kicks are given by,

$$\begin{aligned} p_x \mapsto& p_x \\ &+\frac{q}{p_0}\sum_{m=0}^{\infty}\sum_{n=0}^{\infty}\Big(2\frac{m}{n}x\left(x^2+y^2\right)^{m-1}\left[\Im\left\{(x+\imath y)^n\right\}a_{n,m} - \Re\left\{(x+\imath y)^n\right\}b_{n,m}\right] \\ &+\left(x^2+y^2\right)^l\left[\Im\left\{(x+\imath y)^{n-1}\right\}a_{n,m} - \Re\left\{(x+\imath y)^{n-1}\right\}b_{n,m}\right]\Big) \end{aligned} \tag{6.34}$$

$$\begin{aligned} p_y \mapsto& p_y \\ &+\frac{q}{p_0}\sum_{m=0}^{\infty}\sum_{n=0}^{\infty}\Big(2\frac{m}{n}y\left(x^2+y^2\right)^{m-1}\left[\Im\left\{(x+\imath y)^n\right\}a_{n,m} - \Re\left\{(x+\imath y)^n\right\}b_{n,m}\right] \\ &+\left(x^2+y^2\right)^l\left[\Re\left\{(x+\imath y)^{n-1}\right\}a_{n,m} - \Im\left\{(x+\imath y)^{n-1}\right\}b_{n,m}\right]\Big) \end{aligned} \tag{6.35}$$

$$\delta \mapsto \delta. \tag{6.36}$$

The generalised multipoles are related to the integrated regular multipoles from equation 6.11 by,

$$b_{n,0} = \frac{B_0}{n{R_0}^{n-1}} \int_0^L b_n(s)\, ds \qquad a_{n,0} = \frac{B_0}{n{R_0}^{n-1}} \int_0^L a_n(s)\, ds. \tag{6.37}$$

The physical radius of the dynamic aperture in the region of the inner triplet magnets, for a minimum dynamic aperture of 12σ and β-function of 18 km, is approximately 37 mm. In table 6.1 the higher order radial index terms of $b_{2,m}$ are shown at the entrance face of the magnet. They indicate that the largest coefficient $b_{2,1}$ is approximately $10^{-5}\%$ of the total kick at 37 mm, by contrast the $b_{4,0}$ is 4%. This suggests that the multipole terms will dominate the additional dynamics at the dynamic aperture resulting from the transverse magnetic fields found in the fringe fields. Furthermore, given that at the exit face the multipoles with $m > 0$ will have the opposite sign their total kick will be dependent on the change in x and y over the length of the magnet only. Moreover, the multipoles with $m = 0$ do not change their sign at the exit face and will be dependent on x and y for both faces of the magnet, hence the kick from the multipoles with $m = 0$ will be considerably larger.

	Multipole value	Scaled value $[10^{-4}]$
$b_{2,0}$	22.0987	$1.00 \times 10^{+4}$
$b_{2,1}$	0.0036	1.44×10^{-3}
$b_{2,2}$	1.7024	6.18×10^{-4}
$b_{2,3}$	118.6619	3.87×10^{-5}
$b_{4,0}$	274.8540	$3.69 \times 10^{+2}$

Table 6.1: Generalised integrated multipole coefficients of the inner triplet fringe field at the entrance face. Coefficients in units of Tm^{2-n-2m} for $b_{n,m}$, normalised to the magnet strength of MQXC.1R1. Where the scaled value is given by $(b_{n,m}/b_{2,0}) \times (37\ \mathrm{mm})^{n+2m-2}$

In summary, this section presents a proposed extension of the multipole model

to describe the additional transverse field components present in an s dependent field. A consideration has been made for the fringe fields of a prototype MQXF design showing that the kicks will be dominated by the "standard" multipoles with b_4 having a kick over 10^5 times greater than that of $b_{2,1}$ in the vicinity of the dynamic aperture with the kicks for the multipoles with $m > 0$ almost cancelling at the exit face of the magnet.

6.2.2 Modelling the longitudinal magnetic fields

In the hard edge model the magnetic fields described by equation 6.11 are known to not obey Maxwell's equations at the boundary with the field free region. By computing the vector potential needed to satisfy Maxwell's equations at this boundary it is possible to attain a Hamiltonian expression for the fringe field effect from the longitudinal magnetic fields. This has been derived previously in [164, 154]. The derivation makes use of the property given in equation 6.30 taking the generalised gradients in the limit of a step function. The leading order model is defined from the vector potential expressed with terms up to the second derivative of the generalised gradient functions. This Hamiltonian is integrated in the thin lens limit to find the Hamiltonian describing the effect of the longitudinal magnetic field component. Using the conventions of equation 6.11, the transformation $\mathcal{M}$ across the boundary between the field free region and hard edge model for a skew and normal quadrupole fringe field is given by the Lie transformation [164],

$$\begin{aligned}
\mathcal{M} &= e^{:H_{\text{longitudinal}}:}, \\
H_{\text{longitudinal}} &= \frac{qB_0}{p_0\left(\frac{1}{\beta_0}+\delta\right)R_0}\left[\frac{b_2}{12}\left(3x^2yp_y - 3y^2xp_x + y^3p_y - x^3p_x\right)\right. \\
&\quad \left. + \frac{a_2}{6}\left(x^3p_y + y^3p_x\right)\right], \qquad (6.38)
\end{aligned}$$

where the Lie transformation is defined in equation 2.149. Expanding equation 6.15 to first order in $\vec{a}$ results in,

$$H_{\text{longitudinal}} \approx -\frac{a_x p_x + a_y p_y}{\left(\frac{1}{\beta_0} + \delta\right)}. \tag{6.39}$$

Comparing this result with equation 6.38 leads to expressions for the vector potential corresponding to the B_z field component described in the leading order model;

$$a_x = \frac{qB_0 b_2}{12 p_0 R_0} \left(3xy^2 + x^3\right), \tag{6.40}$$

$$a_y = -\frac{qB_0 b_2}{12 p_0 R_0} \left(3x^2 y + y^3\right). \tag{6.41}$$

The normal part of $H_{\text{longitudinal}}$ is not easy to evaluate due to it containing mixed terms (e.g. $x^3 p_x$) which require a significant amount of manipulation in order to reach a form in which the Lie transformation rule in equation 2.151 can be applied. However, the skew component can be directly evaluated with Hamilton's equations in a symplectic manner. Just considering the skew term of $H_{\text{longitudinal}}$ the map $\mathcal{M}$ can be factorised [164],

$$\mathcal{M} = e^{:H_{\text{longitudinal}}:} = \exp\left(:\alpha \frac{x^3 p_y}{\left(\frac{1}{\beta_0} + \delta\right)}:\right) \exp\left(:\alpha \frac{y^3 p_x}{\left(\frac{1}{\beta_0} + \delta\right)}:\right) + \mathcal{O}(\alpha^2), \tag{6.42}$$

where the normalisation constant α is defined,

$$\alpha = \frac{qB_0 a_2}{6 p_0 R_0}. \tag{6.43}$$

The constant term α can also be defined in terms of k_0 [164] such that,

$$\alpha \equiv \frac{k_0}{6}. \tag{6.44}$$

Applying these Lie transformations leads to the following maps of the leading order model which describes the effect of the longitudinal component of the magnetic field at the entrance face to the magnet,

$$\exp\left(:\alpha\frac{y^3 p_x}{\left(\frac{1}{\beta_0}+\delta\right)}:\right) x = x - \frac{\alpha y^3}{\left(\frac{1}{\beta_0}+\delta\right)}, \tag{6.45}$$

$$\exp\left(:\alpha\frac{y^3 p_x}{\left(\frac{1}{\beta_0}+\delta\right)}:\right) p_y = p_y + \frac{3\alpha y^2 p_x}{\left(\frac{1}{\beta_0}+\delta\right)}, \tag{6.46}$$

$$\exp\left(:\alpha\frac{y^3 p_x}{\left(\frac{1}{\beta_0}+\delta\right)}:\right) z = z + \frac{\alpha y^3 p_x}{\left(\frac{1}{\beta_0}+\delta\right)^2}, \tag{6.47}$$

$$\exp\left(:\alpha\frac{x^3 p_y}{\left(\frac{1}{\beta_0}+\delta\right)}:\right) y = y - \frac{\alpha x^3}{\left(\frac{1}{\beta_0}+\delta\right)}, \tag{6.48}$$

$$\exp\left(:\alpha\frac{x^3 p_y}{\left(\frac{1}{\beta_0}+\delta\right)}:\right) p_x = p_x + \frac{3\alpha x^2 p_y}{\left(\frac{1}{\beta_0}+\delta\right)}, \tag{6.49}$$

$$\exp\left(:\alpha\frac{x^3 p_y}{\left(\frac{1}{\beta_0}+\delta\right)}:\right) z = z + \frac{\alpha x^3 p_y}{\left(\frac{1}{\beta_0}+\delta\right)^2}. \tag{6.50}$$

For the exit face of the magnet the sign of the normalisation factor α changes such that $\alpha \to -\alpha$. However, this map only applies the fringe field component of the skew quadrupole. In order to apply the normal fringe field, the beam is first rotated $-45°$ to effectively rotate the fringe field by $45°$, the fringe field map is then applied and the beam rotated back $45°$ to its original orientation to complete

the transformation. This rotation is performed using the map,

$$\begin{pmatrix} x \\ p_x \\ y \\ p_y \\ z \\ \delta \end{pmatrix} \mapsto \begin{pmatrix} \cos(\theta) & 0 & \sin(\theta) & 0 & 0 & 0 \\ 0 & \cos(\theta) & 0 & \sin(\theta) & 0 & 0 \\ -\sin(\theta) & 0 & \cos(\theta) & 0 & 0 & 0 \\ 0 & -\sin(\theta) & 0 & \cos(\theta) & 0 & 0 \\ 0 & 0 & 0 & 0 & 1 & 0 \\ 0 & 0 & 0 & 0 & 0 & 1 \end{pmatrix} \begin{pmatrix} x \\ p_x \\ y \\ p_y \\ z \\ \delta \end{pmatrix}, \tag{6.51}$$

where θ is the angle of rotation.

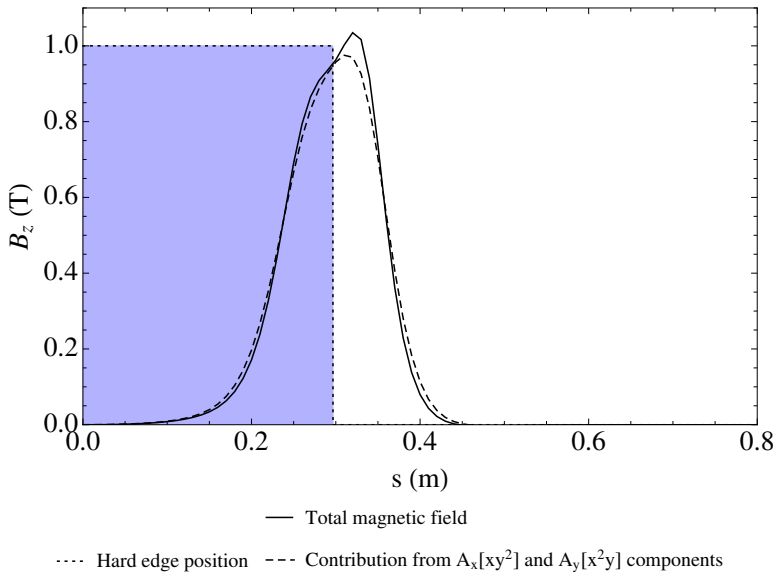

Figure 6.6: B_z field evaluated at x, y=30 mm, normalised to the magnet strength of MQXC.1R1. The resulting B_z field from the transverse vector potential terms $A_x[xy^2]$ and $A_y[x^2y]$ is shown to be a reasonable approximation at this position. The equivalent position of the hard edge model is overlaid.

To consider the realism of such a model a comparison must be made with the actual longitudinal component of the magnetic field. Equation 6.38 implies that the transverse vector potential are dominated by the terms xy^2 in A_x and yx^2 in A_y. In figure 6.6 the contribution to the B_z field from these terms using the generalised gradients which contribute to them is overlaid on the hard edge

model and B_z field data. It can be seen that these terms dominate the B_z field component.

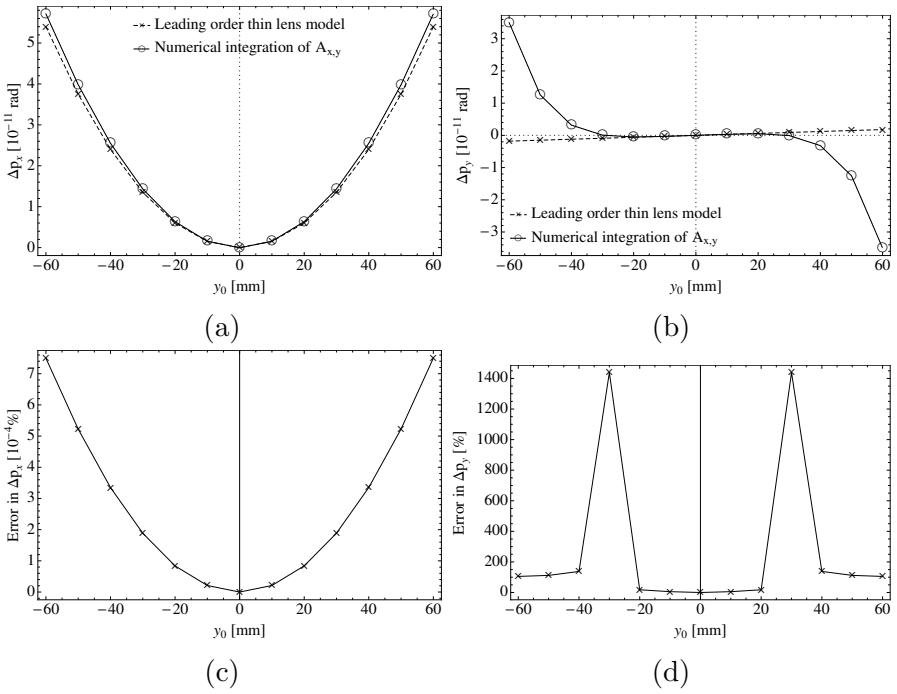

Figure 6.7: Numerical tracking through the B_z component of the fringe field compared with the leading order model, normalised to the magnet strength of MQXC.1R1. Initial conditions $(x, p_x, y, p_y, z, \delta) = (0.001\text{ m}, 0.0001, y_0, 0., 0., 0.)$. Comparisons of the change in (a) p_x, and (b) p_y. Residuals of these changes for the change in (c) p_x, and (d) p_y.

A direct test of the leading order model of the longitudinal magnetic field is performed by using direct numerical integration through the longitudinal component of the fringe field using the Wu-Forest-Robin integrator [107], shown in section 2.5.3. Numerically integrating through the B_z field component resulting from the transverse vector potential does not cause issues relating to comparing the canonical and mechanical momenta because the B_z field goes to zero at either end of the fringe field. This provides a direct comparison with the transfer map from the leading order effect. Figure 6.7 shows that there is reasonable agreement for the variation in p_x with respect to y with a maximum error of $10^{-3}\%$ at $y = 20$ mm. However, at amplitudes greater than 20 mm in y there are orders

of magnitude difference between the model and integration for the change in p_y. This study implies that the leading order model fails beyond a radius of 20 mm.

In summary, a two component model has been shown for the fringe fields in order to operate with the current hard edge magnet model, which contains the whole integrated b_2 multipole component of the transverse fields. The first component of the model considers the effect of the B_z field and is contained in the leading order model [164]. The second component of the model is the fringe multipole model which makes use of the generalised multipoles in section 6.2.1. For this second component it is necessary to take into account the total multipole errors which are not already included by the magnet error table used in the hard edge model. In addition the generalised multipoles for $m > 0$ are also included in this component. A summary of this model is shown in figure 6.8.

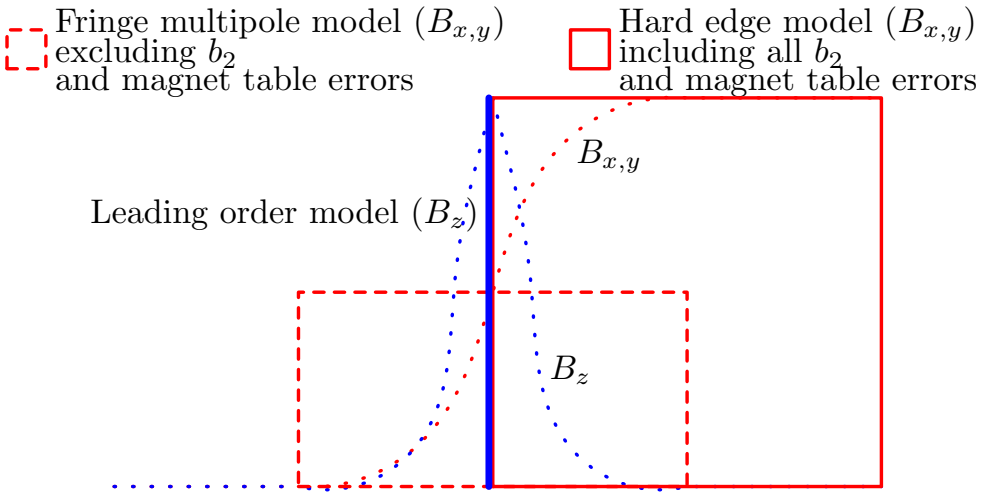

Figure 6.8: Summary of the fringe field model for the inner triplet quadrupoles. Blue indicates the longitudinal magnetic component of the fringe field. Red indicates the transverse magnetic component of the fringe field. The red solid box is the hard edge model containing all of the b_2 component of the magnet and the magnet table errors. The red dashed box is fringe multipole model containing the additional transverse kicks resulting from various multipole errors and the higher order $b_{n,m}$ multipoles. The blue line is the leading order model describing the effect of the longitudinal magnetic component.

6.3 Impact upon the dynamic aperture

The first dynamic aperture study, including a fringe field model, applied the leading order model [164], described in section 6.2.2, at the entrance and exit faces of the IT magnets for IR1 and IR5 in the SLHCv3.1b lattice [68]. In addition to the settings for the dynamic aperture studies described in section 5.1 IT magnets errors from table v6.6 were also included. This error table contains the multipole errors for the hard edge core of the magnet resulting from manufacture. For this study the second component of the fringe field model containing the additional transverse magnetic components of the fringe field was neglected. Furthermore, this study was performed without crab cavities and without beam-beam interaction.

Fringe fields included	Q_x	Q_y
None	62.31000	60.32000
Inner triplet of IR1 and IR5	62.30941	60.31942

Table 6.2: Tune variation resulting from the addition of the leading order fringe field model.

In the preliminary implementation of the fringe field model only the leading order model described in section 6.2.2 was used. This model was implemented as a new element in SixTrack; in both the one turn map and numerical tracking sections of the code. The inner triplet magnets in the model are sliced into 16 thin multipole magnets separated by drift spaces. The fringe field elements were placed before the first multipole slice and after the sixteenth multipole slice for each of the inner triplet magnets in IR1 and IR5 in the SLHCv3.1b lattice.

The fringe fields were seen to introduce a tune shift of approximately 0.2% compared to that of the hard edge lattice, as shown in table 6.2. In order to directly observe the effect of the fringe fields on dynamic aperture, the machine

working point must be corrected to remove this tune shift. If this correction were not performed then the dynamic aperture's dependence on the working point could not be disentangled from the effect of the fringe fields. A global correction of the tune was performed using a set of algorithms based upon normal form techniques in SixTrack [169], using the first set of focusing/ defocusing trim quadrupole magnets (MQT, see figure 2.23) in the arc between IR3 and IR4. These particular magnets were chosen to remove the possibility of breaking the phase advances required by the ATS scheme.

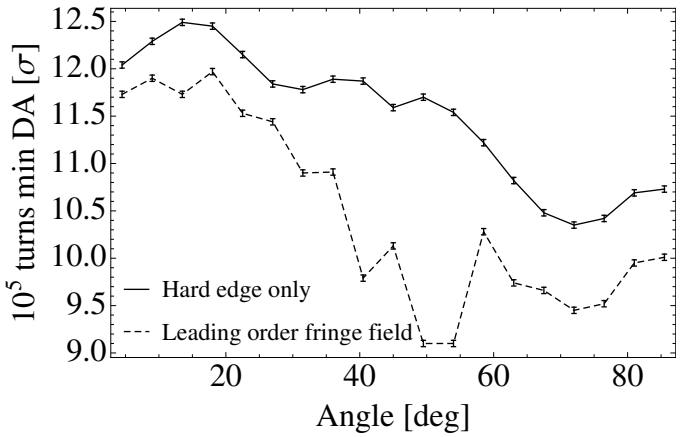

Figure 6.9: Impact of the leading order fringe field model applied to the inner triplet in IR1 and IR5 on minimum dynamic aperture. Model includes arc dipole and quadrupole errors in addition inner triplet errors.

An initial note about figure 6.9 is that the dynamic aperture for the hard edge model is significantly lower than those in chapter 5 which is a result of the addition of the inner triplet errors into the model. Figure 6.9 shows that the leading order fringe field model leads to a fall in the minimum of the minimum dynamic aperture of approximately 1.5σ after the global tune correction has been applied, indicating a significant effect. This is the first such study of dynamic aperture with fringe fields for any version of the LHC. From figure 6.7 it has already been shown that this leading order model is limited in its ability to describe the fields beyond 20 mm. This means that the dynamics from the fringe

field model are wrong at the location of the dynamic aperture (10σ) which at the IT magnets is of order 30 mm; where the normalised emittance is 3.75 mm mrad, $\beta \approx 20$ km and $\gamma_0 \approx 7078$.

6.4 Conclusion

A first study of the IT fringe fields reveals the need to consider the transverse fields as a solution to the Laplace equation in three rather than two dimensions and the presence of a longitudinal component to the magnetic field. An initial simplified model for the fringe fields using the multipole components of the transverse field and the leading order effect from the longitudinal magnetic field was devised. It was shown that within a radius of 20 mm the leading order fringe field model [164] was in reasonable agreement with numerical integration. A first dynamic aperture study using the leading order model [164] was also presented suggesting that the longitudinal field possibly leads to a 1.5σ drop in the minimum of the minimum dynamic aperture after a global tune correction. This is the first such study to be considered for any version of the LHC. However, there is a level of uncertainty on the reliability of this calculation because the dynamic aperture at the inner triplet magnets is at 30 mm which means it falls outside of the 20 mm radius over which the leading order model is valid. In order to overcome this limit additional terms would be required in the Hamiltonian description, however, this would remove the simplicity of the transfer map in its leading order form. It can be concluded that further study of these fringe fields is required in order to both understand their full effect and find any possible correction schemes to recover the resulting dynamic aperture loss. In the future, one might consider the fringe field model described in this chapter to be applied to the nominal LHC model in order to try to experimentally observe the effects of the fringe fields.

Chapter 7

Conclusion

The first question devised at the beginning of this thesis was,

"Which components of the crab cavity dynamics are important when considering the long term stability of the LHC upgrade?"

The context of this question was introduced in chapter 2. In this chapter the concepts of beam dynamics and luminosity for particle colliders were developed to show a need for a luminosity upgrade of the LHC (see section 2.2). The upgraded optics of the ATS scheme enabled a greater squeezing of the beams at the IP with little change to the nominal LHC optics (see section 2.3.2). In addition to this optics scheme, a crab cavity crossing scheme was shown to allow a control of the luminosity (see section 2.4).

In section 2.2.3 it was shown that non-linear components of an accelerator can lead to chaotic motion and the need to understand and define a machines stable aperture. In order to study such a stable (or dynamic) aperture, integration through the lattice of the accelerator is required. It was shown in section 2.5 that a number of different methods for integration were available. These integration methods have to balance numerical precision, physical precision and computational speed. In order to develop a crab cavity model which contained dynamics

relevant to the LHC it was decided to consider two approaches of development: Taylor maps and thin models.

In chapter 3, the development of a Taylor map crab cavity model was shown. A field fitting method was applied to field data created using a finite element solver of one of the cavity designs. This field fitting approach took the data and fitted it to an exact solution of the Helmholtz equation. From this fitted field a vector potential could be found forming a complete analytical Hamiltonian description of the cavity. Using a truncated power series library and a second order explicit integrator a Taylor map for the crab cavity was produced. This Taylor map exhibited a significant number of non-linear features resulting from both the transverse and longitudinal field variations. It was seen that an underlying issue of using a Taylor map for long term tracking was its lack of symplecticity.

In chapter 4 a series of symplectic thin models were formed from the general Hamiltonian developed to produce the Taylor map. In the rigid bunch and axial approximations the longitudinal field variations were ignored and only the transverse variation modelled. In section 4.1 three different models were introduced to represent this transverse variation; the simple kick model, RF multipole kick model and generalised RF multipole kick model. The methods to compute the multipole values were also derived and demonstrated in section 4.2 from which it was shown that there was some sensitivity to the method of measurement.

Comparison of the two model approaches was shown in section 4.3. It was found that, when evaluated at 20 mm, the RF multipole kick model contributed at the 1% level of the total kick and the additional terms of the generalised RF multipole kick model contributed at the level of 0.001%. Furthermore it was seen that to 0.001% there was exact agreement in the momentum kicks between the Taylor map and RF multipole kick model when calculating the RF multipole coefficients through the Helmholtz decomposition approach. At this 0.001% level

it was observed that the dynamics beyond the RF multipole kick model contained in the Taylor map could not be described by the generalised RF multipole kick model.

In chapter 5, a series of dynamic aperture studies were performed and it was shown that under all the different models for the crab cavity the dynamic aperture was consistent to the case without crab cavities within a tolerance of 1σ. Through frequency map analysis it was found that no additional loss mechanisms were introduced by the crab cavities which suggested a reason why this variation in dynamic aperture was small. The Taylor map was successfully used for the dynamic aperture study despite the known symplectic error and shown to confirm an agreement with the RF multipole kick model within 0.4σ across the minimum dynamic aperture. Furthermore it was shown that the sensitivity to the RF multipole coefficient calculation was similarly of this order.

In conclusion to the first question, from this study it has been shown that the use of the RF multipole kick model used to describe the crab cavity dynamics contains the more significant dynamics relevant to the dynamic aperture in the HL-LHC within a tolerance of 0.4σ. To improve beyond this tolerance improvements in the RF multipole calculation would be required. On the scale of the HL-LHC project this means that the RF multipole model should be applied for simulations involving crab cavities and that no further model is required. In terms of wider applications this work provides a tool kit from which to consider cases where the transverse dynamics of a cavity may play an important role, for example those arising from higher order modes in accelerating cavities. One such conceivable project where this might apply is the European Spallation Source project [170].

The second question posed was,

"Are fringe fields important when considering the long term stability of the LHC upgrade?"

In chapter 6 a preliminary study determined a method by which the fringe field might be modelled within the existing simulation framework. In order for the model to be symplectic the Hamiltonian was split to give two separate models; one considering the transverse and the other the longitudinal components of the magnetic field. It was proposed to model transverse components of the magnetic field with a kick model similar to that of the generalised RF multipole kick model based upon the generalised gradient description given in [123]. The longitudinal component was simulated using a leading order model described in [164]. It was found that this leading order model failed beyond a radius of 20 mm when compared with numerical integration. A preliminary dynamic aperture study performed using the leading order approximation applied to the inner triplet quadrupole magnets in IR1 and IR5 indicated a significant fall of 1.5σ in the minimum dynamic aperture after a global tune correction. However, there remains some uncertainty on the validity of this result as the dynamic aperture occurred at a radius of 30 mm inside the inner triplet which is beyond the validity of the leading order model. After investigating the second question it can be concluded that further investigation into the impact of fringe fields on the HL-LHC is required.

In terms of further work to extend and apply these studies two areas of research are considered. The first is to make use of the experience with Taylor maps and RF cavities and apply them to machines in which the there is high sensitivity to the transverse kick from a cavity, for example the spoke cavities in the ESS. The second study is to take the fringe field work and go back to look at the nominal LHC and attempt to see the contribution of the fringe fields to nonlinear coupling at collision and compare with direct experimental measurements.

There are also a number of unanswered questions from these studies, including:

1. Can a more complete symplectic cavity model be made to include the additional dynamics observed in the Taylor maps?

2. Can an indirect measurement be made of the impact of symplectic measure on a dynamic aperture measurement?

3. What are the mechanisms and properties associated with particles that undergo tune wandering?

4. Do fringe fields really matter for the HL-LHC and if so can they be corrected for in the HL-LHC optics?

In conclusion, this work provides insight into methods by which to consider improving the precision of element descriptions in particle accelerators. A methodology for devising models with precise descriptions relevant to the whole accelerator of new accelerator elements has been presented. It has been shown that the most precise description of an element is not always the more relevant to the whole accelerator.

Bibliography

[1] J J Thomson. XL. Cathode Rays. *The London, Edinburgh and Dublin Philosophical Magazine and Journal of Science*, 1897.

[2] J Cockcroft and E Walton. Artificial production of fast protons. *Nature*, **129**:242, 1932.

[3] N R S Tait and R G P Voss. The nuclear structure facility 20/30 MV tandem accelerator. *Part. Accel.*, **5**:181–197, 1973.

[4] G Ising. Prinzip einer methode zur herstellung von kanalstrahlen hoher voltzahl. *Arkiv för matematik, astronomi och fysik*, **18**(30):1–4, 1924.

[5] R Widerøe. Ueber ein neues prinzip zur herstellung hoher spannungen. *Archiv fuer Elektronik und Uebertragungstechnik*, **21**(4):387, 1928.

[6] E Lawrence. Method and apparatus for the acceleration of ions. US PATENT 1,948,384, 1934.

[7] E M Mcmillan. Synchro-cyclotron. US PATENT 2,615,129, 1952.

[8] CERN. Synchrocyclotron. http://home.web.cern.ch/about/accelerators/, 2012.

[9] E Courant, M Livingston, and H Snyder. The strong-focusing synchrotron-A new high energy accelerator. *Phys. Rev.*, **88**:1190, 1952.

[10] G Margaritondo. A Primer in Synchrotron Radiation: Everything You Wanted to Know about SEX (Synchrotron Emission of X-rays) but Were Afraid to Ask. *Journal of Synchrotron Radiation*, **2**(3):148–154, 1995.

[11] CERN. Intersecting Storage Rings. http://cern.ch/hedberg/home/afs/afs.html, 2012.

[12] K Johnsen. The ISR and accelerator physics. *Part. Accel.*, **18**:167–182, 1986.

[13] Fermilab. Tevatron complex. http://www.fnal.gov/, 2012.

[14] CERN. LEP Design Report. Technical report, CERN-LEP/84-01, 1984.

[15] P Higgs. Spontaneous Symmetry Breakdown without Massless Bosons. *Phys. Rev.*, **145**(4):1156–1163, 1966.

[16] O Brüning, P Collier, P Lebrun, et al. LHC design report (Volume I, The LHC main ring). Technical report, CERN-2004-003, 2004.

[17] F Zimmermann. LHC: The Machine. In *Proceedings of the SLAC Summer Institute 2012*, 2012.

[18] ATLAS Collaboration. ATLAS detector and physics performance: Technical design report. Technical report, CERN/LHCC 99-14, 1999.

[19] CMS Collaboration. CMS Physics: Technical Design Report Volume 1: Detector Performance and Software. Technical report, CERN/LHCC 2006-001, 2006.

[20] LHCb Collaboration. LHCb reoptimized detector design and performance: Technical design report. Technical report, CERN/LHCC 2003-030, 2003.

[21] ALICE Collaboration. ALICE: Technical proposal for a large ion collider experiment at the CERN LHC. Technical report, CERN/LHCC 95-71, 1995.

[22] CERN. LHC schematic. http://lhc-machine-outreach.web.cern.ch/lhc-machine-outreach/images/lhc-schematic.jpg, 2013.

[23] M Lamont. Long shut down plan. In *7th HL-LHC Coordination Group*, 2013.

[24] K Foraz. LS1 general planning and strategy for LHC, LHC injectors. In *Proceedings of the LHC perfomance workshop, Chamonix, 2012*, 2012.

[25] R Garoby, H Damerau, S Gilardoni, et al. Status and plans for the upgrade of the LHC injectors. In *Proceedings of the 2013 International Particle Accelerator conference, Shanghai, China*, 2013.

[26] G Apollinari, W Fischer, M Nessi, et al. LHC Collimation Review 2013, Report of the review committee. Technical report, CERN, 2013.

[27] CERN. CERN accelerator complex. https://espace.cern.ch/liu-project/, 2011.

[28] G Hill. On the part of the motion of the lunar perigee which is a function of the mean motions of the sun and moon. *Acta Math*, **8**(1):1–36, 1886.

[29] A Chao, M Tigner, et al. *Handbook of Accelerator Physics and Engineering, 3rd printing*. World Scientific Publishing, 2009.

[30] A Chao. *Physics of collective beam instabilities in high energy accelerators.* Wiley, 1993.

[31] R Wolf. Field error naming conventions for LHC magnets. Technical Report LHC-M-ES-0001 rev 3.0, CERN, 2001.

[32] H Wiedemann. *Particle Accelerator Physics.* Springer, 3rd edition, 2007.

[33] W Herr and B Muratori. Concept of luminosity in particle colliders. In *Proceedings of the CAS 2010 lectures, Varna*, 2010.

[34] W Herr. Beam-beam interactions. In *Proceedings of CAS intermediate course on accelerator physics, Zeuthen, Germany*, 2003.

[35] A Piwinski. Satellite resonances due to beam-beam interaction. *IEEE Trans. Nucl. Sci.*, **24**(3):1408–1410, 1977.

[36] A Valishev and G Stancari. Electron Lens as Beam-Beam Wire Compensator in HL-LHC. *arXiv*, 2013.

[37] F Galluccio and F Schmidt. Slow particle loss in hadron colliders. In *Proceedings of EPAC 1992, Berlin*, 1992.

[38] R Ruth. Single particle dynamics and nonlinear resonances in circular accelerators. Technical report, SLAC-PUB-3836, 1985.

[39] R Tomás Garcia. From Farey sequences to resonance diagrams. *Phys. Rev. Special Topics Accelerators and Beams*, **17**(014001), 2014.

[40] Y Papaphilippou. Linear imperfections and correction. In *Joint Universities Accelerator School*, 2007.

[41] R Bartolini and F Schmidt. Normal form via tracking or beam data. *Part. Accel.*, **59**(2):93–106, 1998.

[42] S White, E H Maclean, and R Tomás Garcia. Direct amplitude detuning measurement with AC dipole. *Phys. Rev. Special Topics Accelerators and Beams*, **16**:071002, 2013.

[43] L S Nadolski. Frequency map analysis: Refined fourier analysis for probing beam dynamics. In *Proceedings of NPAC 2011 lecture series*, 2011.

[44] H S Dumas and J Laskar. Global dynamics and long-time stability in Hamiltonian systems via numerical frequency analysis. *Phys. Rev. Lett.*, **70**(20):2975–2979, 1993.

[45] N Nekhoroshev. Behavior of Hamiltonian systems close to integrable. *Funct. Anal. Appl.+*, **5**(4):338–339, 1971.

[46] J Laskar. The chaotic motion of the solar system: A numerical estimate of the size of the chaotic zones. *Icarus*, **88**(2):266–291, 1990.

[47] Y Papaphilippou and F Zimmermann. Weak-strong beam-beam simulations for the Large Hadron Collider. *Phys. Rev. Special Topics Accelerators and Beams*, **2**(10):104001, 1999.

[48] J Laskar. Frequency map analysis and particle accelerators. In *Proceedings of the 2003 Particle Accelerator Conference, Portland USA*, 2003.

[49] M Giovannozzi. Proposed scaling law for intensity evolution in hadron storage rings based on dynamic aperture variation with time. *Phys. Rev. Special Topics Accelerators and Beams*, **15**(2):024001, 2012.

[50] E Mcintosh and R De Maria. The SixDesk run environment for SixTrack. sixtrack-ng.web.cern.ch/sixtrack-ng/, 2012.

[51] M Giovannozzi, W Scandale, and E Todesco. Prediction of long-term stability in large hadron colliders. *Part. Accel.*, **56**(LHC-Project-Report-45):195–225, 1996.

[52] G Benettin, L Galgani, A Giorgilli, et al. Lyapunov characteristic exponents for smooth dynamical systems and for hamiltonian systems; A method for computing all of them. Part 2: Numerical application. *Meccanica*, **15**(1):21–30, 1980.

[53] J Laskar, C Froeschlé, and A Celletti. The measure of chaos by the numerical analysis of the fundamental frequencies. Application to the standard mapping. *Physica D: Nonlinear Phenomena*, **56**(2):253–269, 1992.

[54] J P Koutchouk, G Sterbini, and K Ohmi. Increasing the integrated luminosity of SLHC by luminosity levelling via the crossing angle. In *Proceedings of the EPAC'08 conference, Genoa, Italy*, 2008.

[55] L Rossi and R De Maria. Summary session 8: High Luminosity (HL-LHC). In *Proceedings of the LHC perfomance workshop, Chamonix, 2011*, 2011.

[56] L Rossi *et al.* (HiLumi LHC collaboration). FP7 High Luminosity Large Hadron Collider Design Study. Technical report, FP7-INFRASTRUCTURES-2011-1, 2011.

[57] ATLAS Collaboration. Observation of a new particle in the search for the Standard Model Higgs boson with the ATLAS detector at the LHC. *Phys. Lett. B*, **716**:1–29, 2012.

[58] CMS Collaboration. Observation of a new boson at a mass of 125 GeV with the CMS experiment at the LHC. *Phys. Lett. B*, **716**:30–61, 2012.

[59] CMS Collaboration. Projected performance of an upgraded CMS detector at the LHC and HL-LHC: Contribution to the Snowmass process. *arXiv preprint arXiv:1307.7135*, 2013.

[60] ATLAS Collaboration. Projections for measurements of Higgs boson cross sections, branching ratios and coupling parameters with the ATLAS detector at a HL-LHC. Technical report, ATL-PHYS-PUB-2013-014, 2013.

[61] S Fartoukh. Breaching the phase I optics limitations for the HL-LHC. In *Proceedings of Chamonix 2011 workshop on LHC Perfomance*, 2011.

[62] F Zimmermann. HL-LHC: Parameter space, constraints & possible options. In *Proceedings of Chamonix 2011 workshop on LHC Perfomance*, 2011.

[63] L Rossi *et al.* (HiLumi LHC collaboration). 1st periodic HiLumi LHC report. Technical report, CERN-ACC-2013-022, 2013.

[64] K Oide and K Yokoya. The crab crossing scheme for storage ring colliders. *Phys. Rev. A*, **40**:315, 1989.

[65] R Bruce, A Lechner, and S Redaelli. HILUMI LHC: Beam halo simulations, Deliverable: D5.3. http://www.cern.ch/HiLumiLHC, 2013.

[66] S Dailler. Schematic layout of one LHC cell. Technical report, LHC-PHO-1999-259, 1999.

[67] L Deniau. FiDel magnet report MB. https://lhc-div-mms.web.cern.ch/lhc-div-mms/tests/MAG/Fidel/, 2009.

[68] S Fartoukh and R De Maria. Optics and layout solutions for HL-LHC with large aperture Nb_3Sn and NbTi inner triplets. In *Proceedings of the 2012 International Particle Accelerator Conference, New Orleans, USA*, 2012.

[69] G Papotti, R Alemany, R Miyamoto, et al. Experience with offset collisions in the LHC. In *Proceedings of the 2011 International Particle Accelerator Conference, San Sebastian, Spain*, 2011.

[70] S Fartoukh. Layout and optics solutions for the LHC insertion upgrade phase I. In *Proceedings of the 2010 International Particle Accelerator Conference, Kyoto, Japan*, 2010.

[71] A Verdier. Chromaticity. In *CAS - CERN Accelerator School : 5th Advanced Accelerator Physics Course, Rhodes, Greece*, 1993.

[72] R B Palmer. Energy scaling, crab crossing and the pair problem. Technical report, SLAC-PUB-4707, 1988.

[73] D A Edwards and M J Syphers. *An introduction to the physics of high energy accelerators*. Wiley, 1993.

[74] Y Sun, R Assmann, J Barranco Garcia, R Tomás Garcia, et al. Beam dynamics aspects of crab cavities in the CERN Large Hadron Collider. *Phys. Rev. Special Topics Accelerators and Beams*, **12**:101002, 2009.

[75] R Barlow, J S Berg, C Beard, et al. EMMA—The world's first non-scaling FFAG. *Nucl. Instrum. & Methods A*, **624**(1):1–19, 2010.

[76] H Padamsee, J Knobloch, and T Hays. *RF superconductivity for accelerators*. WILEY-VCH, 2011.

[77] G Burt. A four rod compact crab cavity for LHC. In *Proceedings of EuCARD 1st annual meeting, Rutherford Appleton Laboratory, UK*, 2010.

[78] K Nakanishi, Y Funakoshi, and M Tobiyama. Beam behaviour due to crab cavity breakdown. In *Proceedings of the 2010 International Particle Accelerator Conference, Kyoto, Japan*, 2012.

[79] G Burt. Introduction to RF cavities for accerators. In *Cockcroft Institute Academic Training*, 2009.

[80] R Calaga, E Ciapala, and E Jensen. Crab cavities for the LHC luminosity upgrade. Technical report, CERN, 2010.

[81] G Burt et al. 4 rod RF design. In *Proceedings of the 5^{th} LHC CC workshop, Geneva, Switzerland*, 2011.

[82] Q Wu. Double quarter wave resonator. In *Proceedings of the 6^{th} LHC CC workshop, Frascati, Italy*, 2012.

[83] J Delayen. Ridged waveguide and modified parallel bar. In *Proceedings of the 5^{th} LHC crab cavities workshop, Geneva, Switzerland*, 2011.

[84] R Calaga and R Tomás Garcia. LHC crab-cavity aspects and strategy. In *Proceedings of the 2010 International Particle Accelerator Conference, Kyoto, Japan*, 2010.

[85] I Ben-Zvi and J M Brennan. The quarter wave resonator as a superconducting linac element. *Nucl. Instrum. & Methods A*, **212**(1):73–79, 1983.

[86] Z Li. Compact HWSR crab cavity for LHC upgrade. Technical report, LHC-CC2010, CERN, 2010.

[87] J Delayen and H Wang. New compact TEM-type deflecting and crabbing rf structure. *Phys. Rev. Special Topics Accelerators and Beams*, **12**(6):062002, 2009.

[88] G Burt. Transverse deflecting cavities. In *Proceedings of the CERN accelerator school, Denmark*, 2012.

[89] B Hall, G Burt, J Smith, et al. Novel geometries for the LHC crab cavity. In *Proceedings of the 2010 International Particle Accelerator Conference, Kyoto, Japan*, 2010.

[90] S Belomestnykh, I Bazarov, V Shemelin, et al. Deflecting cavity for beam diagnostics at Cornell ERL injector. *Nucl. Instrum. & Methods A*, **614**(2):179–183, 2010.

[91] F Schmidt. Version 4.2: Single particle tracking code treating transverse motion with synchrotron oscillations in a symplectic manner. User's Reference Manual. Technical report, CERN, 2008.

[92] B Taylor. Methodus incrementorum directa & inversa. *Impenfis Gulielmi Innys*, 1717.

[93] A J Dragt. Lie methods for nonlinear dynamics with applications to accelerator physics. www.physics.umd.edu/dsat, 2011.

[94] R Kleiss, F Zimmermann, and F Schmidt. The use of truncated Taylor maps in dynamic aperture studies. *Part. Accel.*, **41**:117–132, 1993.

[95] W Wan, C Johnstone, J Holt, et al. The influence of fringe fields on particle dynamics in the Large Hadron Collider. *Nucl. Instrum. & Methods A*, **427**:74–48, 1999.

[96] A Wolski, J Gratus, and R Tucker. Symplectic integrator for s-dependent static magnetic fields based on mixed-variable generating functions. *Journal of Instrumentation*, **7**(P04013), 2012.

[97] A Einstein. On the electrodynamics of moving bodies. *Ann. Phys. (Leipzig)*, 1905.

[98] J D Jackson. *Classical Electrodynamics, 3rd Ed.* Wiley, 2007.

[99] A Wolski. Linear Dynamics: Lecture 2. In *Cockcroft Institute Academic Training*, 2012.

[100] L D Landau and E M Lifshitz. *Mechanics: Volume 1 of Course of theoretical physics*. Pergamon Press, 1976.

[101] J Rees. Symplecticity in beam dynamics: An introduction. Technical report, SLAC-PUB-9939, 2003.

[102] V I Arnold. *Mathematical Methods of Classical Mechanics*. Springer, 1978.

[103] A N Kolmogorov. *Elements of the theory of functions and functional analysis*, volume 1. Graylock Press, Rochester, 1957.

[104] J W Gibb. On the fundamental formula of statistical mechanics, with applications to astronomy and thermodynamics. *Proceedings of the Americal Association for the Advancement of Science*, **33**:57–58, 1884.

[105] Wolfram Research, Inc., Champaign, Illinois. Mathematica Edition: Version 9.0, 2012.

[106] R Ruth. A canonical integration technique. *IEEE Trans. Nucl. Sci.*, **NS-30**(4):2669–2671, 1983.

[107] Y Wu, E Forest, and D Robin. Explicit symplectic integrator for s-dependent static magnetic field. *Phys. Rev. E*, **68**(4):046502, 2003.

[108] E Forest. *Beam dynamics: A new attitude and framework*. Taylor & Francis, 1998.

[109] A Wolski. Nonlinear single particle dynamics in high energy accelerators: Part 3. In *Cockcroft Institute Academic Training*, 2009.

[110] A Wolski. Nonlinear single particle dynamics in high energy accelerators: Part 4. In *Cockcroft Institute Academic Training*, 2009.

[111] H Yoshida. Construction of higher order symplectic integrators. *Physics Letters A*, **150**(5):262–268, 1990.

[112] L Schachinger and R Talman. TEAPOT: A thin-element accelerator program for optics and tracking. *Part. Accel.*, **22**:35–56, 1987.

[113] K Heinemann, G Ripken, and F Schmidt. Construction of nonlinear symplectic six-dimensional thin-lens maps by exponentiation. *arXiv preprint acc-phys*, 1995.

[114] H Grote and F Schmidt. MADX: An upgrade from MAD8. In *Proceedings of the 2003 Particle Accelerator Conference, Portland USA*, 2003.

[115] M Berz and K Makino. Cosy Infinity version 9. *Nucl. Instrum. & Methods A*, **558**:346–350, 2006.

[116] R Kleiss, F Schmidt, and F Zimmermann. The use of truncated Taylor maps in dynamic aperture studies. *Part. Accel.*, **41**:117–132, 1993.

[117] R Kleiss, F Schmidt, and Y Yan. On the feasibility of tracking with differential-algebra maps in long-term stability studies for large hadron colliders. Technical report, CERN SL/92-02 (AP), 1992.

[118] E Forest. Geometric integration for particle accelerators. *J. Phys. A*, **39**(19):5321, 2006.

[119] D Abell. Numerical computation of high-order transfer maps for RF cavities. *Phys. Rev. Special Topics Accelerators and Beams*, **9**(5):052001, 2006.

[120] D Abell. Models and high-order maps for realistic RF cavities using surface field data. In *Proceedings of the 2010 International Particle Accelerator Conference, Kyoto, Japan*, 2010.

[121] ANSYS. HFSS. http://www.ansys.com/, 2011.

[122] A Grudiev. Non-linearity of deflecting field of LHC-CC11. In *Proceedings of the LHC crab cavities workshop, CERN, 2011*, 2011.

[123] C E Mitchell and A J Dragt. Accurate transfer maps for realistic beam-line elements: Straight elements. *Phys. Rev. Special Topics Accelerators and Beams*, **13**:064001, 2010.

[124] M Venturini and A Dragt. Accurate computation of transfer maps from magnetic field data. *Nucl. Instrum. & Methods A*, **427**(1):387–392, 1999.

[125] A Grudiev. Convergence studies on RF multipoles. (private communication), 2012.

[126] U Grenander. *Probability and Statistics: The Harald Cramér Volume*. Wiley, 1959.

[127] Z Li et al. LARP cavity developments. Technical report, LHC-CC10, CERN, Geneva, 2010.

[128] G Ripken and F Schmidt. A symplectic six-dimensional thin-lens formalism for tracking. Technical report, CERN/SL/95-12 (AP), 1995.

[129] A Wolski. Linear Dynamics: Lecture 4. In *Cockcroft Institute Academic Training*, 2012.

[130] E Forest, F Schmidt, and E McIntosh. Introduction to the polymorphic tracking code. Technical report, CERN–SL–2002–044 (AP), 2002.

[131] M Berz. Differential algebraic description of beam dynamics to very high orders. Technical report, SSC-152, 1988.

[132] M Lee and A Stepanov. The standard template library. Technical report, HP Laboratories, 1995.

[133] K Makino and M Berz. COSY INFINITY Version 9. *Nucl. Instrum. & Methods A*, **558**(1):346–350, 2004.

[134] D R Brett, R B Appleby, G Burt, et al. Particle trajectories in a 4 rod crab cavity. *Nucl. Instrum. & Methods A*, **734**(A), 2014.

[135] IEEE Computer Society. IEEE Standard for Floating-Point Arithmetic. Technical report, IEEE, 2008.

[136] H Goldstein, C P Poole, and J L Safko. *Classical Mechanics*. Addison-Wesley, 3rd edition, 2001.

[137] P Wilhem and E Lohrmann. Rounding errors in beam-tracking calculations. *Part. Accel.*, **19**:99–105, 1986.

[138] J Barranco Garcia, R Calaga, R De Maria, et al. Study of multipolar RF kicks from the main deflecting mode in compact crab cavities for LHC. In *Proceedings of the 2012 International Particle Accelerator Conference, New Orleans, USA*, 2012.

[139] A M Lyapunov. The general problem of motion stability. *Mathematical Society of Kharkov*, 1892.

[140] W K H Panofsky and W A Wenzel. Some considerations concerning the transverse deflection of charged particles in radiofrequency fields. *Rev. Sci. Instrum.*, **27**:967, 1956.

[141] H Burkhardt, M Giovannozzi, and T Risselada. Tracking LHC models with thick lens quadrupoles: Results and comparisons with the standard thin lens tracking. In *Proceedings of the 2012 International Particle Accelerator Conference, New Orleans, USA*, 2012.

[142] F Christoph Iselin. The MAD Program: Physical Methods Manual. Technical report, CERN, 1994.

[143] D A Goldberg and G R Lambertson. Dynamic devices. A primer on pickups and kickers. *AIP Conf. Proc.*, **249**(1):537–600, 1992.

[144] L Deniau and A Latina. Evolution of MAD-X in the framework of LHC upgrade studies. In *Proceedings of the 2012 International Particle Accelerator Conference, New Orleans, USA*, 2012.

[145] F Schmidt. Dynamic aperture study for LHC Version 4.1. Technical report, LHC Project Note 30, 1994.

[146] S Fartoukh. An Achromatic Telescopic Squeezing (ATS) scheme for the LHC upgrade. In *Proceedings of the 2011 International Particle Accelerator Conference, San Sebastian, Spain*, 2011.

[147] P Hagen, M Giovannozzi, J P Koutchouk, et al. WISE: A simulation of the LHC optics including magnet geometrical data. Technical report, LHC Project Report 1123, 2008.

[148] L Bottura, T Pieloni, W Scandale, et al. Warm-cold magnetic field correlation in the LHC main dipoles. Technical report, LHC Project Note 326, 2003.

[149] L Bottura, S Fartoukh, V Granata, et al. A strategy for sampling the field quality of the LHC dipoles. Technical report, LHC Project Report 737, 2004.

[150] M Giovannozzi, R De Maria, S Fartoukh, et al. Dynamical aperture studies for the CERN LHC: Comparison between statistical assignment of magnetic field errors and actual measured field errors. In *Proceedings of EPAC 2006, Edinburgh, Scotland*, 2006.

[151] H Grote, F Schmidt, and L H A Leunissen. LHC dynamic aperture at collision. Technical report, LHC-Project-Note-197, 1999.

[152] M Giovannozzi and E Mcintosh. Parameter scans and accuracy estimates of the dynamical aperture of the CERN LHC. Technical report, LHC Project Report 925, 2006.

[153] M Hayes, F Schmidt, and E McIntosh. The influence of computer errors on dynamic aperture results using SixTrack. Technical report, LHC Project Note 309, 2003.

[154] Y Papaphilippou, J Wei, and R Talman. Deflections in magnet fringe fields. *Phys. Rev. E*, **67**(046502), 2003.

[155] M Allitt, M Karppinen, W Venturini-Delsolaro, et al. Field quality and hysteresis of LHC superconducting corrector magnets. In *Proceedings of EPAC 2004, Lucerne, Switzerland*, 2004.

[156] J Barranco Garcia and R Tomás Garcia. RF Multipoles: Modeling and impact on the beam. In *Proceedings of the 2nd Joint HiLumi LHC-LARP Annual Meeting*, 2012.

[157] R Calaga. Crab cavities for the LHC upgrade. In *Proceedings of the LHC perfomance workshop, Chamonix, 2012*, 2012.

[158] Y Chin. Effects of non-zero dispersion at crab cavities on the beam dynamics. In *Proceedings of the International Workshop on Accelerators for Asymmetric B-Factories, KEK, Tsukuba, Japan*, 1990.

[159] R Bartolini and F Schmidt. SUSSIX: A computer code for frequency analysis of non-linear betatron motion. Technical report, CERN SL/Note 98-017 (AP), 1998.

[160] R B Blackmad and J W Tukey. Particular pairs of windows. *The measurement of power spectra, from the point of view of communications engineering*, pages 95–101, 1959.

[161] R Bartolini, A Bazzani, M Giovannozzi, et al. Tune evaluation in simulations and experiments. *Part. Accel.*, **52**(3):147–178, 1996.

[162] H A Enge. Deflecting magnets. *Focusing of charged particles*, 1967.

[163] HiLumi collaboration. HL-LHC main parameters and assumptions. https://espace.cern.ch/HiLumi/WP2/Wiki/HL-LHC2014.

[164] E Forest and J Milutinović. Leading order hard edge fringe fields effects exact in $(1+\delta)$ and consistent with Maxwell's equations for rectilinear magnets. *Nucl. Instrum. & Methods A*, **269**(3):474–482, 1988.

[165] E Todesco et al. MQXF cross section. https://espace.cern.ch/HiLumi/WP3/SitePages/MQXF.aspx, 2013.

[166] E H Maclean. Discussions on LHC non-linear coupling studies. (private communication), 2014.

[167] S Kelly, M Thomas, R B Appleby, et al. Study of the impact of the fringe fields of the large aperture triplets on the linear optics of the HL-LHC. In *Proceedings of the 2013 International Particle Accelerator conference, Shanghai, China*, 2013.

[168] B Dalena et al. Inner triplet fringe field fitting data. (private communication), 2013.

[169] W Scandale, F Schmidt, and E Todesco. Compensation of the tune shift in the LHC, using the normal form techniques. *Part. Accel.*, **35**:53–81, 1991.

[170] H Lengeler. The European spallation source study. *Nucl. Instrum. & Methods B*, **139**:82–90, 1998.